
SEVENTH RECENT ADVANCES IN QUANTITATIVE REMOTE SENSING

Auditori de Torrent, Spain
23 – 27 September 2024

Editor

José A. Sobrino
Global Change Unit
Universitat de València, Spain

Published by
Publicacions de la Universitat de València.
C/del Batxiller, 1-1
46010 València
publicacions@uv.es

SEVENTH RECENT ADVANCES IN QUANTITATIVE REMOTE SENSING

Edited by
José A. Sobrino
Universitat de València, Spain

Publication: G. Sòria

Copyright © 2025 by the Authors

This is an open Access article under the Creative Commons Attribution (CC BY-NC-ND)
<https://creativecommons.org/licenses/by-nc-nd/4.0/>



ISBN: TBC

Preface

The Seventh International Symposium on Recent Advances in Quantitative Remote Sensing was held in Torrent, Spain from 23 to 27 September 2024. It was sponsored and organized by the Global Change Unit (GCU) from the Image Processing Laboratory (IPL), University of Valencia (UVEG), Spain. Other sponsors include:

- City Council of Torrent (Spain);
- L'Auditori Torrent (Spain);
- European Space Agency (ESA);
- National Aeronautics and Space Administration (NASA);
- EOLAB;

This Symposium addressed the scientific advances in quantitative remote sensing in connection with real applications. Its main goal was to assess the state of the art of both theory and applications in the analysis of remote sensing data, as well as to provide a forum for researcher in this subject area to exchange views and report their latest results. In this book 20 of the 143 contributions presented in both plenary and poster sessions are arranged according to the scientific topics selected. The papers are ranked in the same order as the final programme.

To conclude, I would particularly like to thank the participants who have contributed to constructive discussions and the members of the International Scientific Committee, who greatly contributed to select the papers presented at the Symposium providing an attractive scientific programme. The success is also due to the efforts made by the Organizing Committee. Many thanks to all of them.

José A. Sobrino
Symposium Chairperson
Global Change Unit,
Universitat de València

Valencia, 2025

International Scientific Committee:

Chairperson:

J. A. Sobrino University of Valencia, Spain

Members:

G. Asrar	University of Maryland, USA
F. Baret	INRAE, Avignon, France
G. Chehbouni	IRD, France
G. Dedieu	CESBIO, Toulouse, France
M. Drinkwater	European Space Agency, The Netherlands
D. Ghent	University of Leicester, UK
A. Gillespie	University of Washington, USA
R. O. Green	NASA, JPL, Pasadena, USA
G. Gutman	NASA, Washington, D. C., USA
O. Hagolle	CESBIO, Toulouse, France
S. Hook	NASA, JPL, USA
A. Huete	University of Technology, Sydney Australia
G. Hulley	NASA, JPL, USA
Y. Kerr	CESBIO, Toulouse, France
B. Koetz	European Space Agency, Italy
M. Langsdale	King's College London, UK
Z.-L. Li	University of Strasbourg, France
S. Liang	University of Maryland, USA
M. Menenti	Delft University of Technology, The Netherlands
J. Moreno	University of Valencia, Spain
F. Nerry	University of Strasbourg, France
A. Olivos	INRAE, Avignon, France
A. Prata	CSIRO, Australia
J. Privette	NOAA, NCDC, USA
M. Rast	ISSI, Switzerland
H. Ren	Peking University, China
J.-L. Roujean	CESBIO, Toulouse, France
A. Royer	University of Sherbrooke, Canada
Z. Su	University of Twente, The Netherlands
B.-H. Tang	IGSNRR/CAS, Beijing, China
C. J. Tucker	NASA, USA
E. Vermote	NASA, USA
J. P. Wigneron	INRAE, Bordeaux, France
H. Wu	LREIS, IGSNRR, Beijing, China
P.J. Zarco-Tejada	IAS-CSIC, Spain

Organizing Committee:

Chairperson:

P. Gómez Symposium, Torrent, Spain

Members:

J. C. Jiménez	D. Skoković	D. Salinas	L. Wei
G. Soria	R. Llorens	A. Sobrino-Gómez	X. Li
B. Franch	V. Crisafulli	L. De la Fuente	Y. Julien
F. Della Bellver	S. Gimeno	I. Moletto-Lobos	

CONTENTS

Preface

iii

The Methods for the Retrieval of Land Surface Temperature in Central Shijiazhuang Using ASTER Data	1
Biao Zeng, Guo-fei Shang, Ye-lin Shen, Yu-jia Tian, Xia Zhang, Zheng-hong Yan	
VALENSAT project	7
José Antonio Sobrino, Sergio Gimeno, Virginia Crisafulli, Álvaro Sobrino-Gómez, Drazen Skokovic	
Estimation of Soil Organic Carbon on the Qinghai–Tibet Plateau Using a Machine Learning Model Driven by Multi-source Remote Sensing	13
Qi Chen, Wei Zhou, Wenping Yu, Keming Wang	
Exploring Machine Learning Techniques for Temporal Forest Cover Classification in Burned Areas: A comparative Study	17
C. Iranzo, F. Pérez-Cabello	
Feasibility to derive new carbon fluxes products from EUMETSAT satellites in LSA SAF	23
A. Jiménez-Guisado, F.J. García-Haro, M. Campos-Taberner, B. Martínez, S. Sánchez-Ruiz, M.A. Gilabert	
Analysis of the relation of phytoplankton, temperature and salinity in the Western Mediterranean Sea using data DeepESDL cubes	27
Elena Martínez-Mateo, Ana B. Ruescas, Yasir Hassan Khachoo	
Advances on Spanish ecosystem dynamics by combining 20 years of daily GPP and nonlinear embedding method	31
B. Martínez, S. Sánchez-Ruiz, M. Campos-Taberner, A. Jiménez, F. J. García-Haro, M. A. Gilabert	
Surface soil organic carbon estimation based on habitat patches in southwest China	36
Jieyun Xiao, Wei Zhou, Wenping Yu, Ting Wang, Yao Peng	
Fusion of EO and in situ Data for estimating GPP and RECO	41
P.C. Silvestro; Maria P. González-Dugo; M. Muñoz-Gomez; N. Grosso; P. Marti-Rocafull	
Evaluating S-SEBI and SEBS estimates of evapotranspiration at San Rossore (ITALY)	48
Jerzy Piotr Kabala, José Antonio Sobrino, Virginia Crisafulli, Drazen Skokovic, Giovanna Battipaglia	
Detection and Automatic Extraction of the Valencian Coastline Using Sentinel-2	54
Josep Marí Cabrera, Ana B. Ruescas	
A New Remote Sensing Methodology for Estimating Frost Intensity and Damage on Citrus Crops: A Case Study of the Valencian Community	58
S. Gimeno, V. Crisafulli, Á. Sobrino-Gómez, J. A. Sobrino	
Spatial and Temporal Evolution Characteristics of Urban Heat Island in Beijing and Dalian Based on Multi-source Data	64
Yaru Meng, Caixia Gao, Enyu Zhao, Wan Li, Wenping Yu	

Spatiotemporal Evolution and Driving Forces Analysis of the Urban Heat Island in Shijiazhuang	70
Yue Liu, Ruo-han Chen, Xia Zhang, Ce Zhang, Yi-ran Tian, Guo-fei Shang	
The Methods for the NDVI time series reconstruction in North China Plain Using FY-3D data	76
Xiaoxia Hou, Guo-fei Shang, Xia Zhang, Zheng-hong Yan, Ce Zhang	
Remote Sensing Retrieval of Soil Moisture by Using Sentinel-1 SAR Data: A Case Study of Lushan County, Sichuan, China	82
Chen Lu, Xia Zhang, Guofei Shang, Yinhong Xu, Zhaoyang Bai, Yujia Tian	
Research on technology and applications of China's next generation environmental monitoring satellite	87
Fan Mo, Jose Sobrino, Yanhe Yin, Yilan Mao, Jin Huang, Xinwei Zhang, Haiyi Cao, Hua Li	
The new EUMETSAT missions: continuity of LSA SAF vegetation service	92
F.J. García-Haro, M. Campos-Taberner, B. Martínez, A. Jiménez-Guisado, S. Sánchez-Ruiz, M.A. Gilabert, J. Sánchez-Zapero, F. Camacho, E. Martínez-Sánchez	
Developing a new algorithm for the generation of SEVIRI/MSG vegetation products	97
A. Jiménez-Guisado, F.J. García-Haro, M. Campos-Taberner, B. Martínez, S. Sánchez-Ruiz, M.A. Gilabert, J. Sánchez-Zapero, F. Camacho, E. Martínez-Sánchez	
The SpaFLEX-IMP project: Spanish FLEX-S3 Mission Calibration and Validation Plan Implementation	102
R. Díaz-Delgado, P. J. Gómez-Giráldez, M. Jiménez, M ^a P. Cendrero-Mateo, S. Van Wittenberghe, J. J. Peón, A. Monchofí-Estornell, J. Delegido, J. F. Moreno	
AUTHOR INDEX	109

The Methods for the Retrieval of Land Surface Temperature in Central Shijiazhuang Using ASTER Data

Biao Zeng, Guo-fei Shang*, Ye-lin Shen, Yu-jia Tian, Xia Zhang, Zheng-hong Yan
Hebei GEO University
zhangxia396@hgu.edu.cn

ABSTRACT – Land Surface temperature (LST) is a critical parameter for studying global climate change, monitoring agricultural drought, and assessing the ecological environment. This study selected the central urban area of Shijiazhuang City as the research area and used ASTER imagery to perform surface temperature retrieval with the reference channel method, split-window algorithm, and temperature-emissivity separation algorithm. Authenticity checks and model accuracy evaluations were conducted based on meteorological data, LANDSAT surface temperature retrieval data, and MODIS surface temperature products. (1) The overall trends of the retrieval results from the three algorithms are quite similar, with all results falling within the range of 274K to 310K. (2) The differences between the surface temperature retrieval results from the three algorithms and the average surface air temperature are between 3.87°C and 4.08°C, ensuring the basic accuracy of the retrieval. (3) The fitting results of the retrieval from the three algorithms indicate that the degree of linear fit to surface temperature by different algorithms is essentially consistent, and the pixel values of the retrieval results from the three algorithms exhibit spatial consistency. (4) The correlation analysis with the MODIS land temperature product shows that all three algorithms have a moderate to high correlation with the MODIS land temperature product, with good correlation, and the R² values are 0.7174, 0.7163, and 0.7226, respectively. Based on the above conclusions, it is indicated that the best method for surface temperature retrieval in the central urban area of Shijiazhuang City is the temperature-emissivity separation algorithm.

Keywords – Thermal Infrared Remote Sensing, ASTER Data, Temperature-to-Emissivity Separation

1 INTRODUCTION

In regional and even global scales, surface temperature is an essential physical quantity in the processes of surface energy and water balance. Thermal infrared remote sensing technology, characterized by its wide coverage, abundant information, rapid update speed, and high resolution, is one of the most effective means for obtaining surface temperature information. (Li, 2016) The ASTER data possesses five high-resolution thermal infrared bands, with a spatial resolution of 90 meters for these bands, making ASTER data one of the datasets with higher resolution in the current field of thermal infrared remote sensing, which confers a significant advantage in the inversion of surface temperature.

Currently, there is relatively less research on surface temperature inversion methods based on ASTER remote sensing data, primarily due to the difficulty in obtaining precise atmospheric parameter information. The various inversion algorithms proposed for ASTER data mainly achieve surface temperature inversion by improving certain parameters within the algorithms (Ma 2023), such as surface emissivity and atmospheric transmittance. (Cheng, 2003) This study selects the reference channel method, the split-window algorithm (SW), and the temperature

and emissivity separation algorithm to perform surface temperature inversion using ASTER data. Additionally (Meng 2020), it employs LANDSAT data and MODIS land surface temperature product data to validate and compare these methods. (Dash 2002) The aim is to determine the optimal method for conducting surface temperature inversion in the central urban area of Shijiazhuang using remote sensing techniques, thereby providing theoretical and methodological support for high-precision dynamic monitoring of surface temperature in Shijiazhuang city.

2 MATERIALS AND METHODS

2.1 Research Area Overview

Shijiazhuang, the capital of Hebei Province, is situated at the junction of the Jing-Jin-Ji region, the Taihang Mountains, and the North China Plain, serving as a key link between North and Northwest China. This study concentrates on the central urban area of the city, including seven districts and covering about 2379 km², which is 15% of the total municipal area. The study area's location is shown in Figure1.

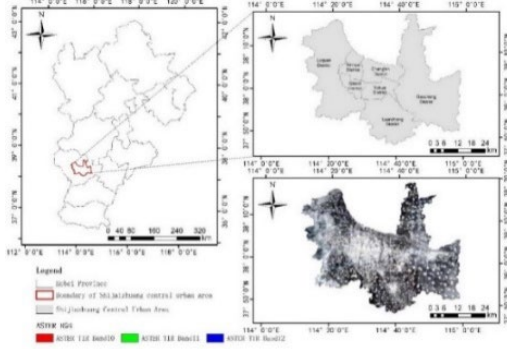


Figure 1 Overview Map of the Study Area

2.2 Data

This study utilized AST_L1T data from May 20, 2022, for the retrieval of land surface temperature, with the imagery being cloud-free and exhibiting good quality. On the same date, MOD021KM data were employed to estimate the atmospheric water vapor content. Furthermore, the MODIS China 1km land surface temperature daily product (MYD11_L2) was utilized to validate the land surface temperature inversion results derived from ASTER data. Landsat remote sensing imagery of the Shijiazhuang area, provided by the United States Geological Survey (USGS) on May 20, 2022, were also incorporated into the study. Meteorological data for Shijiazhuang City were sourced from the National Meteorological Data Center.

2.3 SYSTEM'S MAIN PRINCIPLES AND METHODS

2.3.1 Radiation Transfer Equation

The Radiative Transfer Equation (RTE) is the fundamental principle for the retrieval of LST in thermal infrared remote sensing. In the quantitative remote sensing retrieval techniques for LST, the RTE is considered the most core method. Assuming the ground is a Lambertian surface, the thermal radiative transfer equation can be simplified to Equation (1):

$$B_i(T_i) = (\epsilon_i B_i(T_s) + (1 - \epsilon_i) R_{at}^{\downarrow}) \tau_i + R_{at}^{\uparrow} \quad (1)$$

In this context, T_i represents the brightness temperature, T_s represents the surface temperature, ϵ_i represents the surface emissivity, τ_i represents the atmospheric transmittance, R_{at}^{\downarrow} represents the atmospheric downwelling radiation, R_{at}^{\uparrow} represents the atmospheric upwelling radiation.

2.3.2 Reference Channel Method

The reference channel method uses certain a priori knowledge to determine the emissivity corresponding to a specific spectral channel of the target object. Based on this emissivity, the actual temperature of the object can be determined, and from this, the emissivities of all other channels can be further calculated.

2.3.3 Split-Window Algorithm

In the field of remote sensing, the SW, proposed by (Mao,2006) based on ASTER data, is recognized for its high precision, achieving an accuracy of less than 1°C. This algorithm initially applies a linear simplification to the Planck function within the radiative transfer equation. Subsequently, it derives the surface temperature calculation formula for ASTER data's bands 13 and 14, as follows:

$$T_s = \frac{C_{14}(D_{13} + B_{13}) - C_{13}(D_{14} + B_{14})}{C_{14}A_{13} - C_{13}A_{14}} \quad (2)$$

Where: T_s represents the land surface temperature; A_{13} to D_{14} are the coefficients obtained for solving the equation, which serve as simplified coefficients to facilitate calculation. These coefficients can be derived according to Equation (3):

$$\begin{cases} A_{13} = 0.145236 \times \epsilon_{13} \times \tau_3 \\ B_{13} = 0.145236 \times T_{13} + 33.685 \times \tau_{13} \times \epsilon_{13} - 33.685 \\ C_{13} = (1 - \tau_{13}) \times (1 + (1 - \epsilon_{13}) \times \tau_{13}) \times 0.145236 \\ D_{13} = (1 - \tau_{13}) \times (1 + (1 - \epsilon_{13}) \times \tau_{13}) \times 33.685, \\ A_{14} = 0.13266 \times \epsilon_{14} \times \tau_{14} \\ B_{14} = 0.13266 \times T_{14} + 30.273 \times \tau_{14} \times \epsilon_{14} - 30.273 \\ C_{14} = (1 - \tau_{14}) \times (1 + (1 - \epsilon_{14}) \times \tau_{14}) \times 0.13266 \\ D_{14} = (1 - \tau_{14}) \times (1 + (1 - \epsilon_{14}) \times \tau_{14}) \times 30.273 \end{cases} \quad (3)$$

In the text: ϵ_{13} and ϵ_{14} represent the surface emissivity of the 13th and 14th bands; τ_{13} and τ_{14} are the atmospheric transmittances for the 13th and 14th bands, respectively; T_{13} and T_{14} refer to the brightness temperatures of the 13th and 14th bands, respectively.

2.3.3.1 Brightness Temperature Calculation

The calculation of brightness temperature is based on the Planck equation obtained from, and the brightness temperature can be obtained based on Equation (4):

$$T_i = c_2 / (\lambda_i h (1 + c_1 / \lambda_i^5 R_i)) \quad (4)$$

In the formula, λ_i represents the central wavelength corresponding to the 13th and 14th bands. For ASTER data, they are taken as $\lambda_{13} = 10.6\mu m$ and $\lambda_{14} = 11.3\mu m$; C_1 and C_2 are the first and second spectral constants, respectively taken as $C_1 = 1.19104356 \times 10^{-16} W \cdot m^2$ and

$C_2=1.4387685 \times 104 \mu\text{m} \cdot K$. R_i is the thermal radiance intensity of the land surface in the 13th and 14th bands ($\text{W} \cdot \text{m}^{-2} \cdot \text{sr}^{-1} \cdot \mu\text{m}$).

2.3.3.2 Estimation of Atmospheric Transmittance

This study utilizes MODIS data, which is from the same satellite and dated the same as the ASTER data, to estimate the atmospheric transmittance in the study area by imitating the correlation between atmospheric water vapor content and transmittance established by Mao Kebiao et al. using MODTRAN software as described in the literature. After performing a third-degree polynomial regression analysis on the simulated data, the mathematical relationship between atmospheric water vapor content and atmospheric transmittance for the 13th and 14th bands of ASTER data was obtained, specifically in Equations (5) and (6):

For the 13th band:

$$\begin{aligned} \tau_{13} &= 0.0044\omega^3 - 0.0374\omega^2 - 0.0125\omega + 0.8171 \\ R^2 &= 0.9997 \end{aligned} \quad (5)$$

For the 14th band:

$$\begin{aligned} \tau_{14} &= 0.0046\omega^3 - 0.0361\omega^2 - 0.0425\omega + 0.8600 \\ R^2 &= 0.9997 \end{aligned} \quad (6)$$

2.3.3.3 Estimation of Surface Spectral Emissivity

Mao Kebiao et al. conducted an in-depth study and analysis of the emissivity spectrum library provided by ASTER: within the ASTER 13th and 14th bands (10.15 to 10.95 micrometers and 10.95 to 11.65 micrometers), the emissivity of most land materials is higher than 0.9 and varies very little. The formulas for calculating emissivity are as shown in Equations (9) and (10)

$$\text{NDVI} = (R_{\text{nir}} - R_{\text{red}}) / (R_{\text{nir}} + R_{\text{red}}) \quad (7)$$

$$P_V = (\text{NDVI} - \text{NDVI}_S) / (\text{NDVI}_V - \text{NDVI}_S) \quad (8)$$

$$\varepsilon_{13} = 0.968 + 0.022P_V \quad (9)$$

$$\varepsilon_{14} = 0.970 + 0.020P_V \quad (10)$$

2.3.4 Temperature and Emissivity Separation Method

The TES method's challenge lies in determining temperature without knowing emissivity, resulting in N unknowns for N bands of observed data, plus one more for temperature, making the system underdetermined. Solving this requires additional conditions, often based on prior emissivity knowledge, which varies among inversion algorithms. This paper adopts the ADE algorithm to estimate initial temperature and emissivity, then uses the ratio and MMD methods for iterative calculations to invert land surface temperature.

2.3.5 Single-Window Algorithm

The single-window algorithm, developed by Qin Zhihao et al. based on the theory of land surface thermal radiation transfer equations, is a land surface temperature inversion algorithm specifically designed for data with only a single thermal infrared band. The calculation formula for this algorithm is shown as Equation (7):

$$\begin{cases} \text{LST} = \frac{a(1-C-D) + [b(1-C-D) + C + D] \times T_b + D \times T_a}{C} \\ D = (1 - \varepsilon)[1 + (1 - \varepsilon)\tau] \\ C = \varepsilon\tau \end{cases} \quad (7)$$

In the formula: T_s is the land surface temperature inversion value; T_b is the brightness temperature obtained by the sensor (K); T_a is the atmospheric average effective temperature (K); a and b are empirical coefficients, within the range of 0 to 70°C, $a=-67.355351$, $b=0.458606$; C and D represent intermediate variables; ε denotes the land surface emissivity; τ is the atmospheric transmittance.

3 RESULTS

3.1 Shijiazhuang City Surface Temperature Inversion Results

Using the ref. channel method in ENVI 5.6, we created a surface temp. map of Shijiazhuang (Fig. 2), showing max 307.1028K in city center and min 275.9503K in outskirts. With the split-window algo., we processed data in ENVI for another map (Fig. 2) with peaks at 308.9999K and lows at 274.2680K. For the temp. & emissivity sep. algo., developed in MATLAB, we input ASTER thermal data to get an ENVI-compatible HDR file (Fig. 2), with temps from 306.9436K max to 276.0142K min.

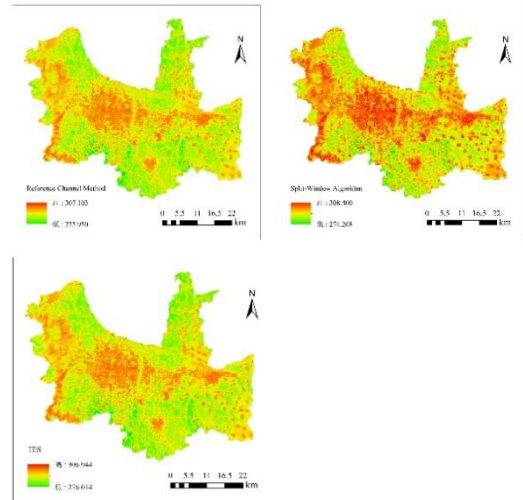


Figure 2 Three LST Inversion Algorithm Results Diagrams

3.2 Accuracy Comparison of Land Surface Temperature Inversion Methods in Shijiazhuang City

3.2.1 Based on meteorological data, the authenticity of land surface temperature is verified.

Considering that it is difficult to obtain real-time meteorological data at the stations in the study area when the satellite passes over, this study decided to only use image technology to obtain the daily average land surface temperature of Shijiazhuang City on the day of the satellite overpass, in order to verify the authenticity of the inversion accuracy. On May 20, 2022, the highest temperature in Shijiazhuang City was 31°C, the lowest temperature was 16.7°C, and the average land surface temperature was 23.9°C. The average statistical temperature of the land surface temperature inversion result obtained by the reference channel method was 20.03°C; the average temperature of the land surface temperature inversion result obtained by the split-window algorithm was 19.82°C; the average temperature obtained by the temperature and emissivity separation method was 20.00°C. The difference between the inversion results of the three different algorithms and the average land surface temperature was between 3.87°C and 4.08°C, which means that the inversion accuracy can be basically guaranteed. All three algorithms are suitable for land surface temperature inversion of ASTER imagery, but the temperature and emissivity separation algorithm has higher precision.

3.2.1 LST Inversion Results Cross-Validation

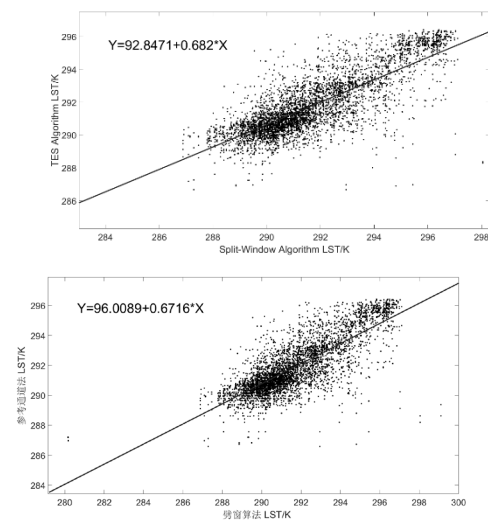


Figure 3 Scatter Plot for Cross-Validation of LST by Three Algorithms

Figure 3 uses numerical inversion results for surface temperature and employs scatter plots to compare the results from three algorithms. The data points are roughly along the line $y = a + bx$, showing similar linear fits for surface temperature across algorithms and consistent spatial pixel value distributions.

3.2.2 Correlation Analysis with MODIS Data

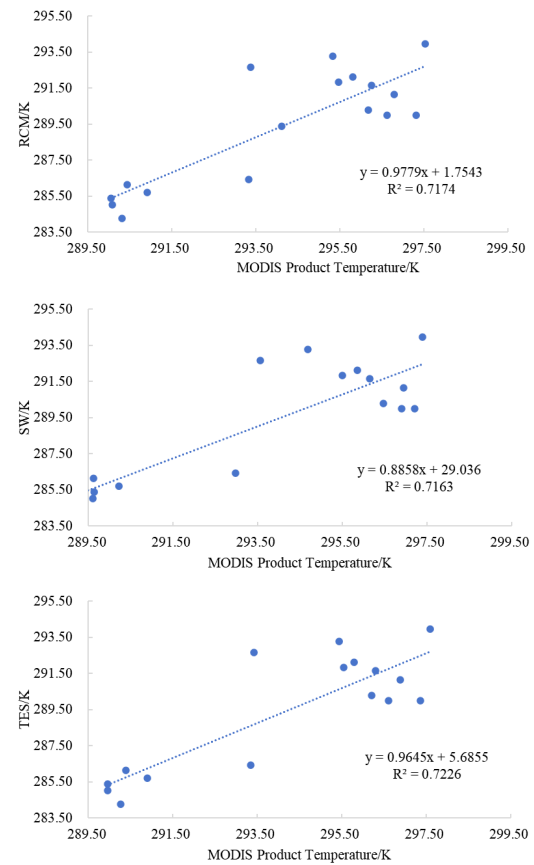


Figure 4 Scatter plot of algorithm LST versus MODIS LST

Figure4 shows that the Reference Channel Method, Split-Window Algorithm, and Temperature-Emissivity Separation (TES) Algorithm have high correlations with MODIS land temperature, with coefficients of 0.7174, 0.7163, and 0.7226, respectively. The TES algorithm has the highest correlation. Figure 4.8 indicates that all three algorithms show similar temperature trends, with sample points mostly between 290K and 300K, suggesting the TES algorithm is slightly more precise.

3.2.3 Correlation Analysis with LANDSAT Data

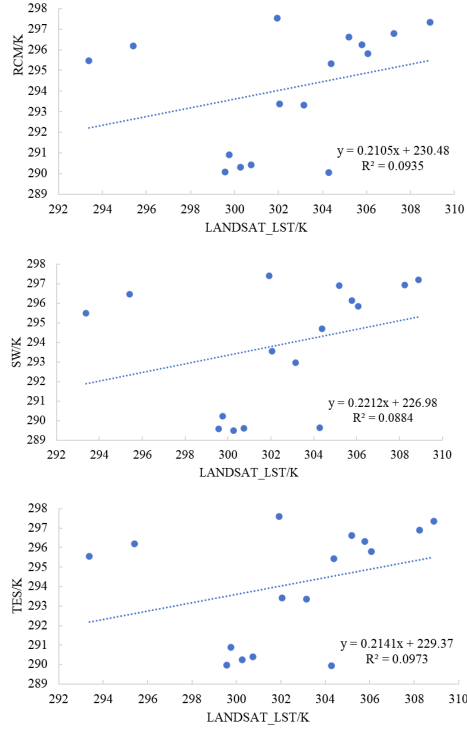


Figure 5 Scatter plot of algorithm LST versus LANDSAT LST

The LANDSAT thermal infrared data were resampled to 90m to match the ASTER dataset's resolution. As shown in Table 4.2, the land surface temperature (LST) inversion results from the three algorithms are generally lower than those from LANDSAT data. Figure 5 shows the correlation between the LST inversion results of the algorithms and LANDSAT data, with correlation coefficients of 0.0935, 0.0884, and 0.0973, respectively, indicating a poor correlation. This discrepancy may stem from differences in image acquisition times, atmospheric conditions, and spatial resolutions. Despite the low correlation coefficients, the TES algorithm shows a slightly higher coefficient, aligning with MODIS land temperature product validation results. This suggests that the TES algorithm is more accurate and suitable for ASTER data inversion of LST in the study area, as it better reflects ground-based temperature conditions.

4 DISCUSSION

LST is key for studying Earth's surface and differs by region. Remote sensing LST models can oversimplify inversion, causing errors. There's a need for better accuracy checks and real-time ground data.

Emissivity retrieval greatly affects LST inversion, as seen in Shijiazhuang's urban center with ENVI5.6. An empirical emissivity of 0.96 was used, but differences between empirical and actual emissivity can affect LST inversion. The temp. and emissivity separation algo.'s empirical formulas may not apply everywhere.

The retrieval results of emissivity have a significant impact on the inversion results of the algorithms. When implementing the land surface temperature inversion of the central urban area of Shijiazhuang City using the reference channel method based on ENVI5.6 software, the main influencing factor is emissivity. The method determines an empirical emissivity of 0.96, based on which the land surface temperature and the emissivity of other channels are obtained. However, there is a noticeable difference between the empirically obtained land object emissivity and the actual land object emissivity, which can adversely affect the inversion of land surface temperature. In the temperature and emissivity separation algorithm, some formulas are empirical and not suitable for use in all research areas.

The accuracy of the split-window algorithm's LST inversion is mainly influenced by atmospheric transmittance, which is affected by the atmosphere's absorption, emission, and scattering of ground longwave radiation. Errors in radiative transfer simulation can impact atmospheric parameter calculations. Standard atmospheres are often used instead of real-time data due to difficulties in obtaining precise real-time atmospheric profiles. Ground data is then used to correct these estimates. This study estimates atmospheric water vapor content using MODIS data and performs atmospheric simulation with MODTRAN software. The cubic relationship used for transmittance calculation can introduce errors, affecting the algorithm's inversion accuracy.

The resolution of the ASTER data used in this paper is 90m. All three inversion methods are based on the premise of uniform and isothermal pixels. However, in reality, the land surface is neither uniform nor isothermal, so the temperature obtained from remote sensing data is not the real temperature but the average temperature of the pixel. The sample points selected for accuracy verification are also the average temperature of the pixel, which may also include different land cover types, so there will be a certain error in the verification.

Despite biases, remote sensing is an efficient method for large-scale LST analysis. To reduce inversion errors, focus on three areas: (1) Improve land surface emissivity accuracy, aiming for an emissivity error less than 0.005 to keep LST inversion error within 1.0°C. (2) Enhance continuous land surface and atmospheric observations to collect sufficient original LST data and atmospheric correction parameters, reducing atmospheric impacts on inversion results. (3)

Utilize high spatial and spectral resolution remote sensing data to minimize pixel impact.

5 CONCLUSION

Based on ASTER data from May 20, 2022, this study implemented the land surface temperature inversion of the central urban area of Shijiazhuang City using three typical land surface temperature inversion algorithms: the reference channel method, the split-window algorithm, and the temperature and emissivity separation method. The accuracy of the inversion results was verified using meteorological data, Landsat data, and MYD11_L2 land surface temperature products.

Three LST inversion algos show slight temp. variations. They're largely consistent spatially but differ at sample points. The ref. channel and temp. emissivity separation methods' results are close, while the split-window algo. has lower lows (274.27K) and higher highs (308.10K). Compared to Shijiazhuang's avg. LST (23.9°C), the ref. channel method gives 20.03°C, split-window 19.82°C, and temp. emissivity separation 20.00°C. Deviations from the meteorological avg. are 3.87°C to 4.08°C, confirming reliable inversion accuracy.

When compared with MODIS land surface temperature data, it was found that the inversion results of the three algorithms were all higher, while compared with the inversion results of the Landsat single-window algorithm, the inversion results of the three algorithms were all lower. This is because there are certain errors in the inversion results of the MODIS land temperature product and Landsat data, which leads to the above problems when compared.

MODIS land temperature data is precise and stable. The three tested algorithms showed good correlation with MODIS data (coefficients of 0.7174, 0.7163, and 0.7226), with the temperature and emissivity separation algorithm having the highest correlation. Although the overall correlation with Landsat data was lower, the separation method was most accurate for LST inversion in Shijiazhuang's central urban area. It's primarily based on remote sensing, making it versatile for various scenarios, including areas with limited data. The study used average LST and MODIS products to assess the algorithms but suggested future research with high-precision atmospheric simulation data.

Moreover, the image data studied in this paper is limited, and three scenes of ASTER images covering the central urban area of Shijiazhuang (with a spatial resolution of 90m) were selected for land surface temperature inversion. In the future, image data with a wider time range and higher resolution can be selected for research.

REFERENCES

- Cheng, B., Liu, S. F., Yang, W. R. Characteristics and applications of Terra satellite ASTER data. *Journal of East China University of Geosciences*, 2003, (01): 15-17.
- Dash, P., Gottsche, F. M., Olesen, F. S., et al. Land surface temperature and emissivity estimation from passive sensor data: theory and practice-current trends. *International Journal of Remote Sensing*, 2002, 23(13): 2563-2594.
- Li, Z. L., Duan, S. B., Tang, B. H., et al. Progress in thermal infrared remote sensing inversion methods for surface temperature. *Journal of Remote Sensing*, 2016, 20(5): 899-920.
- Ma, J. J., Wang, C. L., Huang, X. H. Remote sensing inversion of surface temperature based on ASTER data and product verification - A case study of the Hei he River Basin. *Remote Sensing of Natural Resources*, 2023, 35(01): 198-204.
- Mao, K. B., Shi, J. C., Qin, Z. H., Gong, P., Xu, B., Jiang, L. M. A four-channel algorithm for simultaneously inverting surface temperature and emissivity from ASTER data. *Journal of Remote Sensing*, 2006(04): 593-599.
- Meng, P., Hu, Y., Gong, C. L., et al. Zheng, X. P., Li, Z. L., Zhang, X., Gao, M. F., Duan, S. B., Leng, P., Shang, G. B. A multi-channel thermal infrared remote sensing inversion method for surface temperature. *Patent*. Beijing, CN109446739B, 2020-01-10.
- Xu, J. Q., Bai, C. J., Yin, L., et al. A land surface temperature inversion method based on ASTER data. *Remote Sensing Information*, 2007, (06): 77-80+105.
- Xie, J., Ma, C. M. A., Feng, G., et al. Mapping Daily Evapotranspiration at Field Scale Using the Harmonized Landsat and Sentinel-2 Dataset, with Sharpened VIIRS as a Sentinel-2 Thermal Proxy. *Remote Sensing*, 2021, 13(17): 3420-3420.
- Zheng, X. P., Li, Z. L., Nerry, F., Zhang, X. A new thermal infrared channel configuration for accurate land surface temperature retrieval from satellite data. *Remote Sensing of Environment*, 2019, 231.

VALENSAT project

José Antonio Sobrino, Sergio Gimeno, Virginia Crisafulli, Álvaro Sobrino-Gómez, Drazen Skokovic
Global Change Unit, Image Processing Laboratory, University of Valencia, 46980 Paterna, Spain
jose.sobrino@uv.es

ABSTRACT – *The European Union and the Generalitat Valenciana co-financed the project "Estimación de Indicadores Medioambientales en la Comunidad Valenciana usando datos de Satélite (VALENSAT)," as part of the INVESTIGO 2022 financing plan. The project aims to create a user-friendly website offering free accessible Remote Sensing products to Valencian Community citizens. Landsat, Sentinel, MODIS and METEOSAT images are used to generate products covering a wide range of applications, including monitoring the Urban Heat Island effect, calculating vegetation indices, estimating fire intensity, and assessing water quality. Each product on the website features a detailed section that explains its functionality, applications, and key features. Utilizing Google Earth Engine, interactive apps have been developed to allow users to customize the calculation of specific parameters of interest. Users can download these products tailored to their needs, complemented by practical application examples and proper literature. This initiative ensures real-time access to valuable information, empowering informed decision-making and fostering a deeper understanding of Earth changes within the Valencian Community.*

Keywords – *Remote Sensing, Satellite Data Applications, Valencian Community, Environmental Indicators*

1. INTRODUCTION

The objective of this project is to provide citizens in the Valencian Community with information on environmental processes and land surface changes through satellite image processing. The products generated from satellite image analysis techniques enable better environmental resource management, facilitate actions to address climate change, and allow for the estimation of damage caused by adverse phenomena. To achieve this, geospatial data from various sources, including the Sentinel, Landsat, MODIS, and METEOSAT satellite constellations, has been processed to produce various outputs that are available for free on a dedicated website.

The website offers a diverse range of content, reflecting the breadth of applications in remote sensing. Available products cover areas such as fire analysis, air and water quality assessment, urban heat island studies, drought and frost estimation, land cover change analysis, and more. These outputs have been generated using Python and Google Earth Engine, with most of them offering customization options that allow users to obtain information specific to their area of interest and selected time period.

All products are freely downloadable, facilitating further calculations or the extraction of more precise information. This approach allows even non-experts to benefit from the analyses, bridging the gap between science and the general public (Sonnert, 2002).

2. MATERIAL AND METHODS

2.1. Study area

The study area for the project has been the Valencian Community in Spain. It is worth noting that, depending on the product generated, this product has been applied either to the entirety of the Valencian Community or to a specific area defined by the user.

2.1. Data sets

The satellites used for product generation were Landsat, MODIS, Sentinel-2, ERA5 and Meteosat Second Generation.

2.2. Methodology

Given the wide variety of generated products, each has been derived following its own specific methodology.

2.2.1. Urban Heat Island

SUHI (Surface Urban Heat Island) products have been generated for the area selected by the user. This was done following the methodology proposed by Sobrino & Irakulis (2020), which defines three surrounding zones around the urban area where surface temperature is obtained and then subtracted from the urban area temperature to obtain a SUHI value for each area (Wu, Wf, Wp). This calculation used Landsat and MODIS nighttime images.

2.2.2. Forest fires

Sentinel-2 images at a 20 m resolution, atmospherically corrected using the SLC band of the product, were used.

To calculate the total burned area, the NBR2 index (Delegido et al., 2018) was applied to the pre- and post-fire images. From this, the dNBR2 is obtained by subtracting the pre-fire NBR2 from the post-fire NBR2. Burned areas are considered to be those with NBR2 values above 0.10.

$$NBR2 = \frac{(B11 - B12)}{(B11 + B12)}$$

Once the area of interest is identified, vegetation classification is performed based on the Normalized Difference Vegetation Index (NDVI). NDVI is used to quantify vegetation greenness and is useful for assessing density and changes in health status.

$$NDVI = \frac{(B8 - B4)}{(B8 + B4)}$$

Specific value ranges are used to define vegetation as low, intermediate, or high density (Table 1). All pixels with NDVI values below 0 are masked to remove water areas that may introduce noise into the final product.

Table 1. Vegetation density classes and thresholds.

Vegetation Density	NDVI
Low	NDVI < 0.40
Mix	0.40 ≤ NDVI < 0.75
Full	NDVI ≥ 0.75

Once vegetation classes are determined, a specific index is applied to each class to calculate fire severity. For low-density vegetation areas, the Burned Area Index for Sentinel-2 (BAIS2), a new index developed by Filipponi (2018), is used. For areas with mixed, intermediate-density vegetation, the NBR is applied. In areas with high-density vegetation, the NBR3 index (Delegido et al., 2018) is used. The choice of indices is based on which has the greatest separability for a given vegetation density class, according to Sobrino et al., 2024.

$$BAIS2 = \left(1 - \sqrt{\frac{B06 * B07 * B8A}{B4}} \right) * \left(\frac{B12 - B8A}{\sqrt{B12 + B8A}} + 1 \right)$$

$$NBR3 = \frac{(B7 - B12)}{(B7 + B12)}$$

Thresholds for each index define fire severity levels (Table X), and the burned area is calculated in hectares.

Table 2. Vegetation density classes and thresholds of the corresponding fire severity indices used.

Fire severity degrees	Vegetation density		
	Low	Moderate	High
Low (BAIS2)	BAIS2 < 0.90	0.90 ≤ BAIS2 < 1	BAIS2 ≥ 1
Mix (NBR)	NBR > 0	0 ≥ NBR > -0.30	NBR ≤ -0.30
Full (NBR3)	NBR3 > 0.20	0.20 ≥ NBR3 > -0.30	NBR3 ≤ -0.30

Additionally, fire maps of incidents occurring in the community were generated using MODIS images, as well as the area affected by these fires.

2.2.3. Land Cover

A quantitative analysis of land cover change from 1985 to 2020 was conducted through Landsat image analysis in the Valencian Community (Sobrino et al., 2024). To generate the Land Cover (LC) data, the machine-learning algorithm Random Forest was used. Specific pixels were selected to train the algorithm and assigned to one of the following categories: Water, which includes rivers, lakes, and artificial reservoirs; Urban Area, covering buildings, roads, and industrial structures; Dense Vegetation, which includes forests and irrigated crops; Sparse Vegetation, encompassing areas with low vegetation like harvested crops and scrublands; and Bare Soil, representing riverbeds, beaches, and rock mines. The RF algorithm was run with 150 trees, as recommended by Oshiro et al. (2012).

To analyze LC evolution over the years, linear regression was calculated for each class during the study period. The 2023 LC product was validated by collecting in situ values, covering 5% of the training points, gathered during October 2023 through visual assessments.

2.2.4. Frost

To study the occurrence of frosts in the Valencian Community, we utilized MSG images collected from 2004 until 2023. In total, 85208 images were processed, comprising 24 images for each day (the first image obtained per hour) for the months of January, February, March, April, November, and December (the months when frost occurrences are most likely) across the entire study period.

We have decided to develop a new, simplified methodology based on satellite-measured LST to detect possible frost damages. To account for the varying impacts on flowers, fruits, tree trunks, and stems, we established three critical temperature thresholds based on existing literature (Whiteman, 1957; Conesa et al., 2015; Micheloud et al., 2017). We established four consecutive duration thresholds to assess the potential impact on the plants and developed a classification system for frost intensity levels by combining arbitrarily these parameters. Four categories of damage were established: light damage, moderate damage, severe damage, and permanent damage. These categories are represented in Table X using a range of colors.

Table 3. Damage levels used for image classification. The rows indicate the different temperature thresholds, while the columns represent the time thresholds. The different levels of damage are indicated by colors (Light blue = Light damage; Green = Moderate damage; Orange = Intense damage; Red = Permanent damage).

	$3 \leq h < 6$	$6 \leq h < 12$	$12 \leq h < 24$	$h \geq 24$
-2,3°C				
-4,0°C				
-9,0°C				

To more accurately account for the frequency and intensity of frosts in the Valencian Community over time, we developed damage intensity maps. Each frost category was assigned a specific ‘weight’ value to reflect the severity of damage: 1 for light, 2 for moderate, 3 for severe, and 4 for permanent damage. These values correspond to the increasing intensity of frost impact on plants. The value for each frost category was then multiplied by the number of frost events at each level within the selected time interval. The total intensity for each pixel was calculated by summing the values across all frost categories, resulting in an overall intensity (OI) measure.

$$OI = \sum_i^n \text{number of frost events} \times \text{weight}$$

Damage intensity maps were generated for each year. In this case, considering the seasonality of the data, it was deemed appropriate to use the Seasonal Kendall Test to analyze trends.

2.2.5. Water Quality

The literature indicates a bipartite classification of water types: Type 1 and Type 2 waters (Mishra & Mishra, 2012). In the Valencian Community, we have various reservoirs, rivers, and coastal areas that can be classified into these two types of water. In the specific case of the Albufera, which has been extensively

studied and has a large number of references, we know it is classified as Type 2 water. This implies that to adequately estimate water quality, we must incorporate various indicators that account for the primary factors affecting the Albufera, beyond those related solely to phytoplankton biomass.

For this, the Normalized Difference Turbidity Index (NDTI), which help us evaluate water turbidity (Doña et al., 2011), was calculated. We used Sentinel-2 images, taking advantage of their high resolution, which is particularly beneficial for studying smaller lakes and reservoirs.

2.2.6. Air Quality

Using Sentinel-5P, air quality in the Community was analyzed with NO₂, CO, SO₂, and O₃ products. Then, an air quality classification was produced.

3. RESULTS & DISCUSSION

3.1. Urban Heat Island

In Table 4, the results of the methodology applied for calculating SUHI in the city of Valencia between August 1 and August 31, 2024, are reported. First, the city polygon was generated, and from this, the three buffers corresponding to the surrounding areas were created. A difference of up to 2.3 degrees is observed between urban and rural areas.

Table 4. Results of the SUHI analysis for the City of Valencia during August 2024.

	wu	wf	wp
SUHI _{mean}	0.681	1.078	1.781
SUHI _{max}	1.15	1.548	2.251

3.2. Forest Fires

The burned area methodology was applied to the fire that occurred in Luchente in August 2018 (Figure 1). The results show 2,725.96 hectares burned, of which 22.48 were classified as low severity, 418.84 as moderate, and 2,284.64 as high.

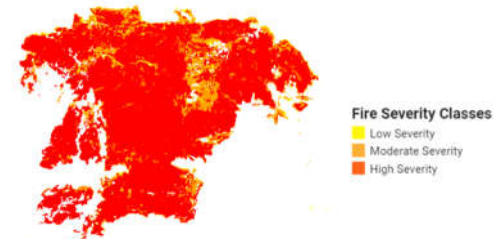


Figure 1. Burned area and severity levels of the fire near Luchente, calculated according to the method developed by Sobrino et al., 2024. The calculation used images from 30.07.18 to 04.08.18 (pre-fire images) and from 24.08.18 to 30.08.18 (post-fire images).

Additionally, Figure 2 presents a map of all the fires that occurred in the Valencian Community between 2000 and 2023.

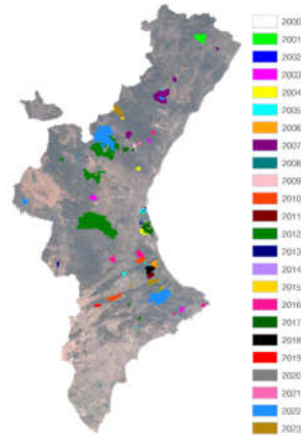


Figure 2. Fires that occurred in the Valencian Community between 2000 and 2023.

3.3. Land Cover

Figure 3 shows the Land Cover map obtained using the Random Forest algorithm for 2023, and Figure 4 shows the percentage of each class obtained from 1985 to 2020.

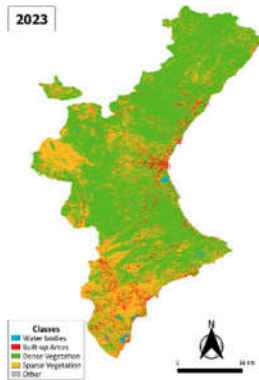


Figure 3. Land cover classification obtained with the Random Forest algorithm, using Landsat 9 imagery, for 2023.

The analysis of land cover change over the decades revealed a significant increase in urban areas, which grew by 87% between 1985 and 2020, affecting vegetation classes, which saw a cumulative decrease of 1.5%.

As for the other classes, the Water class maintained relative stability, showing minor fluctuations. The Bare Soil class exhibited a negative trend, highlighting the influence of urbanization in areas previously classified as rock and beaches.

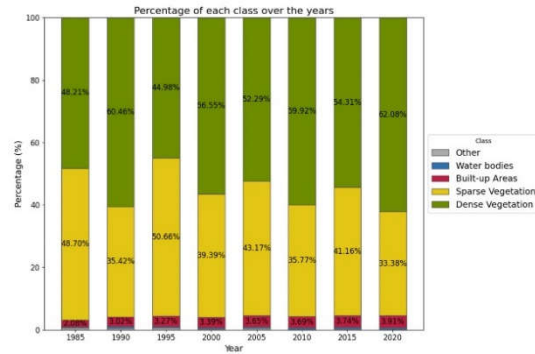


Figure 4. Percentage of Land Cover Classes in the Valencian Community for the Period 1985-2020, with 5-Year Intervals. Classifications Obtained with the Random Forest Algorithm Using Landsat 5-8 Images.

These results provide crucial information on land cover changes that have occurred in the Valencian Community in recent decades, underscoring the transformative impact of human activities on the regional landscape and shedding light on broader environmental implications, such as variations associated with the Urban Heat Island effect. Furthermore, Figure 5 illustrates the increase in urban area in Valencia, Castellón, and Alicante between 1985 and 2020.

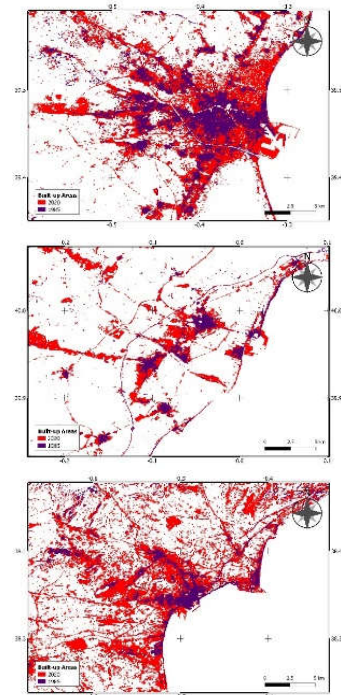


Figure 5. Maps illustrating the expansion of Built-up Areas class in Castellón (top-right), Valencia (top-left), and Alicante (bottom) between 1985 and 2020.

The Built-up Areas class shows a rise of 110.37% (an additional 56.59 km²) in Castellón, a 70.47% increase (adding 143.30 km²) in Valencia, and a remarkable growth of 157.68% (an addition of 100.20 km²) in Alicante.

3.4. Frost

The Kendall Seasonal Trend Test was applied to the entire dataset of damage intensity to observe the overall trend over time. The results (Fig. 6) illustrate the areas of the Valencian Community where the annual damage intensity has changed, taking into account the seasonality of the data. It was observed that across much of the region, there has been a decreasing trend in the intensity of damage caused by low temperatures, with the exception of the coastal zone, where no such damage was recorded. The reduction in vegetation damage over the past decade, especially during March and December and in the interior areas of the region, is likely attributed to rising temperatures associated with climate change.

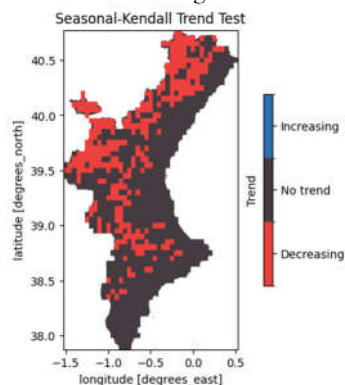


Figure 6. Result map of the Seasonal Kendall Trend Test conducted on the overall frost damage intensity data for the study period (2004-2023).

3.5. Water Quality

NDTI has been calculated in the Albufera lake of Valencia, resulting in high turbidity values (Figure 7).

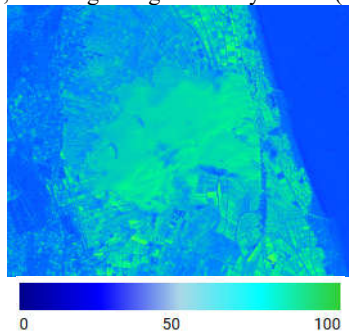


Figure 7. Turbidity Index map of the Albufera lake on 2023.

3.6. Air Quality

Figure 8 shows the air quality map in the Valencian Community for 2023.

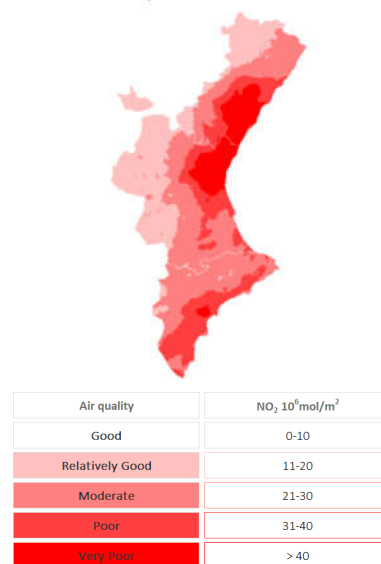


Figure 8. Air quality in the Valencian Community in 2023.

4. CONCLUSIONS

Through this platform, a variety of products covering diverse application areas is made available. The user-friendly format of these resources empowers stakeholders and promotes a proactive approach to environmental management. In the face of climate change challenges, access to reliable information is essential for implementing effective strategies and fostering sustainability within our communities. This initiative marks a significant step toward enhancing our collective capacity to address environmental issues, facilitating informed decision-making and developing of new mitigation strategies.

REFERENCES

- Conesa, N. A., Nicolás, N. J. M., Manera, N. F. J., & Porras, N. I. (2015). Frost damage in lemon orchards in the province of Murcia. *Acta Horticulturae*, 1065, 1417–1422. <https://doi.org/10.17660/actahortic.2015.1065.179>
- Delegido, J., Pezzola, A., Casella, A., Winschel, C., Urrego, E. P., Jimenez, J. C., Sobrino, J. A., Soria, G., & Moreno, J. (2018). Estimación del grado de severidad de incendios en el sur de la provincia de Buenos Aires, Argentina, usando Sentinel-2 y su comparación con Landsat-8.

- Revista de Teledetección, 51, 47.
<https://doi.org/10.4995/raet.2018.8934>
- Doña, C., Miralles, V. C., Sánchez, J. M., Ferril, A., & Camacho, A. (2011). Herramienta para el estudio del estado de eutrofización de masas de agua continentales. *Revista de Teledetección: Revista de la Asociación Española de Teledetección*, 36, 40-50.
http://www.aet.org.es/revistas/revista36/Numero36_04.pdf
- Filipponi, F. (2018). BAIS2: Burned Area Index for Sentinel-2. *Proceedings*.
<https://doi.org/10.3390/ecrs-2-05177>
- Huang, Q., Huang, J., Yang, X., Fang, C., & Liang, Y. (2018). Quantifying the seasonal contribution of coupling urban land use types on Urban Heat Island using Land Contribution Index: A case study in Wuhan, China. *Sustainable Cities And Society*, 44, 666-675.
<https://doi.org/10.1016/j.scs.2018.10.016>
- Liu, L., & Zhang, Y. (2011). Urban Heat Island Analysis Using the Landsat TM Data and ASTER Data: A Case Study in Hong Kong. *Remote Sensing*, 3(7), 1535-1552.
<https://doi.org/10.3390/rs3071535>
- Micheloud, N. G., Castro, D. C., Favaro, M. A., Buyatti, M. A., Pilatti, R. A., & Gariglio, N. F. (2017). Respuesta de diferentes variedades de cítricos a los daños causados por fuertes heladas en la región central de Santa Fe. *DOAJ (DOAJ: Directory of Open Access Journals)*.
<https://doaj.org/article/aaa8750eaa40427a9216fa72d225e70a>
- Mishra, S., & Mishra, D. R. (2011). Normalized difference chlorophyll index: A novel model for remote estimation of chlorophyll-a concentration in turbid productive waters. *Remote Sensing Of Environment*, 117, 394-406.
<https://doi.org/10.1016/j.rse.2011.10.016>
- Portela, C. I., Massi, K. G., Rodrigues, T., & Alcântara, E. (2020). Impact of urban and industrial features on land surface temperature: Evidences from satellite thermal indices. *Sustainable Cities And Society*, 56, 102100.
<https://doi.org/10.1016/j.scs.2020.102100>
- Sobrino, J. A., Gimeno, S., Crisafulli, V., & Sobrino-Gómez, Á. (2024). Analysing Land Cover Change in the Valencian Community through Landsat Imagery: From 1984 to 2022. *Land*, 13(7), 1072.
<https://doi.org/10.3390/land13071072>
- Sobrino, J. A., & Irakulis, I. (2020). A Methodology for Comparing the Surface Urban Heat Island in Selected Urban Agglomerations Around the World from Sentinel-3 SLSTR Data. *Remote Sensing*, 12(12), 2052.
<https://doi.org/10.3390/rs12122052>
- Sobrino, J. A., Llorens, R., Fernández, C., Fernández-Alonso, J. M., & Vega, J. A. (2024). Methodology for burned areas delimitation and fire severity assessment using Sentinel-2 data. A case study of forest fires occurred in Spain between 2018 and 2023. *Recent Advances*, 1-13.
<https://doi.org/10.62880/rars240002>
- Sonnert, G. (2002). *Ivory Bridges: Connecting Science and Society*. MIT Press.
- Whiteman, T. M. (1957). Freezing points of fruits, vegetables and florist stocks /.
<https://doi.org/10.5962/bhl.title.62920>

Estimation of Soil Organic Carbon on the Qinghai–Tibet Plateau Using a Machine Learning Model Driven by Multi-source Remote Sensing

Qi Chen¹, Wei Zhou^{2*}, Wenping Yu², Keming Wang²

¹College of Resources and Environment, Shandong Agricultural University, Taian 271018, China

²School of Geographical Sciences, Southwest University, Chongqing 400715, China

heron.riddle1221@gmail.com; zw20201109@swu.edu.cn;

ywpgis2005@swu.edu.cn; 990201400014@cqjtu.edu.cn

ABSTRACT – Soil Organic Carbon (SOC) is crucial for global carbon cycling and soil health. Given the insufficient understanding of the spatial distribution of SOC density in the Qinghai-Tibet Plateau, this study estimated the density and spatial distribution of SOC in the Qinghai-Tibet Plateau using machine learning (ML) algorithms. Multi-source data, including optical and SAR remote sensing, socioeconomic, topographic, climatic, and soil properties, were collected. ML algorithms—Random Forest (RF), eXtreme Gradient Boosting (XGBoost), and Light Gradient Boosting Machine (LightGBM)—were employed to estimate topsoil SOC density. The results are as follows: (1) Among the three machine learning algorithms used, LightGBM showed the highest validation accuracy ($R^2=0.56$, $RMSE=2.54$ kgC/m², $MAE=2.07$). (2) Spatially, the southeastern part of the Qinghai-Tibet Plateau has the highest topsoil SOC density, with recorded values ranging from 10.02 kg/m² to 11 kg/m², while the northwestern part has the lowest density, with recorded values ranging from 2.38 kg/m² to 4.92 kg/m². Different land cover types showed varying SOC density values, with forests and grasslands having higher SOC densities compared to urban and bare land areas. The findings of this study provide a scientific basis for future soil resource management and improvement of carbon sequestration accounting in the Qinghai-Tibet Plateau.

1 INTRODUCTION

Soil Organic Carbon (SOC) is a critical component of the Earth's terrestrial carbon sink, playing a pivotal role in ecosystem processes and climate change. With global SOC stocks estimated to range from 425 to 2111 Pg C, with a median value of 1158 Pg C as of 2010 (Tian et al., 2015), understanding its distribution and dynamics is essential for comprehending global carbon cycles. For instance, global SOC stocks are estimated at 2344 Pg C in the top 3 meters of soil, with 1502 Pg C residing in the top meter (Jobbágy et al., 2000). These figures underscore the significance of SOC in global carbon storage and its potential impact on climate change.

SOC has a direct influence on soil quality and plant health. Increased SOC levels improve soil structure, enhance water retention capacity, and increase nutrient availability, thereby promoting plant growth (Lal, 2004).

The application of remote sensing technologies and machine learning techniques offers new avenues for accurate SOC estimation. Remote sensing provides comprehensive, rapid, and quantitative information about the Earth's surface, which is crucial for monitoring land use changes (Luo et al., 2021). Machine learning models, such as LightGBM, analyze vast datasets to improve the accuracy of SOC estimates, which is essential for effective land management and

climate change mitigation strategies (Yu et al., 2021). Moreover, machine learning techniques can accelerate process-based biogeochemical cycle computations (Sun et al., 2023).

As a sensitive region to global change, the Qinghai-Tibet Plateau holds significant SOC stocks, with its grassland soils containing 3351973×10^8 tC, accounting for 2.4% of the global soil carbon pool (Wang et al., 2002). Understanding the SOC stocks and emissions in this region is crucial for global carbon cycle assessments and environmental protection measures.

This study aims to simulate SOC density on the Qinghai-Tibet Plateau by integrating SAR and optical remote sensing data with multiple environmental variables, utilizing RF, SVM, and LightGBM machine learning models. Specifically, using the LightGBM model for simulating surface soil organic carbon density in this region is novel.

2. MATERIALS AND METHODS

2.1. Study area

The Qinghai–Tibet Plateau, located in southwestern China (26°00'–39°47'N and 73°19'–104°47'E), spans approximately 2.5 million km², with around 1.5 million km² covered by grassland. Its average elevation exceeds 4,000 meters, and the terrain

features high mountains, plateaus, valleys, and basins. The region experiences a combination of cold arid and plateau monsoon climates, with significant seasonal variations in precipitation and temperature. Vegetation is predominantly alpine grasslands, including meadows, steppes, and deserts. Due to climate change and human activities, 75% of the plateau is considered ecologically fragile with moderate-to-severe degradation (Yu et al., 2011).

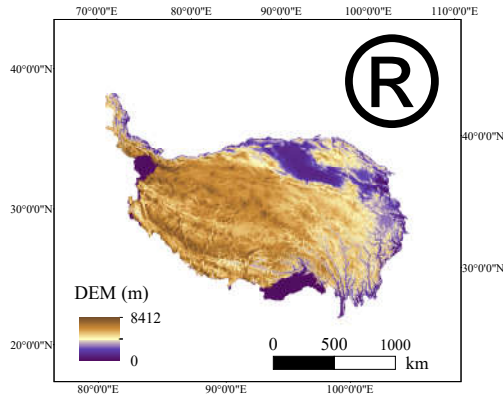


Figure 1. The spatial location of the study area.

2.2. Data resources

The Sentinel-1 Synthetic Aperture Radar (SAR) data, including VV and VH polarizations, were obtained from the European Space Agency's (ESA) Copernicus Open Access Hub (<https://scihub.copernicus.eu/dhus/>). Optical remote sensing data, including the Normalized Difference Vegetation Index (NDVI), were derived from Sentinel-2 imagery, also sourced from the ESA's Copernicus Open Access Hub (<https://scihub.copernicus.eu/dhus/>). Climate data, specifically temperature and precipitation, were acquired from the Global Land Data Assimilation System (GLDAS) (<https://ldas.gsfc.nasa.gov/gldas/>). Land Surface Temperature (LST) data were obtained from Moderate Resolution Imaging Spectroradiometer (MODIS) aboard the Terra and Aqua satellites (<https://modis.gsfc.nasa.gov/data/dataproduct/mod11.php>). Digital Elevation Model (DEM) data were sourced from the Shuttle Radar Topography Mission (SRTM) (<https://earthexplorer.usgs.gov/>). Soil texture data were provided by the Harmonized World Soil Database (HWSD) (<http://www.fao.org/soils-portal/soil-survey/soil-maps-and-databases/harmonized-world-soil-database-v12/en/>). Soil moisture data were obtained from the European Space Agency's Climate Change Initiative (ESA CCI) (<https://esa-soilmoisture-cci.org/>). Population density data were obtained from the Gridded Population of the World (GPW) database (<https://sedac.ciesin.columbia.edu/data/set/gpw-v4-population-count-rev11>).

GDP data were obtained from the World Bank (<https://data.worldbank.org/indicator/NY.GDP.MKTP.CD>). Land Use/Cover Change (LUCC) data were obtained from the Global Land Cover Facility (GLCF) at the University of Maryland (<https://glcf.umd.edu/data/lc/>).

2.3. SOC density estimation model

In the current study, we employed the Random Forest (RF), eXtreme Gradient Boosting (XGBoost), and LightGBM machine learning algorithms to estimate Soil Organic Carbon (SOC) density using the R programming language. The RF model was implemented with the "randomForest" and "caret" packages. We set the default number of trees ("ntree") to 500 and determined the optimal value of the "mtry" parameter using the "caret" package's "expand.grid()" function for grid search optimization. XGBoost incorporates advanced optimization techniques, including regularization, efficient parallel processing, feature selection, and handling of missing values. The "xgboost" library was loaded using the "library(xgboost)" command. For the LightGBM model, we utilized the "lightgbm" and "caret" packages. Parameter tuning was achieved using the "caret" package's functions, such as "expand.grid()" for grid search to find the best parameters. The default number of boosting rounds ("nrounds") was set to 500. We applied the random segmentation method in R to split the dataset into a training set and a test set with a ratio of 7:3.

2.4. Model accuracy comparison

To evaluate the overall accuracy and stability of the three models, we conducted five-fold cross-validation using the following three metrics: the coefficient of determination (R^2), root mean square error (RMSE), and mean absolute error (MAE). A higher R^2 value, approaching 1, indicates a better fit of the model to the data, as it signifies a greater proportion of the variance in the target variable being explained by the model. Lower values of RMSE and MAE indicate less prediction error and a better model fit. The calculation formulas for these metrics are as follows:

$$R^2 = \left(\frac{\sum_{i=1}^n (O_i - \bar{M})(P_i - \bar{P})}{\sqrt{\sum_{i=1}^n (O_i - \bar{O})^2} \sqrt{\sum_{i=1}^n (P_i - \bar{P})^2}} \right)^2 \quad (1)$$

$$RMSE = \sqrt{\frac{1}{n} \sum_{i=1}^n (P_i - O_i)^2} \quad (2)$$

$$MAE = \frac{1}{n} \sum_{i=1}^n |P_i - O_i| \quad (3)$$

where P_i and O_i are predicted and measured SOC density (kgC/m^2), respectively; n represents the number of soil sample points; \bar{P} and \bar{O} indicate the mean values of predicted and measured SOC density, respectively.

2.5. Mapping spatial distribution of SOC

Ultimately, the spatial distribution of SOC was mapped using the optimal predictors and the highest-performing machine learning model. This mapping allowed for an analysis of the spatial distribution pattern of topsoil SOC density across the Qinghai-Tibet Plateau.

3. RESULTS

Among the models evaluated (Table 1), LightGBM demonstrated the most accurate predictions with the lowest prediction errors and the highest R^2 value (RMSE = 2.5417 kgC/m^2 , MAE = 2.0721 , $R^2 = 0.5622$). LightGBM's ability to handle large datasets, capture complex nonlinear relationships, and its computational efficiency through gradient boosting make it particularly suited for our extensive dataset of over three million records. This enables LightGBM to integrate various factors effectively, including climate, soil characteristics, and topography, to produce precise SOC density predictions (Luo et al., 2020; Liu et al., 2024; Li et al., 2021).

The performance of the three models on Average, Median, Standard deviation, and Coefficient of variation is roughly the same, as shown in Table 2 for details.

Table 1. Comparison of performances of models in SOC estimation based on verification test.

Model (kgC/m^2)	RMSE	MAE	R^2
RF	2.96	2.24	0.37
XGBoost	3.09	2.34	0.32
LightGBM	2.54	2.07	0.56

Table 2. Comparison of SOC density values based on estimation models and sampling sites.

Model	Average (kgC/m^2)	Median (kgC/m^2)	Standard deviation (kgC/m^2)	Coefficient of variation (%)
RF	5.33	4.98	2.74	51.45
XGBoost	5.31	4.93	3.17	59.77
LightGBM	5.51	5.27	2.83	51.37

4. DISCUSSION

In our study, we found that the spatial distribution of topsoil SOC density on the Qinghai-Tibet Plateau is significantly influenced by land-cover types (Figure 2b).

Specifically, forests, grasslands, and wetlands exhibit notably higher SOC densities compared to croplands, urban areas, and bare land. The highest SOC density (11 kg/m^2) was observed in forested areas, which aligns with previous findings indicating that land-cover types and land-use management practices are the primary factors affecting SOC accumulation (Wu et al., 2016; Gao et al., 2024).

Significant regional variations in SOC density were also identified (Figure 2a). The eastern part of the Qinghai-Tibet Plateau, characterized by alpine meadows, swamp meadows, and shrublands, displays higher SOC densities. This region is also the origin of major rivers like the Yangtze, Yellow, Lancang, Yarlung, and Tsangpo, contributing to favorable hydrological conditions that support SOC accumulation. Previous studies verified these findings, noting the positive influence of good vegetation cover, suitable climatic conditions, high-quality soil types, and effective land management practices on SOC accumulation (Yi et al., 2023; Li et al., 2019), particularly in river-source regions where SOC density can reach up to 11.00 kg/m^2 .

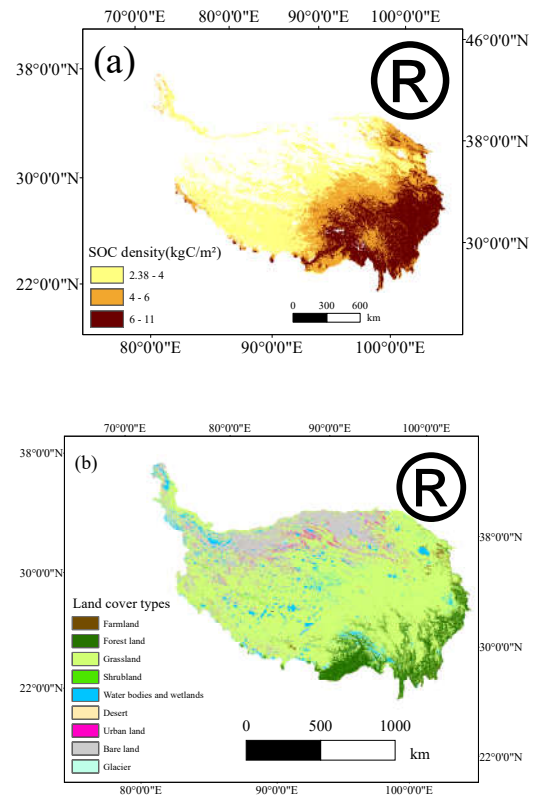


Figure 2. SOC density mapping of Qinghai-Tibet Plateau based on (a) LightGBM model and (b) land-cover types.

In contrast, the western and northern areas of the plateau show lower SOC densities. These regions, predominantly covered by alpine steppe and desert, experience harsh climatic conditions, including low temperatures and limited rainfall, which hinder the accumulation and preservation of organic carbon (Sun et al., 2024; Liao, 2011). Although low temperature conditions are beneficial for the accumulation of organic carbon, a lack of sufficient precipitation can hinder the effective decomposition and transformation of plant residues and litter, thereby affecting the final accumulation of organic carbon (Zhou et al., 2007). Low SOC densities in the northern area, attributed to the prevalence of bare land-cover types, are consistent with earlier research (Li et al., 2017).

In summary, the spatial distribution of SOC on the Qinghai-Tibet Plateau is strongly influenced by land-cover types and climatic conditions, with higher SOC densities in the eastern region due to favorable environmental conditions and land use practices, and lower SOC densities in the western and northern regions due to harsher climatic conditions and sparse vegetation cover.

REFERENCES

- Gao, H., Gong, J., Liu, J., & Ye, T. (2024). Effects of land use/cover changes on soil organic carbon stocks in Qinghai-Tibet plateau: A comparative analysis of different ecological functional areas based on machine learning methods and soil carbon pool data. *Journal of Cleaner Production*, 434, 139854.
- Jobbágy, E. G., & Jackson, R. B. (2000). The vertical distribution of soil organic carbon and its relation to climate and vegetation. *Ecological applications*, 10(2), 423-436.
- Lal, R. (2004). Soil carbon sequestration impacts on global climate change and food security. *Science*, 304(5677), 1623-1627.
- Liao, Y. (2011). Changes in soil organic carbon and soil respiration characteristics in typical low temperature regions of China. (Doctoral dissertation, China University of Geosciences (Beijing)).
- Li, C., et al. (2017). Elevational gradient affects functional fractions of soil organic carbon and aggregate stability in a Tibetan alpine meadow. *Catena*, 156, 139-148.
- Liu, Q., Wang, M. D., Guo, L., Wang, R., Jia, Z. F., Hu, X. J., Tang, Q. K., & Shi, T. Z. (2024). Mapping of soil organic carbon density at farmland scale based on airborne hyperspectral images. *National Remote Sensing Bulletin*, 28(1), 293-305. DOI: 10.11834/jrs.20221805.
- Luo, M., Guo, L., Zhang, H., et al. (2020). Characterization of spatial distribution of soil organic carbon in China based on environmental variables. *Acta Pedologica Sinica*, 57(1), 48-59.
- Luo, J. C., Hu, X. D., Wu, T. J., Liu, W., Xia, L. G., Yang, H. P., Sun, Y. W., Xu, N., Zhang, X., Shen, Z. F., Zhou, N. (2021). Research on intelligent computing model and method of accurate land use and land cover change information driven by high-resolution remote sensing. *Journal of Remote Sensing*, 25(7), 1351-1373. DOI: 10.11834/jrs.20219402.
- Sun, Y., Goll, D. S., Huang, Y., Ciais, P., Wang, Y. P., Bastrikov, V., & Wang, Y. (2023). Machine learning for accelerating process-based computation of land biogeochemical cycles. *Global Change Biology*, 29(11), 3221-3234.
- Sun, Y. J., Zhong, L. S., Yang, X. B., & Zhang, X. (2024). Effects of short-term precipitation reduction on soil organic carbon mineralization and organic carbon fractions in Hainan rubber forests. *Journal of Tropical Biology*, 15(3), 272-280. doi: 10.15886/j.cnki.rdswwb.20230096
- Tian, H., et al. (2015). Global patterns and controls of soil organic carbon dynamics as simulated by multiple terrestrial biosphere models: Current status and future directions. *Global Biogeochemical Cycles*, 29(6), 775-792.
- Wang, G., Cheng, G., & Shen, Y. (2002). Soil organic carbon pools in grassland over the Tibetan Plateau and its global significance. *Journal of Glaciology and Geocryology*, 24(6), 693-700.
- Wu, M., Liu, S. J., Ye, Y. Y., Zhang, W., Wang, K. L., & Chen, H. S. (2016). Spatial variability of surface soil organic carbon and its influencing factors in cultivated slopes and abandoned lands in a Karst peak-cluster depression area. *Acta Ecologica Sinica*, 36(6), 1619-1627.
- Xu, Y., Wang, R. H., Li, Z. Z., & Xu, Y. (2021). Spatial differentiation of soil organic carbon density and influencing factors in typical croplands of China. *Environmental Science*, 42(5), 2432-2439.
- Yu, B. H., & Lv, C. H. (2011). Assessment of ecological vulnerability on the Tibetan Plateau. *Geographical Research*, 30(12), 2289-2295.
- Yu, D. C., Zhao, W. F., Nie, K., & Zhang, G. (2021). Visibility prediction model based on LightGBM algorithm. *Journal of Computer Applications*, 41(4), 1035.
- Yi, P. H., Wu, H. F., Hu, B. A., Wen, X., Han, H. R., & Cheng, X. Q. (2023). Variation characteristics and influencing factors of soil organic carbon storage after returning farmland to forest on the Loess Plateau. *Acta Ecologica Sinica*, 43(24), 10054-10064.
- Zhang, C., Li, C., Han, X. Z., You, M. Y., & Hao, X. X. (2019). Effects of long-term vegetation cover changes on the organic carbon fractions in soil aggregates of mollisols. *Chinese Journal of Plant Ecology*, 43(7), 624-634.
- Zhou, T., Shi, P. J., Luo, J. Y., & Shao, Z. Y. (2007). Estimation of soil organic carbon based on remote sensing and process model. *Journal of Remote Sensing*, (1), 127-136. DOI: 10.11834/jrs.20070117.

Exploring Machine Learning Techniques for Temporal Forest Cover Classification in Burned Areas: A comparative Study

C. Iranzo, F. Pérez-Cabello

*Institute of Research into Environmental Sciences of Aragón (IUCA), University of Zaragoza.
C/ Pedro Cerbuna, 12. 50009 Zaragoza, Spain.
c.iranzo@unizar.es; fcabello@unizar.es*

ABSTRACT – Accurate annual forest cover maps, both pre- and post-fire, are crucial for characterizing spatiotemporal patterns of species distribution, which are essential for informed forest management decisions. In the Aragón region of Spain, a 38-year automated inventory project has been conducted, monitoring 154 fires and 19 distinct forest and shrubland communities on an annual basis. Supervised classification of forest and shrubland classes across large areas is challenging due to the spatial variability of the species to classify. This study aims to evaluate the effectiveness of different machine learning pipelines in addressing the key challenges of large-area classification. Each pipeline includes methods for oversampling underrepresented classes, such as the SMOTENC and ADASYN algorithms, as well as techniques for addressing overrepresented classes, including Tomek Links and Random Undersampling. The four most commonly used machine learning models in operational land cover classification tasks were employed as classifiers: Random Forest (RF), AdaBoost (AB), Support Vector Machines (SVM), and Multi-Layer Perceptron classifier (MLP). The performance of each classification model was evaluated using overall accuracy, as well as class-specific user's and producer's accuracies. The Support Vector Machines and Random Forest models achieved the highest overall accuracies, at 92.5% and 92%, respectively. The most balanced user's and producer's accuracies were obtained when the preprocessing pipeline incorporated the stratified sample and the MinMax scaler, without any additional strategies. The Tomek Links and SMOTENC algorithms produced the second-best results for the user's and producer's accuracy metrics.

Keywords - Fire, Landsat, scikit-learn, python, google earth engine, Land Cover

1. INTRODUCTION

Fire regime defines the changes related to the intensity/severity, recurrence, and extent of fires (Gill and Allan, 2008). The alteration of the fire regime in Aragón, driven by increasing fire intensity and recurrence, has had significant consequences, including biodiversity loss, the invasion of shrub formations, and a reduction in vegetation cover.

Mediterranean communities typically exhibit a rapid post-fire recovery over time, largely due to the preservation of soil conditions and the effectiveness of species' resprouting and seed germination mechanisms. However, high fire severity can negatively impact the anatomical and physiological strategies of affected species (Francos et al., 2018). This, in turn, can exacerbate physiological and taxonomic changes within the communities that recolonize burned areas.

Given the importance of the response capacity of Mediterranean vegetation, to which most of the plant communities in Aragón affected by fire belong, and the spatial variability with which fire manifests, understanding the type of vegetation that has been burned, both before and after the fire, is a key component for assessing spatial resilience, one of the fundamental properties for evaluating ecological resilience.

This work aims to evaluate several machine learning classification models and workflows to produce the most accurate forest/shrub vegetation cover product over burned areas in Aragón. As noted by Maxwell et al. (2018), the optimal algorithm for a specific task may vary depending on the classes being mapped, the nature of the training data, and the predictor variables used. Therefore, it is recommended to test multiple classifiers to determine the most suitable method.

2. MATERIAL AND METHODS

2.1. Study sites

The digitization process was carried out for the fires recorded within the PaF project (Dynamic Analysis of Forest Landscape Resilience to Fire Using Multisensor Spectral Indicators) in Aragón. There are 168 fires plus a 300-meter buffer control zone (no burned vegetation), covering around ≈2,000 square kilometers (Figure 1).

The database includes fire events from 1975 to 2019. Burned areas range from 44.3 hectares to 27,000 hectares, with an average of 1056.5 hectares. Most fires occurred during the summer (149 events), while a smaller number were recorded in winter (19 events).

Regarding fire causes, only 10 fires were initiated by natural events (lightning), while the remaining incidents were linked to human activities. Of the human-related fires, 10 were caused by agricultural machinery, and only 2 were deliberately set.

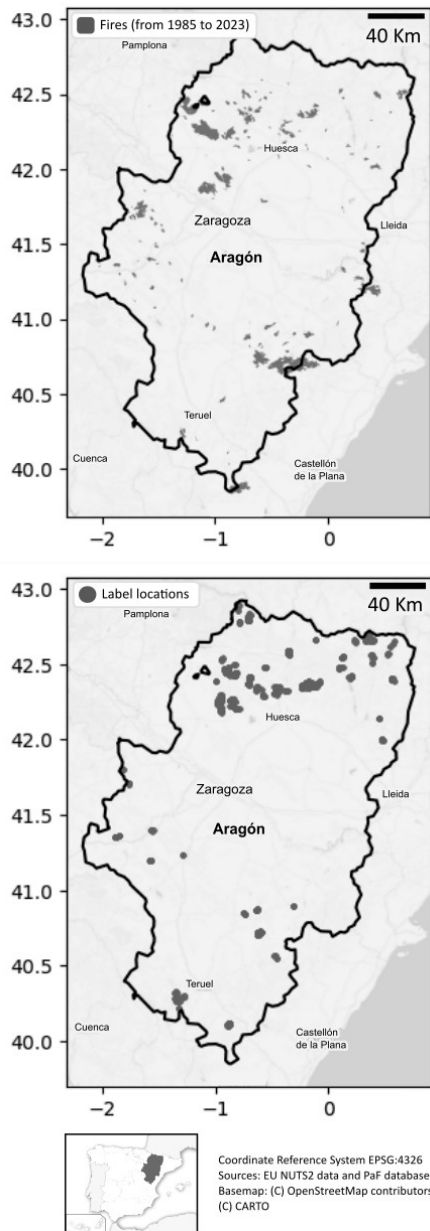


Figure 1. The figure presents the location of the study area in the Aragón region. The top map shows the fires along with their respective control zones for classification. The bottom map displays digitized labels located near the fire events.

2.2. Labels

For the classification process, a dataset containing 3,100 labels describing forest vegetation in the study area, along with their coordinates, was used. This dataset was manually compiled using National Forest Inventory, Corine Land Cover, the Spanish Forestry Map, and the Spanish Land Cover Information System, and aerial photography. The aim of the study is to assess the post-fire regeneration process. To characterize each forest category in its post-fire state, all primary tree classes were associated with their corresponding shrub types (Figure 2).

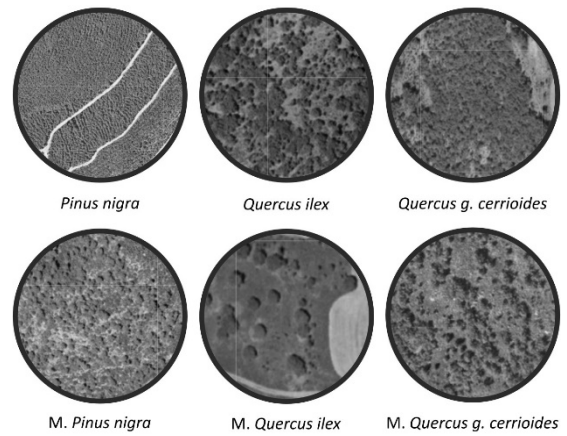


Figure 2. Forest and shrub points using PNOA imagery. Differences in textures between the main forest species and the burned shrub class are observed. The central point of the circles represents a training label.

Shrub labels for burned areas were assigned if the point was located within a burned zone and the land cover information indicated that the area corresponded to a primary tree class. If these conditions were met, the point was labeled as a shrub of the primary class.

To analyze vegetation dynamics before and after fire events, labels were collected over multiple years using the aforementioned forest data sources, covering all years in the fire series. This approach captures temporal changes in vegetation behavior. The available years are 1985, 1989, 1999, 2009, and 2018 (Figure 3).

Considering the extensive area to classify, the main species in Aragón were grouped into six forest vegetation domains (as shown in Table 1).

The distribution of labels was imbalanced (Figure 3). Certain species classes, such as *Pinus sylvestris* L. and *Pinus nigra* J. F. Arnold, were well represented in the land cover products, while others, particularly shrub states of less represented species (e.g., shrub of *Pinus pinaster* Aiton), were underrepresented.

Table 1. Plant communities to classify. The “From” column presents the subdomains included inside species with low spatial representation.

Species	From	Code
<i>Pinus halepensis</i>		Ph
<i>Pinus nigra</i>	<i>Pinus nigra</i> and <i>Pinus pinaster</i>	Pn
<i>Pinus sylvestris</i>		Ps
<i>Pinus uncinata</i>		Pu
<i>Quercus g. cerrioides</i>	<i>Quercus faginea</i> and <i>Fagus sylvatica</i>	Qgc
<i>Quercus ilex</i>	<i>Quercus ilex</i> and <i>Juniperus thurifera</i>	Qi
M. <i>Pinus pinaster</i>		Mpp
M. <i>Pinus sylvestris</i>		Mps
M. <i>Quercus g. cerrioides</i>	Shrub classes from Qgc group.	Mqgc
M. <i>Quercus ilex</i>		Mqi
M. Mediterranean pine	<i>Pinus halepensis</i> shrub and <i>Pinus nigra</i> shrub	Mpm

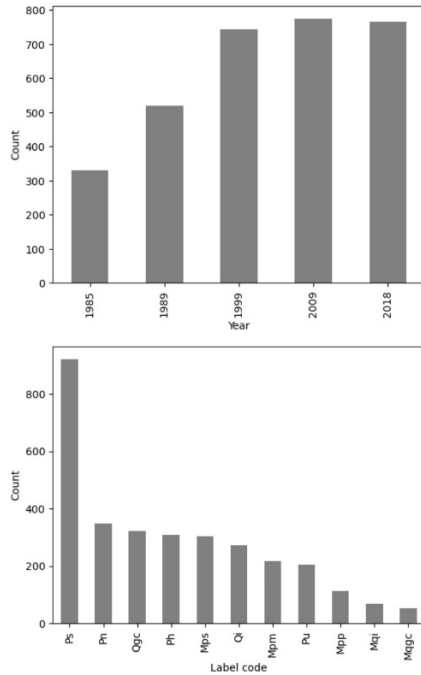


Figure 3. Histograms to visualize the distribution of labels across years and vegetation classes. Shrub classes exhibited low frequencies due to the difficulty of identifying pure shrub pixels.

The imbalance of the latter is attributed to the difficulties in detecting them, due to lower prevalence of these species in isolated communities, as they typically occur as secondary species within forest formations. Furthermore, the plant community most affected by fire in the region was *Pinus sylvestris*, which is the key factor for the larger amount of labels in this class (Gobierno de Aragón. Departamento de Agricultura, Ganadería y Medio Ambiente., 2022).

2.3. Predictor variables

Two types of predictor variables were considered. First, elevation and geological data were included as drivers of vegetation species distribution in Aragón (Braun-Blanquet and De Bolos, 1957; Mateo, 1990; Villar et al., 1999). Second, spectral bands from Landsat images were selected to differentiate between forest and shrub domains over time. This is crucial, as fire-induced transitions between forest and shrub vegetation are not captured by static factors like elevation and geology.

Landsat images were selected due to their temporal coverage, which encompasses most fires within the database. These images offer a medium spatial resolution of 30 meters for visible, near-infrared, and shortwave infrared bands, and 100 meters for thermal bands.

Two elevation-related predictors were considered: height (in meters) and terrain shadow. Height data were obtained from the 5-meter grid Digital Terrain Model of Spain. Hill shade was calculated using the *hillShade* function from the raster R package (Hijmans, 2024). Geology-related predictors were computed with the Aragón Geology Map (from 1993). The first was based on the geological communities, and the second was a binary classification of geological classes into acidic and basic categories, key factors influencing vegetation distribution. These four predictors were combined with the labels using the *extract* function from the raster R package.

Landsat-related predictors were collected using the Google Earth Engine Python API and the Bottom of Atmosphere-corrected Landsat 4, 5, 7, 8, and 9 collections. A cloud filter was applied to the images, followed by the creation of a unique composite for each year in the series (1985 to 2018, corresponding to the years with label data) using the mean value during the summer months. The values for each label were then extracted by position and year, associating each label with the composite image of its corresponding year.

2.4. Modelling techniques

The following machine learning models were employed: Random Forest (RF), AdaBoost (AB) with

a Decision Tree Classifier estimator, Support Vector Machines (SVM), and Multi-Layer Perceptron (MLP), all implemented using scikit-learn python module (Pedregosa et al., 2011). The model hyperparameters were optimized using 3-fold cross-validation. The training data were split into training and testing sets (70/30) using a stratified sampling method. To address class imbalance, four resampling algorithms from the imbalanced-learn package (Lemaître et al., 2017) were evaluated. For undersampling techniques, Random Undersampling and Tomek Links were applied. For oversampling, SMOTENC (Synthetic Minority Over-sampling Technique for Nominal and Continuous) and ADASYN (Adaptive Synthetic algorithm) methods were used.

For the SMOTENC oversampling technique, the soft approach increased the number of minority class instances by 30% for labels with fewer than 150 instances, while the hard approach generated up to 150 instances for these labels. The ADASYN algorithm automatically computed the number of instances to add. For undersampling, the soft approach reduced the majority class instances to 250, while the hard approach reduced them to 150. All pipelines included an initial data scaling step using the MinMax method.

Table 2. Preprocessing pipelines applied to each machine learning model. The "none" strategy is the one obtained with the stratified sample and MinMax scaling, without any other method.

Oversampling	Undersampling	Code
None	None	1
Random hard	ADASYN	2
Random hard	SMOTENC hard	3
Random hard	SMOTENC soft	4
Random soft	ADASYN	5
Random soft	SMOTENC hard	6
Random soft	SMOTENC soft	7
TomeK Links hard	ADASYN	8
TomeK Links hard	SMOTENC hard	9
TomeK Links hard	SMOTENC soft	10
TomeK Links soft	ADASYN	11
TomeK Links soft	SMOTENC hard	12
TomeK Links soft	SMOTENC soft	13

2.5. Validation

The performance of the models was evaluated using overall accuracy and kappa metrics. Additionally, classification errors for each label were assessed using producer's accuracy and user's accuracy. Producer's accuracy represents the complement of the omission error (100 minus the ratio of incorrectly

classified reference sites to the total reference sites for each label). User's accuracy reflects the complement of the commission error (100 minus the ratio of incorrectly classified sites to the total classified sites for each label).

3. RESULTS & DISCUSSION

Regarding the global metrics (Figure 4), the models that achieved the best results were RF and SVM. The pipelines trained with these models produced higher kappa and overall accuracy values compared to AB and MLP. The performance gap between the models may be due to the small size of the training sample, as both AB and MLP typically require larger datasets to fit the model effectively. AB relies on a sequence of weak learners, while MLP requires more data to build a robust multi-layer perceptron.

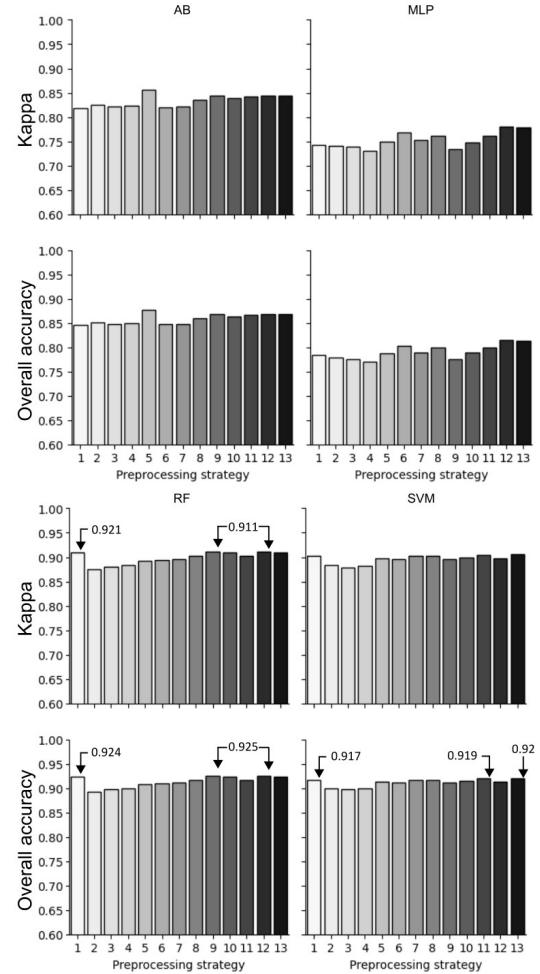


Figure 4. Accuracy metrics based on applied machine learning classifiers and preprocessing strategies.

Regarding the preprocessing pipelines, RF and SVM models showed nearly identical performance. However, Tomek Links undersampling improved both kappa and overall accuracy metrics compared to Random Undersampling. The differences between the simplest pipeline and those using both undersampling and oversampling techniques are reflected in the producer's and user's accuracy metrics (Figure 5).

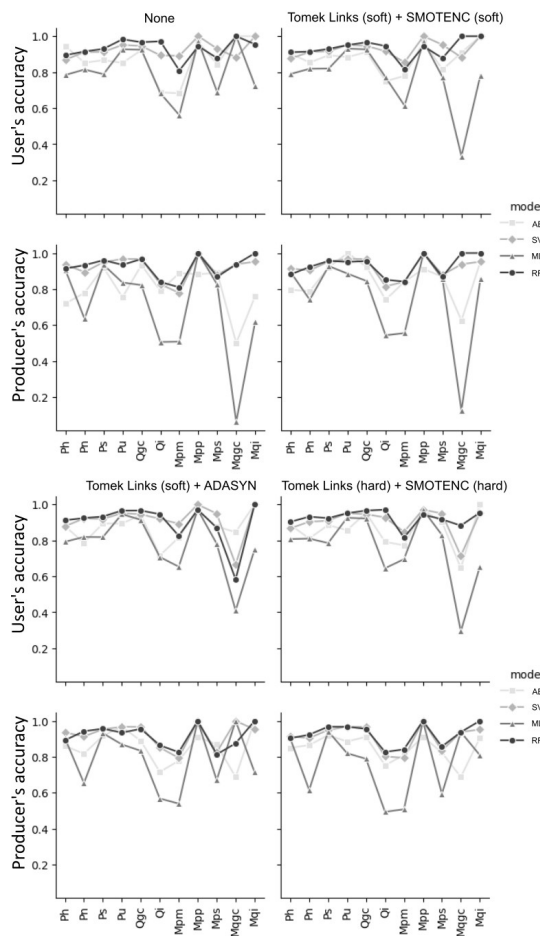


Figure 5. Class-Specific metrics by label class derived from the Confusion Matrix of the best preprocessing pipelines related to the kappa metric. User's accuracy is calculated as one minus the commission error (incorrectly classified sites / total classified sites), while producer's accuracy is calculated as one minus the omission error (incorrectly classified reference sites / total reference sites).

The user's accuracy metric shows little difference between the Tomek Links soft undersampling combined with SMOTENC soft oversampling (code 13) and the pipeline with the None approach. Forest

labels had similar values for both RF and SVM models. In contrast, shrub labels had more variations, like an accuracy reduction in Mpm and Mqgc classes for the SVM model in pipeline code 13. The other two pipelines showed a considerable decrease in shrub label accuracy.

The producer's accuracy for the no-resampling method and the code 13 pipeline was also similar for RF and SVM models, although the RF model slightly improved the Mqgc shrub class in the code 13 pipeline. All four pipelines with the best overall metrics produced comparable results for SVM and RF models on this metric, despite the higher differences being within the shrub classes. Furthermore, they performed better than those of the MLP and AB classifiers.

Random Forest (RF) and Support Vector Machine (SVM) algorithms demonstrate superior classification accuracy for forest species compared to shrub species. This discrepancy may be attributed to the larger number of training labels available for forest species and their more stable representations. Forest species labels are primarily characterized by the elevation and geology of the region, often corresponding to a single forest type. In contrast, shrub species labels are less abundant and typically consist of multiple shrub types, leading to significant variability across different regions and classification problems.

4. CONCLUSIONS

Random Forest (RF) and Support Vector Machine (SVM) classifiers outperform Multi-Layer Perceptron (MLP) and AdaBoost (AB) classifiers. However, despite achieving high overall accuracies, the classification performance for shrub labels is notably poor. Moreover, these high accuracy values should be interpreted with caution, as there is a potential risk of model overfitting.

The optimal model pipeline was the stratified extraction of the training and testing samples and the application of Min-Max scaling (with no other technique), which results in a good model performance. Additionally, the use of Tomek Links undersampling and SMOTENC oversampling with a soft strategy may further improve classifier effectiveness; however, these methods require validation with larger training and test samples.

To address the classification challenges associated with shrub labels, efforts should focus on increasing the number of shrub training labels. Furthermore, incorporating reflectance values from Landsat sensors during the spring season, in addition to the current summer data, could improve shrub classification accuracy.

FUNDING: This research was funded by MCIN/AEI/10.13039/501100011033, grant number PID2020-118886RB-I00, and the predoctoral contracts from the Convocatory (Government of Aragón), corresponding to Cristian Iranzo.

REFERENCES

- F Braun-Blanquet, J., & De Bolos, O. 1957. Las comunidades vegetales de la Depresión del Ebro y su dinamismo. Delegación Medio Ambiente, Ayuntamiento de Zaragoza.
- Francos, M., Úbeda, X., Pereira, P., & Alcañiz, M. 2018. Long-term impact of wildfire on soils exposed to different fire severities. A case study in Cadiretes Massif (NE Iberian Peninsula). *Science of The Total Environment*, 615, 664–671.
<https://doi.org/10.1016/j.scitotenv.2017.09.311>
- Gill, A. M., & Allan, G. 2008. Large fires, fire effects and the fire-regime concept. *International Journal of Wildland Fire*, 17(6), 688–695.
- Gobierno de Aragón. Departamento de Agricultura, Ganadería y Medio Ambiente. 2022. Plan Forestal de Aragón (Formulación Del Plan Forestal Para Su Aprobación Diseño y Ejecución, p. 171).
- Hijmans, R. J. 2024. raster: Geographic data analysis and modeling [Manual].
<https://rspatial.org/raster>
- Lemaître, G., Nogueira, F., & Aridas, C. K. 2017. Imbalanced-learn: A python toolbox to tackle the curse of imbalanced datasets in machine learning. *Journal of Machine Learning Research*, 18(17), 1–5.
- Mateo, G. (1990). Catálogo florístico de la provincia de Teruel. Instituto de Estudios Turolenses-Diputación provincial de Teruel.
- Maxwell, A. E., Warner, T. A., & Fang, F. 2018. Implementation of machine-learning classification in remote sensing: An applied review. *International Journal of Remote Sensing*, 39(9), 2784–2817.
<https://doi.org/10.1080/01431161.2018.1433343>
- Montorio, R., Pérez-Cabello, F., Borini Alves, D., & García-Martín, A. 2020. Unitemporal approach to fire severity mapping using multispectral synthetic databases and Random Forests. *Remote Sensing of Environment*, 249, 112025.
<https://doi.org/10.1016/j.rse.2020.112025>
- Pedregosa, F., Varoquaux, G., Gramfort, A., Michel, V., Thirion, B., Grisel, O., Blondel, M., Prettenhofer, P., Weiss, R., Dubourg, V., & others. 2011. Scikit-learn: Machine learning in python. *Journal of Machine Learning Research*, 12(Oct), 2825–2830.
- Villar, L., Sesé, J. A., & Ferrández, J. V. 1999. Flora del Pirineo Aragonés (Vol. 1). Consejo de Protección de la Naturaleza.

Feasibility to derive new carbon fluxes products from EUMETSAT satellites in LSA SAF

A. Jiménez-Guisado*, F.J. García-Haro, M. Campos-Taberner, B. Martínez, S. Sánchez-Ruiz, M.A. Gilabert

Environmental Remote Sensing Group (UV-ERS), Departament de Física de la Terra i Termodinàmica, Universitat de València, 46100 Burjassot, Valencia, Spain.

* adrian.jimenez@uv.es

ABSTRACT - Quantifying carbon fluxes is essential as they play a critical role in the global carbon cycle and have a direct impact on Earth's climate. The Satellite Application Facility on Land Surface Analysis (LSA SAF) produces and provides access to remotely sensed variables for characterizing terrestrial ecosystems, such as land surface fluxes and biophysical parameters, by leveraging data from EUMETSAT satellites and sensors. Among them, the LSA SAF is Gross Primary Production (GPP), derived from SEVIRI/MSG observations, offers a quantitative measure of carbon uptake by terrestrial vegetation through photosynthesis. This makes GPP a key variable that accounts for carbon exchange between the surface and the atmosphere. During the current phase (CDOP-4), LSA SAF is exploring the feasibility of utilizing the enhanced capabilities of the next generation of EUMETSAT satellites to derive new vegetation products, such as Net Ecosystem Exchange (NEE). NEE is defined as GPP minus Terrestrial Ecosystem Respiration (TER) and provides a direct measure of the net CO₂ exchange between ecosystems and the atmosphere. We assess the performance of advanced and highly efficient machine learning retrieval models for deriving carbon flux variables (GPP, NEE, TER) by integrating SEVIRI/MSG data with ground-based observations from eddy covariance (EC) towers. These EC data provide high temporal resolution estimates of CO₂ net exchanges and are distributed across the most representative terrestrial biomes. An ensemble of SEVIRI/MSG products—including Fractional Vegetation Cover (FVC), Leaf Area Index (LAI), Fraction of Absorbed Photosynthetically Active Radiation (FAPAR), Downward Surface Shortwave Flux (DIDSSF), Evapotranspiration (DMET), Reference Evapotranspiration (METREF), and the BRDF k₀ parameter in the red, NIR, and MIR SEVIRI/MSG bands—served as inputs for the models. Additionally, various state-of-the-art machine learning regression methods were employed for comparison, including neural networks and kernel methods. The results indicate that machine learning methods provide accurate and consistent estimates, demonstrating the potential of data-driven approaches in conjunction with remote sensing data for estimating carbon fluxes.

Keywords - Carbon fluxes, machine learning, LSA SAF

1. INTRODUCTION

Carbon fluxes (CFs) are critical to understanding the global carbon cycle and assessing its influence on climate regulation. The quantification of these fluxes provides insights into the dynamic exchanges of carbon between terrestrial ecosystems and the atmosphere, driven by natural processes such as photosynthesis, respiration, and decomposition (White et al., 2000; Sitch et al., 2008; 2015). Key CFs include Gross Primary Production (GPP), Terrestrial Ecosystem Respiration (TER), and Net Ecosystem Exchange (NEE), each representing a distinct component of ecosystem carbon dynamics. GPP refers to the total amount of carbon captured by vegetation through photosynthesis, while TER accounts for the carbon released through respiration by plants and other organisms. NEE, which is calculated as the difference between GPP and TER, provides a direct estimate of net carbon exchange between an ecosystem and the

atmosphere, thus offering a measure of an ecosystem's role as a carbon source or sink.

The estimation of these fluxes at ecosystem scales often relies on in-situ measurements obtained through networks of eddy covariance (EC) towers (Baldocchi, 2003), including FLUXNET (<https://fluxnet.org/>), ICOS (<https://www.icos-cp.eu/>), or AmeriFlux (<https://ameriflux.lbl.gov>). EC towers measure CO₂ exchange with high temporal resolution, enabling localized insights into carbon uptake and release patterns within their respective footprints. However, to capture the spatial complexity of carbon fluxes on regional and global scales, remote sensing (RS) data provide a viable solution by offering consistent observations across large areas. These data sources often rely on Production Efficiency Models and vegetation indices, or spectral combinations, to approximate GPP and related fluxes, effectively bridging ground observations with broader spatial scales.

The Satellite Application Facility for Land Surface Analysis (LSASAF) is a dedicated processing center serving the European Organization for the Exploitation of Meteorological Satellites (EUMETSAT). It focuses on deriving terrestrial variables essential for ecosystem characterization, including land surface fluxes and other biophysical parameters. The LSA SAF vegetation products are freely disseminated to users through the LSA SAF website (<http://lsa-saf.eumetsat.int>). Currently, the LSA SAF provides GPP products derived from SEVIRI/MSG (Martínez et al., 2020), contributing a quantitative measure of carbon assimilation by vegetation. As LSA SAF advances into its next development phase (CDOP-4), the feasibility of deriving additional carbon flux products—specifically NEE and TER—using EUMETSAT's next-generation satellites is being explored. This expansion could enable more comprehensive assessments of carbon exchanges across varied terrestrial biomes, facilitating the understanding of ecosystem carbon dynamics at broader scales.

To address the complex and interdependent nature of CFs, data-driven techniques have gained prominence. Machine learning regression methods, particularly when combined with RS data, allow for advanced modeling of CFs by incorporating multiple environmental variables and their interactions (Tramontana et al., 2016; Campos-Taberner et al., 2024). This study explores the use of Gaussian Process Regression (GPR) for delivering reliable estimates along with confidence intervals, enhancing both the precision and the spatial-temporal uncertainty characterization.

2. MATERIAL AND METHODS

The methodology of this study is divided into two main components: the datasets and remote sensing products used, and the modeling techniques applied to derive carbon fluxes. The corresponding flowchart used for the retrieval of carbon fluxes is presented in Fig. 1.

2.1. Datasets and remote sensing products

To model carbon fluxes, measurements from eddy covariance tower networks were combined with remote sensing observations from the SEVIRI/MSG instrument. EC towers provide high-frequency, site-specific measurements. For this study, data from 2004 to 2021 were selected from the FLUXNET2015 dataset, allowing validation of MSG-derived carbon flux estimates against on-ground measurements. Daily NEE and TER values were computed by averaging night- and day-time partitioning methods (Reichstein et al., 2012). Following a sign convention where CO₂ flux toward the atmosphere is positive, positive NEE values represent carbon release and negative values represent uptake. The daily values were aggregated into 10-day intervals to align with SEVIRI/MSG temporal resolution.

The SEVIRI/MSG data used in this study included key remote sensing products for characterizing vegetation and land-atmosphere interactions. Model inputs comprised Fractional Vegetation Cover (FVC) for estimating vegetation extent, Leaf Area Index (LAI) to assess photosynthetic activity, and Fraction of Absorbed Photosynthetically Active Radiation (FAPAR) (García-Haro et al., 2019).

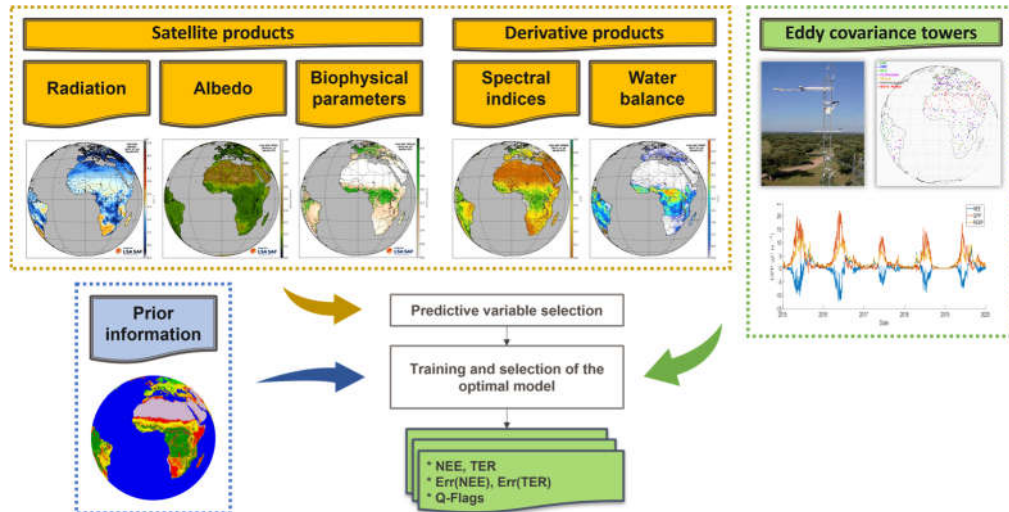


Figure 1. Flowchart used for the retrieval of carbon fluxes (NEE and TER) from the upscaling of tower measurements.

Additional inputs included Downward Surface Shortwave Flux (DIDSSF) for solar energy (Geiger et al., 2008), Evapotranspiration (DMET) and Reference Evapotranspiration (METREF) for water fluxes (Ghilain et al., 2011), and the BRDF k_0 parameter (red, NIR, MIR bands) for vegetation reflectance properties (Roujean et al., 1992). This set of SEVIRI/MSG products provides a comprehensive view of biophysical properties and environmental conditions affecting carbon fluxes across ecosystems.

2.2. Gaussian process regression (GPR)

The carbon flux estimation in this study leveraged machine learning techniques, with a specific focus on Gaussian process regression (Rasmussen and Williams, 2006) to model the relationship between the input SEVIRI/MSG variables and target carbon fluxes. GPR is a non-parametric, Bayesian approach that models the distribution of potential functions that could describe the data. Unlike other regression methods, GPR does not assume a fixed functional form but instead learns a distribution over possible functions, providing flexibility and robustness when dealing with complex, non-linear relationships.

In this study, GPR was trained using SEVIRI/MSG remote sensing variables as predictors and the in-situ CO_2 flux data from EC towers as target variables. By incorporating multiple remote sensing inputs and calibrating the GPR model with high-temporal-resolution EC data, we obtained a probabilistic model capable of capturing the complex interdependencies among vegetation indices, radiation, and water fluxes.

One of the key advantages of GPR in this context is its ability to provide a confidence interval around predictions, which aids in quantifying the uncertainty associated with each carbon flux estimate. This feature is particularly beneficial for large-scale ecosystem assessments, where spatial and temporal variations in data quality and environmental factors can introduce uncertainty into carbon flux estimates.

3. RESULTS & DISCUSSION

Fig. 2 presents representative maps of NEE and TER derived with the proposed methodology for June 25, 2018. Notably, regions with dense vegetation cover, such as the tropical regions in central Africa, Europe and the Amazon rainforest demonstrate substantial CO_2 uptake (negative NEE) and high respiration rates (TER). This aligns with expectations, as these areas are known for high photosynthetic activity and biomass. On the other hand, the regions with the highest uncertainty correspond to the extremes of the disk, where the quality of the MSG products is degraded, as well as in the regions worst represented by the training set.

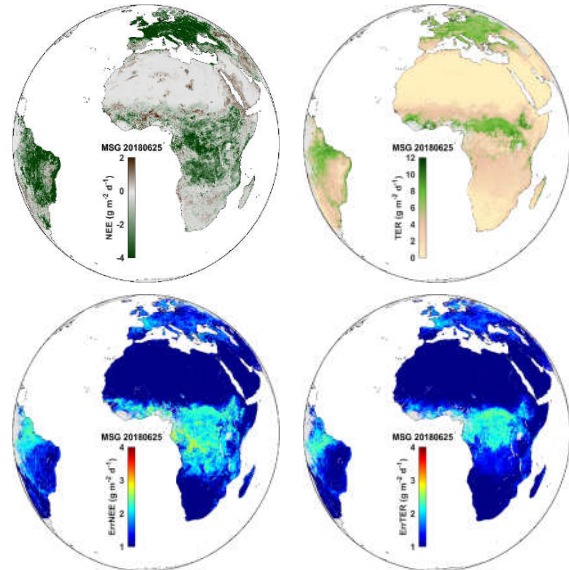


Figure 2. Maps of values and uncertainties of NEE (left) and TER (right) provided by the GPR model.

Fig. 3 displays the temporal profiles of NEE and TER over two representative sites, a savanna ecosystem (top two panels) and an evergreen forest (bottom two panels). The profiles span multiple years, showcasing seasonal and interannual variability in carbon fluxes.

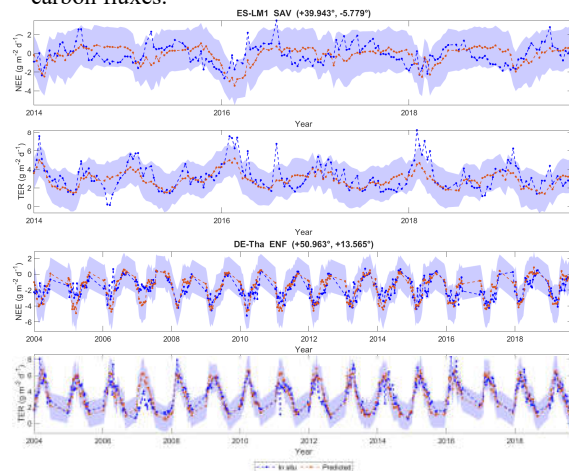


Figure 3. Temporal profiles related to representative savanna (top) and evergreen forest (bottom) sites.

The savanna site exhibits a strong seasonal cycle in both NEE and TER. Peaks in carbon release (positive NEE) generally coincide with the dry season when vegetation activity is limited, while negative NEE values during the wet season indicate increased carbon uptake as vegetation productivity rises. The TER values similarly fluctuate with the seasonal cycle, with

higher respiration during warmer, wet seasons and lower respiration during cooler, dry seasons. In contrast, the evergreen forest site shows a more consistent and pronounced seasonal pattern in both NEE and TER over the years, with notable peaks and troughs corresponding to summer and winter seasons. During summer months, NEE reaches strongly negative values, indicating significant carbon uptake due to high photosynthetic activity. Winter periods show smaller values, with slight carbon release due to reduced photosynthesis. TER at this site also demonstrates seasonal peaks in summer, corresponding to increased respiration rates driven by higher temperatures and biological activity.

The uncertainty bands for the evergreen forest site are narrower overall compared to the savanna site, suggesting higher reliability of model predictions and in-situ measurements in forest ecosystems. This may be due to more stable environmental conditions and denser vegetation, which provide stronger signals for carbon flux estimation models.

These temporal profiles underscore the importance of biome-specific modeling approaches when estimating carbon fluxes. They also illustrate the value of integrating remote sensing data with ground observations to capture seasonal and interannual dynamics accurately across diverse ecosystems.

4. CONCLUSIONS

Overall, the machine learning methods evaluated demonstrated accurate and consistent estimates across various models, highlighting their robustness in carbon flux estimation. Among these, GPR methods stood out, providing not only reliable estimates but also realistic confidence intervals, which contribute valuable information on the spatial and temporal distribution of uncertainties. These findings support the effectiveness of data-driven approaches, particularly when combined with remote sensing data, in estimating carbon fluxes. Such integration presents a promising pathway for advancing the accuracy and reliability of ecosystem carbon flux assessments on a large scale.

5. ACKNOWLEDGMENTS

This work received funding support of LSA SAF (EUMETSAT) and ECCE EO (PID2020-118036RB-I00 funded by MCIN/AEI/ 10.13039/501100011033).

REFERENCES

Baldocchi, D. D. (2003). Assessing the eddy covariance technique for evaluating carbon dioxide exchange rates of ecosystems: past, present and future. *Global change biology*, 9(4), 479-492.

García-Haro, F. J., Camacho, F., Martínez, B., Campos-Taberner, M., Fuster, B., Sánchez-Zapero,

J., & Gilabert, M. A. (2019). Climate data records of vegetation variables from geostationary SEVIRI/MSG data: Products, algorithms and applications. *Remote Sensing*, 11(18), 2103.

Geiger, B., Meurey, C., Lajas, D., Franchistéguy, L., Carrer, D., & Roujean, J. L. (2008). Near real-time provision of downwelling shortwave radiation estimates derived from satellite observations. *Meteorological Applications: A journal of forecasting, practical applications, training techniques and modelling*, 15(3), 411-420.

Ghilain, N., Arboleda, A., & Gellens-Meulenberghs, F. (2011). Evapotranspiration modelling at large scale using near-real time MSG SEVIRI derived data. *Hydrology and Earth System Sciences*, 15(3), 771-786.

Martínez, B., Gilabert, M. A., Sánchez-Ruiz, S., Campos-Taberner, M., García-Haro, F. J., Brümmer, C., ... & Tagesson, T. (2020). Evaluation of the LSA-SAF gross primary production product derived from SEVIRI/MSG data (MGPP). *ISPRS Journal of Photogrammetry and Remote Sensing*, 159, 220-236.

Rasmussen, C. E., & Williams, C. K. (2006). *Gaussian processes for machine learning*. Cambridge, MA: MIT press.

Roujean, J. L., Leroy, M., & Deschamps, P. Y. (1992). A bidirectional reflectance model of the Earth's surface for the correction of remote sensing data. *Journal of Geophysical Research: Atmospheres*, 97(D18), 20455-20468.

Sitch, S., Huntingford, C., Gedney, N., Levy, P. E., Lomas, M., Piao, S. L., ... & Woodward, F. I. (2008). Evaluation of the terrestrial carbon cycle, future plant geography and climate-carbon cycle feedback using five Dynamic Global Vegetation Models. *Global change biology*, 14(9), 2015-2039.

Sitch, S., Friedlingstein, P., Gruber, N., Jones, S. D., Murray-Tortarolo, G., Ahlström, A., ... & Myneni, R. (2015). Recent trends and drivers of regional sources and sinks of carbon dioxide. *Biogeosciences*, 12(3), 653-679.

Tramontana, G., Jung, M., Schwalm, C. R., Ichii, K., Camps-Valls, G., Ráduly, B., ... & Papale, D. (2016). Predicting carbon dioxide and energy fluxes across global FLUXNET sites with regression algorithms. *Biogeosciences*, 13(14), 4291-4313.

White, M. A., Thornton, P. E., Running, S. W., & Nemani, R. R. (2000). Parameterization and sensitivity analysis of the BIOME-BGC terrestrial ecosystem model: Net primary production controls. *Earth interactions*, 4(3), 1-85.

Analysis of the relation of phytoplankton, temperature and salinity in the Western Mediterranean Sea using data DeepESDL cubes

Elena Martínez-Mateo ⁽¹⁾, Ana B. Ruescas ⁽²⁾, Yasir Hassan Khachoo ⁽³⁾

⁽¹⁾ *University of Valencia, Spain, emarma5@alumni.uv.es*

⁽²⁾ *Department of Geography, University of Valencia, Spain*

⁽³⁾ *Università degli studi di Napoli Pathenope, Italy*

RESUMEN – Este estudio analiza la dinámica del mar Mediterráneo en su parte más occidental -una cuenca semi-cerrada evaporativa conectada principalmente al Atlántico por el estrecho de Gibraltar. La cuenca occidental, que incluye el mar de Alborán, es particularmente dinámica debido a la entrada de aguas atlánticas frescas que interactúan con las más densas aguas mediterráneas, creando el frente Almería-Orán (AO). Esta región es clave para estudiar los intercambios entre aguas costeras y de alta mar, esenciales para comprender el transporte de nutrientes o contaminantes desde la costa hacia el mar abierto.

La investigación se enfoca en los procesos submesoescala (1-10 km), analizando variables como la temperatura superficial del mar (SST), la concentración de clorofila (CHL), la altura de la superficie del mar (SSH) y la salinidad (SSS). Estos parámetros permiten monitorear la circulación costera y los intercambios costeros-marinos, con el objetivo de responder a preguntas clave: i) la frecuencia y los factores que influyen en estos intercambios, ii) las áreas donde se forman remolinos con mayor frecuencia, y iii) la identificación de masas de agua derivadas del intercambio entre la costa y el mar abierto.

Para este análisis, se integran datos utilizando productos de Copernicus en el marco XCUBE, almacenado en la plataforma *Deep Earth System Data Lab* (DeepESDL) de la Agencia Espacial Europea (ESA). Esta plataforma facilita el acceso a conjuntos de datos relevantes y proporciona un entorno avanzado para el análisis de datos mediante técnicas de aprendizaje automático e inteligencia artificial, permitiendo una correlación más profunda entre las variables físicas y biológicas en áreas clave como el mar de Alborán.

Palabras clave: frentes, dinámica marina, cubos de datos, aprendizaje máquina

ABSTRACT – This study, focused on the Mediterranean Sea, analyses its behaviour as a semi enclosed evaporative basin primarily connected to the Atlantic through the Strait of Gibraltar. The western basin, which includes the Alboran Sea, is particularly dynamic due to the inflow of fresh Atlantic waters that interact with the denser Mediterranean waters, forming the Almería-Oran front (AO). This region is crucial for studying exchanges between coastal and offshore waters, which are essential to understanding the transport of nutrients or pollutants from the coast to the open sea.

The research focuses on the submesoscale (1-10 km), analysing variable such as Sea Surface Temperature (SST), Chlorophyll-a concentration (CHL), Sea Surface Height (SSH) and Sea Surface Salinity (SSS). These parameters allow for monitoring coastal circulation and coastal-open sea exchanges, with the goal of answering key questions: i) the frequency and factor influencing these exchanges, ii) identifying areas where eddy formations occur more frequently, and iii) identifying water masses derived from coastal-offshore exchanges.

For this analysis, data is integrated using Copernicus products and the XCUBE framework, stored in the European Space Agency's (ESA) *Deep Earth System Data Lab* (DeepESDL). This platform facilitates access to relevant datasets and provides an advanced environment for data analysis through machine learning and artificial intelligence techniques. This allows for deeper correlations between physical and biological variables in key areas such as the Alboran Sea.

Keywords: fronts marine dynamics, data cubes, machine learning

1. INTRODUCTION

Meso – and submesoscale processes in the ocean refer to the dynamics of currents, eddies, and fronts that occur at intermediate spatial and temporal scales. Mesoscale processes typically occur over 10 to 100 km and last from days to months, while submesoscale processes span smaller distance (1 to 10 km) and are more transient, lasting hours to days. These structures are crucial for the vertical and horizontal mixing of physical and biological properties, such as heat, nutrients, and organisms.

In the Alboran Sea, mesoscale and submesoscale processes are particularly important due to the complex interactions between coastal currents and deep ocean waters. The circulation in this area is dominated by the presence of anticyclonic and cyclonic eddies, which impact both local dynamics and the exchange between the Atlantic and the Mediterranean. These structures influence the redistribution of chlorophyll (a proxy for biological productivity) as well as heat and salinity variations, which affect marine biodiversity and fishing patterns.

The specific objectives of this study include: i) analyzing the frequency and factor driving coastal-ocean exchanges; such as variations in sea surface temperature (SST), sea surface salinity (SSS) and sea surface height (SSH), alongside local winds and currents, ii) identifying areas where eddies form most frequently and studying how these structures affect the distribution of nutrients, heat and organisms, iii) identifying and characterizing water masses resulting from coastal-offshore exchanges and determining their role in transporting physical and biological properties, like nutrients and sediments, between different areas, impacting biological productivity and ecosystem structure.

The main novelty of this study is the integration of satellite data from diverse sources, spatial and temporal scales, and its integration data cubes. These cubes will be later utilized for the application of machine learning models to try to find the inherent relations among the different physical and biological variables. This work will be carried out using the advanced tools integrated in the DeepESDL service by ESA.

2. STUDY AREA

The Alboran Sea, located at the westernmost edge of the Mediterranean, is a region of complex and dynamic oceanographic processes. One of its most defining characteristics is the presence of the Atlantic Jet (AJ), a powerful surface current that flows through the Strait of Gibraltar, bringing cooler, less saline Atlantic waters into the Mediterranean (Macías et al., 2007). This current is a key driver of the circulation in the Alboran Sea, where it interacts with the native

Mediterranean waters, resulting in marked spatial and temporal variations in salinity, sea surface temperature, and biological productivity. Oceanic fronts are regions where two distinct water masses meet, often characterized by stark differences in temperature, salinity, and nutrient content (Kirches et al., 2016).

The inflow of the Atlantic Jet Creates two prominent anticyclonic gyres: The Western Alboran Gyre (WAG) and the Eastern Alboran Gyre (EAG). These rotating water masses form due to the interplay between the jet and local topography, as well as wind stress. The Western Alboran Gyre is located near the entrance of the Strait of Gibraltar, while the Eastern Alboran Gyre extends farther eastward (Figure 2). In addition to these large-scale gyres, the Alboran Sea is characterized by smaller, short-lived eddies, which are swirling masses of water that break off from the main current systems. These eddies can be either cyclonic or anticyclonic, depending on their rotation, and they play an important role in transporting nutrients, heat, and salinity throughout the basin.

The interaction between these gyres, eddies, and the Atlantic Jet creates a highly variable environment in the Alboran Sea, where physical processes such as upwelling and downwelling drive the availability of nutrients. For instance, during the spring and summer months, increased SSTs enhance the strength of the Atlantic Jet, reinforcing the gyres and promoting coastal upwelling along the northern coast of the Alboran Sea (Macías et al., 2008). These upwelling events are critical for replenishing surface waters with nutrients, supporting primary production and the overall marine ecosystem in the region.

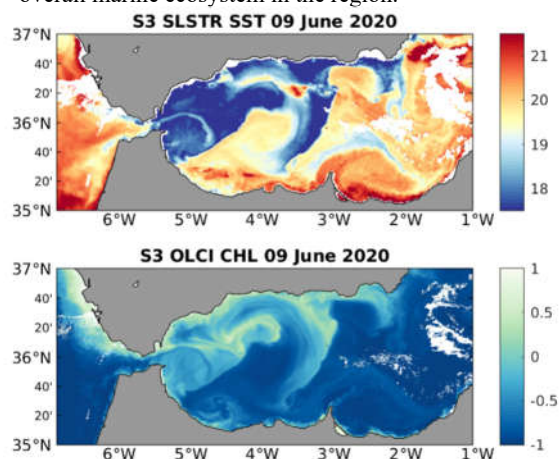


Figure 1. Gyres of Alboran Sea SST and CHL the 9 June 2020. Source: Copernicus

3. DATA

The datasets used in this study are sourced from the Copernicus Marine Service (CMEMS) and ingested

through the Deep Earth System Data Lab (DeepESDL) platform. These datasets are critical for analyzing the oceanographic processes of the Alboran Sea and the Oran front and include key ocean variables such as: SST, SSS, SSH and CHL content (Figure 2).

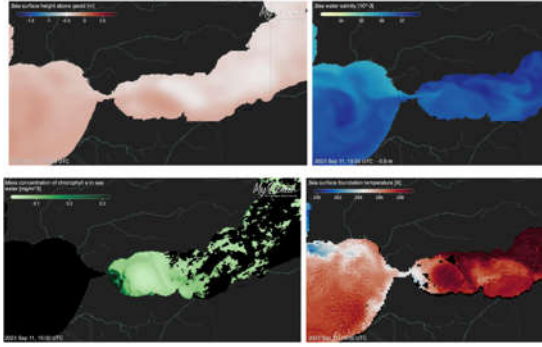


Figure 2. Examples of the used datasets in Alboran Sea. MyOcean

Variable name	Temporal range in CMEMS	Spatial resolution	Temporal resolution
SST	1 Jan 1993 to 29 Nov 2024 (actual)	1 km (0.01 degrees)	Near Real Time (NRT)
SSS	1 Jan 2019 to 8 Nov 2024 (actual)	8 km (1/12 degrees)	Daily
CHL	1 Jan 2002 to 29 Nov 2024 (actual)	1 km (0.01 degrees)	Near Real Time (NRT)
SSH	1 Jan 1993 to 8 Nov 2024 (actual)	8 km (1/12 degrees)	Daily

These datasets are stored into datacubes using the tools available at the DeepESDL platform, an advanced platform designed to integrate and analyze multi-dimensional Earth system data. Using the Pythonic xcube/xarray framework, we have converted diverse data sources into harmonized datacubes by aligning variables on a standardized spatial and temporal grid. This harmonization process includes regridding and temporal aggregation, ensuring that all variables are spatially and temporally consistent, facilitating seamless comparison and analysis (Azcarate et al., 2011; Kirches et al., 2016).

Furthermore, The DeepESDL's structure supports advanced statistical analysis and machine learning workflows, optimizing pattern and trend detection in large-scale and submesoscale processes.

4. METHODOLOGY: CUBES GENERATION AND ALGORITHM IMPLEMENTATION

The methodology used in this study begins with the generation of datacubes, which serve as the foundation for all subsequent analyses. In the cube generation step, DeepESDL platform leverages the xcube/xarray framework, which enables the creation of analysis-ready datacubes by ingesting, preprocessing, and formatting data from multiple sources. The core objective of this framework is to produce multi-dimensional arrays that allow for efficient exploration and analysis of large datasets (Figure 3).

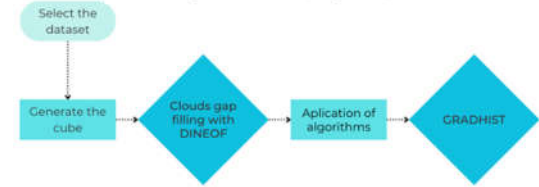


Figure 3. Simplified workflow of the methodology

The second step, once the datacubes are generated, involves filling any missing data points for each variable (Figure 4). This is accomplished using the Data Interpolating Empirical Orthogonal Functions (DINEOF) algorithm (Azcarate et al., 2011). DINEOF is particularly useful when working with satellite-derived datasets, where gaps may arise due to cloud cover, sensor limitations, or transmission errors. DINEOF begins by assuming that missing data points are zero or equal to the mean value for the variable in question. Empirical Orthogonal Function (EOF) analysis is iteratively applied to the dataset. EOFs decompose the dataset into a set of orthogonal modes, representing the dominant patterns of variability. Over successive iterations, DINEOF refines the estimates for the missing data points based on these modes, until a stable solution is reached. The final output is a fully reconstructed dataset, with missing data points filled in based on the observed patterns of variability.

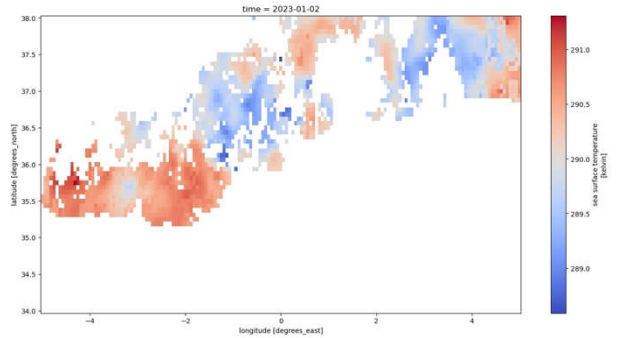


Figure 4. Map extracted from the datacube generated in Alboran Sea from SST.

This ensures that the datasets used in the analysis are complete and continuous, enhancing the robustness of the results. When performing gap filling with the DINEOF algorithm, there is a risk of introducing inaccuracies, as it relies on spatial and temporal patterns to estimate missing data. Although DINEOF is effective for reconstructing oceanographic datasets, such as chlorophyll-a concentrations, its reliability is influenced by the temporal frequency and duration of the original data series. Studies have shown that gap-filled data using DINEOF can differ from in situ measurements, especially in regions with high ocean variability, which may impact analyses of complex phenomena like phytoplankton bloom timing (Hilborn & Costa, 2018; Liu & Wang, 2022)

After the data is reconstructed, the GRADHIST (Kirches, G, 2016) algorithm will be applied to detect oceanic fronts by identifying sharp gradients in variables like sea surface temperature or salinity. GRADHIST analyzes the data cubes to detect zones with strong horizontal gradients. This is crucial for identifying small-scale features such as submesoscale fronts and eddies, which play a key role in the transport of nutrients and the mixing of water masses. The algorithm then characterizes the detected fronts by their intensity, shape, and temporal evolution. This information will be used to study the role of these fronts in driving biological productivity and other oceanographic processes in the Alboran Sea.

5. DISCUSSION AND FUTURE JOB

The results of this study will provide valuable insights into the submesoscale processes of the Alboran Sea, particularly regarding the interactions between coastal and offshore waters. Understanding the dynamics of the Atlantic Jet (AJ), gyres, eddies, and their influence on oceanic fronts and biological productivity is critical for assessing the health and resilience of marine ecosystems in this region. The ability to detect oceanic fronts using advanced algorithms such as GRADHIST and reconstruct incomplete data with DINEOF will allow us to capture fine-scale variability in key oceanographic parameters.

Moving forward, the expansion of this database and the refinement of machine learning algorithms will be essential for advancing our capacity to monitor oceanographic changes. Future work will focus on:

- i) Use different machine learning models to optimize the detection of oceanic fronts.
- ii) Integrating additional datasets, such as LSTM (Land Surface Temperature Mission) simulations, which could enhance our ability to predict the spatial variability, at least of the SST. The significance of this work lies in its methodological advancements and its ability to shed light on the complex oceanographic processes that govern the Alboran Sea and the Almería-

Oran front. This region serves as a natural laboratory for studying Mediterranean-Atlantic water exchanges, and the insights gained from this research could be applied to other transitional marine environments around the world.

6. KEY REFERENCES

- Azcarate, A., Barth, A., Sirjacobs, D., Lenartz, F., & Beckers, J.-M. (2011). Data Interpolating Empirical Orthogonal Functions (DINEOF): A tool for geophysical data analyses. *Mediterranean Marine Science*, 12, 10.12681/mms.64.
- Hilborn, A., & Costa, M. (2018). Applications of DINEOF to satellite-derived chlorophyll-a from a productive coastal region. *Remote Sensing*, 10(9), 1449. <https://doi.org/10.3390/rs10091449>
- Kirches, G., Brockmann, C., Stelzer, K. (2016). GRADHIST — A method for detection and analysis of oceanic fronts from remote sensing data. *Remote Sensing of Environment*, 181, 264-280. <https://doi.org/10.1016/j.rse.2016.04.009>.
- Liu, X., & Wang, M. (2022). A global daily gap-filled chlorophyll-a dataset in open oceans during 2001–2021 from multisource information using convolutional neural networks. *Earth System Science Data*, 15, 5281–5302. <https://doi.org/10.5194/essd-15-5281-2023>
- Macías, D., et al. (2007). Biophysical coupling in the Alboran Sea: Implications for nutrient distribution. *Journal of Marine Systems*, 68(1), 55-68.
- Macías, D., et al. (2008). Meteorological forcing and biogeochemical response in the Alboran Sea. *Journal of Marine Systems*, 71(3-4), 218-232.

ACKNOWLEDGEMENTS

Part of this study was funded by MICIU (IPL – LSTM: PID2020 – 112494RB -I00) We also received support by NoR (ESA) and Brockmann Consult GmbH.

Advances on Spanish ecosystem dynamics by combining 20 years of daily GPP and nonlinear embedding method

B. Martínez, S. Sánchez-Ruiz, M. Campos-Taberner, A. Jiménez, F. J. García-Haro, M. A. Gilabert

Environmental Remote Sensing Group (UV-ERS), Departament de Física de la Terra i Termodinàmica, Facultat de Física, Universitat de València, 46100 Burjassot, Spain.

e-mail: beatriz.martinez@uv.es

ABSTRACT- *The main objective of this study is to detect and quantify monotonic trends in a time series of gross primary production (GPP) in peninsular Spain for two decades, from 2004 to 2022 (the period has been shortened due to meteorological data constraints). Daily GPP values are derived at 1-km spatial resolution from an optimized methodology adapted to the Spanish inland territory to obtain a GPP climate data record. These time series can be analyzed by means of the non-linear Bk-embeddings (NLE) method, which is based on smooth mathematical structures depending on a continuous real parameter κ , with values ranging between zero (original time series) and infinity (trend component, characterizing the inter-annual variation). The continuous variation of κ is crucial for the decomposition of the time series into different temporal components, offering a flexibility that other methods do not provide. The magnitude and direction of trend (increasing or decreasing slope of inter-annual variation) are analyzed in terms of precipitation variations throughout the 2004-2022 period. For that purpose, daily images of precipitation (including the SPI) at 1-km spatial resolution for the same period are obtained from the Spanish Meteorological Agency (www.aemet.es). Statically significant ecosystems changes are enhanced, identified and explained in terms of the aforementioned relationships between GPP and meteorological variables, centering the focus on subtle changes as those due to degradation processes.*

1 INTRODUCTION

A full description of the carbon cycle requires detailed information on spatiotemporal patterns of surface-atmosphere carbon fluxes. One of the main carbon fluxes characterizing terrestrial ecosystems and biodiversity is the gross primary production (GPP), i.e., the amount of carbon absorbed by vegetation to perform photosynthesis, since it establishes the main carbon and energy inputs to ecosystems for producing food, wood, and fiber (Xiao et al., 2019). Consequently, ecosystem dynamics can be characterized analyzing GPP time series, which show a non-stationary behavior due to short-term, seasonal and long-term variations.

This study focusses in long-term variations, which use to be linked to climate variability and, in some cases, are found in areas affected by land degradation processes. Vegetation in these areas is sparse; the subtle changes require a precise methodology to be detected and quantified and the detection of trends ensuring statistical significance is rather difficult due to the associated uncertainties. Degradation processes are found in several countries on the Mediterranean Basin, in particular, Spain.

Mainland Spain territory is analyzed by means of daily GPP time series at 1-km spatial resolution to detect long term vegetation changes. The non-linear Bk-embeddings (NLE) method is used to analyse the time series. It is based on smooth

mathematical structures depending on a continuous real parameter κ , with values ranging between zero (original time series) and infinity (trend component, characterizing the inter-annual variation) (García-Morales, 2017). The magnitude and direction of trend (increasing or decreasing slope of inter-annual variation) are analyzed in terms of precipitation variations throughout the 2004-2022 period.

2 MATERIALS

2.1 Daily GPP time series

The procedure to obtain the daily GPP ($\text{g m}^{-2} \text{d}^{-1}$) images is described in Martínez et al. (2022) and corresponds to:

$$\text{GPP} = \text{PAR} f_{\text{APAR}} \varepsilon_{\text{max}} C_{\text{ws}} T_{\text{min}}. \quad (1)$$

The PAR ($\text{MJ m}^{-2} \text{d}^{-1}$) accounts for the photosynthetically active radiation ($0.4\text{--}0.7 \mu\text{m}$). It is computed as 46% of the daily solar irradiance, which was given by the MSG DIDSSF product (LSA-203) reprocessed and available from 2004 up to the present at <https://landsaf.ipma.pt/>. This product was very satisfactorily validated in the study area and is used as the input of the MSG/SEVIRI GPP product LSA-411.

The daily f_{APAR} (fraction of absorbed PAR) at 1-km spatial resolution is obtained by applying the algorithm proposed by Roujean & Breon (1995) to

MODIS products MCD43A1 and MCD43A2. This algorithm is used to derive the SEVIRI/MSG f_{APAR} product (LSA-425).

ϵ_{max} (g MJ^{-1}) is the ecosystem light use efficiency under optimal conditions and depends on the vegetation type. An optimized vegetation map for the study area is used to assign the ϵ_{max} value to each pixel according to the literature (Martínez et al., 2022).

C_{ws} is a water stress coefficient that is calculated as a linear relationship with the water balance between actual and potential evapotranspiration (AET and PET, respectively). In this case as AET is not available, precipitation is considered when AET is lower than PET (Martínez et al., 2022). PET ($\text{mm m}^{-2} \text{d}^{-1}$) is obtained, according to (Jensen & Hase, 1965) parameterization, from the daily global irradiation from the LSA-203 product, and the daily air temperature.

T_{min} refers to the $T_{\text{min_scalar}}$ used in the MOD17 product (Running & Zhao, 2021). It is a linear ramp function of minimum air temperature that reduces ϵ_{max} accounting for low temperatures, depending also on the vegetation type.

2.2 Precipitation data

Daily precipitation data are provided by the Spanish Meteorological Agency (www.aemet.es) for the 2004–2022 period. The daily images at 5-km spatial resolution are resampled at 1-km resolution. SPI images are computed from them. The SPI quantifies precipitation anomalies by transforming observed precipitation into a gamma distribution for a specific period (WMO, 2012). In this study, the 12-month SPI over the period 2004–2022 are computed to enhance the identification and understanding of vegetation changes.

3 METHODS

Non-linear Bk-embeddings (NLE) are smooth mathematical structures that connect objects with similar or different dimensions (García-Morales, 2017). The dimension reduction involves a mixed convolution of discrete and continuous time variables. The continuous variation of a real parameter $\kappa > 0$ allows constructing the elements of the embedding. The objects connected by the embedding act as fixed points of the latter in the limits $\kappa \rightarrow 0$ and $\kappa \rightarrow \infty$. NLE have proved to be very useful in connecting vector spaces of different dimensions (García-Morales, 2020).

NLE have several key features that make them worthwhile for the analysis of time series. One of them is that this technique allows revealing hidden structures of different scales immersed in the time

series (García-Morales, 2017; García-Morales, 2020). Another key feature is that the objects connected by the embedding can be recovered not only in the limits $\kappa \rightarrow 0$ and $\kappa \rightarrow \infty$ but also for a continuous range of κ values. The value of the scale parameter κ changes with the temporal resolution of the time series since it determines the number of measurements in a specific time interval.

The effectiveness of the NLE method was previously analyzed using 16-day MODIS NDVI TS at 1-km spatial resolution in Spain (Martínez et al., 2025). It detected subtle changes with lower uncertainty than the multi-resolution analysis based on the wavelet transform, MRA-WT, which has been extensively used over the past few decades in several fields such as remote sensing, finance, medicine, etc., (Martínez & Gilabert, 2009; Rhif et al., 2022).

A temporal analysis at local and regional level are carried out. First, the temporal dynamics of GPP using the NLE procedure is performed to derive the inter-annual component ($\kappa=23$). Second, the trend (magnitude and direction) of the inter-annual component is obtained through the combination of the Mann–Kendall test and the Theil–Sen slope estimator, Q_{GPP} as a significant level of p -value of 0.05. Third, the 12-month SPI (SPI12) is considered as the inter-annual variation of precipitation. Both the Mann–Kendall test and Theil–Sen slope are considered to derive the precipitation trend (Q_{SPI12}). In this case, the significant level is relaxed to p -values under 0.3 to have a larger number of pixels to be compared with the GPP trend values.

4 RESULTS

4.1 Local assessment

Eight sites corresponding to different ecosystems are selected (Table 1) and shown in Figure 1 over a hybrid land cover map from Perez-Hoyos et al. (2012). To minimize the problem due to the MODIS coarse spatial resolution, the local analysis has been performed over homogeneous sites. The sites have been chosen to represent differences in plant structure (and consequently in their radiative regime) and are preferably located in: (i) natural parks, such as La Albufera in Valencia (site #6) and Sierra de Cazorla, Segura y las Villas in Jaén (site #2); (ii) forest areas such as Selva de Irati in Pamplona (site #3); and (iii) degradation vulnerable areas from NATURA 2000 network (<https://natura2000.eea.europa.eu/>), such as sites #5 and #8.

Table 1. Selected sites for different land cover types. Codes: EBF (evergreen broadleaved forest), ENF (evergreen needle-leaved forest), DBF (deciduous broadleaved forest), GRA (grassland), ICRO (irrigated crop), SHR (shrubland), and SPV (sparse vegetation).

Site ID	Land cover	Lat/Lon	Province
#1	EBF	43.07N; -8.29E	La Coruña
#2	ENF	38.30N; -2.56E	Jaén
#3	DBF	43.07N; -1.51E	Navarra
#4	ENF	40.75N; -2.09E	Guadalajara
#5	GRA	39.94N; -5.77E	Cáceres
#6	ICROP	39.28N; -0.33E	Valencia
#7	SHR	38.63N; -0.10E	Alicante
#8	SPV	37.07N; -2.37E	Almería

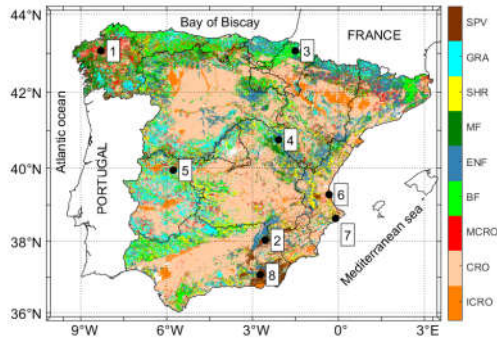


Figure 1. Location of the selected sites over a land cover map. (Codes: see Table 1).

The results of applying NLE to GPP time series for the selected sites at local scale is shown in Figure 2.

The sites #7 and #8, which show negative trends, correspond to natural vegetation located in semi-arid regions (Alicante and Almeria regions) making them particularly vulnerable to desertification. Soil erosion, worsened by overgrazing, deforestation, and poor land management, is one of the primary consequences of land degradation in this area. The area uses to be affected by periodic droughts that exacerbate desertification risks, such as the dry period in 2005 (https://www.aemet.es/es/serviciosclimaticos/vigilancia_clima/).

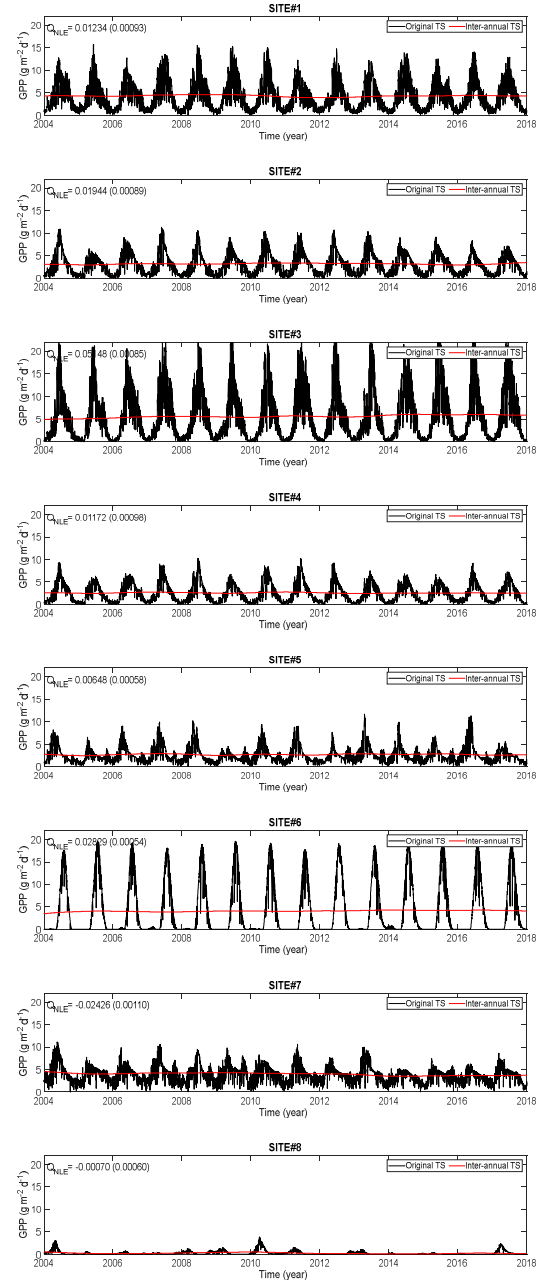


Figure 2. Original time series (black line) and inter-annual component (red line) obtained from the NLE method.

4.2 Regional assessment

Figure 3 shows the results of applying NLE at regional level to map significant changes: the magnitude of the change, i.e. the Theil-Sen slope of the inter-annual component (top), and its direction

and significance (bottom). A non-significant Mann–Kendall test value (0 value) means the null hypothesis (H_0) of this test (no trend exists) may not be rejected, whereas a significant test value (1 value) assumes H_0 is rejected, and a trend is considered. H_0 is rejected at p -value under 0.1 significance levels for the daily GPP time series. A *greening* is observed in northern Spain. Few negative changes (browning) are observed on southern and eastern Spain.

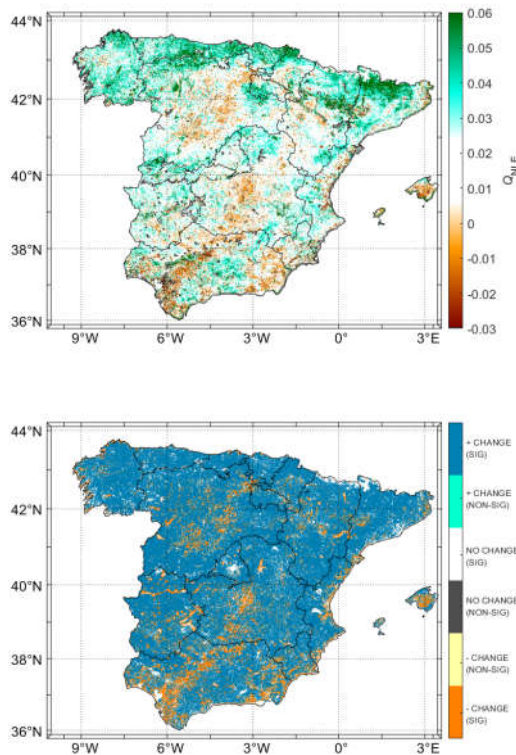


Figure 3. Theil-Sen slope (top) and Mann-Kendall significance test (bottom) for the inter-annual component obtained when the NLE is applied to daily GPP time series.

The spatial trend distribution and magnitude in this study are consistent with the estimates of other studies (Martínez & Gilabert, 2009; Vicente-Serrano et al., 2020; Martínez et al., 2022). It is important to note that it is difficult to inter-compare our derived result with other published results in Spain since the inter-annual trend is highly dependent on the time series length, temporal resolution and time considered for the beginning of the time series. The same area could provide positive inter-annual trends if the beginning of the series agrees with just the moment after a forest fire or negative trend in case the time series finishes with a forest fire.

On the other hand, the Theil-Sen slope computed from monthly SPI12 time series characterize the direction and statistical significance of monotonic trend for precipitation time series (Figure 4).

Inter-annual GPP trends mapped in Figure 3 can be mainly attributed to variations of precipitation during the same period. Exceptions are found in areas also affected by human activity (land abandonment) or hazards events, such as forest fires (eastern Spain in Valencia region, Spain).

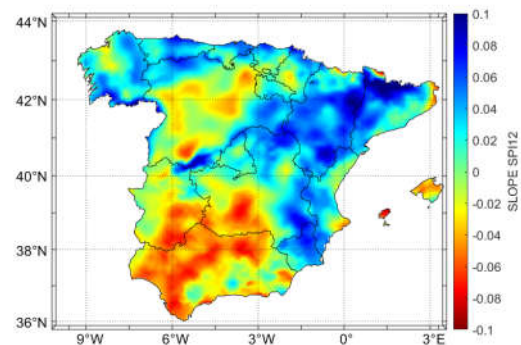


Figure 4. Theil-Sen slope for the monthly SPI12 time series. The p -value condition is relaxed to 0.3 in order to have a larger number of pixels to be compared with the GPP trend values in Figure 3.

5 CONCLUSIONS

The methodology used to infer subtle long-term vegetation changes from daily GPP at 1-km spatial resolution series over Peninsular Spain based on the Non-Linear Embedding (NLE) method. One of the advantages of NLE is that it depends on a kappa parameter; by changing κ we can obtain different temporal components such as the inter-annual component. It has made it possible to map significant inter-annual trends, which have been related to precipitation variability.

A clear agreement between GPP and precipitation patterns was observed, particularly in southeastern Spain, eastern Mediterranean coastland, and central Spain. Evidence of high vulnerability is confirmed in southeastern Spain areas where land degradation areas are detected. These changes are mainly attributed to variations of precipitation as exception of local areas, which may be affected by human activity or hazards events, such as forest fires.

6 ACKNOWLEDGMENTS

This research was supported by the LSA SAF (EUMETSAT) and ECCE EO project (PID2020-118036RB-I00) funded by MCIN/AEI/10.13039/501100011033.

7 REFERENCES

- García-Morales, V. 2017. Nonlinear embeddings: Applications to analysis, fractals and polynomial root finding. *Chaos, Solitons & Fractals*, 99, 312.
- García-Morales, V. 2020. Unifying vectors and matrices of different dimensions through nonlinear embeddings. *Journal of Physics: Complexity*, 1, 025008.
- Jensen, M.E. Haise, H.R. 1965. Estimating evapotranspiration from solar radiation. *Journal of the Irrigation and Drainage Division*, 89, 15–41.
- Martínez, B., Gilabert, M.A. 2009. Vegetation dynamics from NDVI time series analysis using the wavelet transform. *Remote Sensing of Environment*, 113 (9), 1823–1842.
- Martínez, B. Sánchez-Ruiz, S. Campos-Taberner, M, García-Haro, F.J. Gilabert, M.A. 2022. Exploring Ecosystem Functioning in Spain with Gross and Net Primary Production Time Series. *Remote Sensing*, 14, 1310.
- Martínez, B., García-Morales, V., Manzanares, J.A., Gilabert, M.A. 2025. The nonlinear embeddings method for long-term vegetation dynamics. *ISPRS Journal of Photogrammetry and Remote Sensing*, in revision.
- Pérez-Hoyos, A., García-Haro, F.J., San-Miguel-Ayán, J. 2012. A methodology to generate a synergetic land-cover map by fusion of different: Land-cover products. *International Journal of Applied Earth Observation and Geoinformation*, 19, 72–87.
- Rhif, M., Ben Abbes, A., Martínez, B., Farah, I.R., Gilabert, M.A. 2022. Optimal selection of wavelet transform parameters for spatio-temporal analysis based on non-stationary NDVI MODIS time series in Mediterranean region. *ISPRS Journal of Photogrammetry and Remote Sensing*, 193, 216–233.
- Roujean, J.L., Breon, F.M. 1995. Estimating PAR absorbed by vegetation from bidirectional reflectance measurements. *Remote Sensing of Environment*, 51, 373–384.
- Running, S., Zhao, M. 2021. User's Guide Daily GPP and Annual NPP (MOD17A2H/A3H) and Year-end GapFilled (MOD17A2HGF/A3HGF) Products NASA Earth Observing System MODIS Land Algorithm (For Collection 6.1); University of Montana: Missoula, MT, USA, pp. 1–33.
- Vicente-Serrano, S. M., Martín-Hernández, N., Reig, F., Azorin-Molina, C., Zabalza, J., Beguería, S., Domínguez-Castro, F., El Kenawy, A., Peña-Gallardo, M., Noguera, I., García, M. 2020. Vegetation greening in Spain detected from long term data (1981–2015). *International Journal of Remote Sensing*, 41 (5), 1709–1740.
- WMO. Standardized Precipitation Index User Guide; WMO: Geneva, Switzerland, 2012.
- Xiao, J., Chevallier, F., Gomez, C., Guanter, L.; Hicke, J.A., Huete, A.R., Ichii, K., Ni, W., Pang, Y., Rahman, A.F., et al. 2019. Remote sensing of the terrestrial carbon cycle: A review of advances over 50 years. *Remote Sensing of Environment*, 233, 111383.

Surface soil organic carbon estimation based on habitat patches in southwest China

Jieyun Xiao ¹, Wei Zhou ^{*1,2}, Wenping Yu ¹, Ting Wang ¹, Yao Peng ¹

¹ Chongqing Jinpo Mountain Karst Ecosystem National Observation and Research Station, Chongqing Engineering Research Center for Remote Sensing Big Data Application, School of Geographical Sciences, Southwest University, Chongqing 400715, China (e-mail: xjy513930@email.swu.edu.cn).

² State Key Laboratory of Resources and Environmental Information System, Institute of Geographic Sciences and Natural Resources Research, CAS, Beijing 100101, China (e-mail: zw20201109@swu.edu.cn)

ABSTRACT – High-precision digital soil mapping in complex terrain is challenging. This study proposed a new method using the PAM clustering algorithm to partition the study area into distinct habitat patches type. Utilizing multi-source data and three machine learning models, we estimated soil organic carbon (SOC) content in southwest China. Results showed topographic and climatic variables played crucial roles in SOC estimation. Among the three machine learning models, RF and XGBoost demonstrated higher simulation accuracy than SVM (R^2 increased by 2.86% to 82.35%). Meanwhile, the study found that a hybrid model based on different habitat patches achieved higher accuracy than the single model for the whole study area. Such improvements better characterized the spatial variability of SOC and provided important implications for future soil carbon stock account in complex terrain areas.

1 INTRODUCTION

The carbon cycle is the subject of intense focus in global climate change research (Zhou et al., 2020), and soil forms an important component of this cycle. SOC is the total amount of carbon elements contained in soil organic matter, including soil humus, microbial necromass and plant roots, and is the main carbon reservoir in the soil. The level of SOC content not only determines the water and fertilizer retention capacity of soil and the metabolic activities of microorganisms, but also affects atmospheric CO₂ concentration, which has a significant impact on climate change, agricultural production and the global carbon cycle (Chen et al., 2023; Gholizadeh et al., 2018; Zeraatpisheh et al., 2019). Therefore, the accurate simulation and management of SOC content is an important issue in soil science and environmental protection.

In recent decades, more attention has been devoted to estimating and mapping the spatial distribution of SOC with high precision at various spatial scales (Chen et al., 2022). Understanding variability within the spatial distribution of SOC and the factors that influence it is a critical aspect of research in this field (Ren et al., 2023; Yang et al., 2023). Traditional polygon-based soil mapping mainly relies on field sample surveys and laboratory chemical measurements. However, this method (Hudson, 1992) is being supplanted by digital soil mapping (DSM) due to the increasing complexity of soil mapping requirements and the availability of remote sensing data with high

spatial and temporal resolution. DSM is a highly efficient and convenient technique that leverages models constructed using quantitative relationships between soil properties and predictive variables to accurately predict the spatial distribution pattern of soil (Wadoux, 2019). Machine learning algorithms have the capability to model complex nonlinear relationships by learning and training on extensive datasets. As a result, they have a wide range of applications in the simulation and prediction of soil organic carbon content, and are gradually becoming a mainstream method for DSM. Machine learning algorithms such as Support Vector Model (SVM), Random Forest (RF), Extreme Gradient Boosting (XGBoost) and Cubist can be used to establish complex relationships between SOC content and multi-source data, such as soil properties, vegetation indices, climate factors and other factors (He et al., 2021; Moura-Bueno et al., 2021). In addition, machine learning algorithms can visualize the prediction uncertainty, then achieve a high-precision SOC estimation.

DSM performance is highly dependent on the environmental variables that influence soil properties (Nussbaum et al., 2018). Currently, researchers are committed to developing analytical models of SOC variability coupled with factors such as topography, soil type, biotic factors and anthropogenic activities (Tao et al., 2023), with a view to better understanding the spatial distribution patterns of SOC. Soil parent material, climatic factors, biological factors,

topographical factors and human activities are all key environmental factors that change the direction and intensity of soil formation (Ou et al., 2017). At present, remote sensing data from Landsat (Xu et al., 2022), MODIS (Zhang et al., 2021), Sentinel-1 (Yang and Guo, 2019), Sentinel-2 (Vaudour et al., 2019), Sentinel-3 (Lin et al., 2020) and many other satellite sensors combined with different machine learning algorithms have been successfully applied to estimate surface SOC at different scales. Although a large number of environmental variable datasets are easily acquired, the influence of environmental variables on SOC are different for different spatial scales (Lu et al., 2019). Various variable selection methods exist to quantify the predictive importance of environmental variables (Besalatpour et al., 2014; Keskin et al., 2019; Uwiragiye et al., 2022), however, there is not yet some recognized universal optimal feature variable selection method. In addition, although indicators such as land use type can be used as a basis for partition strongly heterogeneous regions for SOC estimation, differences in other environmental variables under the same land use type will also seriously reduce SOC simulation accuracy at large regional scales where SOC exhibits highly spatially heterogeneous. How to choose the optimal combination of environmental variables and how to overcome the challenges of SOC prediction due to heterogeneous surfaces? This needs to be further explored.

In southwest China, significant differences in climate and topography lead to a more complex landscape pattern of habitat patches, resulting in an extremely heterogeneous spatial distribution of SOC. Taking the region as an example, this study integrates various environmental variables such as climate, topography, population and vegetation to partition the study area into habitat patches. On this basis, we used FS to determine the optimal combination of environmental variables, combined it with a machine learning model to build an optimal predictive model for the spatial distribution of SOC, and explore the effect of environmental variables on SOC. The objectives of this study were to: (1) investigate the influence of FS methods on the accuracy of SOC content estimation in the study area; (2) evaluate whether simulation accuracy can be increased by using habitat patches instead of a single model for the entire study area. The results of this study emphasize the importance of habitat patch delineation and FS in soil organic carbon prediction, aiming to provide a reference for the accurate estimation of SOC and its dynamics in the complex terrain of southwest China.

2 MATERIALS AND METHODS

2.1 Study area

The study area occupied a total area of about 1,364,000km² in southwest China (21°04'-34°19'N, 97°15'-112°11'E) and included the provinces of Sichuan, Yunnan, Guizhou, Chongqing and Guangxi (Fig. 1). The region has diverse climate types but is dominated by subtropical monsoon and temperate climates, with average precipitation ranging from 1,000 to 1,600 mm per year.

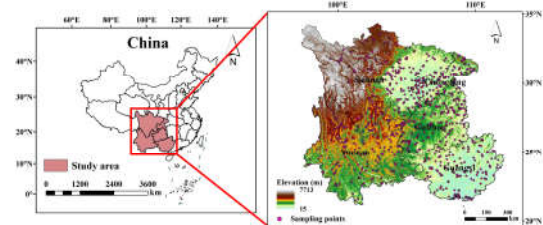


Fig. 1. The location of study area and sampling points.

2.2 Data

Soil survey data for this study were obtained from the *Soil Series of China*. Samples were collected between 2015-2016 and covered a total of 795 valid soil sample points. Soil profile dataset was obtained in southwest China according to uniformity and representativeness. Information such as latitude, longitude, altitude, soil type and soil physicochemical properties were included in sampling points. Samples were collected between 2015-2016 and covered a total of 795 valid soil sample points (Fig. 1). The depth of these soil profiles ranged from 0-120 cm. Considering that surface SOC is more sensitive to fluctuations in external environmental factors, only SOC in soil profiles with a depth of 0-15 cm was selected as the object of study in this study.

A total of 30 environmental variables related to SOC formation and accumulation processes were selected for this study. These variables can fully reflect the spatial changes of soil and are easy to obtain and quantify, including climate, topography, human activities, Landsat8 remote sensing indices and Sentinel-1A "IW" mode for vertical-vertical (VV) and vertical-horizontal (VH) polarization. Table 1 shows the basic information of environmental covariates.

2.3 PAM clustering

In our study, we selected nine factors to partition habitat patch types in the study area: DEM, mean annual temperature, mean annual precipitation, land surface temperature, sand, silt, clay, NDVI and population density. Pixel values of these environmental variables were normalized, and PAM cluster analysis was completed using the "cluster" package in R software.

2.4 Model prediction

Machine learning algorithms such as SVM, RF and XGBoost have been widely used in DSM research. This study utilized these three machine learning algorithms to learn multi-source data such as soil properties, vegetation indices and climatic factors. Through these methods, a complex relationship between SOC content and environmental variables was established (He et al., 2021; Moura-Bueno et al., 2021) to achieve accurate prediction of soil organic carbon content.

We used 5-fold cross validation to test the models' predictive performance. These calculations (R^2 , RPD, RMSE, MAE) were used to select the model with optimal modeling accuracy.

$$R^2 = 1 - \frac{\sum_{i=1}^n (P_i - O_i)^2}{\sum_{i=1}^n (P_i - \bar{O})^2} \quad (1)$$

$$RMSE = \sqrt{\frac{1}{n} \sum_{i=1}^n (P_i - O_i)^2} \quad (2)$$

$$MAE = \frac{1}{n} \sum_{i=1}^n |P_i - O_i| \quad (3)$$

$$RPD = \frac{SD}{\sqrt{\frac{1}{n} \sum_{i=1}^n (P_i - O_i)^2}} \quad (4)$$

where n is the number of soil sample points; The predicted and measured SOC content (/kg) are represented by P_i and O_i , respectively; n represents the number of soil sample points; \bar{O} indicates the mean values of measured SOC content; and SD is the standard deviation of measured SOC content.

3 RESULTS

3.1 Clustering results

The PAM algorithm determined that the optimal number of clusters for the study area was 4. Clustering result is shown in Fig. 2. Habitat patches partition results using PAM clustering analysis: Cluster 1 is mainly distributed in the western part of Sichuan, with higher elevation and grassland coverage; Cluster 2 is mainly distributed in the most of Sichuan Basin and the Yunnan-Guizhou Plateau, with higher cropland coverage and population density; Cluster 3 is mainly distributed in the northwest of Sichuan Basin and its surrounding mountains, and a small part of the Yunnan Plateau, with high woodland coverage; Cluster 4 is mainly distributed across an area Guangxi with lower elevation and high woodland coverage. The number of sampling points after clustering was distributed as follows: 67 sampling points within Cluster 1, 378 sampling points within Cluster 2, 183 sampling points within Cluster 3 and 167 sampling points within Cluster 4.

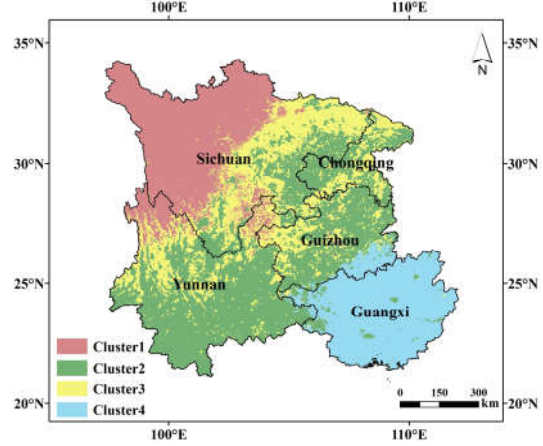


Fig. 2. Habitat patches partition results using PAM clustering analysis

3.2 Model performance

Based on the validation set and taking full variables as control, we found that for Cluster1, Cluster2, Cluster3, Cluster4 and Overall, the accuracy of the three models constructed using FS methods was higher than that of the model using full variables. Additionally, the model constructed using RF for variable selection demonstrated the highest accuracy. This indicated that FS can help the model capture key features better and reduce noise and unnecessary information to improve the model's generalization ability and prediction accuracy.

Using Overall as control, we found that Cluster1 modeling was worse than Overall, but Cluster2, Cluster3 and Cluster4 modeling were all better than Overall. The lack of sampling points in the western part of Sichuan within Cluster1 influenced final prediction results. However, apart from Cluster1, the other prediction models based on PAM clustering had higher simulation accuracy than those based on the whole study area. This may be attributed to the fact that PAM clustering considers more localized features and variations, which enhanced the model's predictive performance.

Using SVM as control, we found that RF and XGBoost performed better on the four clustering regions and Overall. Taking the model constructed by RF selection variables as an example, R^2 values in Cluster1, Cluster3, Cluster4 and Overall were 0.37, 0.62, 0.58 and 0.46 respectively, which was higher than XGBoost by 0.03, 0.03, 0.02 and 0.06, and higher than SVM by 0.09, 0.07, 0.06 and 0.04. Additionally, RF had the lowest RMSE and MAE in these regions compared to SVM and XGBoost. In Cluster2, the R^2 of XGBoost was 0.48, which was 0.01 higher than RF and 0.06 higher than SVM. Similarly, XGBoost had the lowest RMSE and MAE in this region compared to SVM and RF. Higher RPD values represent higher prediction accuracy and

good fit to observed data. Apart from Cluster1 and Overall, RPD of RF and XGBoost was greater than 1.40 on most clustered regions, further validated their superiority in predicting SOC content.

After comparing results, we chose PAM to cluster the study area and to map the predicted spatial distribution of SOC based on RF FS method. We used the RF model for predicting SOC spatial distribution in Cluster1, Cluster3 and Cluster4, and chose the XGBoost model to predict SOC in Cluster2. Additionally, the RF model was also used to predict SOC spatial distribution in Overall for comparison with predictions of the PAM clustering partition.

Table 3 Performance metrics for SOC content across different models and clustering regions; the optimal values highlighted in bold.

Clustering region	Models	Full variables		RF	
		R ²	RMSEMAE	RPDR ²	RMSEMAERPD
Cluster1	SVM	0.17	25.38	17.84	1.06 0.28 24.40 18.86 1.19
	RF	0.31	23.28	17.79	1.13 0.3721.19 15.801.21
	XGBoost	0.31	23.17	17.43	1.17 0.34 20.84 15.80 1.21
Cluster2	SVM	0.36	15.64	11.12	1.15 0.42 11.97 7.01 1.32
	RF	0.40	12.46	7.37	1.27 0.47 10.06 6.84 1.41
	XGBoost	0.39	13.66	7.67	1.24 0.489.58 6.15 1.46
Cluster3	SVM	0.48	18.84	10.73	1.30 0.52 17.91 10.47 1.39
	RF	0.57	14.96	9.64	1.50 0.6211.75 6.03 1.63
	XGBoost	0.53	16.45	10.32	1.37 0.61 14.85 9.39 1.61
Cluster4	SVM	0.46	19.58	11.68	1.27 0.52 15.34 11.40 1.35
	RF	0.53	17.03	10.54	1.49 0.5813.82 8.87 1.51
	XGBoost	0.50	18.05	11.12	1.40 0.56 14.61 10.34 1.49
Overall	SVM	0.35	18.60	9.26	1.20 0.37 15.49 8.68 1.20
	RF	0.37	15.05	9.21	1.25 0.4614.13 8.49 1.35
	XGBoost	0.36	16.57	9.14	1.08 0.40 15.22 8.78 1.27

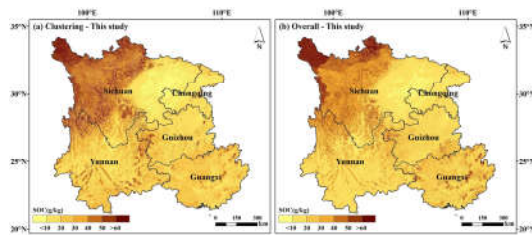


Fig. 3. SOC spatial distribution in the top 0-15cm soil layer.

3.3 SOC map

Based on the results of Fig. 3 (a) Clustering and Fig. 3 (b) Overall, low predicted SOC values were mainly located in the Sichuan Basin, and high predicted SOC values were primarily distributed in the mountainous region of southwest Sichuan, the plateau region of northwest Sichuan, the southern extension of the

Qinghai-Tibet Plateau, the Hengduan Mountains and the Wumeng Mountains of the Yunnan-Guizhou Plateau. This distribution to some extent reflected the dominant role of topography on SOC content and its spatial distribution.

4 CONCLUSION

This study explored the potential of machine learning methods based on PAM clustering and multiple environmental variables in SOC mapping. This approach yielded an estimated average SOC content in the top 0-15cm of the soil in southwest China of 26.57 g/kg with high spatial heterogeneity. Environmental variable factor analysis showed that climatic and topographic factors played crucial roles in predicting SOC, while SAR remote sensing data was only used in Cluster4 and performed poorly in predicting SOC in southwest China. Except for Cluster1, the reliability of SOC estimates based on different habitat patches was significantly higher than that of the whole study area, with R² increased by 2.17% to 34.78% and RMSE decreased by 2.19% to 28.8% in the case of feature selection and modeling based on the RF approach.

5 REFERENCE

- Besalatpour, A.A., Ayoubi, S., Hajabbasi, M.A., Jazi, A.Y. and Gharipour, A., 2014. Feature Selection Using Parallel Genetic Algorithm for the Prediction of Geometric Mean Diameter of Soil Aggregates by Machine Learning Methods. *Arid land research and management*, 28(4): 383-394.
- Chen, Y. et al., 2022. Comparison of feature selection methods for mapping soil organic matter in subtropical restored forests. *Ecological Indicators*, 135: 108545.
- Chen, Z., Qi, S., Shi, Z. and Dominique, A., 2023. National-scale mapping of soil organic carbon stock in France: New insights and lessons learned by direct and indirect approaches. *Soil & Environmental Health*, pp. 100049.
- Gholizadeh, A., Žižala, D., Saberioon, M. and Borůvka, L., 2018. Soil organic carbon and texture retrieving and mapping using proximal, airborne and Sentinel-2 spectral imaging. *Remote Sensing of Environment*, 218: 89-103.
- He, X. et al., 2021. Soil organic carbon prediction using phenological parameters and remote sensing variables generated from Sentinel-2 images. *CATENA*, 205: 105442.
- Hudson, B.D., 1992. The Soil Survey as Paradigm-based Science. *Soil Science Society of America Journal*, pp. 836-841.

- Keskin, H., Grunwald, S. and Harris, W.G., 2019. Digital mapping of soil carbon fractions with machine learning. *Geoderma*, 339: 40-58.
- Lin, C., Zhu, A., Wang, Z., Wang, X. and Ma, R., 2020. The refined spatiotemporal representation of soil organic matter based on remote images fusion of Sentinel-2 and Sentinel-3. *International Journal of Applied Earth Observation and Geoinformation*, 89: 102094.
- Lu, Y., Liu, F., Zhao, Y., Song, X. and Zhang, G., 2019. An integrated method of selecting environmental covariates for predictive soil depth mapping. *Journal of Integrative Agriculture*, 18(2): 301-315.
- Moura-Bueno, J.M., Dalmolin, R.S.D., Horst-Heinen, T.Z., Grunwald, S. and Ten Caten, A., 2021. Environmental covariates improve the spectral predictions of organic carbon in subtropical soils in southern Brazil. *Geoderma*, 393: 114981.
- Nussbaum, M. et al., 2018. Evaluation of digital soil mapping approaches with large sets of environmental covariates. *SOIL*, 4(1): 1-22.
- Ou, Y., Rousseau, A.N., Wang, L.X. and Yan, B.X., 2017. Spatio-temporal patterns of soil organic carbon and pH in relation to environmental factors-A case study of the Black Soil Region of Northeastern China. *AGRICULTURE ECOSYSTEMS & ENVIRONMENT*, 245: 22-31.
- Ren, Y. et al., 2023. China's wetland soil organic carbon pool: New estimation on pool size, change, and trajectory. *Global change biology*, 29(21): 6139-6156.
- Tao, F. et al., 2023. Microbial carbon use efficiency promotes global soil carbon storage. *Nature*, 618(7967): 981-985.
- Uwiragiye, Y. et al., 2022. Modelling and mapping soil nutrient depletion in humid highlands of East Africa using ensemble machine learning: A case study from Rwanda. *CATENA*, 217: 106499.
- Vaudour, E., Gomez, C., Fouad, Y. and Lagacherie, P., 2019. Sentinel-2 image capacities to predict common topsoil properties of temperate and Mediterranean agroecosystems. *Remote Sensing of Environment*, 223: 21-33.
- Wadoux, A.M.J.C., 2019. Using deep learning for multivariate mapping of soil with quantified uncertainty. *Geoderma*, 351: 59-70.
- Xu, Y. et al., 2022. Digital soil mapping of soil total nitrogen based on Landsat 8, Sentinel 2, and WorldView-2 images in smallholder farms in Yellow River Basin, China. *Environmental Monitoring and Assessment*, 194(4).
- Yang, R. and Guo, W., 2019. Modelling of soil organic carbon and bulk density in invaded coastal wetlands using Sentinel-1 imagery. *International Journal of Applied Earth Observation and Geoinformation*, 82: 101906.
- Yang, R., Huang, L., Zhang, X., Zhu, C. and Xu, L., 2023. Mapping the distribution, trends, and drivers of soil organic carbon in China from 1982 to 2019. *Geoderma*, 429: 116232.
- Zeraatpisheh, M., Ayoubi, S., Jafari, A., Tajik, S. and Finke, P., 2019. Digital mapping of soil properties using multiple machine learning in a semi-arid region, central Iran. *Geoderma*, 338: 445-452.
- Zhang, M. et al., 2021. Mapping Soil Organic Matter and Analyzing the Prediction Accuracy of Typical Cropland Soil Types on the Northern Songnen Plain. *Remote Sensing*, 13(24): 5162.
- Zhou, T. et al., 2020. High-resolution digital mapping of soil organic carbon and soil total nitrogen using DEM derivatives, Sentinel-1 and Sentinel-2 data based on machine learning algorithms. *Science of The Total Environment*, 729: 138244.

Fusion of EO and in situ Data for estimating GPP and RECO

P.C. Silvestro¹; Maria P. González-Dugo²; M. Muñoz-Gomez²; N. Grosso¹; P. Marti-Rocafull¹

1: Deimos Space, Madrid, Spain

2: IFAPA, Centro IFAPA Alameda del Obispo, Córdoba, Spain

paolo.silvestro@deimos-space.com; mariap.gonzalez.d@juntadeandalucia.es.

ABSTRACT – The following work is part of a larger European project called ScaleAgData, which aims to upscale real-time sensor data for EU-wide agricultural monitoring. With a consortium of 26 partners from 14 countries, it seeks to govern and organize complex data streams while developing technology to scale farm-level data to regional and EU-wide datasets. Its objectives include innovative data collection, promoting data sharing, and demonstrating benefits in precision farming and agricultural management. The project explores seven innovation areas and establishes six Research and Innovation Labs (RILs) across Europe to evaluate and demonstrate various data upscaling models, providing recommendations for policy-making to enhance competitiveness and sustainability in European agriculture. The work presented is part of the Grassland RI Lab. It aims to develop and evaluate a methodology for estimating standing biomass using a ML solution incorporating satellite Biopars, meteorological information, and soil moisture. The area of interest used to collect data in the field and carry out preliminary validation tests is located in the north of the province of Cordoba. Continuous measurements from two test sites, 50 km apart and equipped with Eddy Covariance (EC) flux towers and environmental sensors (radiation, soil moisture, air temperature, and humidity), were selected for the measurement campaigns (22 and 19 months, respectively). High-frequency (10 Hz) fluctuations were used to calculate the mass fluxes of H₂O and CO₂, between the ecosystem and the atmosphere and all the components of the energy balance. Sentinel-2 and Sentinel-1 images were acquired in correspondence with the field measurements, and from them, the values corresponding to the footprints of the EC towers were extrapolated. The database thus formed was used to train a Feedforward Artificial Neural Network (ANN). Different architectures were tested (number of hidden layers, type of function, linear transfer function, number of nodes per layer, etc) and different combinations of inputs (which EO sensor bands to include, site-specific training or unique training for the entire dataset, etc). From the analysis of the results obtained it was possible to select the best methodology to estimate both Gross Primary Production (GPP) and Ecosystem Respiration (RECO). These results are to be considered preliminary tests, as the available data are not sufficient to form a significant statistical sample. The tests carried out show that for some combinations of architecture and input data, it is possible to obtain a good predictive model, in particular using all training sites and all available Sentinel-2 bands and Sentinel-1 backscatter data. These results encourage the continuation of these tests for larger datasets, especially with a view to including in situ data acquired via Eddy Covariance by exploiting the data sharing network acquired by these sensors distributed throughout the European territory.

Keywords – Sentinel-1, Sentinel-2, ANN, Eddy Covariance, GPP, Grassland.

1. INTRODUCTION

The study we present is part of a much larger project called ScaleAgData. It is a project funded by the Horizon Europe programme (grant agreement No 101086355). ScaleAgData aims to improve in-situ sensor data for agricultural monitoring across the EU. With a consortium of 26 partners from 14 countries, it seeks to govern and organise complex data flows while developing the technology to scale farm-level data into regional and EU-wide datasets. Its objectives include innovative data collection, promoting data sharing and demonstrating the benefits in precision agriculture and farm management. The project explores seven areas of

innovation and establishes six Research and Innovation Labs (RILs) across Europe to evaluate and demonstrate various data upscaling models, providing recommendations for policy making to improve competitiveness and sustainability in European agriculture.

The primary goal of the Grasslands RILab is to enhance the monitoring of grasslands by developing products specifically tailored to this ecosystem. This work aims to show the preliminary results of one of the RI-Lab outcomes: the evaluation of GPP and RECO using a ML solution incorporating satellite data, meteorological information, soil moisture and in-situ measurements.

Estimating gross primary production (GPP), the total amount of CO₂ absorbed by vegetation, is a fundamental step in understanding and quantifying the terrestrial carbon cycle.

In the past decade, various methods have been developed to track the spatiotemporal dynamics of GPP by combining in situ observations with remote sensing data, using either machine learning techniques or semi-empirical models. Despite these advancements, no high-resolution GPP product derived entirely from satellite-based remote sensing data is currently available.

Previous studies have shown, through linear regression models, a notable correlation between GPP and specific vegetation indices such as NDVI, kernel-NDVI, and CIR, with a determination coefficient (r^2) of around 0.6 and a relative root mean square error (RRMSE) of about 0.15. Other research has employed machine learning methods, such as Random Forest, to further enhance model performance, achieving an r^2 of approximately 0.7 and an RRMSE of around 0.1. ([1]–[4])

This work contributes to the state of the art by focusing on experimentation in a specific region, the Mediterranean, which is characterized by a high risk of drought during prolonged periods of the year, and targeting a specific vegetation type: grassland.

It directly applies Earth Observation (EO) data and in situ measurements from an Eddy Covariance (EC) tower, through the development of a dedicated Artificial Neural Network (ANN).

Additionally, it introduces new experiments using EO data for field-scale applications (10/20m ground resolution) in estimating GPP, an area with limited studies in the existing literature.

2. MATERIAL AND METHODS

2.1. Study sites

The study areas where measurements were conducted are illustrated in Figure 1. The two Areas of Interest (AOIs) containing the Eddy Covariance (EC) towers are situated in the Cordoba Dehesa region of southern Spain. This area experiences a continental Mediterranean climate, characterized by an average annual precipitation of approximately 550 mm, with minimum and maximum values of 400 mm and 700 mm, respectively. Precipitation is predominantly concentrated in the autumn (moderate) and spring (intense) seasons. Additionally, the region faces a prolonged drought period from May to September. The average annual temperature is around 17°C, with fluctuations ranging between 10°C and 47°C.

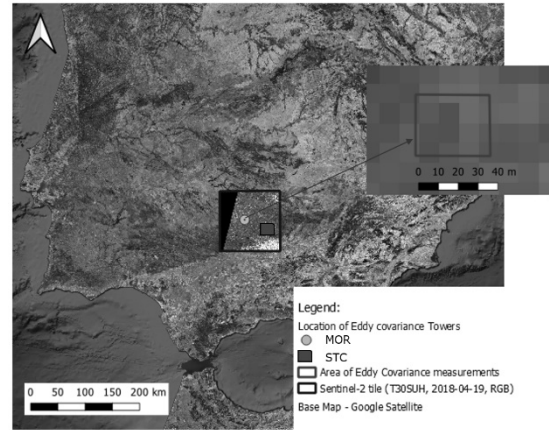


Figure 1: Location of the study areas. The highlighted rectangle Area of Eddy Covariance measurements represents the area where the EC tower falls. The base map of the AOI is a sentinel2 image. It shows the number of S-2 pixels included in the EC footprint.

2.1. In Situ Data sets

The sensors in situ were Eddy Covariance towers and environmental sensors. The firsts measure fluctuations in wind speed and gas concentrations at high frequency (10 Hz) to calculate the mass fluxes of these gases between the ecosystem and the atmosphere, the seconds measure environmental variables such as: soil temperature, solar radiation and soil humidity. CO₂ exchanges were partitioned into Gross Primary Production (GPP) and Ecosystem Respiration (RECO) using models based on the carbon cycle dynamics in the ecosystem and biophysical processes [5], and averaged to daily scale. GPP and RECO are indirectly measured "in situ" and are the key biophysical variables in this study (Figure 2).

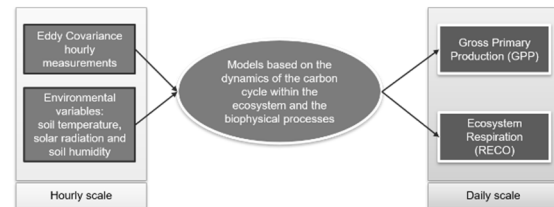


Figure 2: In situ data workflow to elaborate daily GPP and RECO.

The in-situ data were collected in the period 10/2017 - 06/2019 in the AOI called STC and between 10/2020 and 08/2022 for the AOI MOR.

2.2. EO Data sets

The EO data used are those acquired through Sentinel-1 and Sentinel-2.

For this preliminary study, it was decided to use Sentinel-2 as the starting point of the database and to use Sentinel-1 data as support. Therefore, from the catalogue made available by Copernicus, the Sentinel-2 images were selected (more specifically the data acquired through the MSI sensor), processed at Level 2A (Top Of Canopy data), acquired above the tile (which includes both AOIs) T30SUH, in the acquisition period from 1/10/2017 to 1/08/2022 considering a maximum cloud cover of 10%. With these restrictions, the final database is composed of about 300 images.

The data pre-processing flow used was the following: 1) data download via Copernicus API, Raster Clipping of the bands in the AOI format, resampling of the bands with resolutions different from 10m (in order to obtain a single multiband image with 10m resolution), extraction of the pixels that fall entirely within the EC footprint (on average 6 pixels), band-by-band average of the reflectance for each area, normalization (between 0 and 1) of the data (the S2 reflectance being provided between 0 and 10000).

In this way each S2 image provided 11 pieces of information (one per band) corresponding to an "in-situ" measurement. The bands used are: B01, B02, B03, B04, B05, B06, B07, B08, B8A, B09, B11 and B12 [6].

The S1 data chosen (C-SAR sensor) are from Level-1 GRD (dual polarization VV-VH). The Sentinel-1 data selected for this phase of the work are in support of the Sentinel-2 data. The basic idea is to understand how the model performance varies by adding Sentinel-1 data in the algorithm training. Therefore, the S1 data selected for the dataset are those acquired in the vicinity (with an average gap of 24 hours and a maximum of 48) of the S2 data present in the catalogue (selected as previously described). The S1 data chosen (C-SAR sensor) are from Level-1 GRD (dual polarization VV-VH).

The preprocessing workflows of the S1 data were as follows: download of the data of interest, Raster clipping of the 2 polarizations in a single image (as if it were an image with 2 bands) in the AOI format, extraction of the pixels inside the EC footprint and relative average (for each polarization), Data normalization. The S1 data then adds 2 pieces of information (one for each polarization) in correspondence with each field measurement (coinciding with the dates in which S2 images are

available). In this way the database that simultaneously considers in-situ data, S2 data and S1 data is reduced to approximately 200 elements.

2.3. Methodology

The methodology used is based on training an Artificial Neural Network (ANN) using in situ GPP data (and similarly RECO for a distinct model) with EO data. Based on the literature ([7], [8]), we chose to use a feedforward neural network, initially composed of 4 layers: Input Layer, Hidden Layer and an Output Layer. We tested different types of architecture by varying the number of nodes for the Hidden Layers, the number of hidden layers and testing different activation functions for the hidden layers (Hyperbolic Tangent, RELU, Sigmoid and Identity). For the output layer we left one node and the Linear Transfer Function.

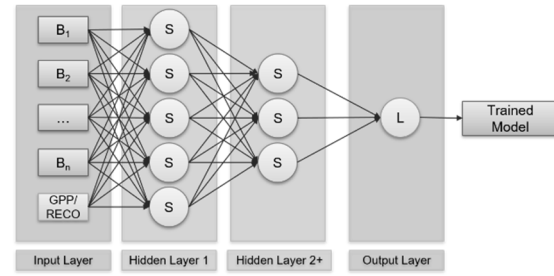


Figure 3: Artificial Neural Network architecture.

The algorithm execution process is described below. The input is the database structured as previously described, where each element provides as many inputs as the bands taken into consideration plus the GPP (or RECO) data measured in situ. In addition to the database inputs, the network architecture parameters are defined (number of hidden layers, number of nodes for the hidden layers following the first, activation function). Once the network architecture has been decided, the dataset is divided into two parts, 80% for training and 20% for validation. The model is generated using the training database and tested with the validation database, then the model performance is evaluated (using RMSE, Relative RMSE and r^2).

We have tested different architectures. The input layer has as many inputs as the number of bands used (we therefore tested different combinations of S2 bands and introduced S1 in combination with S2 as if they were 2 more bands) plus the value of the reference biophysical variable (for each GPP and RECO model respectively). The first hidden layer varied as a function of the inputs; in fact, it was structured with a number of nodes equal to the number of inputs. We therefore performed tests for different activation

functions using 2 identical hidden layers (both with 12 nodes), then once we identified the best performing function, we continued testing different combinations of S2 bands. Once the best performing combination was found, we tested by increasing the number of hidden layers and trying different combinations of the number of nodes (keeping only the first hidden layer constant). We then also inserted the Sentinel 1 data as input and tested again with different numbers of hidden layers and different combinations of the number of nodes.

We then tried several times to find the combination of input and architecture structure that would allow us to obtain the best results, in order to establish the starting point for experimentation with a more complex database.

3. RESULTS & DISCUSSION

Table 1 shows the results for the main tests performed by varying the combination of input data and the parameters that define the ANN architecture.

Table 1: Example of test performed to evaluate the best combination of inputs (type of data, number of bands, ANN architecture) to minimise the Relative RMSE and obtain the best r^2 . [AF: Activation Function, S1: number of Sentinel-1, S2: number of Sentinel-2 bands used in the training, HL: number of nodes for each hidden layers used (e.g. 13;13: 2 layers 13 nodes each)].

AF	S1	S2	HL	RRMSE GPP	r^2 GPP	RRMSE Reco	r^2 RECO
tanh	0	12	13;13	0.06	0.78	0.09	0.28
RELU	0	12	13;13	0.11	0.39	0.11	0.00
logistic	0	12	13;13	0.15	0.30	0.12	0.17
identity	0	12	13;13	0.06	0.75	0.08	0.37
tanh	0	4	5;5	0.12	0.15	0.10	0.10
tanh	0	12	13;5	0.08	0.55	0.09	0.35
tanh	0	12	13;7;5	0.08	0.55	0.09	0.35
tanh	0	12	13;13;13	0.05	0.87	0.07	0.54
tanh	2	12	15;15	0.10	0.54	0.12	0.45
tanh	2	12	15;15;15	0.11	0.54	0.12	0.49
tanh	2	12	15;13	0.09	0.60	0.11	0.35

Basically, the input parameters are S2 data plus the in-situ reference biophysical parameter. The variations on the data were on the choice of the S2 bands (tests with different combinations of bands) and the inclusion or not of the S1 data. As for the architecture, instead, we tested: different activation functions, different numbers of hidden layers and different combinations of nodes per layer.

As for the model for the GPP estimation, the tests performed by varying the Activation Function and keeping constant the other inputs showed that the one with the lowest RRMSE and the highest r^2 is the hyperbolic Tangent. Similar results were obtained using the Identity function.

Once the activation function was fixed, we tested the model with different architectures (continuing to use all the S2 bands) and it turned out that the best architecture is composed of 3 layers with 13 nodes per layer. The results remain more or less constant by increasing the number of layers.

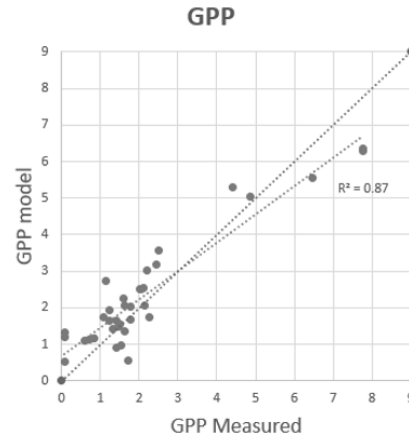


Figure 4: Comparison between GPP measured and GPP of the model trained using only S2 data (all Bands). The architecture was composed by 3 hidden layer, 13 nodes each layer. The activation function used was Hyperbolic Tangent.

It is important to highlight that the S2 data are not homogeneously distributed during the vegetation growth cycle. By superimposing an average growth cycle of one year (i.e. the variation of GPP) with the percentage distribution of S2 data from the database for each month (Figure 5), we note that in periods when cloud cover is high, the GPP is at its maximum while the availability of S2 data is low and vice versa when there are periods of drought (i.e. clear skies) the GPP is at its minimum and the availability of S2 data is maximum. This non-homogeneity in the database decreases the reliability of the results.

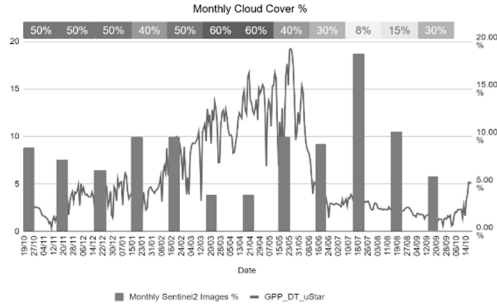


Figure 5: Relationship between GPP yearly cycle, monthly Sentinel-2 image distribution and monthly cloud cover of the AOI.

As mentioned earlier, the S1 data included in the database are only those acquired within ± 48 hours of the corresponding S2 acquisitions. Due to the technical characteristics of the two satellites, it is impossible to achieve a perfect time match between S1 and S2. However, to avoid significantly reducing the size of the already limited database, the time difference was extended to a maximum of 48 hours.

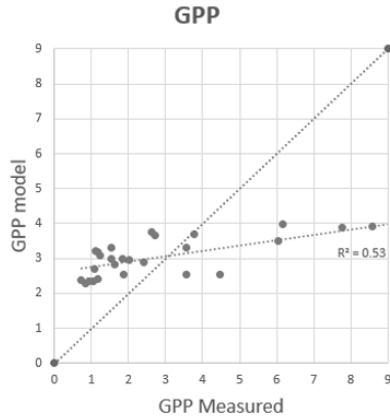


Figure 6: Comparison between GPP measured and GPP of the model trained using S1 and S2 data (all bands). The architecture was composed by 3 hidden layer, 13 nodes each layer. The activation function used was Hyperbolic Tangent.

This time discrepancy is likely the reason why the GPP simulation model, when trained with the inclusion of S1 data, shows a marked decline in performance (Figure 6), with an RRMSE of 0.11 and an r^2 of 0.53.

Similarly to GPP, a model was trained to estimate RECO. In this case, however, the results obtained for all tests are significantly less encouraging than the previous ones.

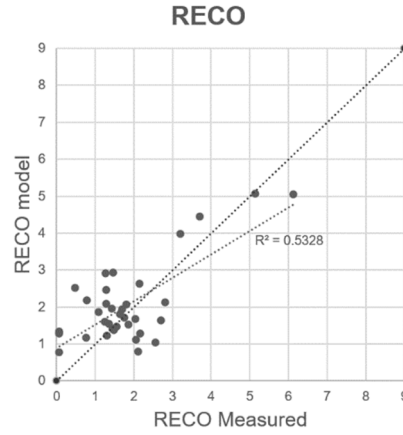


Figure 7: Comparison between RECO measured and RECO of the model trained using only S2 data (all Bands). The architecture was composed by 3 hidden layer, 13 nodes each layer. The activation function used was Hyperbolic Tangent.

As shown in Figure 7, the model that best estimates RECO (considering only S2 data) is the one composed of 3 hidden layers with 13 nodes each (and Hyperbolic Tangent as activation function). In this case, we obtain a RRMSE of 0.07 and an r^2 of 0.53.

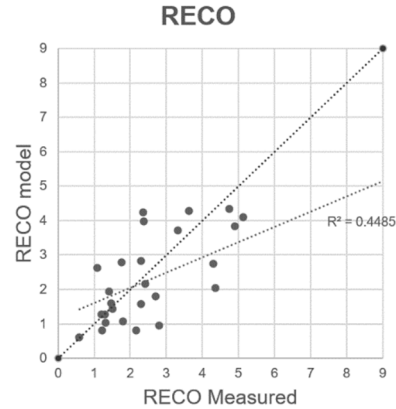


Figure 8: Comparison between RECO measured and RECO of the model trained using S1 and S2 data (all bands). The architecture was composed by 3 hidden layer, 13 nodes each layer. The activation function used was Hyperbolic Tangent.

Again, introducing the S1 data worsens the performance (Figure 8), with an RRMSE of 0.12 and an r^2 of 0.45.

These are preliminary tests, and the available data are not sufficient to form a statistically significant sample. Due to the limited data, it is not possible to carry out specific training for each AOI. A single

training across all test areas has shown results that encourage further testing of this methodology with a larger dataset.

Various tests indicate that acceptable results can only be achieved by using all available Sentinel-2 bands. Tests conducted with only the 10 m spatial resolution bands resulted in a high risk of saturation.

The best results for simulating GPP were obtained using an architecture with three hidden layers, each containing 13 nodes, and employing a hyperbolic tangent activation function with 12 Sentinel-2 bands. Good results were also achievable using both hyperbolic tangent and identity functions in architectures with two hidden layers, each with 13 nodes.

However, tests for the RECO model show that, in its current structure, it does not accurately predict the measured values. The model improves slightly with the introduction of Sentinel-1 data, but not enough to warrant further investigation using this model.

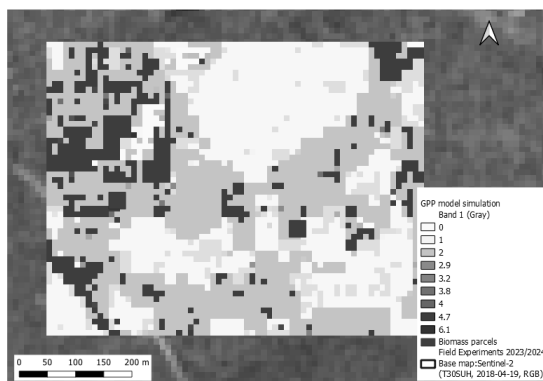


Figure 9: Map of GPP obtained over MOR Area using S2 data and the model that best performed (3 hidden layers, 13 nodes each).

The introduction of Sentinel-1 data into the model results in a decline in performance. This is likely due to the discrepancy in data acquisition between Sentinel-1 and Sentinel-2. While Sentinel-2 allows for consistent analysis of the same "tile" (i.e., images acquired almost always at the same time of day and from the same orbit), this is not possible with Sentinel-1. As a result, to obtain acquisitions close in time to those of Sentinel-2, different tiles must be used (with varying orbits and acquisition times). Additionally, the minimum time gap between Sentinel-1 and Sentinel-2 acquisitions often exceeds 24 hours, introducing further "noise" into the dataset.

For illustrative purposes only, the Figure 9 shows how a GPP map calculated from S2 data using the prototype model developed in this work should appear.

4. CONCLUSIONS

The results obtained from various ANN architectures and input combinations suggest that the developed methodology is suitable for further testing with larger datasets. While the results so far are encouraging, they are based on a database that has two significant limitations: 1) a small number of samples and 2) a non-homogeneous distribution of samples throughout the crop cycle. As a result, the current database serves mainly as a preliminary test of the model architecture and code functionality. A more comprehensive test will require waiting for the completion of the experiment and database expansion.

There is a clear need to increase the database. To address the missing data during the rainy season (March-May), we propose three strategies to integrate into the current model:

1. Train a parallel model using only Sentinel-1 data to assess the correlation between backscatter values in horizontal and vertical polarization and GPP. If a correlation is found (even if it is expected to be weaker than with Sentinel-2 data), this model could complement the Sentinel-2-based model during periods of missing data.
2. Train the model using lower-resolution multispectral data (e.g., MODIS or Sentinel-3) to take advantage of their higher revisit frequency, though at the expense of spatial resolution. This approach would not solve the problem of prolonged cloud cover.
3. Expand the database to include other areas of interest (AOIs) equipped with EC towers that provide GPP data, such as from the European Fluxes Database Cluster.

The next steps of the project will be:

1. Incorporate IFAPA 2022/2024 data.
2. Include all Sentinel-2 tiles over the AOIs in the database (currently limited to Tile T30SUH).
3. Add external EC data. Since the in-situ data comes from Eddy Covariance and environmental measurements, and there is a European network for monitoring CO2 flows, it may be possible to extend the database on a large scale.

The project also aims to develop a similar methodology for biomass data, which is collected in situ over areas larger than the footprint of a single EC tower but at a much lower frequency (every 3 to 4 weeks during the crop cycle, for a total of four annual measurements over two years). These data could be useful for comparing biomass models based on EO-GPP predictions with in situ biomass measurements.

REFERENCES

- [1] P. J. Gómez-Giráldez, C. Aguilar, A. B. Caño, A. García-Moreno, and M. P. González-Dugo, "Remote sensing estimation of net primary production as monitoring indicator of holm oak savanna management," *Ecol. Indic.*, vol. 106, Nov. 2019.
- [2] D. E. Pabon-Moreno, M. Migliavacca, M. Reichstein, and M. D. Mahecha, "On the Potential of Sentinel-2 for Estimating Gross Primary Production," *IEEE Trans. Geosci. Remote Sens.*, vol. 60, 2022.
- [3] M. J. Muñoz-Gómez, A. Andreu, M. D. Carbonero, Á. Blázquez-Carrasco, and M. P. González-Dugo, "Impact of water stress on Mediterranean oak savanna grasslands productivity: Implications for on-farm grazing management," *Agric. Water Manag.*, vol. 303, Oct. 2024.
- [4] S. Bao, L. Alonso, S. Wang, J. Gensheimer, R. De, and N. Carvalhais, "A Robust Light Use Efficiency Model Parameterization Method Based on Ecosystem Properties," 2022.
- [5] T. Wutzler, Lucas-Moffat A, Migliavacca M, Knauer J, Sickel K, Sigut, Menzer O & Reichstein M (2018) Basic and extensible post-processing of eddy covariance flux data with REdDyProc. Biogeosciences, Copernicus, 15, doi: 10.5194/bg-15-5015-2018
- [6] ESA, "SENTINEL-2 User Handbook," 2015.
- [7] M. Weiss and F. Baret, "S2ToolBox Level 2 products: LAI, FAPAR, FCOVER," *Sentin. ToolBox Level2 Prod.*, 2016.
- [8] C. Bacour, F. Baret, D. Béal, M. Weiss, and K. Pavageau, "Neural network estimation of LAI, fAPAR, fCover and LAI×Cab, from top of canopy MERIS reflectance data: Principles and validation," *Remote Sens. Environ.*, vol. 105, no. 4, pp. 313–325, Dec. 2006.

Evaluating S-SEBI and SEBS estimates of evapotranspiration at San Rossore (ITALY)

Jerzy Piotr Kabala^{1*}, José Antonio Sobrino², Virginia Crisafulli², Drazen Skokovic², Giovanna Battipaglia¹

¹Department of Environmental, Biological and Pharmaceutical Sciences and Technologies
University of Campania Luigi Vanvitelli, Via Vivaldi 43, Caserta 81100, Italy

²Global Change Unit. Image Processing Laboratory, University of Valencia. C/ Catedrático José Beltrán, 2. 46980 Paterna, Valencia, Spain.

*corresponding author: jertzypiotr.kabala@unicampania.it

ABSTRACT – Evapotranspiration is a key biogeochemical process, however its accurate estimation over land surfaces is still an open research question. Several methodologies exist, each with its points of strength and drawbacks. Among the remote sensing based technique, the Surface Energy Balance models allow for the estimation of evapotranspiration from observations of land surface temperature, spectral properties of the land surface and meteorological data, which are leveraged for partitioning the radiation incoming at the earth surface into different energy fluxes. Among this category of models S-SEBI algorithm is the simplest, and the less demanding in terms of inputs, thus being particularly useful in data scarce regions. On the other hand, SEBS has a more complex structure and was designed to deal with some heterogeneity in the study area. Both the algorithms might be a viable option for creating high resolution, local scale products of evapotranspiration. This study compares the performance of these two algorithms, against an eddy covariance tower, assuming the eddy covariance tower as the ground truth. The aim of the comparison is to evaluate which is more accurate in reproducing the evapotranspiration dynamics, thus producing a better-quality evapotranspiration product. The study site is located in a flat area of central Italy, in the Toscana region. The algorithms were applied on 57 cloudless Landsat 8 images, while incoming radiation and meteorological data were sourced from the ERA5-Land global reanalysis. These public domain data sources were tested, as they are globally available, and might be the preferred data source in many areas, where other sources are absent. The S-SEBI model estimates of evapotranspiration had an average RMSE of 1.05 mm against the Eddy Covariance tower and an R-squared of 0.6. Despite some differences in the observed values, the model estimates followed well the seasonal trends of the eddy covariance data. The SEBS model showed an accuracy (RMSE) of 0.91 mm at daily timescale with an R-squared of 0.65. The seasonal trends were adequately reproduced by the SEBS model. For both models the bias was low, showing acceptable performance in reproducing the evaporative water fluxes, in spite of the coarse resolution of the meteorological inputs and producing reasonable estimates of actual evapotranspiration. While the models displayed similar accuracy, the S-SEBI model might result more practical in many applications, as it is less demanding in terms of inputs. Where more accurate methodologies can't be applied, this approach might represent a good option for estimating the evaporative water fluxes from land and for spatializing their estimates.

Keywords - Evapotranspiration, surface energy balance, SEBS, S-SEBI, Google Earth Engine

1. INTRODUCTION

Evapotranspiration (hereafter ET), which is the sum of evaporation from unvegetated surfaces, and transpiration from vegetation, constitutes a link between the water and energy cycle. It is a key component of the water balance of land, and thus has multiple effects on climate, hydrology, ecosystem and human society (Jasechko et al., 2013). For these reasons, its accurate estimation is crucial, especially under the ongoing climate change. Up to now, several global evapotranspiration products are available (e.g. the MOD16 product (Mu et al., 2011), GLEAM

(Martens et al., 2017) LSA-SAF (Ghilain et al., 2011)); however, their coarse spatial resolution limits their representativity of local patterns, especially in landscapes with heterogeneous or fragmented land cover. Mapping evapotranspiration is crucial in arid or semiarid areas, in order to improve water management, and achieving a high spatial resolution is advisable over fragmented or heterogeneous landscapes (Cheng and Kustas, 2019).

In these conditions, one possibility is to estimate ET from high resolution (~100 m) imagery in the optical and thermal wavelength, by applying surface energy balance models. This class of models are based

on the assumption that the net radiation at the earth surface is equal to the sum of latent heat of evapotranspiration (LE), sensible heat (H) and heat flux to the soil (G_0). In time several algorithms, employing this principle have been proposed (e.g. SEBAL, SEBS, S-SEBI, TSEB), and they are usually applied to retrieve instantaneous values of LE, that are later upscaled to daily, in order to obtain more meaningful values for practical applications (Bastiaanssen et al., 1998; Norman et al., 1995; Roerink et al., 2000; Su, 2002). In literature, several different approaches were described: the usage of the ratio of daily to instantaneous radiation as scaling factor (Sobrino et al., 2021), or using the ratio of ET to reference ET, which can be assumed to be constant during a single day (Allen et al., 2007) and can be easily computed from meteorological data (Monteith, 1965). Each of these models requires, as inputs, incoming radiation and some meteorological data, beside the remotely sensed imagery. Some of these models are now operationally used as part of an ensemble of models, like for example in the OpenET project (Melton et al., 2022), and used for producing evapotranspiration datasets, that have been widely evaluated against ground measurements of ET. Nowadays, the improved computing capabilities provided by modern technology, allow for running evapotranspiration models on large datasets of remotely sensed imagery, which is helpful in assessing their performance across a wide range of conditions (Laipelt et al., 2021; Senay et al., 2022; Volk et al., 2024). This in turn helps improving the understanding of model points of strength and weakness and gives more information regarding their reliability. Surface energy balance models might constitute a valuable source of field scale evapotranspiration data, for further applications such as quantifying the water budget of specific areas (Mhawej and Faour, 2020), optimizing water management practices (Anderson et al., 2015), or performing ecological studies concerning ecosystem functioning (Roche et al., 2020; Sánchez et al., 2015). The aim of this study is to evaluate the performance of two established surface energy balance models (namely SEBS and S-SEBI) in estimating daily evapotranspiration at a mediterranean forest site, across Landsat images acquired during different years, and using the ERA5-land reanalysis (Muñoz-Sabater et al., 2021) as source of meteorological and radiation data. If the evaluation shows an acceptable error in the estimates, this setup might be employed in future applications, for producing high resolution, local scale evapotranspiration products, especially in data scarce regions,

2. MATERIAL AND METHODS

2.1. Study site

The San Rossore ICOS site (43.73 °N, 10.29 °E, 4 m a.s.l.) was chosen for evaluating the performance of the two models. At this ICOS station, the turbulent fluxes are measured by an eddy covariance tower, monitoring a stone pine forest. It is located in a flat area, at west of the town of Pisa, near the Tyrrhenian sea. The climate of the area is mediterranean, with hot and dry summers, and mild winters, during which most of the rainfall occurs.

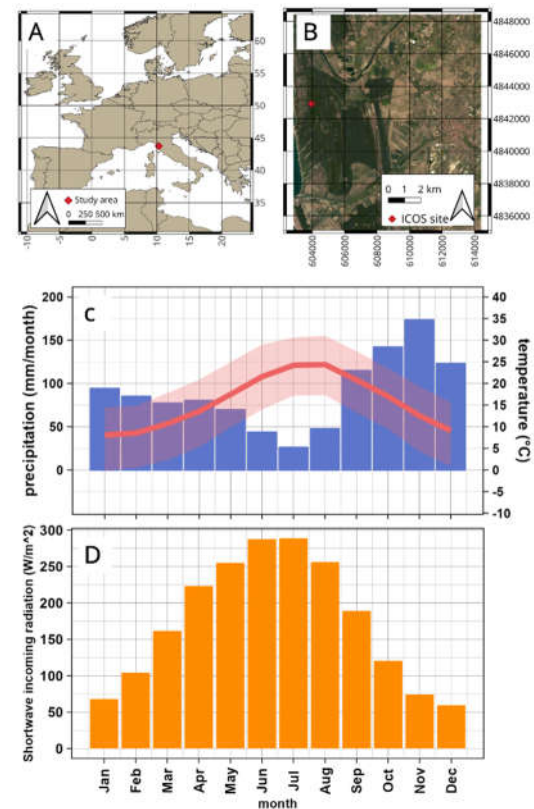


Figure 1. A) Study area location in the mediterranean, B) Landsat 8 RGB composite of the study area, showing the location of the eddy covariance tower, C) Monthly mean temperature (red) and precipitation (blue) of the area, according to the ERA5-land data (1994-2023), D) average incoming shortwave radiation (instantaneous, W/m^2) over the study area, during the study period (2013-2020) according to the ERA5-land reanalysis.

2.1. Data sets

The SEBS and S-SEBI models were run on 57 Landsat 8 images containing the study area. Only images with less than 20% cloud cover were selected from the Level 2 product, with acquisition date comprised between 01-01-2013 and 31-12-2020. The meteorological data were obtained from the ERA5-land reanalysis product. Data preprocessing and download steps were performed in Google Earth Engine.

Regarding the eddy covariance validation data, the archive level 2 dataset was used, containing data acquired between 2013 and 2020 (Arriga et al., 2022).

2.2. Methodology

The original implementation of the SEBS model was used (<https://github.com/jvdkwast/PySEBS>), the model structure is described in details in (Su, 2002). The S-SEBI model was implemented in Google Earth Engine, following the original description in (Roerink et al., 2000). The only modification applied was the adoption of the soil flux formulation following (Su, 2002), (eq. 1 and 2), which is the same of the SEBS model.

$$G = G_0 R_n \quad (1)$$

$$G_0 = 0.05 f_c + 0.315(1 - f_c) \quad (2)$$

Fraction cover was computed as:

$$f_c = \begin{cases} NDVI < 0.2, & 0 \\ 0.2 < NDVI < 0.8, & \left(\frac{NDVI - 0.2}{0.6} \right)^2 \\ NDVI > 0.8, & 1 \end{cases} \quad (3)$$

Where NDVI is the normalized difference vegetation index, computed from the band 4 and 5 surface reflectance, according to equation (4).

$$NDVI = \frac{\rho_{B5} - \rho_{B4}}{\rho_{B5} + \rho_{B4}} \quad (4)$$

Albedo was computed from surface reflectance following equation (5) (Ke et al., 2016).

$$\alpha = 0.13\rho_{B1} + 0.115\rho_{B2} + 0.143\rho_{B3} + 0.18\rho_{B4} + 0.281\rho_{B5} \quad (5)$$

An emissivity value of 0.982 was assumed for vegetation, and 0.971 for bare surfaces, the emissivity of each pixel was then computed weighting these two coefficients for the fraction of vegetation cover, as shown in equation (6).

$$\varepsilon = 0.971(1 - f_c) + 0.982f_c \quad (6)$$

Instantaneous net radiation at the surface was computed following equation (7), where $R_{sw\downarrow}$ is downwelling radiation in the shortwave wavelength,

and $R_{lw\downarrow}$ is downwelling radiation in the thermal wavelength (values sourced from ERA5-land), T_s is the temperature of the surface (LST), α is albedo (equation 5) and ε is emissivity (equation 6).

$$R_n = (1 - \alpha)R_{sw\downarrow} + \varepsilon R_{lw\downarrow} - \varepsilon \sigma T_s^4 \quad (7)$$

After these preprocessing steps, the two models are applied to the imagery (inputs and outputs of each model are summarized respectively in figure 2 and 3, a detailed description of the models can be found in the respective references). Finally, instantaneous LE estimates by the models, are scaled to daily ET (mm) by multiplying a scaling factor, that is the ratio between instantaneous and daily incoming shortwave radiation (equation 8), and dividing by the latent heat of vaporization of water (equation 9).

$$c_{di} = \frac{R_{sw,daily\downarrow}}{R_{sw,instantaneous\downarrow}} \quad (8)$$

$$ET_{daily} = c_{di} \frac{LE_{inst}}{2.46 \times 10^6} \quad (9)$$

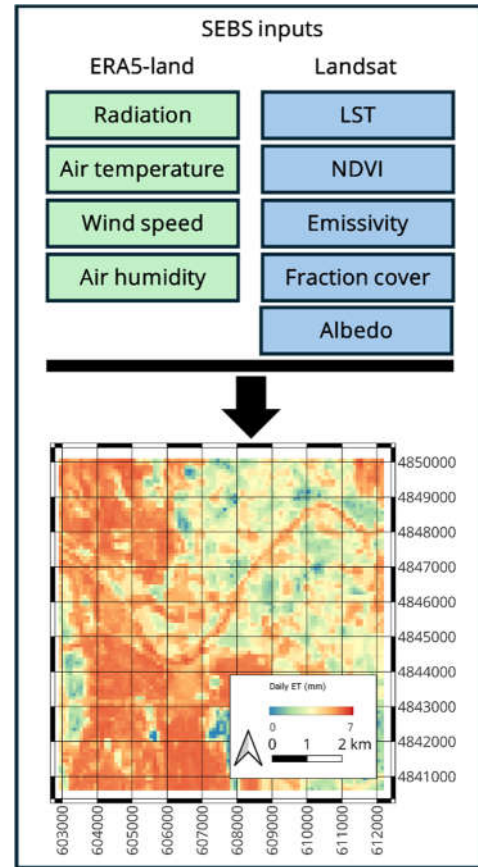


Figure 2. SEBS model inputs and outputs summary.

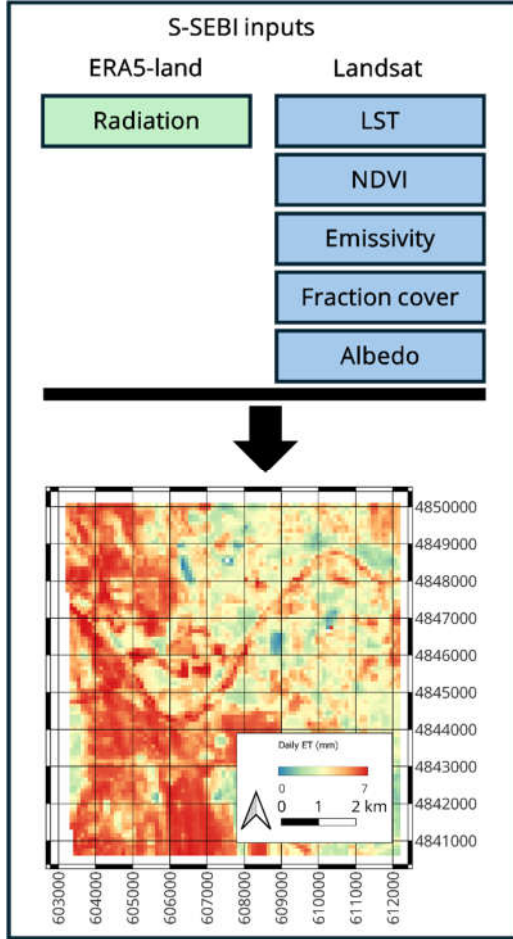


Figure 3. S-SEBI model inputs and outputs summary.

2.4. Evaluation metrics

Model performance was assessed with six common goodness of fit metrics, widely used in hydrological modelling: RMSE (root mean squared error), MAE (mean absolute error), R (Pearson's correlation coefficient), R^2 (coefficient of determination), KGE (Kling-Gupta efficiency) and percentage bias. The computation was performed with the *hydroGOF* R package (Zambrano-Bigiarini, 2020), their mathematical formulation is shown in equations 10-15.

$$RMSE = \sqrt{\frac{1}{N} \sum_{i=1}^N (X_i - O_i)^2} \quad (10)$$

$$MAE = \frac{1}{N} \sum_{i=1}^N |X_i - O_i| \quad (11)$$

$$R = \frac{\frac{1}{N-1} \sum_{i=1}^N (X_i - \mu_X)(O_i - \mu_O)}{\sqrt{\sigma_X^2 \sigma_O^2}} \quad (12)$$

$$R^2 = \frac{\left(\frac{1}{N-1} \sum_{i=1}^N (X_i - \mu_X)(O_i - \mu_O) \right)^2}{\sigma_X^2 \sigma_O^2} \quad (13)$$

$$KGE = 1 - \sqrt{(R - 1)^2 + \left(\frac{\sigma_X}{\sigma_O} - 1 \right)^2 + \left(\frac{\mu_X}{\mu_O} - 1 \right)^2} \quad (14)$$

$$\% \text{ bias} = \frac{100 * \sum_{i=1}^N (X_i - O_i)}{\sum_{i=1}^N O_i} \quad (15)$$

Where X refers to the modelled values, O to the observed values, N is the number of observations, μ is the mean, and σ is the standard deviation.

3. RESULTS & DISCUSSION

3.1. Modelled evapotranspiration

ET estimated by SEBS, amounted to 2.77 ± 1.54 mm/day, during the 57 dates of image acquisition analysed in this study, while the average of the values estimated by S-SEBI was XXX, and average ET measured at the eddy covariance tower was 2.73 ± 1.13 mm/day, showing a very good agreement among them. Estimated and measured ET showed overall a good agreement (Fig. 4); the accuracy metrics are reported in detail in table 1.

The SEBS model slightly outperformed S-SEBI, showing better values for all the accuracy metrics analysed.

Table 1. Comparison of the accuracy metrics for the two models.

Model	SEBS	S-SEBI
RMSE	0.91	1.05
MAE	0.75	0.86
R	0.8	0.78
R²	0.65	0.60
KGE	0.59	0.49
% bias	1.6	3.2

On average, the models slightly underestimated ET during the cold months, with low incoming radiation, and overestimated it during the summer months. The SEBS values were often closer to the eddy covariance measurements, than the S-SEBI ones. This highlights that care should be taken to avoid the potential conditional biases that might arise from the application of these techniques. The combination of different models, based on different approaches, producing ensemble products might be a suitable strategy for mitigating the problem in operational applications (Sun et al., 2019; Volk et al., 2024).

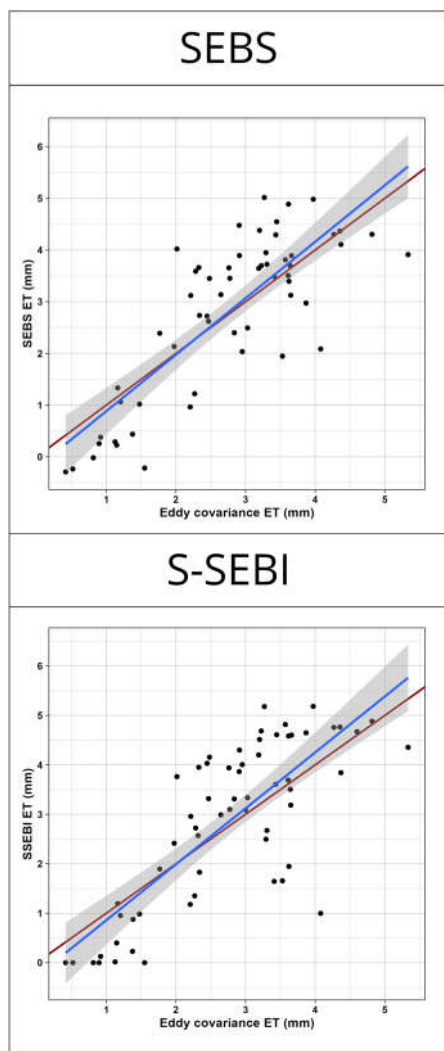


Figure 4. Scatterplot of modelled daily ET against eddy covariance measurements.

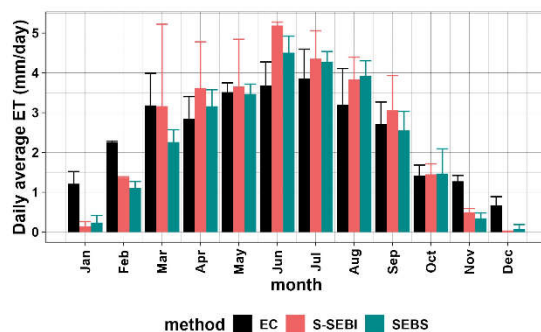


Figure 5. Comparison of the average modelled values and eddy covariance data by month (mean and standard deviation).

4. CONCLUSIONS

The results of this study show that the SEBS and S-SEBI models are suitable for producing local scale evapotranspiration products, by exploiting Landsat imagery and ERA5-land reanalysis. This approach can be exploited for retrieving ET in data scarce areas, where ground measurements of the meteorological conditions are unavailable (Allies et al., 2020). The quantification of ET is crucial for several scientific applications, and for improving the water management in arid or semi-arid environments. Future research might comprise a wider scale evaluation of these and other surface energy balance models, and a quantitative analysis of the drivers of their inaccuracies, in order to improve the models, to work better under a broad range of environmental conditions.

REFERENCES

- Allen, R.G., Tasumi, M., Trezza, R., 2007. Satellite-based energy balance for mapping evapotranspiration with internalized calibration (METRIC)—Model. *Journal of irrigation and drainage engineering* 133, 380–394.
- Allies, A., Demarty, J., Olioso, A., Bouzou Moussa, I., Issoufou, H.B.-A., Velluet, C., Bahir, M., Maïnassara, I., Oi, M., Chazarin, J.-P., Cappelaere, B., 2020. Evapotranspiration Estimation in the Sahel Using a New Ensemble-Contextual Method. *Remote Sensing* 12. <https://doi.org/10.3390/rs12030380>
- Anderson, R., Lo, M.-H., Swenson, S., Famiglietti, J., Tang, Q., Skaggs, T., Lin, Y.-H., Wu, R.-J., 2015. Using satellite-based estimates of evapotranspiration and groundwater changes to determine anthropogenic water fluxes in land surface models. *Geoscientific Model Development* 8, 3021–3031.
- Arriga, N., Goded, I., Manca, G., ICOS Ecosystem Thematic Centre, 2022. Warm winter 2020 ecosystem eddy covariance flux product from San Rossore 2. <https://doi.org/10.18160/EPYB-PSFM>
- Bastiaanssen, W.G., Menenti, M., Feddes, R., Holtslag, A., 1998. A remote sensing surface energy balance algorithm for land (SEBAL). 1. Formulation. *Journal of hydrology* 212, 198–212.
- Cheng, J., Kustas, W.P., 2019. Using Very High Resolution Thermal Infrared Imagery for More Accurate Determination of the Impact of Land Cover Differences on Evapotranspiration in an Irrigated Agricultural Area. *Remote Sensing* 11. <https://doi.org/10.3390/rs11060613>
- Ghilain, N., Arboleda, A., Gellens-Meulenberghs, F., 2011. Evapotranspiration modelling at large scale using near-real time MSG SEVIRI derived data. *Hydrology and Earth System Sciences* 15, 771–786.
- Jasechko, S., Sharp, Z.D., Gibson, J.J., Birks, S.J., Yi, Y., Fawcett, P.J., 2013. Terrestrial water fluxes dominated by transpiration. *Nature* 496, 347–350. <https://doi.org/10.1038/nature11983>
- Ke, Y., Im, J., Park, S., Gong, H., 2016. Downscaling of MODIS One Kilometer Evapotranspiration Using Landsat-8 Data and Machine Learning Approaches. *Remote Sensing* 8. <https://doi.org/10.3390/rs8030215>

- Laipelt, L., Kayser, R.H.B., Fleischmann, A.S., Ruhoff, A., Bastiaanssen, W., Erickson, T.A., Melton, F., 2021. Long-term monitoring of evapotranspiration using the SEBAL algorithm and Google Earth Engine cloud computing. *ISPRS Journal of Photogrammetry and Remote Sensing* 178, 81–96.
- Martens, B., Miralles, D.G., Lievens, H., Schalie, R.V.D., Jeu, R.A.M.D., Fernández-Prieto, D., Beck, H.E., Dorigo, W.A., Verhoest, N.E.C., 2017. GLEAM v3: Satellite-based land evaporation and root-zone soil moisture. *Geoscientific Model Development* 10, 1903–1925. <https://doi.org/10.5194/gmd-10-1903-2017>
- Melton, F.S., Huntington, J., Grimm, R., Herring, J., Hall, M., Rollison, D., Erickson, T., Allen, R., Anderson, M., Fisher, J.B., 2022. OpenET: Filling a critical data gap in water management for the western United States. *JAWRA Journal of the American Water Resources Association* 58, 971–994.
- Mhawej, M., Faour, G., 2020. Open-source Google Earth Engine 30-m evapotranspiration rates retrieval: The SEBALIGEE system. *Environmental Modelling & Software* 133, 104845. <https://doi.org/10.1016/j.envsoft.2020.104845>
- Monteith, J.L., 1965. Evaporation and environment, in: *Symposia of the Society for Experimental Biology*. Cambridge University Press (CUP) Cambridge, pp. 205–234.
- Mu, Q., Zhao, M., Running, S.W., 2011. Improvements to a MODIS global terrestrial evapotranspiration algorithm. *Remote sensing of environment* 115, 1781–1800.
- Muñoz-Sabater, J., Dutra, E., Agustí-Panareda, A., Albergel, C., Arduini, G., Balsamo, G., Boussetta, S., Choulga, M., Harrigan, S., Hersbach, H., 2021. ERA5-Land: A state-of-the-art global reanalysis dataset for land applications. *Earth system science data* 13, 4349–4383.
- Norman, J.M., Kustas, W.P., Humes, K.S., 1995. Source approach for estimating soil and vegetation energy fluxes in observations of directional radiometric surface temperature. *Agricultural and Forest Meteorology* 77, 263–293. [https://doi.org/10.1016/0168-1923\(95\)02265-Y](https://doi.org/10.1016/0168-1923(95)02265-Y)
- Roche, J.W., Ma, Q., Rungee, J., Bales, R.C., 2020. Evapotranspiration Mapping for Forest Management in California's Sierra Nevada. *Frontiers in Forests and Global Change* 3. <https://doi.org/10.3389/ffgc.2020.00069>
- Roerink, G., Su, Z., Menenti, M., 2000. S-SEBI: A simple remote sensing algorithm to estimate the surface energy balance. *Physics and Chemistry of the Earth, Part B: Hydrology, Oceans and Atmosphere* 25, 147–157.
- Sánchez, J.M., Bisquert, M., Rubio, E., Caselles, V., 2015. Impact of Land Cover Change Induced by a Fire Event on the Surface Energy Fluxes Derived from Remote Sensing. *Remote Sensing* 7, 14899–14915. <https://doi.org/10.3390/rs71114899>
- Senay, G.B., Friedrichs, M., Morton, C., Parrish, G.E.L., Schauer, M., Khand, K., Kagone, S., Boiko, O., Huntington, J., 2022. Mapping actual evapotranspiration using Landsat for the conterminous United States: Google Earth Engine implementation and assessment of the SSEBop model. *Remote Sensing of Environment* 275, 113011. <https://doi.org/10.1016/j.rse.2022.113011>
- Sobrino, J.A., Souza da Rocha, N., Skoković, D., Suélen Käfer, P., López-Urrea, R., Jiménez-Muñoz, J.C., Alves Rolim, S.B., 2021. Evapotranspiration estimation with the S-SEBI method from landsat 8 data against Lysimeter measurements at the Barrax Site, Spain. *Remote Sensing* 13, 3686.
- Su, Z., 2002. The Surface Energy Balance System (SEBS) for estimation of turbulent heat fluxes. *Hydrology and earth system sciences* 6, 85–100.
- Sun, H., Yang, Y., Wu, R., Gui, D., Xue, J., Liu, Y., Yan, D., 2019. Improving Estimation of Cropland Evapotranspiration by the Bayesian Model Averaging Method with Surface Energy Balance Models. *Atmosphere* 10. <https://doi.org/10.3390/atmos10040188>
- Volk, J.M., Huntington, J.L., Melton, F.S., Allen, R., Anderson, M., Fisher, J.B., Kilic, A., Ruhoff, A., Senay, G.B., Minor, B., Morton, C., Ott, T., Johnson, L., Comini de Andrade, B., Carrara, W., Doherty, C.T., Dunkerly, C., Friedrichs, M., Guzman, A., Hain, C., Halverson, G., Kang, Y., Knipper, K., Laipelt, L., Ortega-Salazar, S., Pearson, C., Parrish, G.E.L., Purdy, A., ReVelle, P., Wang, T., Yang, Y., 2024. Assessing the accuracy of OpenET satellite-based evapotranspiration data to support water resource and land management applications. *Nature Water* 2, 193–205. <https://doi.org/10.1038/s44221-023-00181-7>
- Zambrano-Bigiarini, M., 2020. hydroGOF: Goodness-of-Fit Functions for Comparison of Simulated and Observed Hydrological Time Series.

Detection and Automatic Extraction of the Valencian Coastline Using Sentinel-2

Josep Marí Cabrera, Ana B. Ruescas

*Departamento de Geografía, UV, Avda. Blasco Ibañez 28,
jomaca4@alumni.uv.es, ana.b.ruescas@uv.es*

RESUMEN – La erosión de la línea de costa es un fenómeno que ocasionalmente puede causar pérdidas materiales y/o ecosistémicas. Aunque el conocimiento de estos riesgos de erosión resulta de vital importancia para la correcta gestión de la costa, su predicción es complicada y requiere de un monitoreo temporal para conocer las causas de su degradación y afección. El objetivo de este trabajo es proponer una metodología sencilla que permita la extracción de la línea de costa mediante la utilización de imágenes satélite de diferentes años. Con dicha metodología hemos podido realizar la extracción automática de la línea de costa de todas las imágenes del Sentinel-2, para el tramo comprendido entre el puerto de Sagunt y el puerto de Gandia, en el periodo 2019-2023, y cuantificar sus pérdidas o ganancias tomando la línea media en este periodo como referencia.

Palabras clave: costa, erosión, automatización, Sentinel-2

ABSTRACT – *Shoreline erosion is a phenomenon that can occasionally cause material and/or ecosystem losses. Although the knowledge of these erosion risks is of vital importance for the correct management of the coast, its prediction is complicated and requires temporal monitoring to know the causes of its degradation and affection. The aim of this work is to propose a simple methodology that allows the extraction of the coastline using satellite images from different years. With this methodology we have been able to carry out the automatic extraction of the coastline from all Sentinel-2 images, for the stretch between the port of Sagunt and the port of Gandia, in the period 2019-2023, and quantify their gains or losses by taking the average line in this period as a reference.*

Keywords: coast, erosion, automation, Sentinel-2

1. INTRODUCTION

Coastal areas, especially on the Mediterranean and specifically on the Valencian coast, are particularly productive and vulnerable ecosystems that suffer from increasing pressure due to urban overcrowding and climatic hazards (Vosdoulas et al., 2020). The complexity of the coastline as a dynamic system is manifested through interactions between numerous natural and human processes at various temporal and spatial scales.

Shoreline dynamics, determined by the relationship between sedimentation and erosion, present significant challenges, with 25% of the European coastline undergoing processes of erosion. In addition to being unique ecosystems, beaches play crucial roles: they act as natural defenders against waves, provide recreational spaces and are essential for coastal communities (Carmona et al., 2014). Factors such as urban sprawl, construction of coastal infrastructure and climate change contribute to the evolution of the coastline. Rapid urbanization along the Valencian coastline since the 1960s has altered coastal dynamics, generating changes in sediment balances and affecting geomorphology. The construction of reservoirs and the lack of recognition of climate change also play key roles.

Exacerbated by climate change, coastal erosion not only threatens the existence of beaches, but also increases the risk of flooding, resulting in significant economic and social losses. Artificial beach regeneration and the construction of seawalls are common measures, although their effectiveness is limited and they only shift the problem elsewhere.

The study of coastal evolution through observation, aerial photography and remote sensing reveals the magnitude of changes. The use of satellite imagery offers a long-term perspective, allowing the trends and responses to specific events to be detected. This study proposes a simple methodology for the automatic observation of the coastline using high-resolution satellite imagery. This technique can identify processes such as erosion, sedimentation and flooding, which are fundamental to understanding coastal evolution and its impacts on biodiversity, habitats and human communities (Bodi et al. 2015).

Developing efficient monitoring techniques to manage the Valencian coast is crucial for reducing the risks associated with erosion and preserving coastal integrity. Addressing these challenges ensures the sustainability of these valuable ecosystems and the protection of the communities that depend on them.

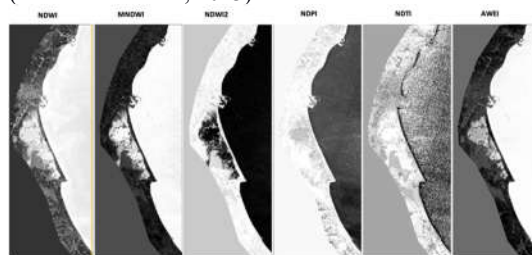
2.1. Area of study

A map of the eastern coast of Spain, showing the coastline from Marjal de Moros in the north to Puerto de Gandia in the south. The sea is labeled MAR MEDITERRANEO. Towns listed along the coast include Marjal de Moros, Puerto de Sagunto, Playa de Puzos, Playa del Parque, Playa de Melisano, Playa de Miraflores, Puerto de Valencia, Playa de Franco, Playa de El Suro, Playa de la Estrella, Playa del Recreo, Playa del Perpetual, Playa de San Ferrnandez, Playa del Ray, Playa del Suspen, Cabo de Cullera, Playa del Turis, Playa del San Antonio, Playa de Tancos, Playa del Gesso, Playa Puig de Santia, and Puerto de Gandia. A scale bar at the bottom left shows distances up to 60 km. A compass rose is located at the top right.

Since the 1960s, the Valencian coast has undergone major transformations that have come about due to the booming tourist sector that shifts its focus on 'sun and beach', and a strong development of the service sector and urban massification along the coastline. However, these spaces are currently threatened by the regression of the beaches, brought by the halting of sedimentary arising as a consequence of newly created reservoirs and the obstruction in the longitudinal transport of the coastal dynamics caused by large infrastructures and structural measures.

In this case study, the methodological solutions are focused on the automatic extraction of the coastline from Sentinel-2 satellite images acquired in the optical range of the electromagnetic spectrum, and with an average spatial resolution of 10 meters pixel size. Sentinel-2 satellite imagery with a level 2 atmospheric correction (L2A) and a cloud cover of less than 10% has been used for the period 2019-2023.

There are different types of indicators to recognize the coastline, so it is important to bear in mind that the definition of the coastline is not an absolute concept and can vary in different contexts and spatial and temporal scales. In this case study, we considered the line that differentiates between water and land pixels. For this separation we applied several indices to the Sentinel-2 scenes. The comparison of the different results is shown in Figure 2. The indices that present a closer representation to what is observed *in situ* are the modified normalized difference water index, MNDWI (Xu, 2006) and the normalized difference water index itself, NDWI (McFeeters, 1996). These two indices that manage to represent greater detail and differentiation between the land/water line, while other indices delimit a poorly defined coastline and add lot of noise to the images (see Marí-Cabrera, 2023).



The aforementioned indices and others (NDWI, MNDWI, NDPI, NDTI, AWEI) were applied by means of a command line script using a graph (GPT) to automate the process using SNAP v.9 software. A vector mask was applied using a polygon to delimit our area of interest and then resampled to 10 meters, using MSI band 2 as a reference. The output format is a GeoTIFF file.

Subsequently, a classification of the images was carried out. The binary image was classified into two classes: water body and land area. In classifying this image, the Otsu's threshold approach (Otsu, 1979) has

been employed. This method is used to obtain the best possible estimate of the threshold value for distinguishing the separation between sea water and land. This filter was also applied automatically on the images using a Python script. The classified water body was associated with the following water body types: ocean water, river/canal water, inland water and wetlands. The geometric structure of these water bodies varied from a single isolated pixel to a cluster of water body pixels. Isolated pixels of a single water body act as noise in the classified image, so they must be removed to obtain a clearer and more detailed result.

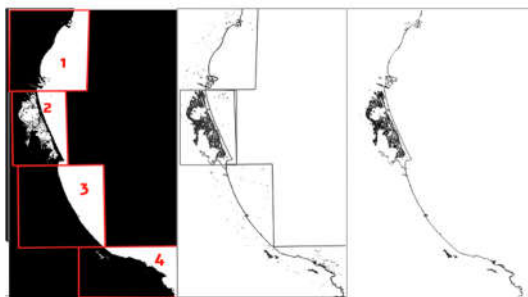


Figura 3. Application of the OTSU filter from the MNDWI index and creation of 4 boxes for extraction/trimming. Trimming of the coastline into four different parts to speed up the vectorization process. Vectorization/polygonization of the coastline (Polyline); and noise removal during the vectorization phase

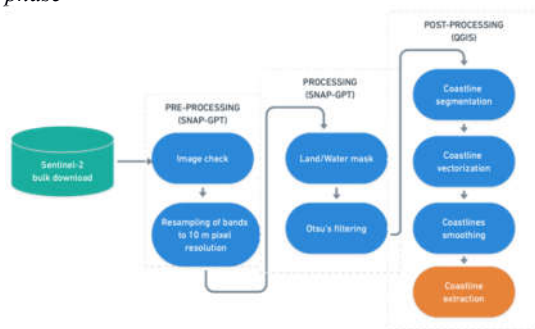


Figure 4. Methodology chart

For the extraction and validation of the coastline from the Otsu filter images, we used Quantum Geographic Information System (QGIS) version 3.30.2. From the image with the Otsu filter, a new majority filter has been applied to generalize and reduce the misclassifications of the single or small groups of isolated pixels. This filter is often used to eliminate noise or isolated pixels by attributing them the value of the most repeated pixel in their proximity. Also, four vector rectangles have been estimated, which have been used as a mask for the extraction of

the data of interest, and to speed up the conversion from raster format to vector layer (Figure 3). Therefore, once the filtering has been applied, the conversion from raster to vector has been made, using the 'Polygonise' function, the result of which is the delimitation of the coastline. Figure 4 shows a schematic of the entire methodology used.

3. ANALYSIS OF THE RESULTS

The results obtained fit very well the shapes of the coast, although some differences can be observed to the south of Cape of Cullera, just at the Punta Negra breakwater located between *Playa del Racó* and *Playa del Cap Blanc* (Figure 5). Basically, these small errors may be due to very narrow structures such as dikes, which refer to a small group of pixels classified as land, and which are surrounded by pixels classified as water, so that some of these land-pixels have been erroneously reclassified as water-pixels due to their proximity during the application of the smoothing process.

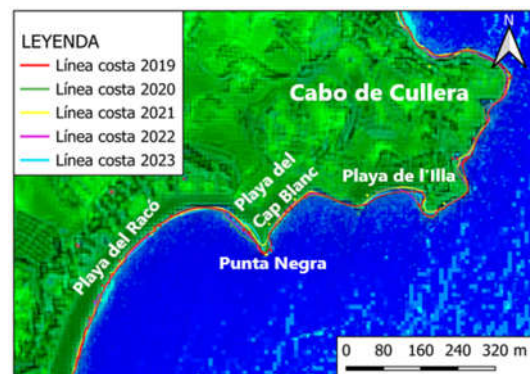


Figura 5. Comparison between the coastlines of the different years (2019-2020-2021-2022-2023). Base image from 2019.

For the extraction of quantitative results, a reference axis has been drawn, as close as possible to the external line of the beach (where the beach ends) and as parallel as possible to the coastline in based images of 2019. Five transects perpendicular to the reference axis and touching the coastlines have been delineated every 200 meters of the beach. The 'Intersection of lines' function has been used to create both a point where the transect crosses the coastline for each year, and another point where the transect crosses the reference axis. Finally, the 'Nearest distance' function in QGIS has been used to generate a layer that calculates the distance between the intersection point of the reference axis with the intersection points of the shorelines of each year for each transect (Figure 6).



Figure 6. Extraction of the beach width through the intersection between the stretches and the coastlines of the different years (2019-2020-2021-2022-2023). Base image for 2019.

In this way, by simply calculating the difference between each distance line drawn, we can know how many meters the shoreline has advanced or receded for each year (see Table 1).

Table 1. Average loss/gain of coastline (m) according to transects or periods of years in Cullera

Differential Distance (m)	Transect 1	Transect 2	Transect 3	Transect 4	Transect 5	Average loss/gain according to periods
Period 1: 2019-2020	33,65 m	6,77 m	-9,17 m	-1,67 m	-11,58 m	3,60 m
Period 2: 2020-2021	-50,38 m	-6,24 m	14,02 m	2,98 m	8,45 m	-6,23 m
Period 3: 2021-2022	30,55 m	0,25 m	-4,50 m	4,12 m	6,06 m	7,30 m
Period 4: 2022-2023	-39,88 m	5,35 m	4,49 m	10,46 m	-8,44 m	-5,60 m
Average loss/gain according to transects	-6,52 m	1,53 m	1,21 m	3,97 m	-1,38 m	

4. DISCUSSION

The methodology proposed in this work is based on a mixture of what is proposed in other research papers focused on automatic shoreline extraction (Ghorai, D. and Mahapatra, M., 2020). In this sense, the results obtained in this work are comparable to other more complex methodologies.

It is worth mentioning that there are some limitations to the methodology employed. If one wants to analyze the observed coastline changes at a local scale in detail, there are other methodologies that provide much more accurate results using high resolution, geo-referenced aerial photographs. Our approach for coastline estimation would benefit of higher spatial resolution images, for instance compared to orthophotos, some areas could be misinterpreted like pixels containing waves, small buildings, pools, boats, etc. This can be partially corrected or reduced using other indices and filters such as W11 and W12, CET or CWI, which might improve the results obtained.

Of course, other types of images can also be processed, such as the Landsat series, which could complement and validate the information provided by Sentinel-2.

It should also be mentioned that this methodology has provided a good definition of the structure and extent of the Albufera and could therefore be applied in future research to changes in the surface area and volume of water in the lagoon in different seasonal or temporal periods, accompanied by information extracted by a LiDAR system for the extraction of georeferenced points with height, or by means of *in situ* soundings.

Finally, it should be noted that there has been no validation with *in situ* measurements for the years evaluated in this study. This is one of the aspects that we would like to work on in the future, taking current measurements to be able to compare backwards in time. It would also be interesting to compare the methodology proposed in this work with the more complex and accurate model proposed in the research of Pardo-Pascual et al. 2022.

5. REFERENCES

- Bodí, C., Rodilla, M. y Martí, A. (2015): *Cambios en los sistemas dunares de la costa del municipio de Cullera*. Universidad Politécnica de Valencia
- Carmona, P. y Ruiz, J.M. (2014): Procesos geomorfológicos en llanos de inundación y lagos costeros mediterráneos. El cambio ambiental histórico en la Albufera de Valencia (España). ISSN:0214-1744, *Cuaternalario y Geomorfología*.
- Ghorai, D. y Mahapatra, M. (2020): Extracting Shoreline from Satellite Imagery for GIS Analysis. *Remote Sensing in Earth Systems Sciences*, 3.
- Marí, J. 2023. Metodología automática para la detección y extracción de la línea de costa a partir de imágenes Sentinel-2. Caso aplicado desde el puerto de Sagunto al puerto de Gandia. Trabajo Fin de Máster, Universitat de València, España.
- Otsu, N. (1979): A thresholding for detection method from gray-level histograms, *IEEE Transactions on Systems, Man and Cybernetics*, vol. 9
- Pardo-Pascual, J.E., Cabezas-Rabadán, C., y Palomar-Vázquez, J.M. (2022): Estudio de los cambios de posición de la línea de costa en las playas del segmento València-Cullera (1984-2020) a partir de imágenes de satélite de resolución media de libre acceso. *Cuadernos de Geografía*, 108-109.
- Pardo-Pascual, J.E. y Sanjaume, E. (2019): J.A. Morales (ed.) *Beaches in Valencian coast. The Spanish coastal systems*
- Vousdoukas, M. I., Ranasinghe, R., Mentaschi, L., Plomaritis, T. A., Athanasiou, P., Luijendijk, A., y Feyen, L. (2020): Sandy coastlines under threat of erosion. *Nature Climate Change*, 10(3).

A New Remote Sensing Methodology for Estimating Frost Intensity and Damage on Citrus Crops: A Case Study of the Valencian Community

S. Gimeno, V. Crisafulli, Á. Sobrino-Gómez, J. A. Sobrino

Global Change Unit. Image Processing Laboratory, University of Valencia. C/ Catedrático José Beltrán, 2. 46980 Paterna, Valencia, Spain.

sergio.gimeno-crespo@uv.es; virginia.crisafulli@uv.es; alvaro.sobrino@uv.es;
jose.sobrino@uv.es

ABSTRACT – Citrus cultivations represent one of the major economic pillars of the Valencian Community (Spain). Frost events pose a significant threat to these plantations, resulting in substantial economic losses. This study aims to assess the frequency and intensity of frost occurrences in the region, from 2004 to 2023, utilizing Second Generation Meteosat satellite imagery. These images provide daily Land Surface Temperature (LST) data at 15-minute intervals. Days with frost were identified as those where temperatures fell below -2.3°C , a threshold beyond which citrus plants are susceptible to damage. Various temperature thresholds were selected to correspond with different levels of potential damage to the crops. The study also considered the duration of these frost events, to develop an intensity classification that estimates the impact on citrus crops. Annual comparisons were made to track trends in frost occurrence and eventual thermal anomalies. Validation was performed using in situ data from the Spanish national meteorological agency (AEMET). Results reveal a decline in the severity of frosts and in their frequency. In particular, we observe a substantial decline in frosts classified according to our method as “moderate damage” and an almost disappearance of those of “intense” or “permanent damage”. These observations agree with the predictions of an increase in aridity in the region, and open up new scenarios linked to the expansion of citric cultivation at altitude, in areas where production is usually better in quality, even if potentially threatened by low temperatures. Comparing our results with the farmers' observations, we can also state that the presented methodology is efficient in assessing the degree of damage generated by the frost, and could be used to insure fields during the winter season.

Keywords - Citrus crops, Remote Sensing, frost damage, Valencian Community

1. INTRODUCTION

Recent studies (Balfagon et al., 2021; Wang et al., 2022; Karamidehkordi et al., 2023) have shown that climate variations, including changes in temperature and precipitation, directly affect the quality and yield of citrus fruits. Generally, citrus trees adapt well to various climates, but their growth is constrained by low temperatures and frosts, which can be a limiting factor for agricultural production in arid and semi-arid climates, such as those in certain Mediterranean regions (Maracchi et al., 2005; Alhader, 2021). Although climate warming is reducing the frequency of frost events, vegetation is increasingly exposed to frost due to the extension of the growing season (Deng et al., 2020; Liu et al., 2018).

Frost is commonly defined as the lowering of air to below the freezing point, which is 0°C (Snyder & Melo-Abreu, 2005; Deng et al., 2020). However, in the context of citrus agriculture, frosts are considered impactful when the Land Surface Temperature (LST) detected by satellite drops to -2.3°C or below (Caselles & Sobrino, 1989). It has been clearly proved that at these temperatures, the tissues of the orange fruits can be permanently damaged, resulting in lower yields in

future seasons and a decrease in fruit quality (Zabihi et al., 2016; Reyes et al., 2019; Alhader, 2021).

In the last years, the use of Remote Sensing (RS) technologies for frost monitoring has advanced significantly, becoming an indispensable tool for accurate and timely assessment of agricultural conditions during and after frost events (Wang et al., 2020; Li et al., 2021). The second-generation METEOSAT (MSG) satellites, operated by EUMETSAT, are particularly effective for this purpose because of their high temporal resolution (15 minutes), which enables continuous monitoring of Earth conditions. In this context, having precise and up-to-date knowledge of the territory and the frost risk affecting the area is essential to help farmers improve their adaptive capacities and resilience, reducing their vulnerability to adverse climatic events (Murray & Ebi, 2012; Zabihi et al., 2016; Generalitat Valenciana, 2018). We focused on citrus crops, given their significant economic and nutritional value (Codoñer-Franch & Valls-Bellés, 2010; Zhong & Nicolosi, 2020), as well as their widespread global consumption. We decided to monitor the frequency and intensity of frosts over the past 20 years in the Valencian

Community, a region where the citrus agricultural sector is highly developed, representing more than half of Spain's total citrus cultivated area (Balfagon et al., 2021), and positioning Spain as the world's sixth-largest producer of fresh citrus (FAO, 2021). To achieve this goal, we propose a practical remote sensing method to quantify the extent of frost damage, using the minimum temperature reached and the duration of the frost as key indicators.

2. MATERIAL AND METHODS

2.1. Study area

The Valencian Community is a coastal region in the eastern part of the Iberian Peninsula, situated between 39° north latitude and 0° west longitude, overlooking the Mediterranean Sea. Its topography, characterized by the absence of significant mountain ranges, combined with its Mediterranean climate, featuring hot, humid summers and relatively mild winters, creates an ideal environment for various types of cultivation, particularly citrus fruits, with oranges being the most prominent.

2.1.1. Data sets

To study the occurrence of frosts in the Valencian Community, we utilized MSG images collected from 2004 until 2023. This satellite constellation captures images of the study area every 15 minutes; however, we opted to consider only one image per hour to streamline the dataset while maintaining high representability.

In total, 85208 images were processed, comprising 24 images for each day (the first image obtained per hour) for the months of January, February, March, April, November, and December (the months when frost occurrences are most likely) across the entire study period. From these images, we selected the MSG LST band of the MLST product, which provides information on LST at a spatial resolution of 3 km.

2.2. Methodology

First, the LST data obtained from the satellite were compared with those recorded by the AEMET 'Villafranca' meteorological station, located in the Castellón region, to verify the representativeness of the satellite data, for the year 2023.

Due to the scarcity of easily applicable methodologies that are understandable to farmers and do not require a large amount of diverse input data (Da Silveira et al., 2023), we have decided to develop a new, simplified methodology based on satellite-measured LST to detect possible frost damages. To account for the varying impacts on flowers, fruits, tree trunks, and stems, we established three critical temperature thresholds based on existing literature

(Whiteman, 1957; Conesa et al., 2015; Micheloud et al., 2017). Since the duration of frost also plays a crucial role in determining the extent of damage to a plantation (Snyder & Melo-Abreu, 2005), we established four consecutive duration thresholds to assess the potential impact on the plants. We developed a classification system for frost intensity levels by combining arbitrarily these parameters. Four categories of damage were established: light damage, moderate damage, severe damage, and permanent damage. These categories are represented in Table 1 using a range of colors. However, it is important to note that this classification is indicative and does not account for factors that are crucial but difficult to monitor via satellite.

Table 1. Damage levels used for image classification. The rows indicate the different temperature thresholds, while the columns represent the time thresholds. The different levels of damage are indicated by colors (Light blue = Light damage; Green = Moderate damage; Orange = Intense damage; Red = Permanent damage).

	$3 \leq h < 6$	$6 \leq h < 12$	$12 \leq h < 24$	$h \geq 24$
-2,3°C				
-4,0°C				
-9,0°C				

Using the established methodology, each month of the years under consideration was classified accordingly. To more accurately account for the frequency and intensity of frosts in the Valencian Community over time, we developed damage intensity maps. Each frost category was assigned a specific 'weight' value to reflect the severity of damage: 1 for light, 2 for moderate, 3 for severe, and 4 for permanent damage. These values correspond to the increasing intensity of frost impact on plants. The value for each frost category was then multiplied by the number of frost events at each level within the selected time interval. The total intensity for each pixel was calculated by summing the values across all frost categories, resulting in an overall intensity (OI) measure (Eq. 1).

$$OI = \sum_i^n \text{number of frost events} \times \text{weight} \quad (1)$$

Before applying the methodology to the entire community, a temperature anomalies analysis was conducted across the Valencian Community. The LST data were then analyzed using the Mann-Kendall Test to identify any significant differences between the averages of the periods from 2004 to 2013 and from 2014 to 2023.

Subsequently, following Eq. 1, damage intensity maps were generated for each month and year. The

Mann-Kendall Test was then applied to analyze the individual trend for each month over the entire period from 2003 to 2024. Damage intensity maps were also generated for each year. In this case, considering the seasonality of the data, it was deemed appropriate to use the Seasonal Kendall Test to analyze trends.

To verify whether the citrus crops in the region are indeed affected by frost, we compared our results with the distribution map of citrus agricultural areas provided by the "Centro de Descargas" of the Spanish National Geographical Information Centre, updated to 2022. We also examined the relationship between frost damage and elevation by comparing the frost map with the Digital Elevation Model of the Valencian Community, also provided by the "Centro de Descargas". Finally, we validated the proposed methodology for classifying frosts by reviewing relevant articles and publications that confirmed the presence of damage to orange crops in the areas and periods identified by our study.

3. RESULTS & DISCUSSION

3.1. LST evaluation

The LST data obtained from the MSG satellite were validated by comparing them with the air temperature values recorded by the AEMET 'Villafranca' station for the year 2023, resulting in an R^2 of 0.91 and an RMSE of 1.5. (Fig. 1) for nighttime data (from 00:00 to 06:00). This result confirms the accuracy and reliability of satellite data.

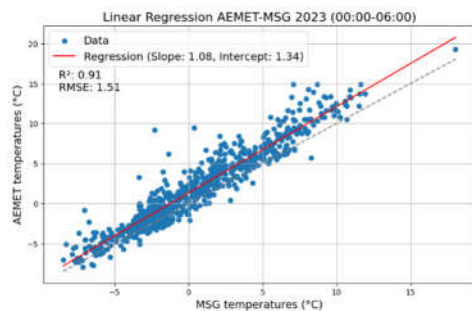


Figure 1. Linear correlation graphs between LST data and air temperature data from the Villafranca weather station for the nighttime hours.

3.2. LST analysis on the Valencian Community

Initially, an analysis of the LST was conducted for the study period, and anomalies were calculated for each year. A comparison of average minimum, mean, and maximum LST between the decades 2004-2013 and 2014-2023 (Fig. 2) revealed that temperatures were consistently higher in the latter decade across all cases. This finding is particularly significant in our study, as rising temperatures can ultimately lead to a decrease in frost events and less frost damage to vegetation.

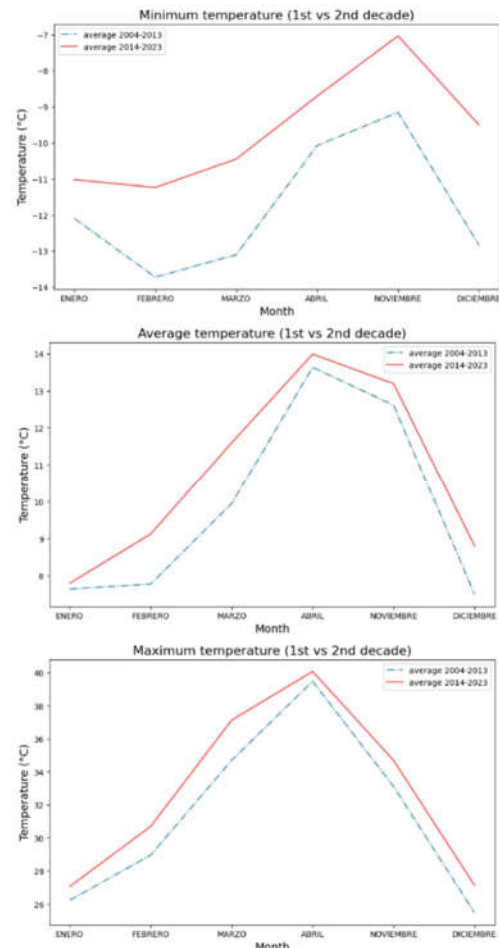


Figure 2. Comparison of the average minimum, mean, and maximum LST measured in the first decade (2004-2013) with those measured in the second decade (2014-2023) of the study period.

3.3. Methodology application

Subsequently, damage intensity maps were generated for each year and each month using the methodology previously described. To identify potential trends, the Mann-Kendall test was conducted on each monthly image. The months that exhibit a clear and consistent downward trend are March and December. In contrast, January, February, and November show a decreasing trend only in certain limited areas. No trend was observed in April, which aligns with previous data indicating the absence of significant damage during that month throughout the study period. The decrease in vegetation damage over the last decade, particularly during March and December and along the intern part of the region, is probably due to rising temperatures linked to climate change.

The Kendall Seasonal Trend Test was applied to the entire dataset of damage intensity to observe the overall trend over time. The results (Fig. 3) illustrate the areas of the Valencian Community where the annual damage intensity has changed, taking into account the seasonality of the data. It was observed that across much of the region, there has been a decreasing trend in the intensity of damage caused by low temperatures, with the exception of the coastal zone, where no such damage was recorded. The reduction in vegetation damage over the past decade, especially during March and December and in the interior areas of the region, is likely attributed to rising temperatures associated with climate change.

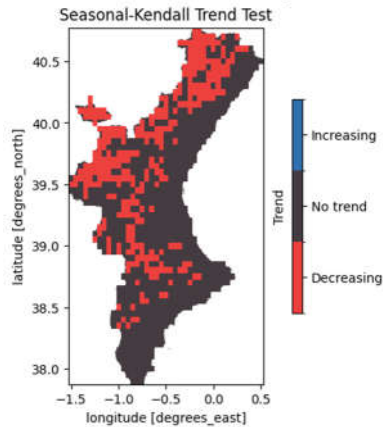


Figure 3. Result map of the Seasonal Kendall Trend Test conducted on the overall frost damage intensity data for the study period (2004-2023).

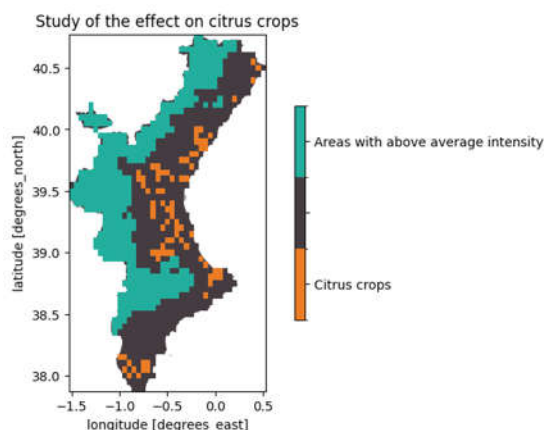


Figure 4. Overlay map of areas where above average intensity frosts occurs and areas cultivated with citrus in the Valencian Community.

Once the areas most affected by frosts were identified and their trends over recent years were analyzed, we aimed to determine whether these frosts indeed impact the regions where citrus fruits are

cultivated and thus pose a risk to growers. To this end, we compared the frost damage intensity map with the citrus cultivation area map provided by the Spanish National Geographical Information Centre. Our observations indicate that, although some areas overlap, most citrus-growing regions are not affected by severe frost (Fig. 4).

This reflects how farmers strongly consider frost risk when deciding which crops to plant, as this phenomenon can cause significant damage to yields, leading to substantial economic losses.

Finally, to better understand the relationship between frost occurrence and its spatial distribution, a comparison was made between the overall damage intensity map (Fig. 18) and altitude (Fig. 3). The linear regression line obtained reveals a significant correlation ($p < 0.05$), with an R-value of 0.64 (Fig. 5), showing that more severe frosts generally occur at higher elevations.

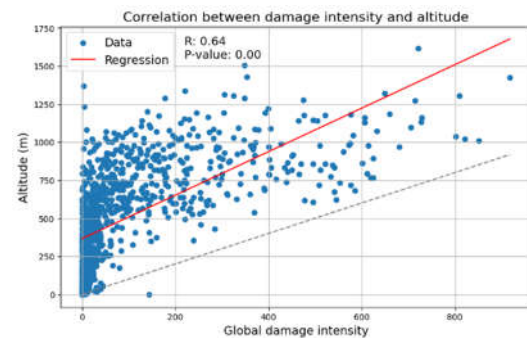


Figure 5. Linear correlation graph between the overall frost damage intensity registered over the study period (2004-2023) and altitude.

4. CONCLUSIONS

Climate change poses a significant challenge that we will need to address in the coming years, particularly for highly vulnerable activities such as agriculture. To ensure effective resource management in response to these challenges, it is essential to have precise local-level information to guide decision-making (Deng et al., 2020).

In this context, our work provides several key conclusions:

- Satellite-derived LST data, in this case from MSG, prove to be a useful and reliable tool for monitoring frost events.
- In the Valencia Community, there has been a decrease in frost occurrences over the past decade, particularly with regard to intense frost events.
- Citrus cultivation areas seem to be increasingly less exposed to frost risk in the study area, even at higher elevations above sea level.

The demonstrated decrease in the intensity and frequency of frost events can be beneficial for the region's citrus growers, as it reduces the likelihood of plant damage and subsequent economic losses. Considering this downward trend and recognizing that citrus crops are also threatened by excessively high temperatures, we recommend using the maps produced in this study to assess potential new sites for citrus cultivation that were previously too risky due to frost exposure. Growing citrus fruits at higher elevations could help mitigate risks from heat waves, severe aridity, flooding, and excessive salinity, which are becoming more prevalent in this region due to global warming.

Nonetheless, it is always advisable to consider various perspectives during the decision-making process, such as those of local farmers who are among the best experts on regional challenges (Loboguerrero et al., 2018). Moreover, factors beyond altitude, such as slope, wind, and relative humidity, should also be taken into account.

The methodology proposed in this work could also be applied to assess damage levels for insurance purposes. This is an effective strategy for protecting agricultural economies from adverse climatic events like frosts (Venner & Blank, 1995). Additionally, it could be valuable for future studies in other regions, such as in the development of risk maps, or for different economically significant crops prone to frost damage, such as wine grapes.

REFERENCES

- Alhader, M. M., & Hafez, M. S. (2021). The effect of some climatic variables and frosts waves on citrus crops. *Al-Adab Journal*, 138, 51–66. <https://doi.org/10.31973/aj.v1i138.1310>
- Balfagón, D., Arbona, V., & Gómez-Cadenas, A. (2021). El futuro de los cítricos: Impacto del cambio climático en la citricultura. *Mètode Revista De Difusió De La Investigació*, 12. <https://doi.org/10.7203/metode.12.20319>
- Caselles, V., & Sobrino, J. (1989). Determination of frosts in orange groves from NOAA-9 AVHRR data. *Remote Sensing of Environment*, 29(2), 135–146. [https://doi.org/10.1016/0034-4257\(89\)90022-9](https://doi.org/10.1016/0034-4257(89)90022-9)
- Codoñer-Franch, P., & Valls-Bellés, V. (2010). Citrus as functional foods. *Current Topics in Nutraceutical Research*, 8(4), 173–184. <https://www.cabdirect.org/abstracts/20113371292.html>
- Conesa, N. A., Nicolás, N. J. M., Manera, N. F. J., & Porras, N. I. (2015). Frost damage in lemon orchards in the province of Murcia. *Acta Horticulturae*, 1065, 1417–1422. <https://doi.org/10.17660/actahortic.2015.1065.179>
- Da Silveira, F., Da Silva, S. L. C., Machado, F. M., Barbedo, J. G. A., & Amaral, F. G. (2023). Farmers' perception of the barriers that hinder the implementation of agriculture 4.0. *Agricultural Systems*, 208, 103656. <https://doi.org/10.1016/j.agsy.2023.103656>
- Deng, G., Zhang, H., Yang, L., Zhao, J., Guo, X., Ying, H., Riha, W., & Guo, D. (2020). Estimating Frost during Growing Season and Its Impact on the Velocity of Vegetation Greenup and Withering in Northeast China. *Remote Sensing*, 12(9), 1355. <https://doi.org/10.3390/rs12091355>
- FAO. (2021). CITRUS FRUIT FRESH AND PROCESSED: Statistical Bulletin 2020. Citrus Fruit Statistical Compendium 2020. Rome. <https://openknowledge.fao.org/server/api/core/bitsstreams/4760a5b5-f3b2-41c7-8713-ccdb1a5f8c08/content>
- Generalitat Valenciana. (2018). Valencian Climate Change and Energy Strategy 2030. Retrieved September 9, 2024, from <https://mediambient.gva.es/es/web/cambio-climatico/2020-2030>
- Karamidehkordi, E., Sadati, S. a. H., Tajvar, Y., & Mirmousavi, S. H. (2023). Climate change vulnerability and resilience strategies for citrus farmers. *Environmental and Sustainability Indicators*, 20, 100317. <https://doi.org/10.1016/j.indic.2023.100317>
- Li, W., Huang, J., Yang, L., Chen, Y., Fang, Y., Jin, H., Sun, H., & Huang, R. (2021). A practical remote sensing monitoring framework for late frost damage in wine grapes using Multi-Source satellite data. *Remote Sensing*, 13(16), 3231. <https://doi.org/10.3390/rs13163231>
- Liu, Q., Piao, S., Janssens, I. A., Fu, Y., Peng, S., Lian, X., Ciais, P., Myneni, R. B., Peñuelas, J., & Wang, T. (2018). Extension of the growing season increases vegetation exposure to frost. *Nature Communications*, 9(1). <https://doi.org/10.1038/s41467-017-02690-y>
- Loboguerrero, A. M., Boshell, F., León, G., Martínez-Baron, D., Giraldo, D., Mejía, L. R., Díaz, E., & Cock, J. (2018). Bridging the gap between climate science and farmers in Colombia. *Climate Risk Management*, 22, 67–81. <https://doi.org/10.1016/j.crm.2018.08.001>
- Maracchi, G., Sirotenko, O., & Bindi, M. (2005). Impacts of present and future climate variability on agriculture and forestry in the temperate regions: Europe. In *Springer eBooks* (pp. 117–135). https://doi.org/10.1007/1-4020-4166-7_6

- Micheloud, N. G., Castro, D. C., Favaro, M. A., Buyatti, M. A., Pilatti, R. A., & Gariglio, N. F. (2017). Respuesta de diferentes variedades de cítricos a los daños causados por fuertes heladas en la región central de Santa Fe. DOAJ (DOAJ: Directory of Open Access Journals). <https://doaj.org/article/aaa8750caa40427a9216fa72d225e70a>
- Murray, V., & Ebi, K. L. (2012). IPCC Special Report on Managing the Risks of Extreme Events and Disasters to Advance Climate Change Adaptation (SREX). *Journal of Epidemiology & Community Health*, 66(9), 759–760. <https://doi.org/10.1136/jech-2012-201045>
- Reyes, J. J., & Elias, E. (2019). Spatio-temporal variation of crop loss in the United States from 2001 to 2016. *Environmental Research Letters*, 14(7), 074017. <https://doi.org/10.1088/1748-9326/ab1ac9>
- Snyder, R. L., & Melo-Abreu, J. (2005). Frost protection: fundamentals, practice and economics. Volume 1. <http://hdl.handle.net/10400.5/4727>
- Venner, R., & Blank, S. C. (1995). Reducing citrus revenue losses from frost damage: wind machines and crop insurance. *Giannini Foundation Information Series*, 95–1. <https://ideas.repec.org/p/ags/dgiais/251898.html>
- Wang, S., Chen, J., Rao, Y., Liu, L., Wang, W., & Dong, Q. (2020). Response of winter wheat to spring frost from a remote sensing perspective: Damage estimation and influential factors. *ISPRS Journal of Photogrammetry and Remote Sensing*, 168, 221–235. <https://doi.org/10.1016/j.isprsjprs.2020.08.014>
- Wang, S., Xie, W., & Yan, X. (2022). Effects of future climate change on citrus quality and yield in China. *Sustainability*, 14(15), 9366. <https://doi.org/10.3390/su14159366>
- Whiteman, T. M. (1957). Freezing points of fruits, vegetables and florist stocks /. <https://doi.org/10.5962/bhl.title.62920>
- Zabihi, H., Vogeler, I., Amin, Z. M., & Gourabi, B. R. (2016). Mapping the sensitivity of citrus crops to freeze stress using a geographical information system in Ramsar, Iran. *Weather and Climate Extremes*, 14, 17–23. <https://doi.org/10.1016/j.wace.2016.10.002>
- Zhong, G., & Nicolosi, E. (2020). Citrus origin, diffusion, and economic importance. In *Compendium of plant genomes* (pp. 5–21). https://doi.org/10.1007/978-3-030-15308-3_2

Spatial and Temporal Evolution Characteristics of Urban Heat Island in Beijing and Dalian Based on Multi-source Data

Yaru Meng^{1,2}, Caixia Gao^{1,*}, Enyu Zhao³, Wan Li¹, Wenping Yu⁴

1 National Engineering Laboratory for Satellite Remote Sensing Applications, Aerospace Information Research Institute, Chinese Academy of Sciences, Beijing 100094, China;

2 School of Electronic, Electrical and Communication Engineering, University of Chinese Academy of Sciences, Beijing 100049, China;

3 College of Information Science and Technology, Dalian Maritime University, Dalian 116026, China

4 School of Geographical Sciences, Southwest University, Chongqing 400715, China;

** Corresponding author*

Email addresses: gaocaixia@aoe.ac.cn

ABSTRACT: The Urban Heat Island (UHI) effect significantly impacts urban environments and residents' quality of life, particularly with accelerating urbanization and climate change. This study explored the evolving trends of the Surface Urban Heat Island Intensity Index (SUHII) in Beijing and Dalian, using MYD11A2 satellite data and supplementary datasets on the Google Earth Engine platform. The analysis focused on spatiotemporal variations in SUHII from 2003 to 2023, providing insights into the dynamics of heat island patterns in both cities. The methodology involved delineating rural reference areas to calculate day and night SUHII, enabling detailed comparisons of SUHII. By assessing the shifts in heat island distributions and their centers of gravity, the research highlights both shared patterns and regional differences between Beijing and Dalian. Key findings include: ① Both cities experience increased SUHII, with Beijing's heat islands predominantly migrating southwest, while Dalian's shift southeast. ② In Beijing, areas without heat islands and those with strong heat islands decrease, while other classifications expand; in Dalian, areas without heat islands and cold islands shrink, while weak heat islands increase. ③ In 2023, heat islands in Beijing are primarily concentrated in the southeast, while Dalian's are mainly in the southwest, and the proportion of no heat island areas in Dalian is higher than that in Beijing. These findings provide valuable scientific insights for urban planning and climate adaptation strategies.

1 INTRODUCTION

The Urban Heat Island (UHI) effect, where city centers are warmer than surrounding rural areas due to altered energy exchange mechanisms (Oke, 1982), was first highlighted by Manley (Manley, 1958) and quantitatively analyzed by Oke (Oke, 1973). This phenomenon has significant repercussions on the urban environment and the well-being of its residents. Specifically, the UHI effect leads to increased energy demand, diminished air quality (Gonzalez-Trevizo et al., 2021), and exacerbates public health issues (Yang, G et al., 2021; Yin et al., 2023). The advent of remote sensing has facilitated detailed analyses of the Surface Urban Heat Island (SUHI), providing insights into its spatial distribution and trends over time (Liu, H et al, 2023). Noteworthy investigations include Cao Ge et al.'s study on the intensification of SUHI during heatwaves in Dalian, using 2018-2019 Landsat 8 images (Cao et al, 2024), alongside Liu Y et al.'s examination of SUHI trends in major Chinese and global megacities from multi-source datasets, including MODIS, NOAA, DMSP/OLS, NDVI, socioeconomic

and DEM data, illustrating the marked impact of urbanization on SUHI intensification (Liu, Y et al, 2018).

Despite these insights, research predominantly remains case-specific, lacking systematic exploration of SUHI variations between coastal and inland cities influenced by distinct climates, urban structures, and other factors. Besides, the reliance on remote sensing data from specific periods restricts a comprehensive temporal understanding (Zhou et al, 2018). This study, leveraging Google Earth Engine (GEE) for its cloud computing capabilities, conducts a comparative analysis of Beijing and Dalian from 2003 to 2023. It assesses SUHI evolution and explores mitigation strategies, thus aiming to elucidate SUHI formation mechanisms and inform urban planning and management.

2 STUDY AREA

Beijing, situated between 39°26' and 41°03' north latitude and 115°25' to 117°30' east longitude, has a temperate monsoon climate, characterized by hot summers and cold, dry winters. Economically, Beijing

emphasizes services, high-tech, and creative industries, with urban planning aimed at reducing congestion and fostering regional integration within the Beijing-Tianjin-Hebei area (Liu, J et al, 2020).

Dalian, located at the southern end of the Liaodong Peninsula, experiences a temperate monsoon climate with cool summers and mild winters. The Zhongshan District, characterized by its high degree of urbanization and role as a commercial hub, exhibits the highest intensity of development. Dalian's economic strategy is geared towards optimizing its port capabilities, bolstering foreign trade, and fostering the growth of high-tech industries. This strategy aims at positioning Dalian as a modern international city (Zhao, Y, 2015).

Both cities' geographical and climatic features, along with their economic and urban strategies, provide valuable insights into the SUHI effect. Beijing offers a case study in managing SUHI in large inland cities, while Dalian provides perspectives on coastal influences on SUHI. Their comparative analysis deepens understanding of UHI mechanisms and supports effective urban sustainability strategies in rapidly urbanizing settings.

3 DATASETS AND METHODS

3.1 Extraction of Rural Background Data

This study adopted the urban-rural dichotomy model proposed by Liu Yonghong et al. (Yonghong, L et al, 2017), which integrates multi-source data to mitigate errors associated with fixed-area definitions. This approach has been extensively validated in urban heat island research (Liao, S et al, 2022; Qiao, Z et al, 2019; Wang, Y et al, 2021). To delineate rural and suburban areas, we employed four specific criteria on the GEE platform, adhering to the thresholds established by Liu Yonghong's study (Yonghong, L et al, 2017).

Furthermore, this study used the GEE platform for the acquisition and preprocessing of rural background data, encompassing elevation, Normalized Difference Vegetation Index (NDVI), land cover, and nighttime light data. Precision filtering was applied using parameters from the "DetailedQA" and "QC" bands to minimize cloud interference, as detailed in Table 2-1.

3.2 Assessment of Rural Background Temperature and Surface Urban Heat Island Intensity Index (SUHII)

This study used the MODIS MYD11A2 V6.1 product on the Google Earth Engine (GEE) platform, providing average land surface temperatures (LST) at a 1-kilometer spatial resolution over an 8-day cycle (NASA/MODIS, 2020). "LST_Day_1km" and "LST_Night_1km" bands were selected to assess daytime and nighttime surface temperatures from 2003 to 2023.

Tab. 2-1 Data introduction and parameter description

GEE ID	Sensor	Resolution	Band	Year
CGIAR/SRTM 90_V4	SAR	90m	elevation	2000
MODIS/061/MOD13A2	AQUA/TERRA	1000m	NDVI, Detailed QA	2003-2023 year by year
MODIS/006/MCD12Q1	AQUA/TERRA	500m	LC_Type1, QC	2003-2020 year by year
NOAA/DMSP-OLS/NIGHTTIME_LIGHTS	OLS	927.67m	stable_lights	2003-2012 year by year
NOAA/VIIRS/001/VNP46A2	DNB	500m	Gap_Filled_DNB_BRDF_Corrected_NTL	2013-2023 year by year

The conversion of LST values from digital number (DN) values to Celsius is described by equation (1):

$$T_s = DN \times 0.02 - 273.15 \quad (1)$$

where T_s represents LST and DN represents pixel brightness values.

Furthermore, this study used the SUHII classification method proposed by Ye et al. (Ye, C et al, 2011), for classifying temperature variations into seven levels from strong cold islands to strong heat islands. The calculation of SUHII is provided in equation (2):

$$SHUI_i = T_i - \frac{1}{N} \sum_i T_r \quad (2)$$

Equation (2) also explains that $SHUI_i$ is the urban heat island intensity (°C) for the i-th pixel, T_i is the LST of the i-th pixel, N denotes the total number of pixels within the rural background, and T_r is the temperature observed in the rural background.

Additionally, this study used centroid shift analysis to explore spatial dynamics and transitions among urban heat island categories from 2003 to 2023. These methods were used to compute the movements of heat island zones and to visualize the changing patterns of land cover associated with urban heat islands over the study period (Y. Yang et al, 2018).

4 RESULTS

4.1 Analysis of the Spatial and Temporal Distribution of SUHII at Monthly Scale

To investigate the SUHII, we first plotted the mean SUHII values for daytime, nighttime, and diurnal averages across different months and years, as shown in Figures 1-a, 1-b, and 1-c. Overall, Beijing and Dalian exhibit distinct seasonal variations in SUHII. SUHII

values are higher in summer and lower in winter. Specifically, Beijing shows significantly higher SUHII values in summer and lower values in winter compared to Dalian. This difference may be attributed to Dalian's coastal climate and urban layout, which differ from the inland conditions of Beijing, influencing their respective urban heat island effects.

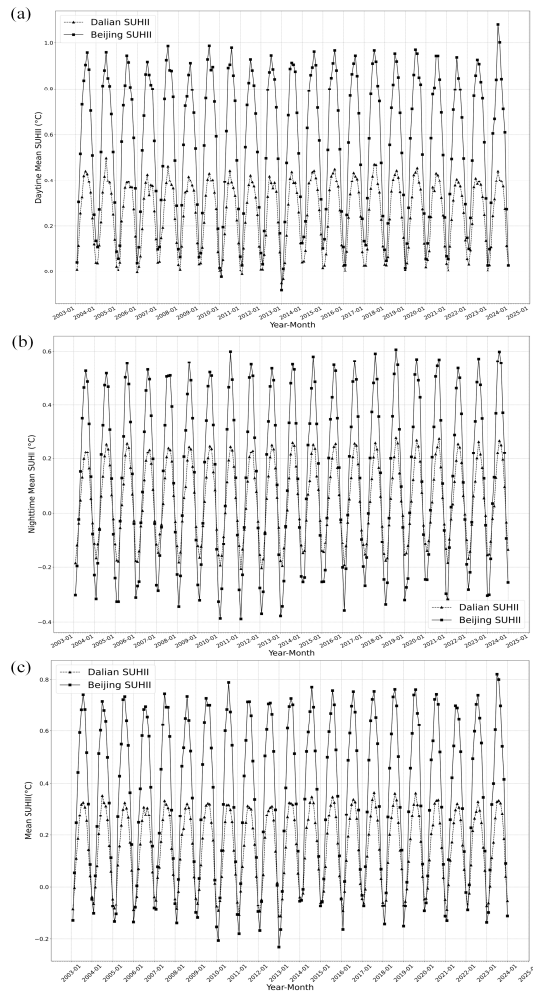


Fig. 1 Monthly SUHII Line Charts of Beijing and Dalian: (a) Daytime, (b) Nighttime, (c) Daytime and Nighttime Average

As depicted in Figures 1-b, daytime SUHII in Beijing ranges from -0.2°C to 1.2°C , while in Dalian, it ranges from -0.2°C to 0.6°C . Overall, Beijing exhibits larger monthly variations in SUHII compared to Dalian. Nighttime SUHII in Beijing ranges from -0.4°C to 0.7°C , whereas in Dalian, it ranges from -0.3°C to 0.3°C . Notably, nighttime SUHII values in January, November, and December are markedly lower in Beijing than that in Dalian (Figure 1-c).

4.2 Analysis of the Spatial and Temporal Distribution of SUHII at Annual Scale

To understand the interannual variations of SUHII, this study statistically analysed the annual mean SUHII values for daytime, nighttime, and diurnal averages, as depicted in Figures 2-a, 2-b, and 2-c. The average daytime SUHII values in Beijing and Dalian are 0.56°C and 0.25°C , respectively, with peak values occurring in 2014 at 0.59°C and 0.27°C , and minimum values in 2012 at 0.53°C and 0.23°C (Figure 2-a). For nighttime SUHII, Beijing and Dalian average values are 0.14°C and 0.05°C , respectively, reaching maximum values in 2023 at 0.17°C and 0.06°C . The lowest nighttime SUHII values are recorded in 2012 at 0.10°C for Beijing and in 2011 at 0.03°C for Dalian (Figure 2-b).

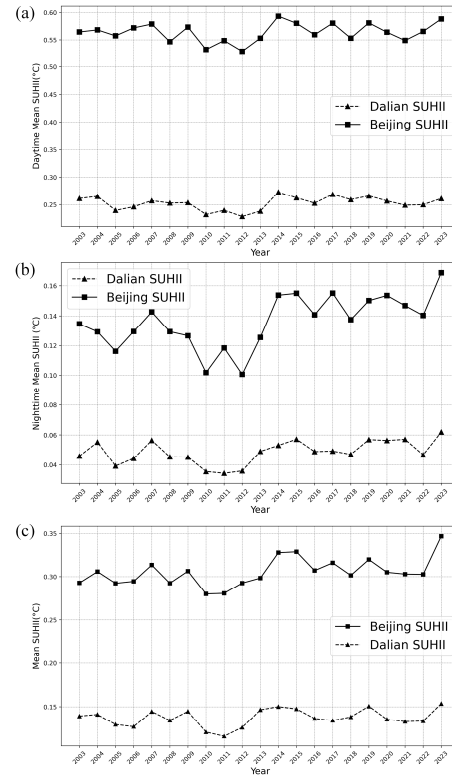


Fig. 2 Annual SUHII Line Charts of Beijing and Dalian: (a) Daytime, (b) Nighttime, (c) Daytime and Nighttime Average

Overall, SUHII values are higher in Beijing compared to Dalian, with average SUHII values of 0.3°C and 0.14°C , respectively. The maximum SUHII values for both cities occurred in 2023 at 0.35°C and 0.15°C , while the minimum SUHII values were observed in 2010 at 0.28°C for Beijing and in 2011 at 0.12°C for Dalian (Figure 2-c).

From 2003 to 2023, Beijing's heat island zones, ranging from weak to strong, are primarily in the

southeast, while cold island zones are located in the northwest, northeast, and southwest regions. Between 2010 and 2013, despite a stable number of heat islands, both cold and heat island areas in Beijing expand, especially weak heat islands in Pinggu, Tongzhou, Daxing, and Shunyi districts, mirroring trends in annual average surface temperatures (Figure 3-a). From 2013 to 2023, Beijing experiences a steady increase in heat island zones, with strong heat islands notably expanding in Daxing, Tongzhou, and Fangshan. In contrast, Huairou and Yanqing show a reduction in cold island areas.

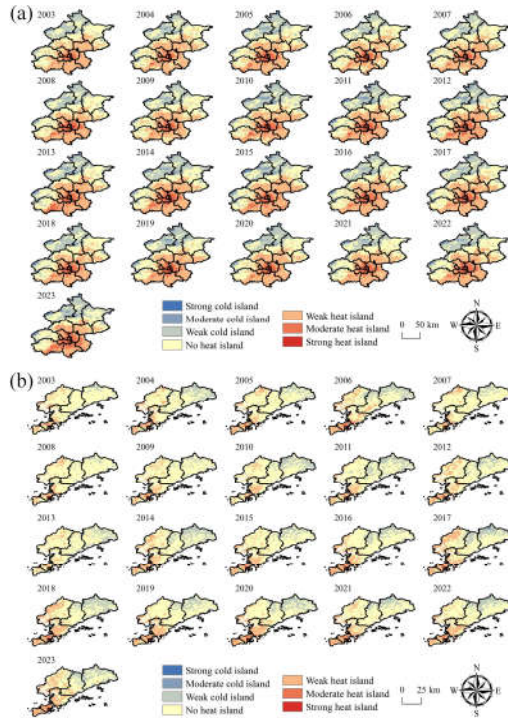


Fig. 3 Distribution Map of Heat Island Types: (a) Beijing, (b) Dalian

Comparatively, Dalian has fewer strong cold and heat islands from 2003 to 2023, with more prevalent weak heat and cold islands (Figure 3-b). Heat islands in Dalian are mostly in the southwest, whereas cold islands were in the northeast, especially in the mountainous areas of Zhuanghe and Pulandian. Similar to Beijing, from 2010 to 2013, Dalian shows no reduction in heat islands but an increase in both cold and heat island zones, with significant expansion in weak heat islands in Wafangdian and Jinzhou districts. This trend continues through 2023, with a generally stable increase in heat island zones and a decrease in cold island coverage, particularly in Zhuanghe city, accompanied by a notable rise in weak heat island areas in Wafangdian and Jinzhou districts in 2022-2023.

This study analyzed the evolution of heat and cold islands in Beijing and Dalian from 2003 to 2023, as depicted in Figures 4-a and 4-b. In Beijing, the heat island area follows a fluctuating pattern, decreasing from 7011.16 km² to 6728.97 km², with coverage shifting from 41.49% to 39.82% of the total area. The peak and trough values for heat islands are observed in 2015 (7503.89 km²) and 2006 (6341.89 km²), respectively. Concurrently, cold island areas exhibit a pattern of increase, decrease, and then increase again, expanding from 4129.43 km² to 5026.97 km², with coverage rising from 24.44% to 29.75%. The largest and smallest cold island areas occur in 2012 (5173.24 km²) and 2007 (3955.83 km²), respectively. Areas with no heat islands display a decreasing trend from 5756.82 km² to 5141.47 km², with coverage declining from 34.07% to 30.42%.

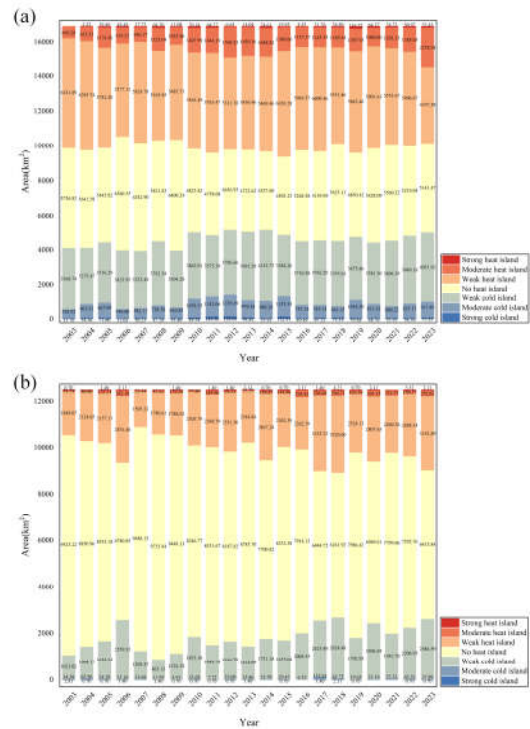


Fig. 4 Annual Area Statistics of Each Heat Island Type from 2003 to 2023: (a) Beijing, (b) Dalian

Similarly, in Dalian, heat island areas initially increase, then decrease, and subsequently increase again, expanding from 1904.50 km² to 3447.61 km². This trend reflect a rise in area coverage from 15.25% to 27.61%, with the smallest and largest areas recorded in 2007 (1560.65 km²) and 2018 (3554.98 km²). The cold island areas parallel this trend, growing from 1058.21 km² to 2625.18 km², with coverage increasing from 8.48% to 21.02%. The minimal and maximal

extents of cold islands are in 2008 (876.26 km²) and 2018 (2688.34 km²). The area without heat islands shows a declining trend, reducing from 9523.219 km² to 6413.84 km², and the proportion of the total area decreases from 76.27% to 51.37%, with the smallest area in 2018 (6241.92 km²) and the largest in 2008 (9735.84 km²).

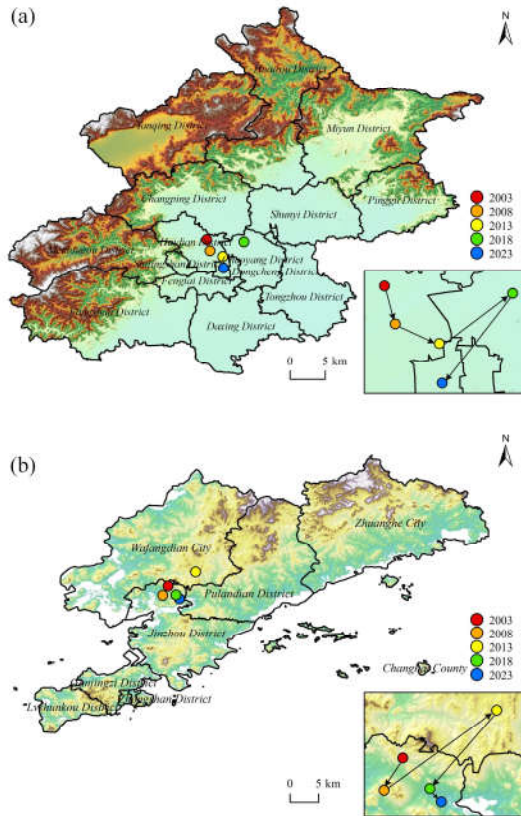


Fig. 5 Shift of Center of Gravity in Heat Island Regions from 2003 to 2023: (a) Beijing, (b) Dalian

4.3 Analysis of the Centroid Shifts of SUHII at Annual Scale

To analyse and predict the centroid shifts in heat island areas, this study plotted Figures 5-a and 5-b. As shown in Figure 5-a, from 2003 to 2008, Beijing's urban development centroid experiences a significant spatial shift, moving approximately 16.00° to the southeast. Subsequently, during the period from 2008 to 2013, the direction of centroid shift continues southward but with a notably increased angle of 65.83°, reflecting dynamic changes in urban development. Moving into the phase from 2013 to 2018, there is an adjustment in the direction of centroid shift towards northeast, with an angle of 55.63°. Finally, from 2018 to 2023, the centroid of urban development shifts toward southwest with an adjusted angle of 38.03°.

In Figure 5-b, during the period from 2003 to 2008, Dalian's centroid of heat island areas exhibits a shift towards the southwest direction at an angle of 30.20°. Over the subsequent five years (2008 to 2013), the centroid shifts to the southeast, increasing the angle to 54.61°. Furthermore, from 2013 to 2018, the centroid again shifts towards the southwest direction, with an angle of 40.37°. In the most recent five years from 2018 to 2023, the observed centroid shift direction is southeast at an angle of 41.30°.

5. DISCUSSION

This research employs innovative methods and multi-source data to analyze the dynamic changes of SUHII, enhancing understanding of the complex characteristics of urban heat island effects.

However, despite its comprehensive scope, this study also exists limitations. The analysis is constrained by the resolution of MODIS remote sensing data, which is less suited for fine-scale urban heat dynamics. Additionally, the study's reliance on existing datasets limits its ability to normalize variations in nighttime light data, potentially affecting the accuracy of rural background extractions and the subsequent analysis of SUHII trends. Therefore, further research should integrate more recent and higher-resolution data to refine the understanding of urban heat island effects and their drivers. This will aid in developing more effective mitigation strategies, thereby contributing to urban sustainability efforts globally.

6. CONCLUSIONS

In this study, we conducted a detailed analysis of the SUHII in Beijing and Dalian from 2003 to 2023, revealing the complex temporal and spatial trends of these phenomena. Through a comparative analysis of these two cities, we enhanced our understanding of the differences in urban heat island effects between coastal and inland cities, providing insights that may inform targeted mitigation strategies.

Significant variations in heat island intensities are observed between the two cities, with notable differences in how these areas expand or contract over time. The analysis confirms the role of several natural and anthropogenic factors in shaping these dynamics, including vegetation cover and urban density. Based on these insights, the study proposes targeted mitigation strategies such as optimizing green space distribution, enhancing building energy efficiency, and promoting green infrastructure development to lower urban temperatures and enhance the quality of urban life.

This analysis offers practical guidance for urban planners and policymakers to develop effective strategies for mitigating UHI effects, promoting more sustainable and comfortable urban environments. Future research should continue to refine these

strategies and assess their effectiveness, furthering our understanding of urban heat islands and their mitigation amidst global climate change.

AUTHOR CONTRIBUTIONS

Yaru Meng: Conceptualization, Experimental Design, Methodology, Project Administration, Writing. **Caixia Gao:** Funding, Data Curation, Analysis, Writing. **Enyu Zhao:** Data Collection, Experimentation, Analysis, Writing. **Wan Li:** Resources, Supervision, Writing. **Wenping Yu:** Conceptualization, Methodology, Writing.

DECLARATION OF COMPETING INTEREST

The authors declare that they have no known competing financial interests or personal relationships that could have appeared to influence the work reported in this paper

ACKNOWLEDGMENTS

The authors thank the teams at NASA/MODIS for their support and for providing the data that has been essential to our study.

FUNDING

This work was supported by the General Program of National Natural Science Foundation of China under Grant 42271395.

REFERENCES

- Cao, G., Jin, C., Zhang, Z., and Hou, M. (2024). Analysis of the impact of high temperature heat wave on the characteristics of urban heat island change in Dalian City. *Journal of the Hebei Academy of Sciences*, 41(1), 11–20.
- Gonzalez-Trevizo, M. E., Martinez-Torres, K. E., Armendariz-Lopez, J. F., Santamouris, M., Bojorquez-Morales, G., and Luna-Leon, A. (2021). Research trends on environmental, energy and vulnerability impacts of Urban Heat Islands: An overview. *Energy and Buildings*, 246, 111051.
- Liao, S., Cai, H., Tian, P., Zhang, B., and Li, Y. (2022). Combined impacts of the abnormal and urban heat island effect in Guiyang, a typical Karst Mountain City in China. *Urban Climate*, 41, 101014.
- Liu, H., Ma, Z., Li, M., and He, B. (2023). Examination and Evaluation of Urban Heat Island Effect Based on Satellite Remote Sensing: Taking Wuhan as an Example. *Journal of Human Settlements in West China*, 38(6), 38–45.
- Liu, J., Jiang, F., and Qian, C. (2020). Systematic Study on the Coordinated Development of Beijing-Tianjin-Hebei Region. *China Soft Science*, 4, 142–153.
- Liu, Y., Fang, X., Xu, Y., Zhang, S., and Luan, Q. (2018). Assessment of surface urban heat island across China's three main urban agglomerations. *Theoretical and Applied Climatology*, 133(1–2), 473–488.
- Manley, G. (1958). On the frequency of snowfall in metropolitan England. *Quarterly Journal of the Royal Meteorological Society*, 84(359), 70–72.
- NASA/MODIS(2020). MYD11A2.061 MODIS/Aqua Land Surface Temperature and Emissivity 8-Day L3 Global 1km SIN Grid. NASA EOSDIS Land Processes DAAC. <https://doi.org/10.5067/MODIS/MYD11A2.061>, Accessed in the 12h of March of 2024.
- Oke, T. R. (1973). City size and the urban heat island. *Atmospheric Environment* (1967), 7(8), 769–779.
- Oke, T. R. (1982). The energetic basis of the urban heat island. *Quarterly Journal of the Royal Meteorological Society*, 108(455), 1–24.
- Qiao, Z., Huang, N., Xu, X., Sun, Z., Wu, C., and Yang, J. (2019). Spatio-temporal pattern and evolution of the urban thermal landscape in metropolitan Beijing between 2003 and 2017. *Acta Geographica Sinica*, 74(3), 475–489.
- Wang, Y., Ren, Y., Song, L., and Xiang, Y. (2021). Responses of extreme high temperatures to urbanization in the Beijing-Tianjin-Hebei urban agglomeration in the context of a changing climate. *Meteorological Applications*, 28(5), e2024.
- Yang, G., Ren, G., Zhang, P., Xue, X., Tysa, S. K., Jia, W., Qin, Y., Zheng, X., and Zhang, S. (2021). PM_{2.5} Influence on Urban Heat Island (UHI) Effect in Beijing and the Possible Mechanisms. *Journal of Geophysical Research: Atmospheres*, 126(17), e2021JD035227.
- Yang, Y., Liu, Y., Li, Y., and Du, G. (2018). Quantifying spatio-temporal patterns of urban expansion in Beijing during 1985–2013 with rural-urban development transformation. *Land Use Policy*, 74, 220–230.
- Ye, C., Liu, Y., Liu, W., Liu, C., and Quan, W. (2011). Research on Urban Surface Heat Environment Monitoring Indexes and Its Application. *Meteorological Science and Technology*, 39(1), 95–101.
- Yin, Y., Zhang, H., An, H., Lei, J., Li, M., Song, J., and Han, W. (2023). Heat island characteristics and influencing factors of urban agglomerations in the Yangtze River Economic Zone based on GEE. *Chinese Journal of Ecology*, 42(1), 160–169.
- Yonghong, L., Xiaoyi, F., Shuo, Z., Qingzu, L., and Weijun, Q. (2017). Research on quantitative evaluations of heat islands for the Beijing-Tianjin-Hebei Urban Agglomeration. *Acta Ecologica Sinica*, 37(17).
- Zhao, Y. (2015). *Overall Urbanization based metropolis' spatial development: Dalian Case* [Doctor, Dalian University of Technology]. https://kns.cnki.net/kcms2/article/abstract?v=kHMw6kznbpqKMCKIumoy8K_EppPRczDwxXcS4wnyqLKmyuDqK1kh0jG0khtPZWWr5C_cvGEptNEo4LZADnJOV3yDGE_LxmdK-0FIJITuOYaAF2MH93Swrm80zh_YiXSanduniplatform=NZKPTandlanguage=gb
- Zhou, D., Xiao, J., Bonafoni, S., Berger, C., Deilami, K., Zhou, Y., Frolking, S., Yao, R., Qiao, Z., and Sobrino, J. A. (2018). Satellite Remote Sensing of Surface Urban Heat Islands: Progress, Challenges, and Perspectives. *Remote Sensing*, 11(1), 48.

Spatiotemporal Evolution and Driving Forces Analysis of the Urban Heat Island in Shijiazhuang

Yue Liu¹, Ruo-han Chen¹, Xia Zhang^{1, 2, 3, *}, Ce Zhang¹, Yi-ran Tian¹, Guo-fei Shang^{1, 2, 3}

¹*School of Land Science and Spatial Planning, Hebei GEO University, Shijiazhuang 050031, China*

²*Hebei Center for Ecological and Environmental Geology Research, Hebei GEO University, Shijiazhuang 050031, China*

³*Hebei International Joint Research Center for Remote Sensing of Agricultural Drought Monitoring, Hebei GEO University, Shijiazhuang 050031, China*

*Corresponding author: E-mail: zhangxia396@hgu.edu.cn

ABSTRACT The urban heat island (UHI) effect in Shijiazhuang has led to significant ecological and environmental concerns. Previous research mainly focused on its spatial and temporal characteristics, with limited exploration of contributing factors. This study analyses UHI in Shijiazhuang from 2000 to 2020 using Landsat ETM+/OLI data and the Mono-window Algorithm (MW) for land surface temperature analysis. The SARIMA model projects future temperature trends. By incorporating factors like NDVI, DEM, POP, and NPP with spatial autocorrelation methods, the study reveals their dynamic relationships with UHI. A multi-scale analysis model identifies the optimal urban scale for assessing UHI evolution and its drivers. Results show significant spatial clustering, with the UHI area expanding annually by 44.288 km², and a centroid shifting south-eastward. Seasonal patterns indicate UHI reduction in autumn, accompanied by the largest centroid shift, while spring shows minimal change. Projections predict a more intense UHI effect by 2030, with peak temperatures in summer. NDVI emerges as the most influential factor, followed by DEM, which suppresses UHI. After 2005, other factors begin promoting UHI. The best model fit is found at a 3KM*3KM scale, with NDVI, NPP, and PPT as the top contributors. Interactions between DEM and NDVI or PPT are particularly strong, with a significant interactive effect of 0.972.

Keywords - urban heat island; bivariate spatial autocorrelation; MGWR model; factor interaction

1 INTRODUCTION

In recent years, the rapid advancement of urbanization in Shijiazhuang has not only made remarkable economic and cultural achievements, but also is faced with serious environmental problems, among which the intensity of urban heat island effect has become the focus of much attention. As a significant link in the process of urbanization, the phenomenon of urban heat-island has always been the core of the attention of environmental scientists and urban planners.

Since the urban heat island (UHI) phenomenon was first identified by Howard in 1833, it has become a significant focus of research. Early studies primarily explored how urbanization influences local climates and its role in global climate change (Grimmond, 2007). The intensity of the UHI effect is largely driven by factors such as increased impervious surfaces and reduced vegetation, which alter the urban radiative balance, increase sensible heat flux, and decrease latent heat flux (Arnfield, 2003). This effect significantly impacts energy consumption, weather patterns, and atmospheric circulation over cities (Voogt J A & Oke T R, 2003; Rosenzweig C et al., 2006). Recent research

has focused on the spatiotemporal evolution of UHI, using multi-temporal remote sensing data to analyze its patterns and relationships with urban development. For instance, studies have monitored UHI trends in regions like the Chang-Zhu-Tan urban agglomeration and the Guangdong-Hong Kong-Macao Greater Bay Area, revealing significant spatiotemporal shifts and the influence of human activities (Wang et al., 2020; Dng et al., 2023; Min et al., 2018; Hu Nanlin et al., 2022). Additionally, researchers have investigated the driving factors of UHI, considering how urban structures and regional climates contribute to its intensity (Zhang Z. et al., 2022; Umer K. et al., 2021; Niu Lu et al., 2022). Various remote sensing technologies and statistical models have been employed to study UHI, with significant advances in temperature retrieval algorithms and GIS spatial analysis (Keivan Deilami et al., 2018; Ana C. Teodoro et al., 2021; Payam Amir Saber Mirzaei and Fariborz Haghighat, 2010; Huizhi Ren and Qihao Weng, 2009).

Current research on the heat island effect focuses mainly on spatial and temporal distribution and migration changes. There is a lack of research on the impact of other elements on the urban heat island effect, and this study intends to select a variety of factors

combined with a comprehensive analysis of the heat island effect.

2 MATERIALS AND METHODS

2.1 Study Area

Shijiazhuang, situated in the south-central region of Hebei Province, is the provincial capital. Its geographical coordinates range from 37°27'N to 38°47'N and 113°30'E to 115°20'E. It borders Hengshui to the east, Xingtai to the south, Shanxi Province to the west, and Baoding to the north. The city's maximum north-south extent is approximately 148 km, while its maximum east-west span reaches about 175 km. The city's perimeter measures 760 km, encompassing a total area of 15,848 km² (Figure 1)

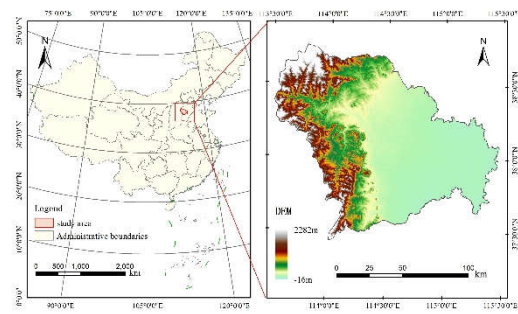


Figure 1 Overview of the study area

2.2 Multi-Source Data

This study primarily employed remote sensing images from the Landsat7 ETM+ and Landsat8 OLI_TIRS series, which were sourced from the open-access platform (<https://earthexplorer.usgs.gov>). The selected images were of sufficient quality for analysis. In processing the Landsat data, this study conducted essential radiometric and geometric corrections.

Considering the findings from existing research and the characteristics of the city, several commonly used and easily quantifiable indices were selected, such as: population density (<https://landscan.ornl.gov/>), DEM(<http://srtm.csi.cgiar.org/srtmdata/>), GDP(<https://github.com/thestarlab/ChinaGDP>), PM2.5(<https://zenodo.org/record/6398971>), NDVI(<http://data.tpdc.ac.cn>), NPP(<https://dataverse.harvard.edu>), PET(<https://data.tpdc.ac.cn>), PPT(<https://data.tpdc.ac.cn>).

2.3 Methods

We employed the Mono-Window algorithm to retrieve surface temperature data and subsequently classified the results into distinct heat island categories. Utilizing the directional distribution method alongside the centroid model, we conducted a comprehensive analysis of the spatiotemporal distribution patterns of

the UHI effect across various years and seasons. To forecast future trends in UHI dynamics, the SARIMA model was applied. Further, bivariate spatial autocorrelation analysis was employed to investigate the relationships between the UHI effect and its influencing factors over different time periods. Ultimately, a multi-scale spatial analysis model was developed, and the fitting accuracy of the geographically weighted regression model was assessed across different spatial scales. The geo-detector method was then used to analyze the contribution rates and interactions of various influencing factors, providing deeper insights into the mechanisms driving urban heat island formation. The specific process is shown in Figure 2

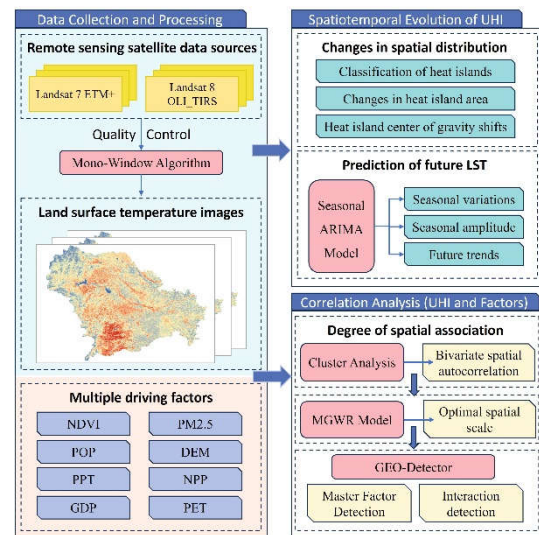


Figure 2 Framework for the research process

1) According to the characteristics of Landsat data, the atmospheric correction method in the mono-window algorithm is used to invert the land surface temperature. Under the premise of obtaining the average atmospheric operating temperature (T), surface specific emissivity (ϵ) and atmospheric transmittance (τ), the influence of atmospheric radiation on surface thermal radiation is estimated and eliminated, and the surface thermal radiation intensity is obtained, and then the thermal radiation intensity is converted into the corresponding surface temperature value.

2) The standard deviation ellipse is a commonly used tool in spatial statistical analysis to describe the shape and dispersion of data distributions. By illustrating the distribution of UHI data points, the standard deviation ellipse offers a visual representation of spatial dispersion. The size of the ellipse reflects the extent to which data points are dispersed relative to the overall mean.

3) The Seasonal Auto-regressive Integrated Moving Average (SARIMA) model is a time series forecasting method that extends the ARIMA model (Box et al. 1970; Mathew A et al. 2016) to account for seasonality. Implemented using the Box-Jenkins methodology for model identification, estimation, and forecasting, the SARIMA model is particularly effective for real-time predictions and is known for its high accuracy.

3 RESULTS

3.1 UHI Retrieval Results

The heat island area in Shijiazhuang in 2000 covered 4577.56 km², mainly concentrated in the western region, with strong heat island phenomena in the northwest and southwest. By 2005, the heat island areas remained concentrated in the northwest and southwest, but the southwest area decreased by 854.40 km². In 2010, the heat island effect in the northwest eased and began to spread toward the central urban area, with the overall heat island area continuing to decrease by 753.85 km². In 2015, the heat island area further reduced by 90.93 km². By 2020, the heat island in the city center had expanded significantly, with an overall increase of 44.29 km² (Figure 3).

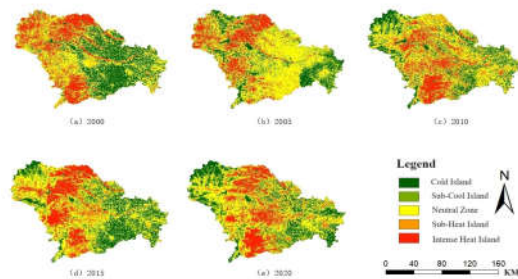


Figure 3 Distribution of urban heat island

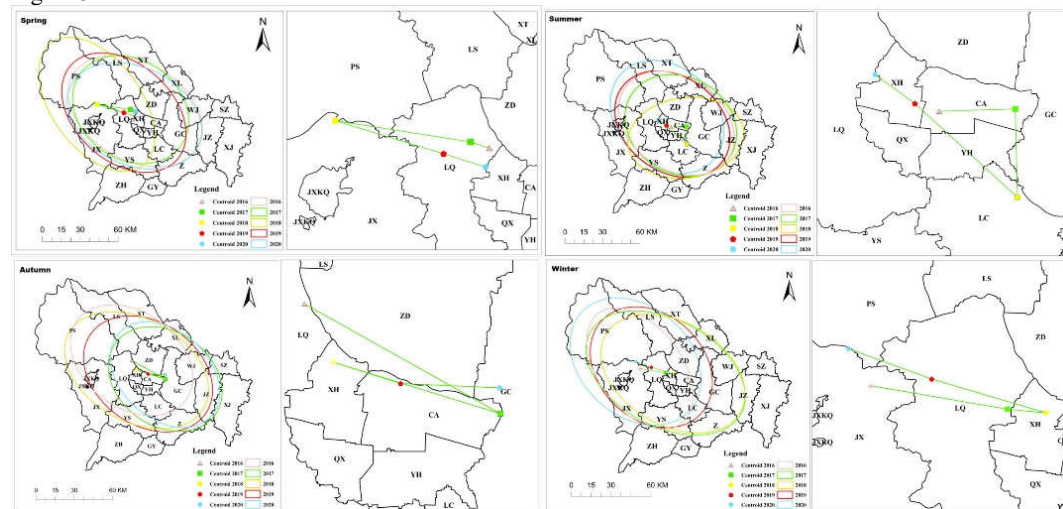


Figure 4 Shijiazhuang UHI centroid shifts by season (2016-2020)

3.2 Spatial Changes UHI In Shijiazhuang Across Seasons

Visualizing the standard ellipses of the Urban Heat Island in Shijiazhuang from 2016 to 2020 across different seasons provides a clear picture of its spatial distribution and temporal shifts (Figure 4).

In spring, the UHI showed a "northwest-southeast" pattern, with the centroid moving 3.87 km southward between 2016 and 2020, remaining mainly within Luquan District except for 2018. In summer, the predominant "northwest-southeast" pattern shifted to "southwest-northeast" in 2018, with the centroid moving 11.8 km northwest, fluctuating across several districts and steadily heading towards Luquan District since 2018. In autumn, the UHI followed a "northwest-southeast" trend, with the centroid shifting 28.51 km southeastward over five years, moving across various districts. In winter, the "southeast-northwest" pattern saw the centroid shift 6.14 km northwestward between 2016 and 2020, with a consistent northwest movement since 2018.

3.3 Results of LST Prediction

By performing seasonal statistics on the maximum, average, and minimum values of LST from 2016 to 2020, and by visualizing the original sequence and predicted values of seasonal LST in Shijiazhuang for the same period (Figure 6), several trends emerge: In the original sequence of seasonal LST, the seasonal LST in 2017, 2018, and 2020 remained relatively stable, fluctuating around a constant value, indicating a relatively stable seasonal pattern.

However, the seasonal LST in 2016 and 2019 showed larger fluctuations, reflecting more pronounced seasonal changes.

In the forecast sequence, the LST in Shijiazhuang from 2021 to 2030 is expected to show a slight upward trend, with regular cyclical fluctuations on a seasonal basis. The LSTs corresponding to different seasons are closely related, showing minor changes between seasons, while the LST fluctuations within each year across the four seasons are more significant.

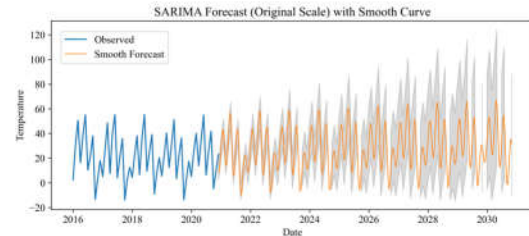


Figure 5 LST prediction for Shijiazhuang

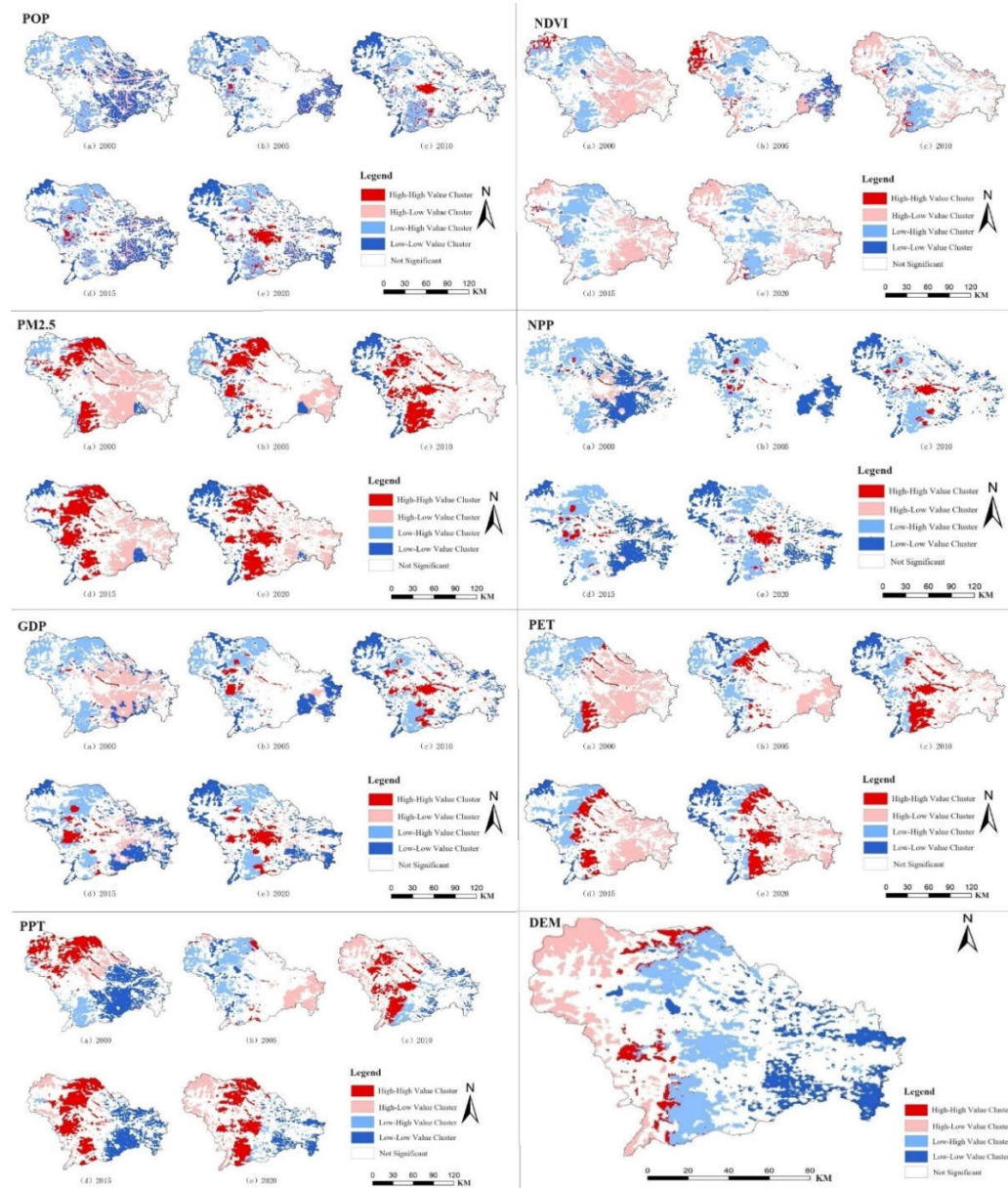


Figure 6 Cluster analysis of the key factors associated with the UHI index

4 DISCUSSION

4.1 Bivariate UHI Spatial Clustering Patterns

The bivariate spatial autocorrelation LISA cluster map is an effective tool for visualizing the spatial relationships between two variables. To investigate the spatial clustering and differentiation between urban heat islands and their influencing factors, a local autocorrelation analysis was conducted, which revealed the clustering patterns of urban heat islands in relation to various factors (Figure 6).

The relationship between population density and the urban heat island (UHI) index in Shijiazhuang highlights urbanization and environmental changes. Initially dispersed in 2000, these variables showed no significant spatial correlation, but by 2010, a strong correlation emerged, with the urban core exhibiting high population density and increased UHI intensity. From 2000 to 2020, a negative correlation between NDVI and the UHI index became evident, indicating that higher vegetation reduces the UHI effect, while GDP positively correlated with UHI, particularly in the urban core, due to economic growth and reduced green space. PET's influence on UHI shifted from negative in 2000 to positive by 2020, reflecting intensified heat island effects with higher temperatures and evapotranspiration. High PM2.5 areas also expanded alongside stronger UHI effects, emphasizing the need for air quality management. Since 2005, NPP has positively correlated with UHI, with urban center areas showing increased urbanization and heat island intensity. Precipitation also positively correlates with UHI, contributing to its intensification, particularly in the city center. Finally, DEM showed a negative correlation with UHI, with higher elevations linked to weaker UHI effects, and lower elevations to stronger effects. Overall, as Shijiazhuang develops, the UHI index has become more closely associated with these factors, particularly in the urban core.

4.2 Analysis of MGWR model and Geo-detector

DEM has a predominantly negative impact on the urban heat island (UHI) index in Shijiazhuang, with stronger effects in the southwest and northwest, diminishing toward the east. However, the city center and its surroundings show a positive correlation. GDP exerts a weak but generally positive influence on the UHI, strongest in the east and decreasing westward. NDVI significantly suppresses the heat island effect, especially along the central north-south axis, with regression coefficients showing the strongest negative influence. NPP positively correlates with the UHI index, with its influence increasing from west to east. PET has a relatively weaker effect, peaking in the northwest and gradually lessening southeastward. PM2.5 negatively affects the UHI, with its impact decreasing from

northwest to southeast, while population density shows a positive correlation, intensifying the UHI effect from northwest to southeast. Precipitation (PPT) has one of the most significant impacts, positively correlating with the UHI, particularly in the city center. This analysis highlights the varying contributions of these factors to the UHI effect, providing insights for urban planning and environmental management using the MGWR model.

The Interaction Detector analysis revealed that the combined effect of two factors on SUHI was significantly stronger than individual effects, particularly between DEM and NDVI or PPT, with q values of 0.972. Even GDP, which had the lowest individual impact, showed enhanced effects when interacting with factors like NDVI, NPP, PM2.5, and PPT. Other interactions, such as DEM with GDP or POP, and NDVI with PET, were weaker but still showed some enhancement. Overall, the study highlights that multiple factors interact in complex, nonlinear ways to significantly strengthen the SUHI effect in Shijiazhuang.

5 CONCLUSION

- (1) The urban heat island effect in Shijiazhuang showed a decline in the annual urban heat island area from 4577.56 km² to 4430.53 km², indicating a weakening trend. Seasonal variations revealed a decrease in the heat island area during autumn, while other seasons experienced an increase. The SUHI generally followed a southeast-northwest direction, with the centroid shifting southward in spring and northwestward in summer and winter. The most significant shift occurred in autumn, moving southeast by approximately 28 km.
- (2) The SARIMA model accurately predicted future trends, suggesting a slight increase in LST from 2021 to 2030, with seasonal peaks expected in summer 2030.
- (3) Bivariate spatial autocorrelation identified NDVI as the most effective in mitigating the urban heat island effect, followed by DEM. Other factors, which initially suppressed the heat island effect before 2005, began to exacerbate it afterward. The ranking of contributing factors to SUHI is NDVI > NPP > PPT > DEM > PM2.5 > POP > PET > GDP, with DEM and NDVI or PPT interactions having the most significant impact on SUHI, while GDP and POP interactions had the least impact.

REFERENCES:

- Almeida C R, Teodoro A C, Gonçalves A. Study of the urban heat island (UHI) using remote sensing data/techniques: A systematic review[J]. *Environments*, 2021, 8(10): 105.
- Arnfield A J. Two decades of urban climate research: a review of turbulence, exchanges of energy and water, and the urban heat island[J]. *International Journal of Climatology: a Journal of the Royal Meteorological Society*, 2003, 23(1): 1-26.
- Box G E P, Pierce D A. Distribution of residual autocorrelations in autoregressive-integrated moving average time series models[J]. *Journal of the American statistical Association*, 1970, 65(332): 1509-1526.
- Deilami K, Kamruzzaman M, Liu Y. Urban heat island effect: A systematic review of spatio-temporal factors, data, methods, and mitigation measures[J]. *International journal of applied earth observation and geoinformation*, 2018, 67: 30-42.
- Deng X, Gao F, Liao S, et al. Spatiotemporal evolution patterns of urban heat island and its relationship with urbanization in Guangdong-Hong Kong-Macao greater bay area of China from 2000 to 2020[J]. *Ecological Indicators*, 2023, 146: 109817.
- Grimmond S U E. Urbanization and global environmental change: local effects of urban warming[J]. *The Geographical Journal*, 2007, 173(1): 83-88.
- Hu Nanlin, Ren Zhibin, Dong Yulin, Fu Yao, Guo Yujie, Mao Zhixia, Chang Xinyue. Spatio-temporal Evolution of Heat Island Effect and Its Driving Factors in Urban Agglomerations of China[J]. *SCIENTIA GEOGRAPHICA SINICA*, 2022, 42(9): 1534-1545
<https://doi.org/10.13249/j.cnki.sgs.2022.09.003>.
- Khalil U, Aslam B, Azam U, et al. Time series analysis of land surface temperature and drivers of urban heat island effect based on remotely sensed data to develop a prediction model[J]. *Applied Artificial Intelligence*, 2021, 35(15): 1803-1828.
- Mathew A, Sreekumar S, Khandelwal S, et al. Prediction of land-surface temperatures of Jaipur city using linear time series model[J]. *IEEE journal of selected topics in applied earth observations and remote sensing*, 2016, 9(8): 3546-3552.
- Min M, Zhao H, Miao C. Spatio-temporal evolution analysis of the urban heat island: A case study of Zhengzhou City, China[J]. *Sustainability*, 2018, 10(6): 1992.
- Mirzaei P A, Haghighat F. Approaches to study urban heat island—abilities and limitations[J]. *Building and environment*, 2010, 45(10): 2192-2201.
- NIU Lu, ZHANG Zheng-feng, PENG Zhong, JIANG Ya-zhen, LIU Meng, ZHOU Xiao-min, TANG Rong-lin. China's surface urban heat island drivers and its spatial heterogeneity. *CHINA ENVIRONMENTAL SCIENCE*, 2022, 42(2): 945-953.
- Rajasekar U, Weng Q. Urban heat island monitoring and analysis using a non-parametric model: A case study of Indianapolis[J]. *ISPRS Journal of Photogrammetry and Remote Sensing*, 2009, 64(1): 86-96.
- Rosenzweig C, Solecki W, Slosberg R. Mitigating New York City's heat island with urban forestry, living roofs, and light surfaces[J]. A report to the New York State Energy Research and Development Authority, 2006: 1-5.
- Voogt J A, Oke T R. Thermal remote sensing of urban climates[J]. *Remote sensing of environment*, 2003, 86(3): 370-384.
- Wang Z, Liu M, Liu X, et al. Spatio-temporal evolution of surface urban heat islands in the Chang-Zhu-Tan urban agglomeration[J]. *Physics and Chemistry of the Earth, Parts A/B/C*, 2020, 117: 102865.
- Zhang Z, Paschalis A, Mijic A, et al. A mechanistic assessment of urban heat island intensities and drivers across climates[J]. *Urban Climate*, 2022, 44: 101215.

The Methods for the NDVI time series reconstruction in North China Plain Using FY-3D data

Xiaoxia Hou¹, Guo-fei Shang^{1, 2, 3}, Xia Zhang^{1, 2, 3, *}, Zheng-hong Yan¹, Ce Zhang¹

¹*School of Land Science and Spatial Planning, Hebei GEO University, Shijiazhuang 050031, China*

²*Hebei Center for Ecological and Environmental Geology Research, Hebei GEO University, Shijiazhuang 050031, China*

³*Hebei International Joint Research Center for Remote Sensing of Agricultural Drought Monitoring, Hebei GEO University, Shijiazhuang 050031, China*

*Corresponding author E-mail: zhangxia396@hgu.edu.cn

ABSTRACT – Long time-series NDVI remote sensing datasets have been widely used in studies of global or regional ecological environment, vegetation, land cover dynamic changes, and plant biophysical parameter inversion. However, influenced by a combination of cloud cover, aerosols, bi-directional reflection of ground objects, and solar altitude angle, plus plenty of noises contain in the datasets, which limits the in-depth analysis and application of the data. Therefore, NDVI data reconstruction is an important task before its application. In this study, North China Plain is taken as the study area, and its NDVI data is reconstructed in time series respectively using Maximum Value Composite(MVC), Asymmetric Gaussian model(A-G), Savitzky-Golay(S-G), Double-Logistic(D-L) and Harmonic analysis of time series(HANTS) methods based on FY-3D Medium Resolution Spectrum ImagerII (MERSI-II) data, the Normalized Difference Vegetation Index of moderate resolution imaging spectroradiometer(MODIS_NDVI) product dataset and FY_NVI product dataset. The correlation coefficient (R), and root mean squared error (RMSE) are used to evaluate the accuracy of the results, and the suitability of different data sources and different land cover types for each reconstruction method is obtained. The results show that the MVC has the best reconstruction result in different land cover types, the methods of S-G filtering and the A-G fitting have the smoothest reconstruction curves, and the HANTS has poor performance; In the fidelity evaluation, the S-G filtering method has the best fidelity with the largest area of $R > 0.8$ and $RMSE < 0.08$, followed by the methods of A-G and D-L, and the HANTS does the worst.

Keywords - time-series analysis; data reconstruction; NDVI; FY-3D; MODIS

1 INTRODUCTION

The vegetation index is a method to monitor the ground vegetation status by remote sensing means, which uses the characteristics of plant spectra with obvious absorption bands in the red band and stronger reflection bands in the near-infrared (NIR) band to reflect the vegetation status by the combination of reflectance calculation (Meng et al. 2011), and these two bands contain more than 90% of the vegetation information in Earth observation satellites. Since the 1960s, vegetation index has been the focus and hot topic of research on resources and environment and agricultural vegetation remote sensing, and a large number of models have emerged for vegetation index extraction. NDVI curves are temporal signals composed of NDVI time series data that present cycles and variations in time related to the biological characteristics of vegetation, such as seasonal fluctuations and interannual variations in vegetation activity (Fan et al. 2018). At present, the methods

concerning NDVI time-series data reconstruction can be summarized into five major categories: threshold denoising, function-based filtering and smoothing, curve fitting, synthesis and others. Various methods are currently applied by domestic and foreign scholars in different regions and fields of research around the world, respectively, and there is no consensus on the advantages and disadvantages of each algorithm (Song et al. 2011b and Wang et al. 2015). There is basically no clearly one algorithm superior to the other for these data reconstruction methods, but it varies depending on the study area, vegetation cover type characteristics and data sources.

In summary, the selection and proposal of the reconstruction algorithm require full consideration of the characteristics of the study area and data sources, and extensive validation. As an important grain, cotton and oil production base in China, the North China Plain is rich in land cover types and is an excellent experimental site for ecological environment research at mid-latitudes. However, with different filtering

methods, there is still no complete, exhaustive and reliable analysis of the filtering effect on the time-series data of different vegetation types. Moreover, the selection of filtering methods is also mostly based on the research results of other related regions, which reduces the accuracy of remote sensing monitoring, affecting and limiting the development of long-term remote sensing monitoring research and the application of new methods, so this study fills the gap. Since most foreign NDVI time-series data products are widely used by scholars, it is particularly important to research domestic satellites. FY-3D, as the new generation of Chinese polar-orbiting meteorological satellites, plays an important role in global climate observation and fine forecasting. In this paper, domestic satellite FY-3D, FY_NVI and MODIS_NDVI are selected as data sources, and using the methods of MVC, A-G, S-G, D-L and HANTS to reconstruct their NDVI data in time series, and qualitatively and quantitatively analyze the time-series curve characteristics of eight major vegetation types, meanwhile, the fitting reconstruction results of five algorithms in different data sources are summarized.

2 RESEARCH AREA AND DATA SOURCES

2.1 Research area

This paper takes the North China Plain as the study area, which includes the Beijing-Tianjin-Hebei region, Shandong Province, and Henan Province, excluding parts of Jiangsu Province and Anhui Province, which are in the North China Alluvial Plain. The North China Plain is located in the eastern coastal region of China, with the geographical coordinates of $31^{\circ}23' \sim 42^{\circ}37'N$ and $110^{\circ}21' \sim 122^{\circ}43'E$ (as shown in Figure 1), of which the plain area is about $33\text{km}^2 \times 104\text{km}^2$. As the main wheat and cotton production region in China, the cultivated area accounts for about 72% of the total area, and it is the main part of the eastern Great Plains, as well as the second largest alluvial plain typical of China. The study area includes the mountains of the Yanshan, Taihang, and others at altitudes over 2,000m, with most locations having an average elevation of 50m or less. There are many rivers in the plain, the southern part is adjacent to the Huai River, and the eastern part is near the Bohai Sea and the Yellow Sea; the climate in the south central plains is a warm temperate semi-arid monsoon climate zone on the east coast of Eurasia, while the north is a warm temperate humid to semi-humid climate zone with an average annual rainfall of 500~1000mm, concentrated in July and August, and the annual precipitation decreases from the southeast to northwest, the land cover type within the plain is shown in Figure 1 (c).

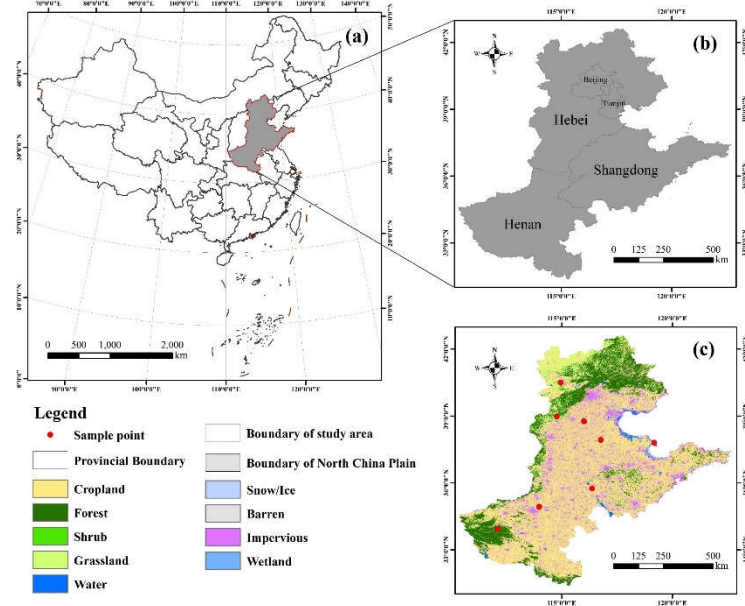


Figure 1. Overview of the study area. (a) geographical location, (b) division of provinces and cities, (c) land cover. Provincial administrative boundary data comes from <https://map.tianditu.gov.cn/> (last access: 1 August 2024)

2.2 Data sources

2.2.1 FY-3D MERSI-II

Medium Resolution Spectrum Imager II (MERSI-II) is a sensor on board the second generation of polar orbiting satellite Fengyun-3D (FY-3D) by China. It integrates the functions of two imagers on the original FY-3D, Visible and Infrared Radiometer (VIRR) and Medium Resolution Spectrum Imager (MERSI), to obtain characteristic parameters of global, all-sky land surface and sea surface for global remote sensing monitoring by detecting emission and reflection of radiation from ground targets (Gu et al. 2003, Dong et al. 2010 and Jin et al. 2018). In this study, MERSI-II remote sensing data from 2019-2021 are taken as the data source, and the visible-NIR channel (channel 3, 0.650 μ m; channel 4, 0.865 μ m) can be used in extracting NDVI. The data are obtained from the National Satellite Meteorological Center (NSMC) Wind and Cloud Satellite Remote Sensing Data Service Network (<http://data.nsmc.org.cn/PortalSite/Data/Satellite.aspx>)

2.2.2 FY_NVI

FY NVI time-series datasets are NDVI products synthesized by MERSI-II sensors for earth observation. FY_NVI is a key product on FY-3D, and as the retirement of the MODIS sensor approaches, it is essential to adopt and validate the information from the newly launched domestic satellite. The spectral response functions of the MERSI-II and the MODIS in the visible and NIR channels are extremely similar, providing a convenient replacement for MODIS_NDVI in the future.

2.2.3 MODIS_NDVI

Moderate resolution imaging spectroradiometer (MODIS) is the primary optical sensor of Earth Observing System (EOS) program, which onboard Terra and Aqua satellites launched by the U.S. National Aeronautics and Space Administration (NASA). The NDVI data used in this study are MOD13Q1/Terra Vegetation Indices 16-Day L3 Global 250m SIN Grid V005 from the MODIS land surface product, spanning from 2019 to 2021, covering the North China Plain study area with tile numbers h26v04, h26v05, h27v04, h27v05, and the projection type of the data is Sinusoidal. The data is taken from (<https://ladsweb.moda-ps.eosdis.nasa.gov/>)

2.2.4 Land cover data

The land cover data used in this study is the annual China Land Cover Dataset (CLCD) produced by the team of Professors Jie Yang and Xin Huang based on 335,709 Landsat images on Google Earth Engine from 1985 to 2021 <https://doi.org/10.5281/zenodo.5816591>

3 METHODS

3.1 NDVI time series reconstruction

In this study, five methods of MVC (Holben et al. 1986), A-G (Gu Zhihui 2003), S-G (Chen et al. 2004), D-L (Pieter et al. 2005), and HANTS (Roerink 2000) are used to reconstruct the NDVI time series of FY-3D data and MODIS_NDVI product (MOD13Q1) data of North China Plain from 2019 to 2021, to quantitatively evaluate the applicability and reconstruction accuracy of each method in the study area.

3.2 Evaluation

3.2.1 Reconstruction of image visual contrast

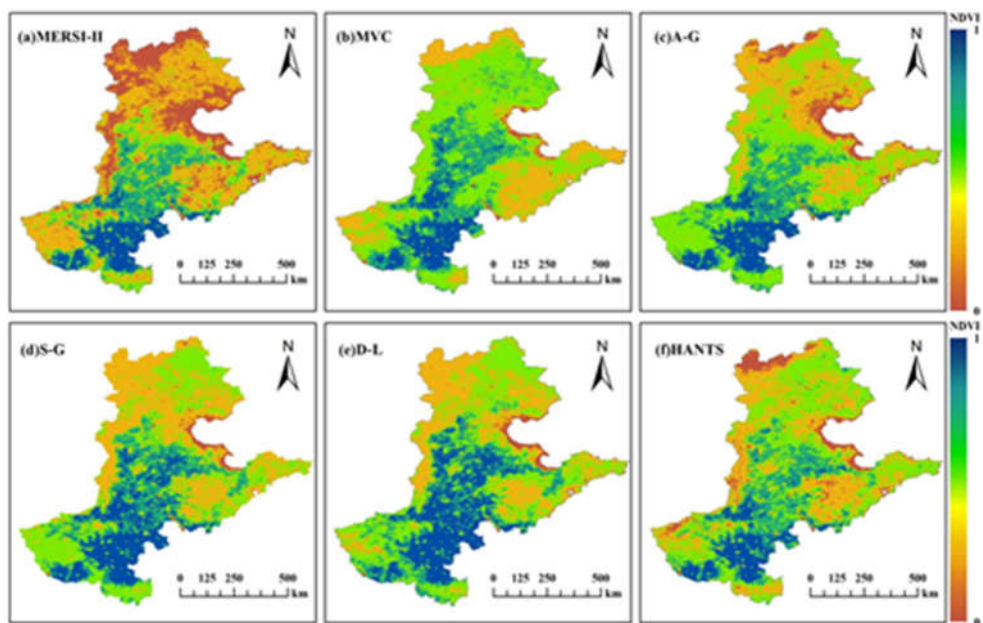
After cloud detection of the original FY-3D data, the images with obvious cloud coverage are selected, and the images with obvious noise in one phase are selected by combining with the quality file MODIS_QA file of MODIS data, and the reconstructed NDVI time series data are compared on the images, and analyzing the effect of five different reconstruction methods on noise processing by visual interpretation. Supplementary Figure 1-3.

3.2.2 Comparison of reconstruction curves

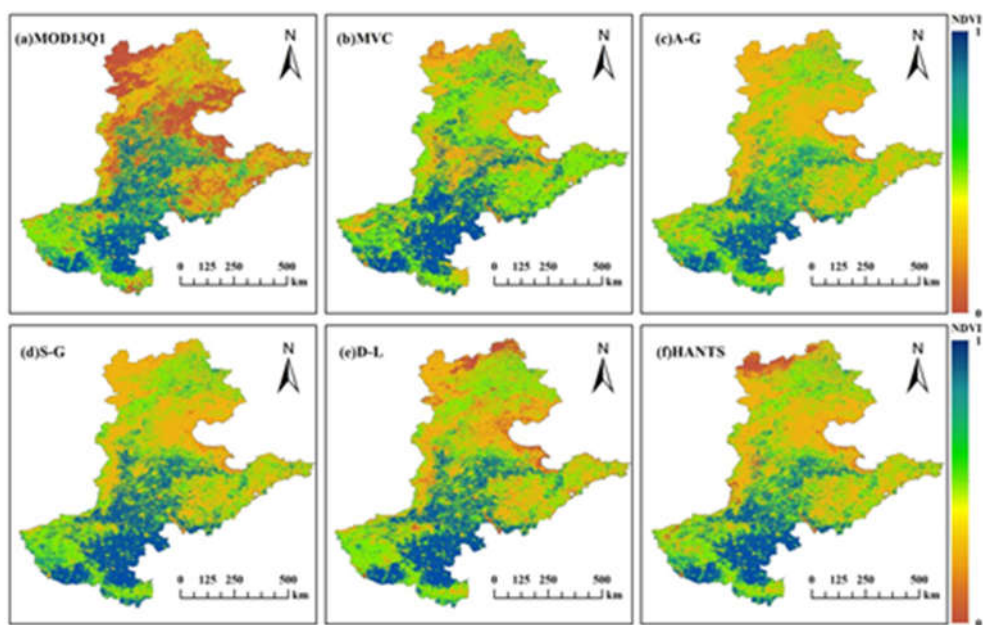
Using land cover data at 30m resolution for three periods from 2019-2021 in the North China Plain, sample points are selected in areas where no land cover type shift has occurred. The principle of selecting sample points is to be spatially evenly distributed, and the points should be selected in the areas affected by clouds and other noise in different degrees from FY-3D and MODIS. After the selection of points, the changes in the curves before and after reconstructing images in different land cover types are compared and analyzed among the five reconstruction methods.

3.2.3 Fidelity Analysis

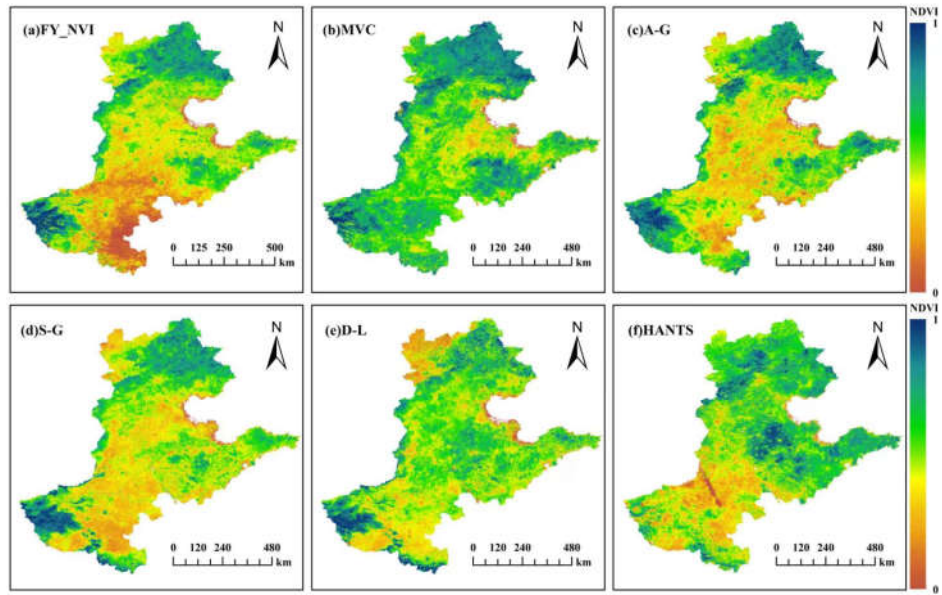
By comparing the R and RMSE of the original data with the reconstructed data, the fidelity of the reconstruction method is compared. Supplementary Figure 4.



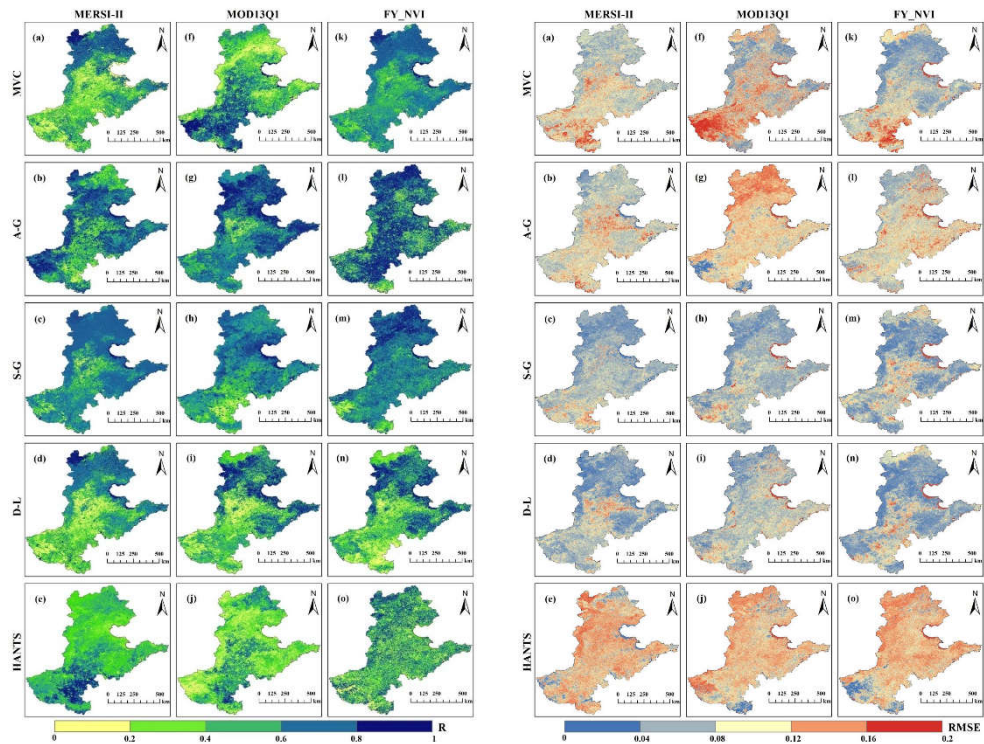
Supplementary Figure 1 | FY-3D MERSI II Images of NDVI values for the raw and smoothed data for the time interval April 1 – April 30,2020.



Supplementary Figure 2 | MOD13Q1 Images of NDVI values for the raw and smoothed data for the time interval March 1 – March 30,2020.



Supplementary Figure 3 | FY_NVI Images of NDVI values for the raw and smoothed data for the time interval June 1 – June 30,2020.



Supplementary Figure 4 | R and RMSE spatial evaluation results for the three reconstructed data

4 RESULTS

In this study, using FY-3D MERSI-II, MODIS_NDVI and FY_NVI, the North China Plain is selected as the study area, and its NDVI data are reconstructed in time series by MVC, A-G, S-G, D-L, and HANTS methods, respectively. The results of the reconstruction are evaluated by a number of evaluation indicators, resulting in the applicability of data sources and land cover types for the five reconstruction methods, which can be summarized as:

(1) The reconstruction result and fidelity evaluation of S-G filtering in three data sources are best in FY_NVI, and the result of MODIS_NDVI is better than FY-3D MERSI-II, but the reconstruction result is worse compared with FY-3D MERSI-II. The visual comparison of images in the reconstruction result have a certain effect of removing the noise in the original image to different degrees, and the reconstruction curve is smoother, but the reconstruction result have the phenomenon of low.

(2) The applicability of A-G fitting to different data sources varies, FY_NVI has the best reconstruction result and fidelity evaluation, MODIS_NDVI is second, while it is worse in the application of FY-3D MERSI-II data, and the same method can all remove noise to a certain extent, and the reconstruction curve is a smooth curve with some missing values not filled.

(3) The reconstruction and fidelity analysis of the D-L curve fitting showed the best reconstruction result of FY_NVI, and FY-3D MERSI-II reconstruction is superior to MODIS_NDVI. In addition, MODIS_NDVI has the best fidelity, wind cloud data and NDVI behave more consistently, the reconstructed curve is a flat curve, there is an over-fitting phenomenon, some growth details are lost, and the difference is larger compared with the original curve.

(4) HANTS has poor performance compared with other reconstruction methods. The reconstructed NDVI curves are smooth, which can effectively remove noise, but there is an over-fitting phenomenon, and the method is suitable for the reconstruction of NDVI time-series data with large time intervals or continuous missing.

(5) MVC is better among several methods and it can remove the noise in images well. Among them, the reconstruction result of FY_NVI product data is the best, while FY-3D MERSI-II data is the second one. The R and RMSE of all three are relatively stable in the fidelity analysis, but the smoothness of the reconstructed curves is poor and the values are falsely high.

REFERENCES

- Chen J, GU Z H, MASAYUKI, et al. A Simple Method for Reconstructing a High-Quality NDVI Time-Series Data Set Based on the Savitzky-Golay Filter[J]. Remote Sensing of Environment, 2004, 91(3): 332-344.
- Dong, C. H., J. Yang, and N. M. Lu, et al. 2010. "Main performance and application of Fengyun-3A Star (FY-3A)." JOURNAL OF GEO-INFORMATION SCIENCE 12(04): 458-465.
- G. J. Roerink, M. Menenti, W. Verhoef. Reconstructing cloudfree NDVI composites using Fourier analysis of time series[J]. International Journal of Remote Sensing, 2000, 21(9).
- Gu, Z. H. 2003. "A Study of Calculating Multiple Cropping Index of Crop in China Using SPOT/VGT Multi-Temporal NDVI Data." Beijing Normal University.
- Holben B N. 1986. Characteristics of maximum-value composite images from temporal AVHRR data. International Journal of Remote Sensing[J], 7(11): 1417-1434.
- Jin, C. 2018. "A Study on cloud detection algorithm of FengYun-3D Spectral Imager over Land." Nanjing University of Information Technology and Engineering.
- Meng, J. H., B. F. Wu, and X. Du. 2011. "Method to construct high spatial temporal resolution NDVI Data Set-STAVFM." Journal of Remote Sensing 15 (1): 44-59.
- Pieter S.A. B. Clement, and A. K. Arild Høgda. 2005. "Improved monitoring of vegetation dynamics at very high latitudes: A new method using MODIS NDVI." Remote Sensing of Environment 100 (3).
- Song, C. Q., C. S. You, H. L. Ke, and G. H. Liu. 2011b. "Methods and Application of three Time NDVI Reconstruction in North Tibet." Journal of the Earth-based Information Science 13 (01): 133-143. doi:10.3724/SP.J.1047.2011.00133.
- Wang, Q. K., X. F. Yu, Q. T. Shu, et al. 2015. "MODIS EVI timing data reconstruction method and fitting analysis." Journal of Geo-information Science 17 (6): 732-741. doi:10.3724/SP.J.1047.2015.00732.

Remote Sensing Retrieval of Soil Moisture by Using Sentinel-1 SAR Data: A Case Study of Lushan County, Sichuan, China

Chen Lu, Xia Zhang, Guofei Shang, Yinhong Xu, Zhaoyang Bai, Yujia Tian
Hebei International Joint Research Center for Remote Sensing of Agricultural Drought
Monitoring, Hebei GEO University, Shijiazhuang, 050031, China
shangguofei@hgu.edu.cn

ABSTRACT – Soil moisture is vital for agriculture, ecology, meteorology, and hydrology, necessitating accurate, real-time monitoring. A study in Lushan County used Sentinel-1 SAR imagery to assess soil humidity, employing different polarization modes and the semi-empirical water cloud model to correct vegetation's impact on radar signals. Support vector regression (SVR) modeled the nonlinear relationship between soil water content and backscattering coefficient, evaluated by RMSE and determination coefficient. The study found the VV polarization method, with an average backscatter coefficient of -17.50 dB and an RMSE of 0.0342 cm³/cm³, to be more accurate and sensitive to soil moisture changes than VH polarization. The SVR model effectively characterized soil moisture, with VV polarization providing better inversion results. This method is ideal for soil moisture monitoring, offering valuable insights for agriculture, water cycles, and vegetation coverage.

Keywords–Soil moisture; polarization; Sentinel-1 SAR; Backscatter

1 INTRODUCTION

Large-scale monitoring and inversion of soil moisture are key elements of modern agricultural research and ecological and environmental assessments (Xiao, B. et al , 2007). MRS detects electromagnetic radiation and scattering features of ground objects in the microwave wavelength range of 1 mm–1 m, thereby facilitating the identification and analysis of various physical parameters (Fang, X. et al , 2022). Synthetic Aperture Radar (SAR) has a fixed revisit period and is the most widely used active MRS method. It can also be used to conduct multi-temporal observation data inversion (Zhang, S, 2022; Li, X., 2019). Since the 1980s, Chinese and foreign scholars have developed empirical, semi-empirical, and theoretical inversion models to understand the relationship between radar backscatter coefficient and soil surface moisture (Jiao, Y., 2022).

We used Lushan County as the study area and utilized Sentinel-1 SAR images from September 2022. First, radar images were preprocessed. Second, the WCM was used to eliminate the influence of the vegetation layer, and soil backscatter coefficients were extracted under different polarizations. Third, support vector regression (SVR) was used to develop a soil moisture regression model for soil moisture inversion in the study area, and root mean square error (RMSE) and coefficient of determination (CoD) were used to evaluate the model. Utilizing active MRS to monitor the spatial distribution of soil moisture can facilitate agricultural development and crop yield estimations, as well as serve as a reference and theoretical basis for drought response and other work.

2 MATERIALS AND METHODS

2.1 Study area overview

Lushan County is in the northeast of the administrative area of Ya'an City in the southwest Chinese province of Sichuan. The county is located at 30°01'–30°49'N, 102°52'–103°11'E. The terrain elevation in Lushan County is higher in the north and lower in the south (Li, W. et al, 2021). The study area has a pleasant inland humid subtropical climate with warm winters and cool summers, four distinct seasons, and abundant rainfall. The average annual temperature is 15.9°C, average annual precipitation is 1276.7 mm, and average annual sunshine is 887.2 h. Precipitation is relatively concentrated from May to September, with greater precipitation in July and August. The Lushan River, spanning a length of 128.5 km, is formed by the confluence of 556 rivers and streams. The geographical location of the study area is shown below (Figure 1).

2.2 Data

The Sentinel-1 SAR (Du, S. et al , 2022) image data used in this study was downloaded from the Copernicus Open Access Hub (<https://scihub.copernicus.eu/dhus>).

The radar data for Lushan County is the Level-1 ground range detected (GRD) product in the IW observation mode. Satellite images of Lushan County on September 2, 2022, were obtained from the website. The images cover the research area in this study. The polarization modes are VV+VH, and the average incidence angle is 39.45°.

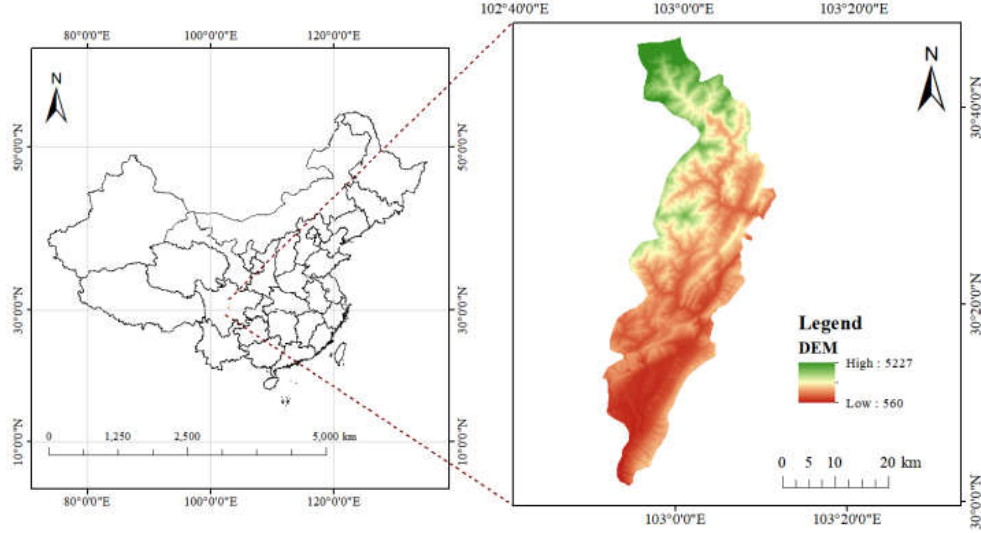


Figure 1. Geographic location of the study area.

They could be used for soil moisture inversion after preprocessing (orbit correction, radiometric calibration, speckle filtering, mosaic creation and clipping, and terrain correction).

Measured soil moisture data was obtained from the 1-km resolution daily all-weather surface soil moisture dataset for China downloaded from the National Tibetan Plateau Data Center (<https://data.tpdc.ac.cn/product>).

2.3 WCM

Water cloud model (WCM) is a semi-empirical model based on microwave remote sensing radiation transfer theory, which is especially suitable for soil water retrieval research of dwarf vegetation (such as crops), and is suitable for the study area of this paper. For this study area, see formulas (3) to (5)

$$\sigma_{total}^0(\theta) = \sigma_{veg}^0(\theta) + r^2(\theta)\sigma_{soil}^0(\theta) \quad (3)$$

$$\sigma_{veg}^0(\theta) = aVWC \cos(\theta)[1 - r^2(\theta)] \quad (4)$$

$$r^2(\theta) = \exp[-2bVWC \sec(\theta)] \quad (5)$$

The WCM can provide the soil surface backscatter coefficient. The calculation method is given in Eq (6).

$$\sigma_{soil}^0 = [\sigma_{total}^0 - a * VWC(1 - r^2(\theta))] \cos \theta / \exp(-2b * VWC \sec \theta) \quad (6)$$

Wherein, θ is the incidence angle of the electromagnetic waves; $\sigma_{total}^0(\theta)$ is the total backscatter coefficient of the vegetation-covered ground surface; $\sigma_{veg}^0(\theta)$ is the vegetation layer backscatter coefficient; a and b are vegetation type

parameters; $\sigma_{soil}^0(\theta)$ is the soil layer backscatter coefficient; VWC is the vegetation water content; and $r^2(\theta)$ is the double-layer attenuation factor of microwave penetration through the vegetation layer.

This study refers to the land cover type parameters used by Bindish et al. (Bindlish, R. et al, 2001). As the study area comprises cultivated land, grassland, and other types of vegetation cover, the values of parameters a and b were set to 0.0012 and 0.091.

2.4 Regression model of bare soil backscatter coefficient and soil moisture with SVR

SVR model is suitable for linear regression with limited samples. Based on SVR, a soil moisture inversion model was developed in Lushan County. The steps are as follows: (1) Remove abnormal data, select 30 samples for testing, and train the rest. (2) Build the data set, input the VV and VH polarization coefficients under WCM, and determine the optimal combination. (3) Cross-validation to determine the c and g parameters. (4) RMSE and CoD were used to evaluate the prediction results.

2.5 Model evaluation

We evaluated the accuracy of the soil moisture inversion model through the CoD (R^2) and RMSE (Chen et al, 2020), as shown in Eqs. (7) and (8).

$$RMSE = (\sum_{i=1}^n (Q_i - P_i)^2 / n)^{-1/2} \quad (7)$$

$$R^2 = 1 - \sum_{i=1}^n (Q_i - P_i)^2 / \sum_{i=1}^n (Q_i - P_i)^2 \quad (8)$$

where Q_i is the measured soil moisture, P_i is the estimated soil moisture, P_j is the average measured value, and n is the number of verification data.

3 RESULTS

3.1 Backscatter coefficients before and after vegetation influence correction

The radar backscatter coefficient obtained through preprocessing is the backscatter coefficient received by the sensor, and the soil backscatter coefficient is obtained after correction. The two polarization methods are compared in Figure 2

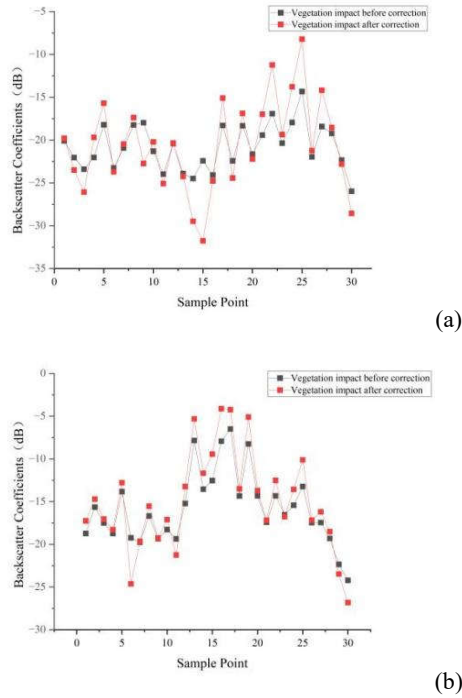


Figure 2. Comparison of backscattering coefficient before and after correction. (a): VH polarization; (b): VV polarization.

Figure 2 shows that the vegetation layer has a considerable influence on the bare soil layer's backscatter coefficient. Separation and correction using the WCM produce a more realistic backscatter coefficient for the bare soil layer. It can be concluded from the analysis of the acquired data that the two methods have a greater influence on the total coefficient than that of vegetation. The average soil backscatter coefficient was -17.50 dB with VV polarization and -23.93 dB with VH polarization. A comparison of the average values revealed a smaller backscatter coefficient under VV polarization, indicating a lesser influence of VV polarization.

3.2 Analysis of soil moisture results

Using Sentinel-1 to interpret the study area, this study selected only the VV polarization data, and ArcGIS was used to obtain a soil moisture distribution map. (Figure 3).

The Figure 3 shows that the RWC in Lushan County was 57.32 – 85.95 , thereby the overall soil moisture content was relatively high. This indicates that the area has relatively high vegetation cover, abundant water, and good vegetation growth, all of which are true. The distribution map again verified that under VV polarization, the SVR model was suitable for conducting soil moisture inversion in Lushan County. The soil backscatter coefficient was obtained from the Sentinel-1 SAR data using the WCM. In the VV polarization mode, the SVR model is suitable for soil moisture inversion in Lushan County as it effectively characterizes soil moisture status, making it the ideal method for monitoring soil moisture.

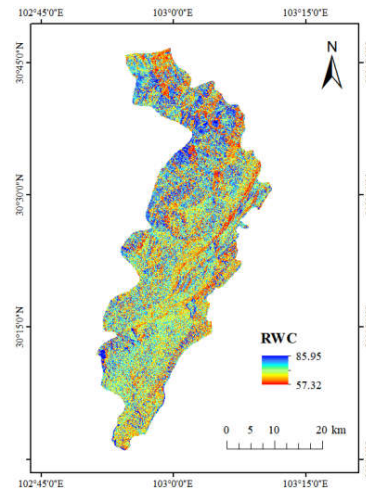


Figure 3. Soil water distribution in Lushan County.

3.3 Evaluation of model results

The closer the value of R^2 to 1, the better the model fit, and the lower the RMSE value, the higher the accuracy. The evaluation relationship is shown in Figure 4.

Figure 4 shows that the soil backscatter coefficient is affected by and positively correlated with soil moisture. The correlation differs between the two polarization modes. The VV polarization backscatter coefficient is more sensitive to soil moisture content and produces good inversion results. The VV polarization was 0.5572 , and the VH polarization was 0.3472 . The RMSE of VV polarization was 0.0342 cm^3/cm^3 and that of VH polarization was 0.0485 cm^3/cm^3 . The data results show that VV polarization is better for soil moisture inversion than VH polarization.

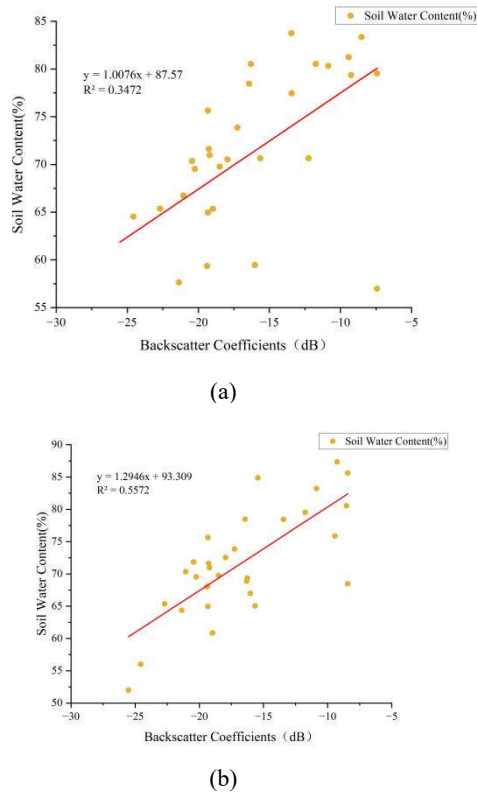


Figure 4. The relationship between the backscattering coefficient and the soil water content. (a): VH polarization; (b): VV polarization.

4. DISCUSSION

Because of the difficulty of field measurement and the limitation of NDVI data, NDWI is better in estimating vegetation moisture. NDWI should be used in future studies.

When the difference of surface vegetation is large, the empirical model does not match the actual parameters, which affects the soil backscattering coefficient of water cloud model. Future studies should synchronize remote sensing data with surface experiments to reduce errors.

Soil backscattering coefficient is affected by vegetation layer and is closely related to soil moisture, surface roughness and texture. These factors should be considered to improve the accuracy of soil water inversion. Radar incidence Angle should be adapted to terrain fluctuation, and other factors should be considered in model construction.

5. CONCLUSIONS

Using Lushan County as the research area, we employed active MRS to monitor soil moisture together with data from Sentinel-1 SAR. Following a comparison of theoretical, empirical, and semi-empirical models of surface microwave scattering in vegetation-covered areas, we selected the semi-empirical WCM to correct the influence of surface vegetation in the backscatter signal and obtain the soil backscatter coefficient. To fit the non-linear relationship between soil moisture content and backscatter coefficient, a regression model based on SVR was developed. The following are the main conclusions of this study:

(1) Optical remote sensing data is vital for the acquisition of surface parameters and can be used as auxiliary data for MRS soil moisture inversion to improve accuracy. In areas with ground surfaces covered with vegetation, the influence of the vegetation layer on the backscatter signal should be considered.

(2) The SVR model proved capable of characterizing soil moisture in Lushan County, and the inverted soil moisture results were highly similar to the measured soil moisture values. The VV polarization was 0.5572, and the VH polarization was 0.3472. The RMSE of VV polarization was $0.0342 \text{ cm}^3/\text{cm}^3$ and that of VH polarization was $0.0485 \text{ cm}^3/\text{cm}^3$. The soil backscatter coefficient of VV polarization had a greater correlation with the measured soil RWC, producing more reliable results than that of VH polarization. The distribution map of soil moisture in Lushan County produced from the final inversion results indicated that soil moisture was generally high in Lushan County, with an RWC of 57.32–85.95, indicating sufficient soil moisture, which accords with reality. The soil backscatter coefficient was obtained from the Sentinel-1 SAR data using the WCM. With VV polarization, the SVR model was suitable for conducting soil moisture inversion in Lushan County, as it is able to characterize the soil moisture status, making it the ideal method for monitoring soil moisture.

REFERENCES

- Bindlish, R.; Barros, A. P. Parameterization of vegetation backscatter in radar-based, soil moisture estimation. *J. Remote Sensing of Environment*. 2001,76(1):130-137.
- Chen, Q.; Zhou, Z. F.; Wang, L. Y.; Dan, Y. S.; Tang, Y. T. Study on surface soil moisture inversion in karst rocky desertification areas based on multi-phase Sentinel-1 SAR data. *J. Journal of Infrared and Millimeter Wave*. 2020,39 (05): 626-634.

- Du, S. J.; Zhao, T. J.; Shi, J. C. Sentinel-1 and Sentinel-2 jointly vert surface soil moisture. J. Remote Sensing Technology and Application. 2022,37 (06): 1404-1413.
- Fang, X. Y.; Jiang, L. M.; Cui, H. Z. Study on soil moisture inversion in the Qinghai-Tibet Plateau based on Sentinel-1 radar data. J. Remote Sensing Technology and Application. 2022,37 (06): 1447-1459.
- Jiao, Y. Z.; Zhang, A. B.; Wang, H. F. Soil water inversion based on Sentinel-1A data. J. Surveying and spatial Geographic Information. 2022,45 (02): 40-44.
- Li, W.; Wang, R. L.; Liang, M. Z. Application of topographic factors in the evaluation of soil and water loss in Lushan County. J. Anhui Agriculture Bulletin. 2021,27(16):168-171.
- Li, X. Y. Remote sensing inversion of surface soil moisture based on Sentinel-1 SAR data. Northwest University. 2019.
- Xiao, B.; Sha, J. M. Overview of the remote sensing inversion method for soil moisture. J. Remote-sensing Information. 2007,No.94(06):94-98.
- Zhang, S. Plot plot scale soil water inversion based on Sentinel-1 SAR data. And Guizhou Normal University. 2022. <https://doi.org/10.27048/d.cnki.ggzsu.2022.000743>.

Research on technology and applications of China's next generation environmental monitoring satellite

Fan Mo¹, Jose Sobrino², Yanhe Yin¹, Yilan Mao¹, Jin Huang¹, Xinwei Zhang¹, Haiyi Cao¹, Hua Li³

¹*China Academy of Space Technology, Beijing 100094, China*

²*University of Valencia, Image Processing Laboratory, Valencia, Spain*

³*State Key Laboratory of Remote Sensing Science, Aerospace Information Research Institute, Chinese Academy of Sciences, Beijing 100101, China*

E-mail: mofanraul@qq.com

ABSTRACT – China's environmental monitoring satellites include HuanJing-1, HuanJing-2, GaoFen-5, DaQi-1 and other satellites, and the monitoring methods cover visible light, infrared, hyperspectral, laser, etc. They have formed a relatively comprehensive and complete monitoring system, with the ability to monitor pollution emissions from large industrial zones, global greenhouse gas distribution, global pollutant gas distribution, etc. The next generation of environmental monitoring satellites will focus on the monitoring of ground emission point sources, improve the spatial resolution of payloads on the basis of existing satellites, and find information such as abnormal temperature and pollutant gas concentration on the ground through the combination of visible light, infrared and hyperspectral, so as to actively discover ground emission sources and provide a basis for ground personnel to go to the site for verification and law enforcement. At the same time, the satellite will be equipped with an onboard processing system, which processes the payload data in orbit, and directly transmits the processing results to the end user in the form of text information or slice images, greatly improving the response speed of pollution events.

Index Terms—environmental monitoring satellite, infrared imaging, land surface temperature, on-board processing, real-time transmission, disaster emergency quick response

1. INTRODUCTION

Due to the rapid development in recent decades, China is currently facing a very prominent environmental pollution problem. In this context, China has put forward the national strategic goals of carbon peak by 2030 and carbon neutrality by 2060. Monitoring and remediation of environmental pollution sources is an important measure to improve environmental quality and achieve strategic goals [1].

Environmental pollution sources are generally accompanied by thermal radiation while producing pollution, and the gas or sewage discharged by them will change the composition of the surrounding atmosphere and water. Taking advantage of this feature, satellite data can be used to find thermal anomalies in user applications, and the structure and texture characteristics of the target can be obtained by combining simultaneous visible light data to determine whether it is a typical emission source, and finally the retrieval results of pollutant gas or water composition from the emission source can be used to confirm whether there is illegal discharge. Through the

simultaneous measurement of temperature, texture and composition, it provides a direct basis for ground verification and law enforcement.

Infrared remote sensing can be used to obtain land surface temperature [2], and hyperspectral remote sensing can obtain pollutant gas and greenhouse gas concentration information through data retrieval [3, 4]. Therefore, the satellite needs to be equipped with visible light payloads, infrared payloads, and spectrometers to achieve high spatial resolution, and all payloads work jointly to achieve monitoring goals. At the same time, the imaging swath of high resolution remote sensing satellites is usually narrow, so the satellite platform needs to have an agile working mode, which can expand the swath by doing Multi-stripes Splicing Imaging, or achieve efficient image acquisition for targets such as the Yangtze River, the Yellow River, and the coastline in China by curve imaging mode.

In addition, in China's environmental law enforcement work, ground-based observation vehicles or drones are often used to conduct on-the-spot observations near pollution discharge sites [5]. But observation vehicles and drones need to know in advance where

contamination will occur, and this information can be obtained through satellites. The onboard processing system on the satellite can process the payload observation data in real time in orbit, and distribute the processing results directly to the ground observation vehicle, which can support applications of end users. At the same time, the image data processed on the satellite can also be directly distributed to research institutions at home and abroad for use by researchers in various countries.

2. MISSION OBJECTIVES

The main goal of the mission is to use high resolution imaging capabilities to observe the land surface and atmosphere, to achieve the identification and location of pollution sources, and to evaluate the area and effect of pollution.

2.1 Industrial gas pollution sources monitoring

The emission sources of industrial pollution include thermal power plants, metal smelting, and chemical plants, and they have significant temperature characteristics during the emission period. Taking the power industry as an example, in China's active thermal power units, the boiler exhaust gas temperature is generally maintained at about 125~150 °C, and the lignite boiler is about 170°C. The flue gas entering the chimney is about 125 °C, and the flue gas temperature entering the chimney is about 50 °C ~80 °C (Figure 1). According to the temperature of the chimney, it can be judged whether the emission is desulfurized.

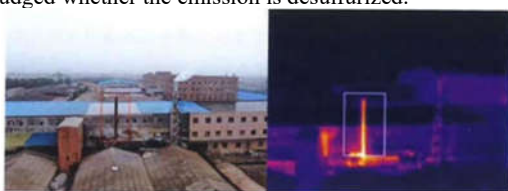


Figure 1. Infrared imaging results in the chimney emission state.

In addition to temperature anomalies, industrial pollution sources will also produce polluting gases or greenhouse gas emissions, including but not limited to: O₃, SO₂, NO₂, CO₂, CH₄, etc. The satellite carries out the detection of pollution source gas concentration information, obtains the observation results of the absorption peaks of several typical pollutant gases and greenhouse gas characteristic spectrums, and retrieve the column concentrations of pollutant gases and

greenhouse gases, which can realize the monitoring and evaluation of industrial emission point sources and serve specific applications of ecological environment users.

2.2 Water pollution monitoring

Water pollution includes urban black and odorous water, thermal plume from coastal nuclear power plant and so on. In general, polluted water has the characteristics of high temperature. Therefore, water pollution can be distinguished by temperature retrieval from long wave infrared remote sensing data (Figure 1). In addition, pollutant dumping from factories and enterprises usually occurs at night. By using day and night imaging characteristics of infrared remote sensing, the abnormal phenomena of water at night can be effectively detected, and the regulation of pollutant dumping will be achieved.

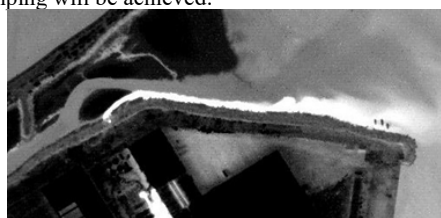


Figure 2. Infrared image of water pollution.

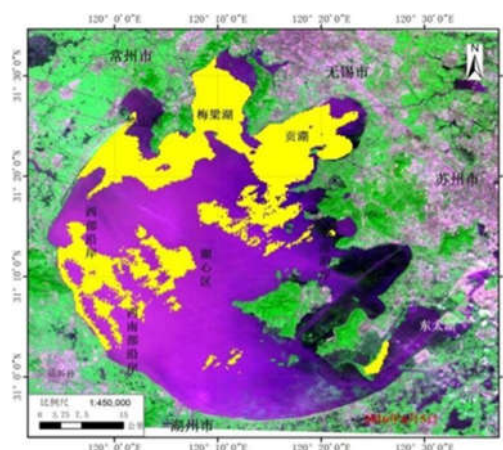


Figure 2. Remote sensing monitoring map of Taihu Lake blooms.

In addition to water temperature, regular monitoring of the water environment of large water bodies in Chinese mainland is also an important application of relevant departments, mainly for the monitoring of water quality

of major rivers and key lakes and reservoirs such as Taihu Lake, Chaohu Lake and Dianchi Lake (Figure 2). The remote sensing monitoring of water quality characteristic parameters is mainly based on the optical characteristics of the water body, and the quantitative estimation model of chlorophyll, suspended solids, transparency, eutrophication index and other parameters is established for data retrieval.

2.3 Methane point source emissions monitoring

Methane is the second most critical gas responsible for the Earth's warming effect, and the continued growth of methane in the atmosphere will have an impact on the Earth's radiative balance. The field with the largest single contribution to global methane emissions from human activities is the production of oil and gas, resulting from leaks from drilling and fracking processes and the vast pipeline infrastructure that transports liquid and gaseous petroleum products, which spans 4.2 million kilometers in the United States alone. Other major sources of methane include landfills, wastewater treatment plants, and the agricultural industry (mainly from cattle and other livestock). Scientists, policymakers, and the oil and gas industry are increasingly recognizing that reducing anthropogenic methane emissions is a necessary component of any successful climate strategy, and the difficulty of accurately detecting methane emissions from the oil and gas industry has been a serious challenge for industry and regulators. Since the characteristic spectral bands of atmospheric methane molecular absorption are mainly located in the shortwave infrared bands with wavelengths of $1.65\mu\text{m}$ and $2.3\mu\text{m}$ [6], remote sensing payloads for atmospheric methane measurements are usually operated in these bands. Observations can be made by spectrometer imaging, or by multispectral cameras [7], which has a significantly higher spatial resolution.

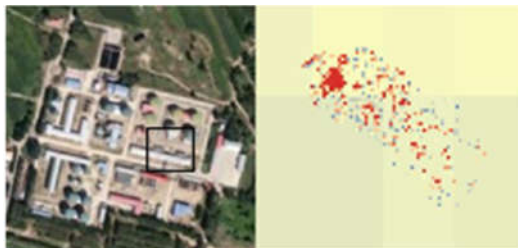


Figure 3. Methane concentration distribution image.

2.4 Fire and volcano eruption detection

The main fire points in China are forest and grassland fires and straw burning, and the temperature is at about $500\sim 1200\text{K}$. According to the radiant energy, it should be mainly concentrated in the mid-wave infrared band of $2.8\sim 5.7\mu\text{m}$.

Fire and volcano eruption detection is an important application direction of infrared remote sensing. Fire and volcano eruption not only seriously endangers forest and urban resources, but also has adverse effects on the ecological environment, which may result in huge economic losses. High temperature targets are ideal objects for onboard processing, and it is necessary to design a real-time transmission downlink, by which users are able to master disaster information as quickly as possible.

3. SATELLITE DESIGN

3.1 Coverage and acquisition capacity

A sun-synchronous orbit at an altitude of about 500 km, and the local time of descending node at 13:30 is chosen. According to the inclination of the satellite's orbit, it can guarantee coverage of the area between 80° north and south latitudes.

Considering the satellite's attitude maneuvering capability at 45° , the maximum revisit time for any target on Earth is 4 days, and the average revisit time is less than 2 days. When considering the nighttime imaging capability of infrared payloads, the average revisit time for any location on Earth is about 1 day.

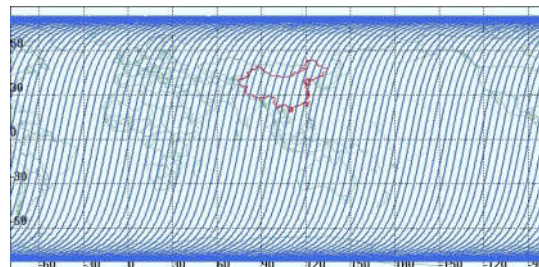


Figure 4. Schematic diagram of the ground trajectory of the satellite in operation for 5 days.

3.2 Payload design

According to the mission requirements, the satellite needs to have visible light, infrared, hyperspectral and other imaging capabilities. Therefore, it is proposed to configure two payloads, one is Multi-spectral Infrared Advanced Camera (MIRAC), equipped with visible and

infrared spectral bands to achieve ground imaging. The other is High-resolution Atmospheric Spectral Imager (HASI), which enables atmosphere detection. MIRAC has four imaging channels, which are VNIR, SWIR, MWIR, and LWIR, and the spectral range is shown in Table 2. The spatial resolution of the visible light band reaches 0.5 meters, and the spatial resolution of each infrared spectrum is better than 10 meters, which is used for the accurate identification of ground thermal anomaly point sources. The swath is better than 35 kilometers.

HASI has three imaging channels, which are UV, NIR, SWIR, and the spectral range is shown in Table 3. The spatial resolution reaches 1 km, the swath is better than 35 kilometers, and HASI has the ability to obtain gas concentration anomalies at the scale of industrial zones. In addition, the combination of the two spectral bands separately from HASI SWIR and MIRAC SWIR can have the ability to identify methane point sources with high spatial resolution.

Table 2. Spectral bands of MIRAC.

Spectral bands	Number of bands	Value (μm)
VNIR	5	0.45 ~ 0.90
SWIR	4	2.145 ~ 2.365
MWIR	1	3.5~4.1
TIR	4	8.475 ~ 12.5

Table 3. Spectral bands of HASI.

Spectral bands	Value (nm)	Spectral resolution (nm)
UV	305~495	0.6
NIR	747~773	0.12
SWIR	1598~1668	0.15

3.3 Onboard processing system(OBP)

Onboard processing system performs scene-splitting, radiometric correction, geometric correction, and temperature/methane retrieval for payload data to obtain distribution products. Using the distribution information, the abnormal high temperature points on the land surface and the abnormal high temperature areas on the water surface are identified, and the event report is formed, which is forwarded to the corresponding ground receiving terminal through the short message channel of the BeiDou navigation satellite, and the rapid distribution of information is automatically realized by mass sending functions such as mobile phone text messages. The slice image corresponding to the event information is designed as a temperature/methane distribution product containing anomaly point information, and is directly transmitted to the ground receiving terminal through the satellite broadcast distribution channel. The above information is

directly distributed to the user terminal, providing fast and direct data services for on-site environmental monitoring and law enforcement.

3.4 Working mode

The payload will be installed on an agile platform. Benefit from high agility, the satellite has a variety of working modes on-orbit [8], which are showed in Figure 4. These working modes can support monitoring of cities, industrial zones, rivers coastlines etc.

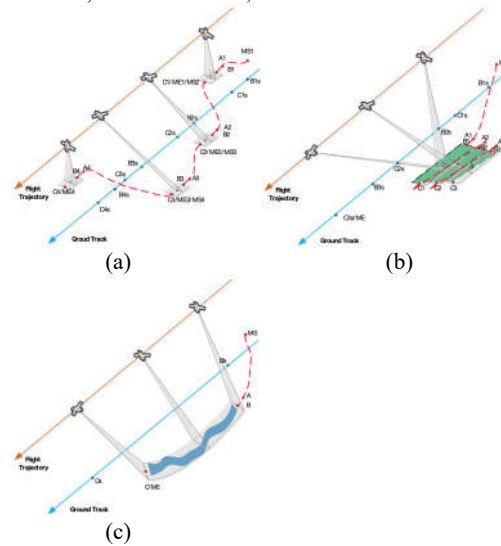


Figure 4. Sketch map of imaging working modes. (a) Multipoint Target Observation. (b) Regional Target Observation. (c) Curve Target Observation.

4. CONCLUSION

In order to improve the quality of the ecological environment and serve the national strategy "Carbon peak and carbon neutrality", China's next-generation environmental monitoring satellite scheme is proposed to meet the needs of ground emission source monitoring. The satellite adopts the high-resolution detection method of "visible light + multispectral + full-spectrum infrared + hyperspectral" to achieve accurate identification and positioning of industrial pollution sources, water pollution, methane emission point sources, etc. The satellite has a flexible working mode and can perform curve imaging on targets such as rivers and coastlines. The onboard processing system is used to process the payload data in orbit, and processing results will be directly distributed to users, improving the timeliness of environmental incident response.

5. REFERENCES

- [1] Q. Wang, "Progress of environmental remote sensing monitoring technology in China and some related frontier issues." *National Remote Sensing Bulletin*, vol. 25, no. 1, pp. 25–36, 2021.
- [2] José A. Sobrino et al., "Review of Thermal Infrared Applications and Requirements for Future High-Resolution Sensors." *IEEE Transactions on Geoscience and Remote Sensing*, vol. 54, no. 5, pp. 2963–2972, 2016.
- [3] L. Y. Liu et al., "Satellite remote sensing for global stocktaking: methods, progress and perspectives." *National Remote Sensing Bulletin*, vol. 26, no. 2, pp. 243-267, 2022.
- [4] Daniel J. Jacob et al., "Satellite observations of atmospheric methane and their value for quantifying methane emissions." *Atmospheric Chemistry and Physics*, no. 16, pp. 14371-14396, 2016.
- [5] J. Y. Wu et al., "Progress and Prospects of Ecological and Environmental Monitoring Network Construction in China." *Environmental Monitoring in China*, vol. 37, no. 2, pp. 1–7, 2021.
- [6] Sudhanshu Pandey et al., "Daily detection and quantification of methane leaks using Sentinel-3: a tiered satellite observation approach with Sentinel-2 and Sentinel-5p." *Remote Sensing of Environment*, vol. 296, p. 113716, 2023.
- [7] Elena Sánchez-García et al., "Mapping methane plumes at very high spatial resolution with the WorldView-3 satellite." *Atmospheric Measurement Techniques*, 2022, 15(6): 1657-1674.
- [8] J. Yu, J. J. Xi, L. J. Yu, F. H. Jiang, "Study of One-orbit Multi- stripes Splicing Imaging for Agile Satellite." *Spacecraft Engineering*, vol. 24, no. 2, pp. 27-34, 2015.

The new EUMETSAT missions: continuity of LSA SAF vegetation service

F.J. García-Haro^{1*}, M. Campos-Taberner¹, B. Martínez¹, A. Jiménez-Guisado¹, S. Sánchez-Ruiz¹, M.A. Gilabert¹, J. Sánchez-Zapero², F. Camacho², E. Martínez-Sánchez²

¹ *Environmental Remote Sensing Group (UV-ERS), Departament de Física de la Terra i Termodinàmica, Universitat de València, 46100 Burjassot, Valencia, Spain.*

² *Earth Observation Laboratory (EOLAB), 46980 Paterna, Valencia, Spain.*

* j.garcia.haro@uv.es

ABSTRACT - The EUMETSAT Satellite Application Facility on Land Surface Analysis (LSA SAF) focuses on developing and implementing algorithms that fully leverage remotely sensed data from EUMETSAT satellites. LSA SAF provides key variables for characterizing terrestrial ecosystems and their role in Earth's energy balance. These include land surface fluxes, such as Gross Primary Production (GPP), and three critical biophysical variables related to the amount, structure, and state of vegetation: Leaf Area Index (LAI), Fraction of Absorbed Photosynthetically Active Radiation (FAPAR), and Fractional Vegetation Cover (FVC). Currently, LSA SAF generates two operational lines of vegetation products. The first is a suite of products (FVC, LAI, FAPAR, GPP) derived from the SEVIRI sensor aboard the geostationary Meteosat Second Generation (MSG) satellites 1-4 (Meteosat 8-11). A Climate Data Record (CDR) is freely available, offering homogeneous time series starting from 2004 at daily and 10-day resolutions, which are essential for climate and environmental applications. The second line produces FVC, LAI, and FAPAR variables based on data from the AVHRR sensor aboard the Meteorological Operational Satellites (currently MetOp A and B) of the EUMETSAT Polar System (EPS). These products are available in near real-time (NRT) with global coverage and a 10-day frequency. This work outlines the current status and upcoming developments of LSA SAF vegetation products, including expert knowledge, accuracy assessments, and examples of potential applications. During the current phase (CDOP-4), LSA SAF plans to release a CDR of FVC, LAI, and FAPAR derived from EPS products (covering 2007 onwards), representing a back-processing of existing NRT/operational data. The current algorithms are being upgraded and expanded to fully exploit the enhanced capabilities of future EUMETSAT missions. A suite of LSA SAF vegetation products will be available shortly after the operational distribution of data from the Meteosat Third Generation (MTG/FCI) and EPS-Second Generation (EPS-SG/VII) sensors, ensuring service continuity. Additionally, current efforts include assessing the feasibility of deriving new vegetation products, such as Canopy Water Content (CWC) and Net Ecosystem Exchange (NEE). The operational lifespan of EUMETSAT satellites places LSA SAF in a prime position to serve as a key provider of climate and environmental monitoring products and services.

Keywords - LSA SAF, vegetation products, EUMETSAT missions, Climate Data Records

1. INTRODUCTION

Terrestrial ecosystems are vital for regulating the Earth's climate, energy, and water cycles, influencing carbon dynamics and environmental stability. Effective monitoring of these ecosystems requires reliable data on key vegetation variables. The EUMETSAT Satellite Application Facility on Land Surface Analysis (LSA SAF) supports this need by providing remotely sensed vegetation products that characterize the structure, health, and productivity of land surfaces. Since its inception, LSA SAF has transformed EUMETSAT satellite data into actionable information, aiding both regional and global climate applications (Trigo et al., 2011). To maximize accessibility, the LSA SAF products are freely disseminated to users through its website (<http://lsa-saf.eumetsat.int>).

Currently, LSA SAF's product portfolio includes essential vegetation variables such as Leaf Area Index (LAI), Fractional Vegetation Cover (FVC), Fraction of Absorbed Photosynthetically Active Radiation (FAPAR), and Gross Primary Production (GPP). FVC measures the proportion of ground covered by vegetation, offering insights into the spatial extent of plant cover. LAI indicates the total leaf area per ground unit, essential for understanding plant biomass and productivity. FAPAR represents the fraction of solar radiation absorbed by green vegetation, which is directly linked to photosynthetic activity. GPP provides estimates of the carbon dioxide absorbed by vegetation, serving as a proxy for ecosystem productivity (Martínez et al., 2020).

These variables offer insights into ecosystem function and carbon fluxes and support long-term climate analysis. LSA SAF generates these products

through two main processing lines: the first uses data from the geostationary Meteosat Second Generation (MSG) satellites to produce near-real-time (NRT) coverage and a Climate Data Record (CDR) dating back to 2004 with daily and 10-day intervals (García-Haro et al., 2019); the second leverages data from the polar-orbiting MetOp satellites, providing global near-real-time coverage with 10-day updates (García-Haro et al., 2018).

As EUMETSAT prepares to launch the next generation of satellites, including Meteosat Third Generation (MTG) and EPS-Second Generation (EPS-SG), LSA SAF is updating its algorithms to take advantage of these enhanced capabilities. This work provides an overview of the current status and applications of LSA SAF's vegetation products and outlines planned developments to support next-generation missions.

2. LSA SAF VEGETATION PRODUCTS

This section outlines the vegetation products generated from the MSG and EPS data, along with upcoming developments under future EUMETSAT missions (see Fig. 1).

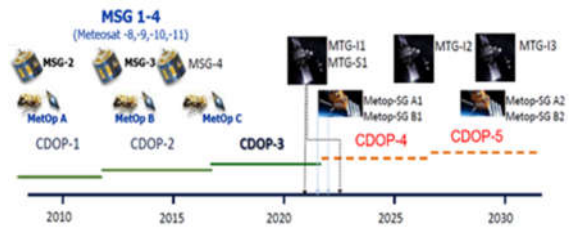


Figure 1. Timeline of the different phases of LSA SAF (CDOP-1 to -5) and the approximate launch dates of the main EUMETSAT satellites.

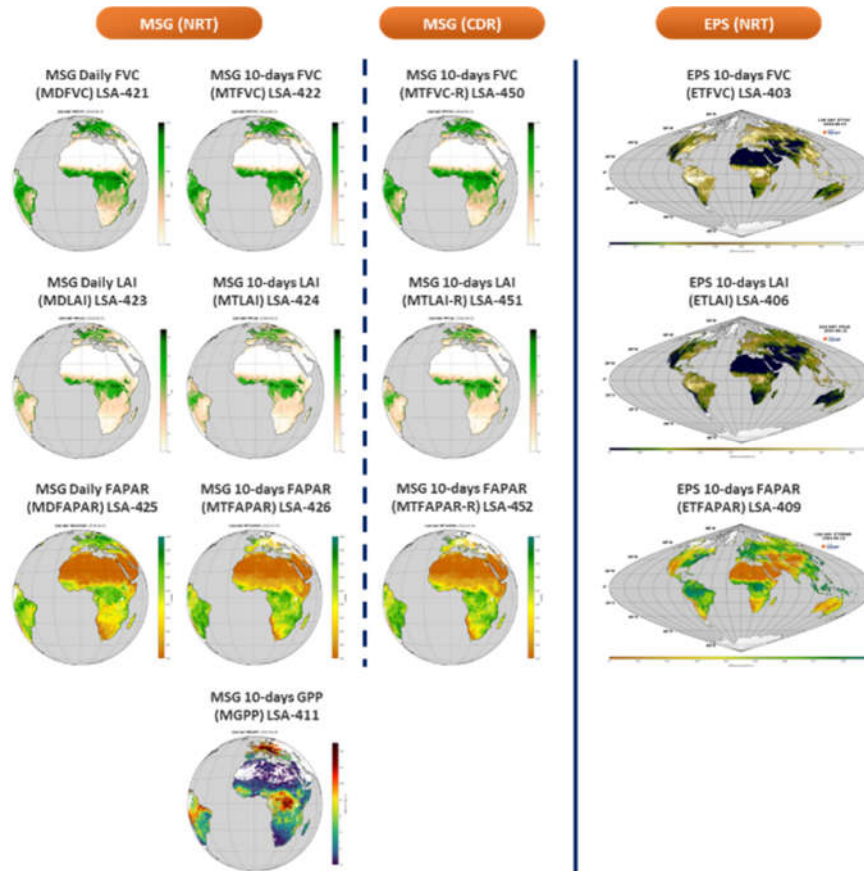


Figure 2. Operational LSA SAF vegetation products derived from MSG and EPS satellite data, presented in daily and 10-day intervals

2.1. Meteosat Second Generation (MSG)

The LSA SAF's vegetation products from the MSG series (specifically the SEVIRI sensor aboard Meteosat satellites 8-11) are tailored for near-real-time monitoring of vegetation dynamics. SEVIRI's geostationary orbit enables frequent observations, capturing diurnal variations in vegetation properties and surface fluxes across Europe, Africa, and parts of the Atlantic.

This frequent monitoring is critical for applications requiring high temporal resolution, such as drought monitoring, agricultural management, and real-time ecosystem health assessments.

Fig. 2 presents the four primary vegetation variables currently generated through the MSG NRT line, available at both daily and 10-day intervals. In addition to NRT data, LSA SAF offers a CDR for FVC, LAI, and FAPAR, dating back to 2004. This consistent, 10-day interval time series supports long-term climate studies and environmental monitoring. The availability of both NRT and historical data enables comprehensive trend analysis, facilitating an understanding of vegetation changes over nearly two decades.

2.2. EUMETSAT Polar System (EPS)

Complementing the geostationary MSG data, the EPS line provides global vegetation products based on data from the AVHRR sensor aboard the polar-orbiting MetOp satellites. With a 10-day revisit frequency and near-global coverage, EPS VEGA products are particularly useful for applications requiring spatially extensive datasets, such as global climate models and land use assessments.

This suite includes FVC, LAI, and FAPAR, each updated every 10 days in near real-time. The polar-orbiting characteristics of EPS, summarized in Table 1, enable data collection over a wider range of latitudes, covering regions not visible from MSG, such as the polar areas. This capacity to monitor global vegetation with regular updates is crucial for tracking seasonal and interannual variations in vegetation and understanding their impact on global carbon and water cycles.

Recently, the LSA SAF service reprocessed the EPS MetOp-A archive (2007–2014) to generate a CDR of the EPS VEGA products, extending the dataset from 2007 onward. A typical example of time profiles is provided in Fig. 3. This dataset is expected to be released operationally by December 2024 (Camacho et al., 2024).

2.3. Future missions

The upcoming MTG and EPS-SG missions will greatly enhance LSA SAF's vegetation monitoring capabilities with higher spatial and temporal resolution, improved radiometric accuracy, and expanded spectral coverage.

Table 1. Characteristics of LAI, FVC and FAPAR products generated from MSG and EPS data.

Satellite	MSG	EPS
Coverage	MSG full disk	Global
Spatial res.	3 km × 3 km (at subsatellite point)	0.01° (~ 1 km × 1 km)
Projection	SEVIRI instrument (MSG-Disk)	EPS/AVHRR sinusoidal
Size	3712 × 3712	36000 × 18001
Format	HDF5 signed integer 16 bits: products 8 bits: quality flag	HDF5 signed integer 16 bits: products 8 bits: quality flag
Frequency	Daily and 10-daily	10-daily
Temporal coverage	2004-present	2007-present

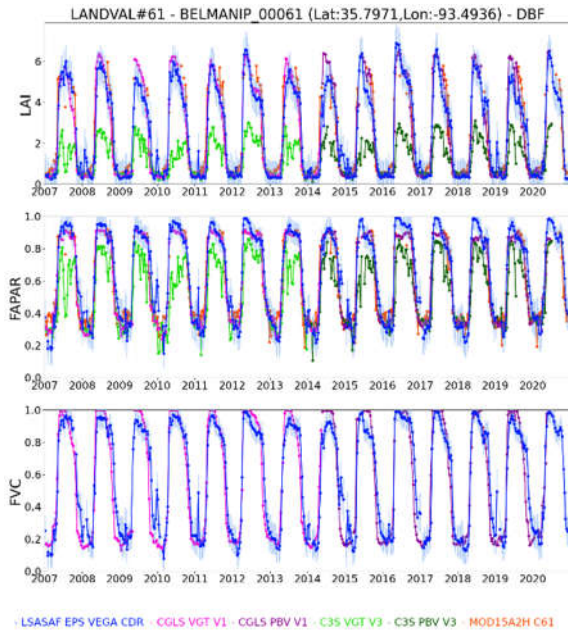


Figure 3. Example of the EPS CDR validation against other reference products.

With the Flexible Combined Imager (FCI), MTG will provide more frequent and higher-resolution observations than SEVIRI, allowing for more precise monitoring of FVC, LAI and FAPAR. This increased

detail will support near-real-time tracking of diurnal vegetation changes, making it ideal for applications requiring high-frequency data. On the other hand, the Visible and Infrared Imager (VII) on EPS-SG will support global vegetation monitoring with 10-day updates. The improved spatial resolution and spectral capabilities will be crucial for detailed observations of vegetation health and productivity across diverse regions.

These missions represent a major advancement for LSA SAF, enabling expanded and more accurate vegetation products for climate research and environmental management, detailed in Table 2. Additionally, LSA SAF is evaluating new vegetation products, such as Canopy Water Content (CWC) (García-Haro et al. 2020) and Net Ecosystem Exchange (NEE), which could offer further insights into ecosystem function and resilience (Jiménez-Guisado et al., this issue).

Table 2. Vegetation products of the upcoming EUMETSAT missions.

Satellite	MTG		EPS-SG/VII
Frequency	Daily	10-daily	10-daily
FVC	MTDFVC (LSA-414)	MTTFVC (LSA-415)	ESG_FVC (LSA-428)
LAI	MTDLAI (LSA-416)	MTTLAI (LSA-417)	ESG_LAI (LSA-429)
FAPAR	MTDFAP AR (LSA-418)	MTTFAP AR (LSA-419)	ESG_FAP AR (LSA-430)
GPP	-	MTTGPP (LSA-427)	-

3. CASE STUDIES

LSA SAF vegetation products have a wide range of practical applications, supporting environmental monitoring, climate change studies, and agricultural management (García-Haro et al. 2019). As exemplified in the LSA SAF web site (see Fig. 4), these products are used to monitor drought conditions, assess crop health, track forest productivity, and manage water resources. By providing key metrics like LAI, FVC, and FAPAR in near real-time, LSA SAF helps decision-makers and researchers analyze ecosystem dynamics and respond to environmental challenges across regions and climate zones.



Figure 4. Illustrative examples of applications available on LSA SAF's website, developed by the Slovenian Environment Agency (ARSO).

4. CONCLUSIONS

The LSA SAF remains committed to providing high-quality vegetation products that support climate and environmental applications on a global scale. Currently, LSA SAF provides operational vegetation products derived from MSG and EPS, offering consistent long-term biophysical variables essential for monitoring terrestrial ecosystems and understanding their role in Earth's climate and carbon cycles. By continuously improving its processing algorithms and preparing for the enhanced capabilities of the upcoming Meteosat Third Generation and EPS-Second Generation missions, LSA SAF is well-positioned to ensure the continuity and advancement of its services. The development of new CDRs and the potential addition of innovative products, such as CWC and NEE, reflect LSA SAF's proactive approach to meeting emerging user needs.

These advancements underscore LSA SAF's role as a critical provider of satellite-derived data on vegetation, energy balance, and carbon dynamics, supporting a wide range of climate, ecological, and resource management applications. As EUMETSAT's missions evolve, LSA SAF will continue to deliver accurate, reliable, and consistent vegetation data, thereby strengthening its contributions to global climate monitoring and environmental sustainability efforts.

5. ACKNOWLEDGMENTS

This work received funding support of LSA SAF (EUMETSAT) and ECCE EO (PID2020-118036RB-I00 funded by MCIN/AEI/ 10.13039/501100011033). Thanks are due to our ARSO colleagues for developing case studies related with the LSA SAF products.

REFERENCES

- Camacho, F., Sánchez-Zapero, J., & Martínez-Sánchez, E. (2024). Quality assessment of the LAI, FAPAR and FVC climate data records derived from the EUMETSAT Polar System data in the LSA SAF service. Conference presentation at AGU24.
- García-Haro, F. J., Campos-Taberner, M., Muñoz-Mari, J., Laparra, V., Camacho, F., Sanchez-Zapero, J., & Camps-Valls, G. (2018). Derivation of global vegetation biophysical parameters from EUMETSAT Polar System. *ISPRS journal of photogrammetry and remote sensing*, 139, 57-74.
- García-Haro, F. J., Camacho, F., Martínez, B., Campos-Taberner, M., Fuster, B., Sánchez-Zapero, J., & Gilabert, M. A. (2019). Climate data records of vegetation variables from geostationary SEVIRI/MSG data: Products, algorithms and applications. *Remote Sensing*, 11(18), 2103.
- García-Haro, F. J., Camacho, F., Martínez, B., Campos-Taberner, M., Fuster, B., Sánchez-Zapero, J., & Gilabert, M. A. (2019). Climate data records of vegetation variables from geostationary SEVIRI/MSG data: Products, algorithms and applications. *Remote Sensing*, 11(18), 2103.
- García-Haro, F. J., Campos-Taberner, M., Muñoz-Mari, J., Laparra, V., Camacho, F., Sanchez-Zapero, J. Camps-Valls, G. (2020). Derivation of global vegetation biophysical parameters from EUMETSAT Polar System, *ISPRS Journal of Photogrammetry and Remote Sensing*, 139: 57-74.
- Jiménez-Guisado, A., García-Haro, F. J., Campos-Taberner, M., Martínez, B., Sánchez-Ruiz, S., & Gilabert, M. A. (2024). Feasibility to derive new carbon fluxes products from EUMETSAT satellites in LSA SAF, 7th International Symposium on Recent Advances in Quantitative Remote Sensing (RAQRS2024), this issue.
- Martínez, B., Gilabert, M. A., Sánchez-Ruiz, S., Campos-Taberner, M., García-Haro, F. J., Brümmer, C., ... & Tagesson, T. (2020). Evaluation of the LSA-SAF gross primary production product derived from SEVIRI/MSG data (MGPP). *ISPRS Journal of Photogrammetry and Remote Sensing*, 159, 220-236.
- Trigo, I. F., Dacamara, C. C., Viterbo, P., Roujean, J. L., Olesen, F., Barroso, C., ... & Arboleda, A. (2011). The satellite application facility for land surface analysis. *International Journal of Remote Sensing*, 32(10), 2725-2744.

Developing a new algorithm for the generation of SEVIRI/MSG vegetation products

A. Jiménez-Guisado^{1*}, F.J. García-Haro¹, M. Campos-Taberner¹, B. Martínez¹, S. Sánchez-Ruiz¹, M.A. Gilabert¹, J. Sánchez-Zapero², F. Camacho², E. Martínez-Sánchez²

¹ *Environmental Remote Sensing Group (UV-ERS), Departament de Física de la Terra i Termodinàmica, Universitat de València, 46100 Burjassot, Valencia, Spain.*

² *Earth Observation Laboratory (EOLAB), 46980 Paterna, Valencia, Spain.*

* adrian.jimenez@uv.es

ABSTRACT – *The EUMETSAT Satellite Application Facility on Land Surface Analysis (LSA SAF) provides near-real-time and offline products, along with user support for a broad range of land surface variables. Currently, LSA SAF operates two processing lines to generate vegetation products from EUMETSAT satellite data. First, products such as FVC, LAI, FAPAR, and GPP are derived from the geostationary SEVIRI (Spinning Enhanced Visible and Infrared Imager) aboard MSG (Meteosat Second Generation) satellites 1-4 (Meteosat 8-11), with data available from 2004 onwards. These products are provided at two temporal resolutions—daily and 10-day—across the Meteosat disk, covering Europe, Africa, the Middle East, and parts of South America. Second, FVC, LAI, and FAPAR are generated globally from data obtained by the AVHRR sensor aboard the Meteorological Operational Satellites (currently MetOp A and B) of the EUMETSAT Polar System (EPS). Unlike the SEVIRI/MSG vegetation product processing, which relies on stochastic spectral mixture and statistical methods, the EPS algorithm employs a hybrid approach, combining the generalization capabilities of physical radiative transfer models with the precision and computational efficiency of machine learning methods. A key priority for LSA SAF is ensuring consistency across products from different missions, both within and between them. Although both the MSG and EPS algorithms use similar inputs (i.e., atmospherically corrected, cloud-cleared k0 BRDF products in three channels: red, NIR, and MIR), which are part of the MSG surface albedo (MDAL) product, discrepancies arise due to differences in spatial and temporal resolutions, processing workflows, and other factors. Additionally, while a Climate Data Record (CDR) for MSG products has been available since 2004, a minor discontinuity occurred in 2022 due to an MDAL algorithm upgrade, which incorporated aerosol correction and other improvements. This work aims to address these issues by developing a new algorithm for generating MSG vegetation products. This new algorithm is based on an upgraded and improved version of the current EPS algorithm. An accuracy assessment is also performed, benchmarking the new algorithm against current MSG products and other relevant satellite-derived vegetation products. The goal is to produce continuous and homogeneous time series of LSA SAF vegetation parameters (FVC, LAI, FAPAR) from SEVIRI/MSG, suitable for climate and environmental applications, while ensuring a smooth transition from SEVIRI/MSG to the upcoming FCI/MTG sensors.*

Keywords - *LSA SAF, SEVIRI/MSG, vegetation products, hybrid approach*

1. INTRODUCTION

The Satellite Application Facility for Land Surface Analysis (LSA SAF) focuses on developing and retrieving land surface variables using data from the European Organization for the Exploitation of Meteorological Satellites (EUMETSAT) (Trigo et al., 2011). It aims to improve the understanding of terrestrial processes and land-atmosphere interactions, providing near-real-time and offline data for ecosystem characterization and energy balance assessments. LSA SAF's products, including essential biophysical variables (Bojinski et al., 2014) like Leaf Area Index (LAI), Fractional Vegetation Cover (FVC), and the Fraction of Absorbed Photosynthetically Active Radiation (FAPAR)—known collectively as the

VEGA suite. All operational LSA SAF products are freely disseminated to users through the LSA SAF website (<http://lsa-saf.eumetsat.int>).

The operational VEGA products are derived from two sources: the Spinning Enhanced Visible and InfraRed Imager (SEVIRI) on geostationary Meteosat satellites, and the Advanced Very High Resolution Radiometer (AVHRR) on EUMETSAT's polar orbiting satellites (MetOp-A, B, and C). Each data source employs distinct algorithms for estimating biophysical variables. For example, LAI and FVC on SEVIRI are derived through different methods (García-Haro et al., 2019), while the AVHRR-based EPS algorithm uses a hybrid approach combining radiative transfer models with machine learning for joint retrieval (García-Haro et al., 2018).

An advantage of hybrid retrieval methods is their global applicability across diverse land cover types, with Gaussian Process Regression (GPR) often outperforming other methods. However, GPR's high computational cost on large datasets presents challenges. To address this, sparse GPR methods have been introduced, using a reduced set of representative points to make the approach more efficient.

This work proposes a unified retrieval algorithm for LAI, FVC, and FAPAR, improving the EPS method by refining the training data and introducing Sparse Multi-output GPR (SMGPR) for joint retrieval. The new method is tested on SEVIRI data to produce 10-day VEGA products, with performance assessed against current LSA SAF products and other reference datasets. The structure of the paper includes descriptions of the proposed algorithm, results, product comparisons, and a quality assessment.

2. MATERIAL AND METHODS

2.1. Proposed algorithm

The proposed SMGPR strategy is a two-step hybrid algorithm: (1) it simulates a database of surface reflectance for a wide range of conditions using the PROSAIL RTM; (2) it employs an advanced non-parametric machine learning regression method to learn the relationship between the simulated reflectances and the corresponding canopy variables. Fig. 1 illustrates the workflow of the proposed methodology, contrasting it with the current SEVIRI/MSG and AVHRR/EPS approaches.

The training database is built with reflectance simulations using PROSAIL, which combines the PROSPECT and SAIL models (Jacquemoud et al., 2009). PROSPECT handles leaf optical properties based on biochemical composition and structure, while SAIL models canopy reflectance, factoring in structural and environmental parameters. The spectral responses for SEVIRI channels are used alongside the selection of bare areas that reflect the variability across the MSG disk, making this approach similar to EPS/MetOp (García-Haro et al., 2018) but with enhancements for better simulation realism.

The enhancements involve using the TRY plant trait database (Kattge et al., 2011) to more accurately represent the actual distribution of leaf traits, as well as the inclusion of the Normalized Difference Infrared Index (NDII) as a predictor variable, which improves the estimation of biophysical variables by reducing saturation effects (García-Haro et al., 2020).

To achieve accurate canopy variable predictions, the inversion algorithm has been based on a novel Sparse Multi-output Gaussian Process Regression (SMGPR).

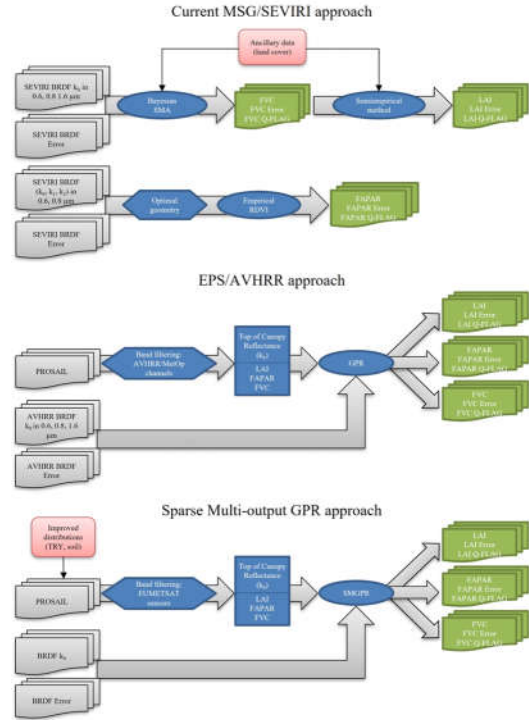


Figure 1. Flowchart of current operational MSG and EPS algorithms, as well as the proposed approach.

Standard GPR provides predictions with quantified uncertainties based on Gaussian distributions (Williams and Rasmussen, 2006; Snelson, 2008). These predictions depend on a mean function (typically set to zero) and a covariance function, both governed by hyperparameters optimized during training. However, traditional GPR models are computationally intensive when trained on large datasets. Sparse Gaussian Processes (SGPs) address this by using a subset of “inducing points” to approximate the full covariance matrix, greatly reducing computational costs while preserving prediction accuracy. On the other hand, sparse multi-output GPR extends the sparse version to model multiple outputs, introducing a single covariance function shared across outputs, enabling joint optimization of hyperparameters. This formulation has shown to improve the model's accuracy and allows to handle large datasets. The overall prediction error combines the model-derived standard deviation with data input uncertainty to yield robust confidence intervals.

2.2. Products and datasets

The LSA SAF vegetation products for both MSG and EPS satellites have been rigorously validated

against both field data and other satellite datasets, following the CEOS Land Product Validation (LPV) protocols. Currently, LSA SAF is developing Climate Data Records (CDRs) spanning the entire MSG and EPS operational periods. These CDRs are generated by reprocessing near-real-time (NRT) operational data using consistent algorithms and inputs.

The VEGA products retain the temporal and spatial characteristics of their input surface albedo data updated on a 10-day cycle. Recently, an enhanced surface albedo product, ALv2, was introduced with improved atmospheric corrections for aerosol optical depth (AOD), leveraging data from the European Centre for Medium-Range Weather Forecasts (ECMWF). Although a new CDR for ALv2 was generated by reprocessing the SEVIRI archive, the MSG VEGA near-real-time products continue to use ALv1 to maintain consistency in the VEGA dataset (Carrer et al., 2018; Juncu et al., 2022).

For comparison between the LSA SAF products, the 10-day MSG products on the 15th of each month (derived using a 31-day window) were assumed to correspond to the EPS products on the 25th of the month (derived using the previous 20 days). Quality control layers were applied to exclude low-quality data. The intercomparison is based on the widely adopted 720-site land validation (LANDVAL1.1) global sampling (Sánchez-Zapero et al., 2023), which includes homogeneous sites representative of global biomes and environmental conditions, designed for the indirect validation of satellite products.

3. RESULTS & DISCUSSION

To assess the quality of the proposed SMGPR approach, the trained model has been applied to actual observations of MSG isotropic surface reflectance (k_0) over an 18-year period (2004–2021). The full record of the latest version (v2) of ten-day albedo was used as input to produce time series of VEGA products at 10-day intervals. Examples of the derived VEGA MSG-SMGPR are shown in Fig. 2 for 15th June 2018. The products show realistic values over the whole MSG disk, with no spatial artefacts and excellent completeness. The figure also display uncertainty estimates associated with the generated products, which provides valuable information required in a number of applications.

The differences between LAI, FVC, and FAPAR maps derived from the proposed methodology, MSG-SMGPR, and the two existing LSA SAF vegetation products (MSG and EPS) have been evaluated. An example of difference maps corresponding to 15th June 2018 is also presented in Fig. 3.

The results have shown that MSG-SMGPR shows strong alignment with MSG for both LAI and FVC, with differences generally under 0.5 for LAI and

0.1 for FVC. The discrepancies for EPS products are slightly smaller, with all three products exhibiting a similar pattern of variation, indicating consistency. However, MSG-SMGPR systematically overestimates values along the edges of the MSG disk due to differences in input data.

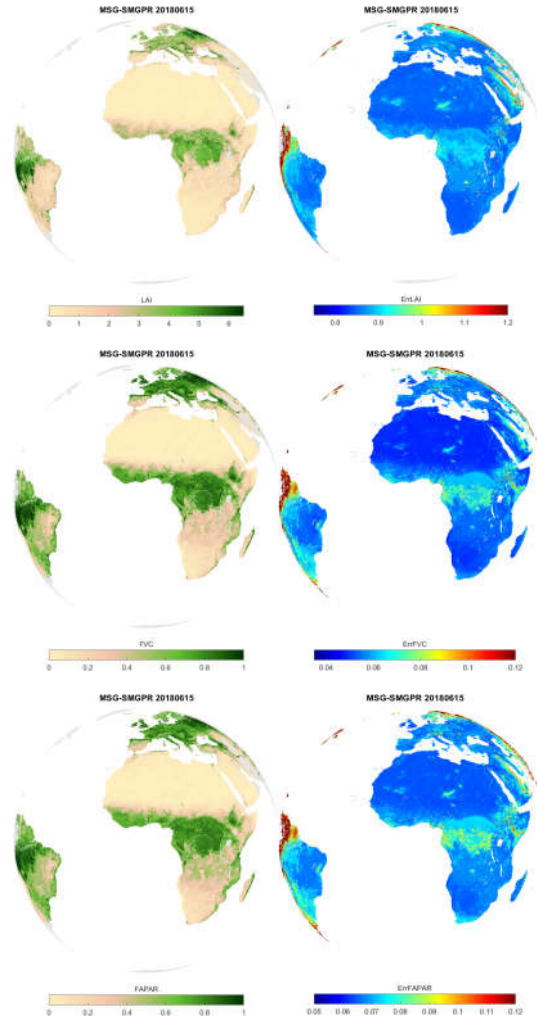


Fig. 2. Left: LAI, FVC and FAPAR produced from SMGPR on 15th June 2018. Right: corresponding uncertainty estimates.

A more comprehensive assessment has been also performed, covering all seasons and the entire overlapping period across the LANDVAL network of sites (see Fig. 4). The results show that the MSG-SMGPR prototype successfully reduces the discrepancies between the current LSA SAF vegetation products, and the uncertainty requirements are now met for the majority of observations.

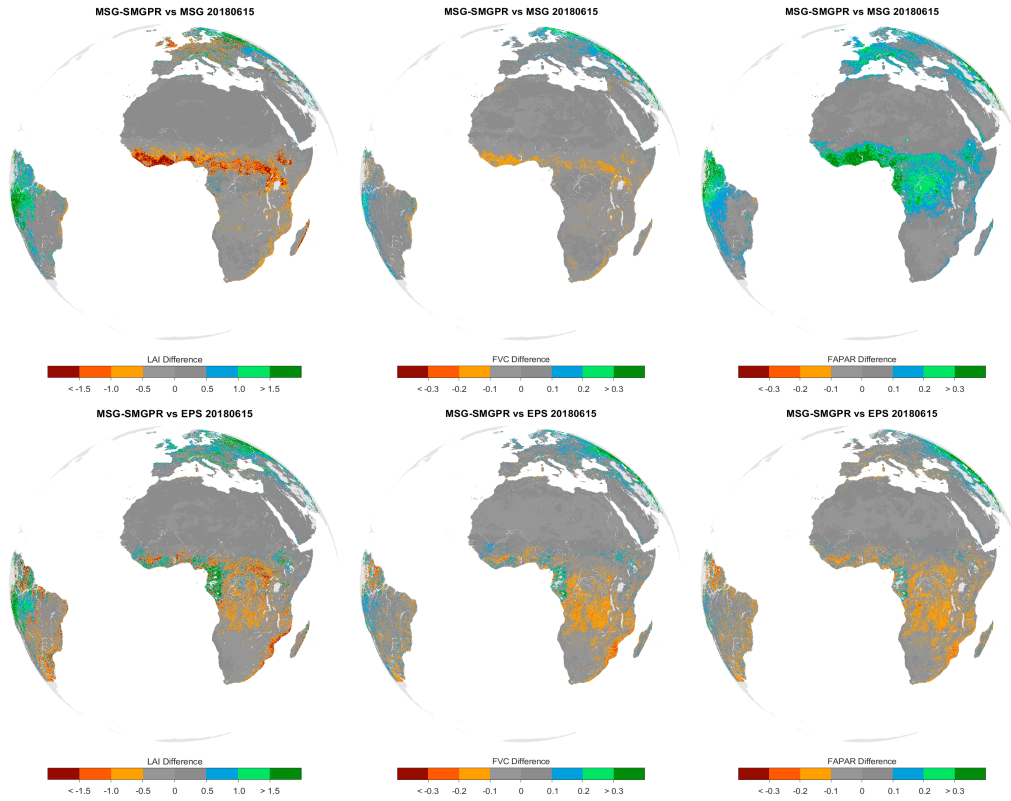


Figure 3. Maps of differences between the proposed algorithm versus MSG (top) and EPS (bottom).

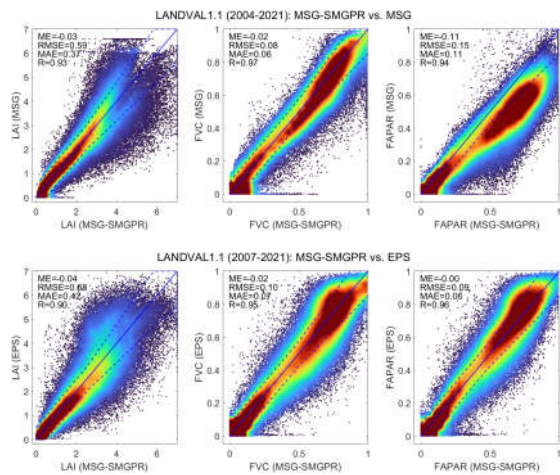


Figure 4. Scatter plots versus MSG (top) and EPS (bottom) over all LANDVAL 2.1 sites within the MSG disk.

4. CONCLUSIONS

The development of a new algorithm, derived from the enhanced EPS approach, effectively harmonizes SEVIRI/MSG vegetation products, significantly reducing existing inconsistencies. Unlike the current MSG FAPAR, the new version achieves high consistency with EPS data and demonstrates strong spatial and temporal continuity. This advancement will enable the production of continuous and homogeneous time series of LSA SAF vegetation parameters from SEVIRI/MSG, making these products highly suitable for climate and environmental applications. Additionally, this work supports a seamless transition of LSA SAF services from SEVIRI/MSG to the future FCI/MTG, ensuring continuity and reliability for users and applications.

5. ACKNOWLEDGMENTS

This work received funding support of LSA SAF (EUMETSAT) and ECCE EO (PID2020-118036RB-I00 funded by MCIN/AEI/ 10.13039/501100011033).

REFERENCES

- Bojinski, S., Verstraete, M., Peterson, T. C., Richter, C., Simmons, A., & Zemp, M. (2014). The concept of essential climate variables in support of climate research, applications, and policy. *Bulletin of the American Meteorological Society*, 95(9), 1431-1443.
- Carrer, D., Moparthy, S., Lellouch, G., Ceamanos, X., Pinault, F., Freitas, S. C., & Trigo, I. F. (2018). Land surface albedo derived on a ten daily basis from Meteosat Second Generation Observations: The NRT and climate data record collections from the EUMETSAT LSA SAF. *Remote Sensing*, 10(8), 1262.
- García-Haro, F. J., Campos-Taberner, M., Muñoz-Mari, J., Laparra, V., Camacho, F., Sanchez-Zapero, J., & Camps-Valls, G. (2018). Derivation of global vegetation biophysical parameters from EUMETSAT Polar System. *ISPRS journal of photogrammetry and remote sensing*, 139, 57-74.
- García-Haro, F. J., Camacho, F., Martínez, B., Campos-Taberner, M., Fuster, B., Sánchez-Zapero, J., & Gilabert, M. A. (2019). Climate data records of vegetation variables from geostationary SEVIRI/MSG data: Products, algorithms and applications. *Remote Sensing*, 11(18), 2103.
- García-Haro, F. J., Campos-Taberner, M., Moreno, Á., Tagesson, H. T., Camacho, F., Martínez, B., ... & Gilabert, M. A. (2020). A global canopy water content product from AVHRR/Metop. *ISPRS Journal of Photogrammetry and Remote Sensing*, 162, 77-93.
- Jacquemoud, S., Verhoef, W., Baret, F., Bacour, C., Zarco-Tejada, P. J., Asner, G. P., ... & Ustin, S. L. (2009). PROSPECT+ SAIL models: A review of use for vegetation characterization. *Remote sensing of environment*, 113, S56-S66.
- Juncu, D., Ceamanos, X., Trigo, I. F., Gomes, S., & Freitas, S. C. (2022). Upgrade of LSA-SAF Meteosat Second Generation daily surface albedo (MDAL) retrieval algorithm incorporating aerosol correction and other improvements. *Geoscientific Instrumentation, Methods and Data Systems*, 11(2), 389-412.
- Kattge, J., Diaz, S., Lavorel, S., Prentice, I. C., Leadley, P., Bönsch, G., ... & Wirth, C. (2011). TRY—a global database of plant traits. *Global change biology*, 17(9), 2905-2935.
- Rasmussen, C. E., & Williams, C. K. (2006). *Gaussian processes for machine learning*. Cambridge, MA: MIT press.
- Sánchez-Zapero, J., Martínez-Sánchez, E., Camacho, F., Wang, Z., Carrer, D., Schaaf, C., ... & Cosh, M. (2023). Surface ALbedo VALidation Platform: Towards CEOS LPV Validation Stage 4—Application to Three Global Albedo Climate Data Records. *Remote Sensing*, 15(4), 1081.
- Snelson, E. L. (2008). *Flexible and efficient Gaussian process models for machine learning*. University of London, University College London (United Kingdom).
- Trigo, I. F., Dacamara, C. C., Viterbo, P., Roujean, J. L., Olesen, F., Barroso, C., ... & Arboleda, A. (2011). The satellite application facility for land surface analysis. *International Journal of Remote Sensing*, 32(10), 2725-2744.

The SpaFLEX-IMP project: Spanish FLEX-S3 Mission Calibration and Validation Plan Implementation

R. Díaz-Delgado¹, P. J. Gómez-Giráldez¹, M. Jiménez², M^a P. Cendrero-Mateo³, S. Van Wittenberghe³, J. J. Peón², A. Moncholí-Estornell³, J. Delegido³, J. F. Moreno³

¹Remote Sensing & GIS Lab. Doñana Biological Station (LAST-EBD) CSIC, C/ Americo Vespucio 26. 41092, Sevilla, Spain.

²National Institute of Aerospace Technology (INTA), Crta. de Ajalvir km 4, Torrejón de Ardoz, 28850, Madrid, Spain.

³Laboratory for Earth Observation, Image Processing Laboratory, University of Valencia, C/ Catedrático Agustín Escardino, n° 9, 46980, Paterna, Spain.

sobrin@uv.es; susana.garcia-monteiro@uv.es; yves.julien@uv.es

ABSTRACT – The European Space Agency's FLuorescence EXplorer-Sentinel 3 (ESA FLEX-S3) mission, scheduled for launch in 2026, aims to remotely detect vegetation fluorescence (SIF) of vegetation at a resolution of 300x300 meters. SIF, emitted by chlorophyll pigments, serves as an accurate proxy for plant photosynthesis and stress indicators. Cal/Val activities are essential to refine FLEX-S3 products before the resulting data are integrated into vegetation models. While ESA manages Level 1 products, Member States, such as Spain, oversee the Cal/Val plans for Level 2 products, thus promoting interoperability. The SpaFLEXImp initiative aims to implement a FLEX Cal/Val plan, standardizing protocols, and establishing a coordinated network of sites. Led by the National Institute of Aerospace Technology (INTA), the project involves the University of Valencia and the Doñana Biological Station-CSIC. With a long experience in in situ, airborne, and spaceborne measurements, the teams will conduct specific Cal/Val campaigns in 3 sites, making Spain a European and international reference for terrestrial Cal/Val activities. Spain's stable weather conditions and diversity of land uses make it an ideal location for Cal/Val activities, but it has not yet been included in the international Cal/Val test site network. The SpaFLEXImp project therefore aims to develop and implement a detailed Cal/Val plan that includes pre-launch and post-launch activities. Pre-launch activities include data acquisition and processing to refine models and algorithms, while post-launch activities verify and improve algorithm performance and product accuracy. The importance of the project is to contribute to the success of the FLEX-S3 mission, to standardize Cal/Val protocols, and to establish Spain as a leader in European and international land Cal/Val activities. With its experienced consortium and well-defined plan, SpaFLEXImp is poised to make significant contributions to the field of Earth observation and vegetation monitoring

Keywords - FLEX-S3, sun-induced fluorescence, Cal/Val sites, Cal/Val protocol, uncertainty, error propagation

1. INTRODUCTION

The European Space Agency's FLuorescence EXplorer-Sentinel 3 (ESA FLEX-S3) mission aims to remotely detect and quantify the sun-induced fluorescence (SIF) of vegetation at a resolution of 300x300 meters. ESA's FLEX mission will orbit in tandem with Sentinel-3 and will bring on board the FLORIS sensor. FLORIS is a high-resolution imaging spectrometer acquiring data in the 500–780 nm spectral range, with a sampling of 0.1 nm in the oxygen bands (759–769 nm and 686–697 nm) and 0.5–2.0 nm in the red edge, chlorophyll absorption and PRI (Photochemical Reflectance Index) bands (figure 1). FLEX is scheduled for launch in 2026.

SIF is emitted by chlorophyll pigments and it serves as a proxy for plant photosynthesis and stress indicators (Moreno, 2021; Frankenberg and Berry,

2018; Mohammed et al., 2019). Calibration and validation (Cal/Val) activities are paramount to refine FLEX-S3 products to be used in global vegetation models. ESA headquarters manages FLEX Level 1 products, and ESA Member States, such as Spain, are encouraged to develop Cal/Val strategies for Level 2 products.

The SpaFLEXImp initiative, led by the National Institute of Aerospace Technology (INTA), is coordinating the Spanish Cal/Val strategy. INTA is a leading research centre in aerospace equipped with a C295MW aircraft with adaptable pods to bring the Headwall Chlorophyll-Fluorescence Imager (CFL). The Earth Observation Laboratory (LEO-UV) of the University of Valencia and the GIS and Remote Sensing Laboratory (LAST-EBD) of the Doñana Biological Station also participate in the initiative.

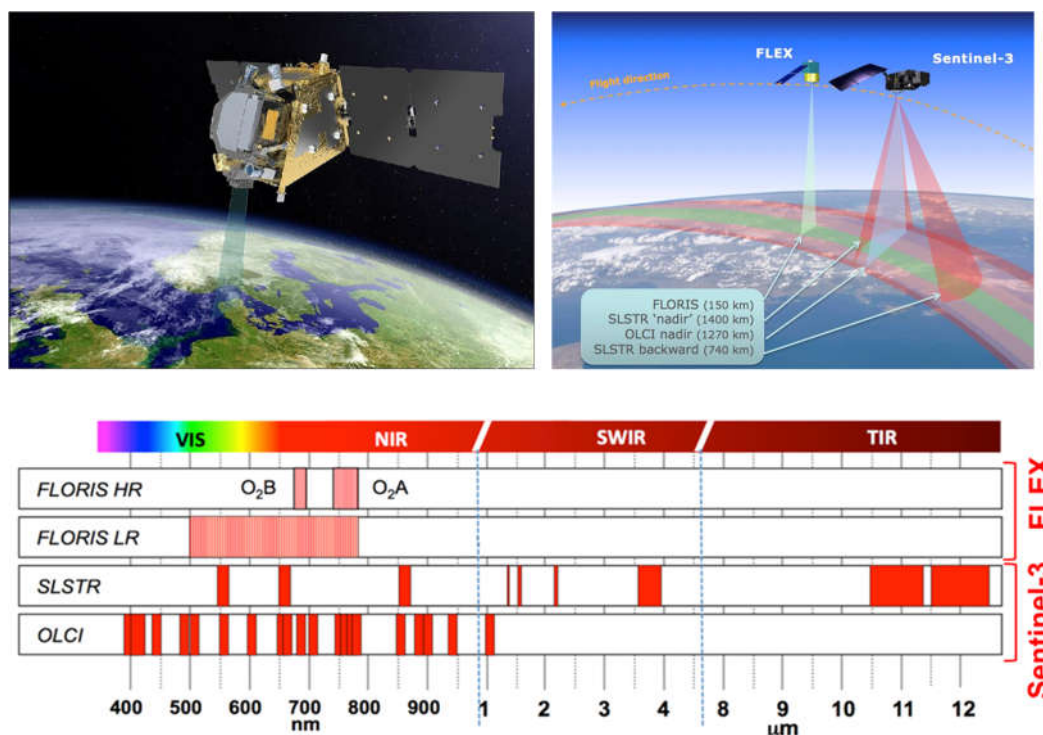


Figure 1. The FLEX satellite and FLORIS spectral bands compared to Sentinel-3 sensors and mission design in tandem (source: EOPortal).

SIF signal is very low, ca. 10 orders of magnitude less than vegetation radiance, what makes challenging decoupling the signal from noise. Spectroradiometric measurements rely on the use of absorption features in the atmosphere, such as the solar Fraunhofer lines or the Earth's O₂ absorption bands. FLEX-S3 mission requirements have been set to uncertainties lower than 30% based on calibration and validation (Cal/Val) protocols. Reliable estimates of photosynthetic efficiency require uncertainties lower than 10% for fluorescence emission, solar irradiance, and 1% for apparent reflectance. Calibration involves comparing FLEX-S3 products to ground-truth measurements, taking into account instrument performance, retrieval algorithm errors, and site-specific variability (ESA 2018).

Spain offers larger areas with very stable weather conditions and a high diversity of land uses for Cal/Val activities. However, Spain is not included in any of the different international Cal/Val initiatives. The SpaFLEXImp research project aims to develop and implement a detailed Cal/Val plan which includes pre-launch and post-launch activities. Pre-launch activities include data acquisition and data processing to refine models and algorithms. On the other hand, post-launch activities will verify and improve algorithm performance and products accuracy.

The project seeks to contribute to the success of the FLEX-S3 mission, by enhancing FLEX products and providing standardized Cal/Val protocols. The project aims to position Spain as a leader in European and international land Cal/Val activities. SpaFLEXImp experienced consortium is compromised to make significant contributions in Earth Observation and vegetation monitoring.

2. MATERIAL AND METHODS

The final objective of SpaFLEXImp is not only to define the Spanish Cal/Val plan for the FLEX mission, but also setting the basis to standardize Cal/Val protocols and establish a coordinated network of Cal/Val sites across the Spanish territory, making Spain a reference country for land Cal/Val activities at European and international level.

The magnitude of this project demands the coordination of an interdisciplinary team, integrating experts in ground spectral-measurements, instrument characterization, Cal/Val strategies, Level-2 products retrieval and Cal/Val test-sites managers. The consortium is coordinated by INTA's Remote Sensing Systems Area (RSSA-INTA). The Laboratory of Earth Observation of the University of Valencia (LEO-UV) has participated and led preparatory research projects for the FLEX mission. LEO-UV has been the driving

force of the candidate mission in terms of instrument design, data process, and FLEX Level 2 final products development. Finally, the Laboratory of GIS and Remote Sensing of Doñana Biological Station (LAST-EBD) from CSIC, provides its expertise on the validation of EO products based on the in-situ instrumentation and measurements deployed by the Research Infrastructure ICTS-Doñana. In addition, the Instituto Técnico Agronómico Provincial de Albacete (ITAP) and the Centro de Investigación y Tecnología Agroalimentaria de Aragón (CITA), also participate in the project providing the ‘Las Tiesas’ agricultural field and ‘Sarrión’ forest Cal/Val test-sites.

This overarching objective will be built upon the following five specific objectives detailed in figure 2, which include the contribution of each subproject to their achievement:

- O1: To test and implement an in situ Cal/Val protocol for FLEX-S3 Products. This objective is led by SP1 with the participation of SP2 and SP3 to implement bottom-up calibration and validation protocols for the pre and post-launch of FLEX-S3 mission.
- O2: To consolidate the Spanish network of instrumented test-sites for FLEX-S3 mission Cal/Val activities. This objective is led by SP1 with the participation of SP2. Implementation of autonomous and ad-hoc Cal/Val campaigns for multi-sensor and multi-scale SIF and reflectance measurements over different ecosystems with different heterogeneity values and with the aim to include more Cal/Val test sites in the future.

- O3: To foster fluorescence and reflectance fiducial measurements *via* airborne and proximal sensing. This objective is led by SP3 with the participation of SP2 and SP1, to provide accurate SIF and reflectance measurements, and to instrument the Cal/Val test sites with infrastructures funded by MICIN.
- O4: To set up full end-to-end uncertainty budgets for fluorescence and reflectance. This objective is led by SP1 with the participation of SP2 and SP3 aiming to characterize uncertainty and analyse error propagation in the proximal sensing of SIF and reflectance, indoor and outdoor, following the Guide to the Expression of Uncertainty in Measurement (GUM) methodology ().
- O5: To gain knowledge about the relationships between fluorescence, photosynthesis and GPP. This objective is led by SP2, with the participation of SP3, to finely tune the Level-2 algorithms *via* experimental campaigns.

2.1. Cal/Val Strategy

The Cal/Val strategy is based on the recommendations of CEOS (Morissette et al. 2006) and follows a "bottom-up" strategy where SIF top-of-canopy (TOC) measurements are upscaled to the FLEX-S3 medium resolution scale using aerial or satellite imagery (Mohammed et al., 2016). Based on previous research projects and on the FLEX Mission Requirements Document (ESA, 2018), SpaFLEXImp will follow a procedural strategy to characterize:

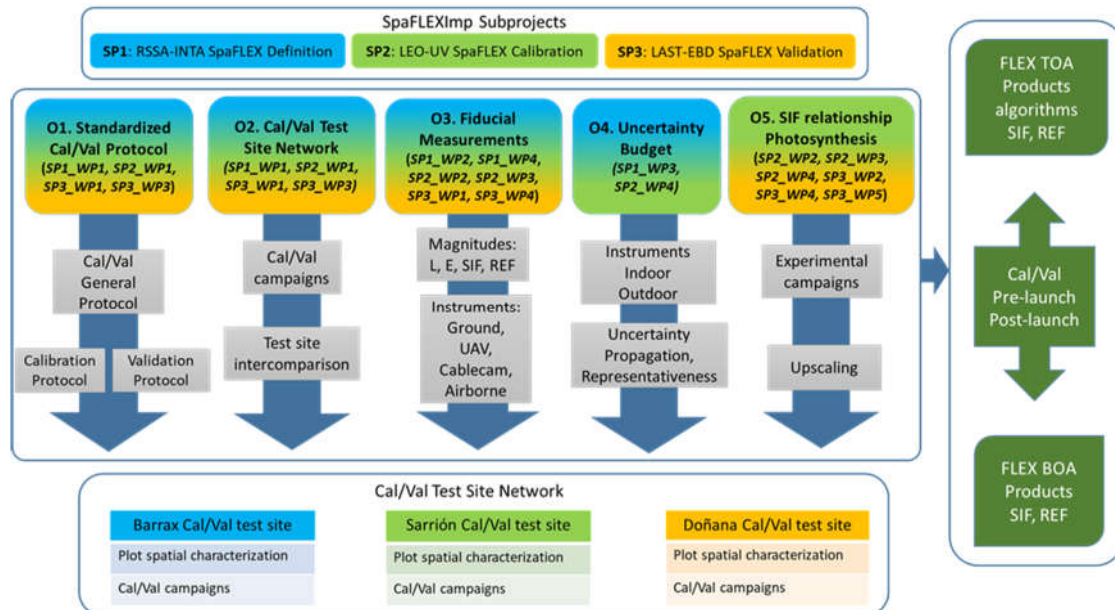


Figure 2. SpaFLEXImp subprojects (SP) and main objectives (O).

- 1) Instrument Performance and Calibration Assessment: a detailed instrument performance and calibration protocol will be developed to characterize the uncertainty of the incoming radiance (E) and reflected radiance (L). For each ground and airborne instrument, a comprehensive radiometric, spectral, non-linearity, and temperature uncertainty characterization will be performed at INTA facilities.
- 2) Error propagation in the retrieval algorithm: we will retrieve the SIF using the SpecFit method (Cogliati et al., 2015). In order to propagate the E and L uncertainties in the SpecFit retrieval algorithm, we will first distinguish between systematic and random errors, taking into account the correlation between the input parameters as well as the covariance between the parameters and the measurement error. Later, we will develop a hybrid approach where both Monte Carlo (Peón et al., 2024) and derivative approaches are implemented.
- 3) Spatial/temporal variability of Cal/Val sites: we propose three different Cal/Val sites covering a gradient of heterogeneity ranging from low (Barrax: an agricultural area), medium (Sarrión: forest area) to high (Doñana: forests and shrublands) heterogeneity (figure 3). Each Cal/Val site is already well characterized (e.g. detailed soil type maps, meteorological conditions, plant species and cover, etc.). UAVs and airborne sensors will be used to characterize the heterogeneity of the Cal/Val site (~ actual vegetation) at high spatial resolution. For each Cal/Val site, ground sampling strategies will be defined based on the spatial heterogeneity analysis (e.g., number of sampling points and sampling strategy). Regarding the ground sampling strategy at elementary sampling units (ESU), a multi-sensor and multi-scale approach will be used, where we will combine leaf and canopy top measurements to obtain an integrated value of reflectance and SIF over a 300x300 FLEX-S3 pixel area (Moncholi-Estornell et al., 2023).

Accordingly, uncertainty characterization of the final apparent reflectance and SIF is defined as the summation in quadrature of independent uncertainty sources. The final uncertainty is reported as the expanded uncertainty at the 95% confidence interval:

$$U_{final} = \sqrt{(u_{instrument})^2 + (u_{representativity})^2 + (u_{retrieval})^2}$$

where $u_{instrument}$ includes the instrument characterization (e.g., noise, radiometric, nonlinearity, spectral calibration); $u_{representativity}$ captures the Cal/Val spatial heterogeneity; and $u_{retrieval}$ includes the error introduced by the model used to retrieve SIF (e.g., SpecFit).

The strategies tested in this study aim to set the roadmap for the Cal/Val protocols of the future FLEX-S3 mission. A significant added value of the SpaFLEXImp strategy is that it can be applied to other high and medium spatial resolution land optical Earth observation missions (e.g. EnMAP, CHIME, Sentinel-2, New Ingenio).

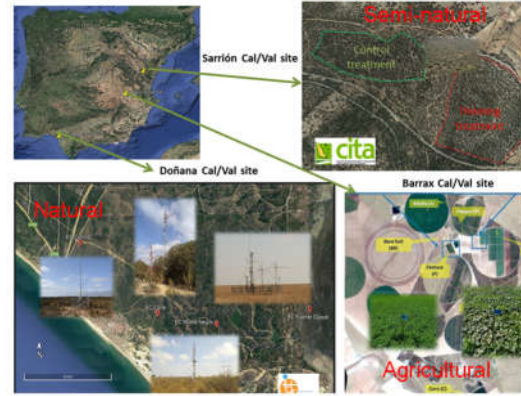


Figure 3. Location of SpaFLEX Cal/Val test sites

3. RESULTS & DISCUSSION

3.1. Characterization of spatial heterogeneity

A preliminary analysis of spatial heterogeneity for the Sarrión and Manzanera Cal/Val sites was performed using Sentinel-2 MSI L2A spring images. FaPAR, Cab and FCOVER were calculated using the algorithms available in SNAP ESA software. Spatial autocorrelation indicated a higher spatial variability for Cab images (Moran Index = 0.11) and spatial regression among them was higher than 0.83. Based on the low variance of these variables we stratified the area in two regions and calculated the number of ESU according to:

$$n = \left(\frac{Z \cdot \sigma}{E} \right)^2$$

where n is the number of ESU, Z is the confidence value (e.g. for 95% confidence $Z\alpha=1.96$), σ is the Standard Deviation of the variable and E is the acceptable proportion of sampling error (0.1 for SIF and 0.01 for reflectance).

As a result a total number of 4 ESU were defined per plot. Square plots are 300x300 m size and are centred on Eddy Covariance towers. Two ESU were randomly located in every stratum (figure 4).

3.2. Assessing heterogeneity within ESU

Once defined the location and number of ESU per plot we designed an exhaustive sampling campaign in order to characterize spatial variability within ESU (figure 5).

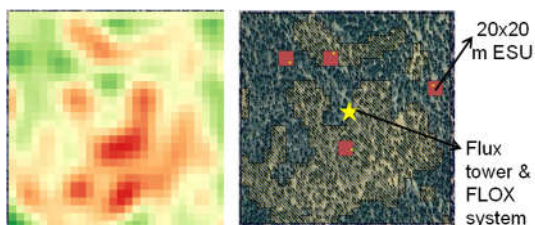


Figure 4. Spatial interpolation of Cab for Sarrión Cal/Val site and location of ESU (red squares).

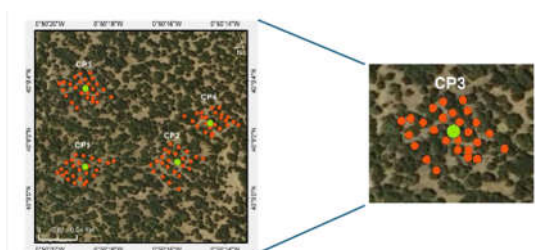


Figure 5. Proposed distribution of sampling points within ESU for the Manzanera Cal/Val site.

Data collected during the field campaign using the different field and airborne sensors will be used to define the minimum number of sampling points within ESU as well as to test different upscaling procedures to achieve FLEX pixel requested standard errors.

4. CONCLUSIONS

SpaFLEXImp scientific and technological results will have a relevant impact on the remote sensing user and scientific communities. It will not only provide new ways of exploiting FLEX products but other Earth Observation missions, improving products accuracy and quality over missions' lifetime. Standardization of Cal/Val methods and implementation of metrological practices, calculating uncertainty budget and regular inter-comparisons will certainly improve all processing steps involved in FLEX-S3 product generation.

The Spanish Cal/Val test site network will be consolidated and designed considering site spatial distribution and variability, the available infrastructure at every site and analytical capabilities. SpaFLEX network will provide a gradient of environmental factors across the Cal/Val sites covering vegetation heterogeneity (e.g., SIF emissions, biochemical and structural characteristics) and biophysical conditions (e.g., atmospheric composition, irradiance, temperature, and water availability). Our project will carry out a thorough analysis of SIF retrieval performance, including analysis of atmospheric effects on image correction and unraveling the trade-offs between SIF and ecosystem processes (e.g. Gross Primary Productivity –GPP, Evapotranspiration –ET, drought, etc.).

This interdisciplinary collaboration will join forces and exploit synergies to set up the basis for standardization of Cal/Val protocols for Land Vegetation products. ESA is already funding research projects to develop FLEX-S3 Level 1 calibration procedures. However, Level 2 products (Top-Of-Canopy reflectance and vegetation fluorescence) and Levels 3 and 4 are still lacking standardized Cal/Val strategies. SpaFLEXImp is stepping up to take the lead in these FLEX-S3 Cal/Val activities in Spain to collaborate with ESA. In this sense, our Cal/Val implementation will be very valuable for the validation of other ESA current and future satellite land missions such as EnMAP, Sentinel-2 or CHIME. We aim to address the need for inter-sensor interoperability in the optical domain of other Cal/Val initiatives such as CEOS WGCV and Copernicus Ground-Based Observations for Validation (GBOV).

The project is also expected to contribute to the improvement of data quality provided by EO products in natural vegetation areas. These areas usually show heterogeneous land covers and have rarely been used as validation sites. The use of these highly instrumented natural areas, such as the ICTS-Doñana, will certainly contribute to a better understanding of vegetation stress and condition in relation to extreme events and global warming. Moreover, the advanced FLEX-S3 derived products, such as GPP or plant phenology, will reveal the essential role of natural ecosystems in the carbon and water cycles, enhancing the knowledge of these relevant ecosystem services.

Finally, the current proposal matches the services portfolio of eLTER Research Infrastructure, offering its network of 500 eLTER sites across Europe to become a future Cal/Val network for the Copernicus In Situ Component. SpaFlexImp is a pioneering pilot study, and in particular for the validation strategy contributing to develop standardized protocols and requirements for the selection and use of eLTER sites and platforms as Cal/Val test sites. eLTER provides harmonized and standardized common essential ecosystem variables (Standard Observations) across Europe, including GPP and phenology, where results from SpaFLEXImp will provide a basis for the whole network.

5. ACKNOWLEDGEMENTS

The SpaFlexImp Research Coordination Project (PID2022-137022OB-C31, C-32 and C-33) is funded by the Ministerio de Ciencia, Innovación y Universidades under the Plan Estatal de Investigación Científica, Técnica y de Innovación and the Proyectos de Colaboración Internacional (PCI2023-145955-2, PCI2023-146023-2 and PCI2023-145988-2).

REFERENCES

- Moreno, J.F. 2021. Advances in the Retrieval and Interpretation of Solar-Induced Vegetation Chlorophyll Fluorescence Using Passive Remote Sensing Techniques, IEEE International Geoscience and Remote Sensing Symposium IGARSS, Brussels, Belgium, 2021, pp. 1915-1918. Doi: 10.1109/IGARSS47720.2021.9554239.
- Frankenberg, C., Berry, J. 2018. 3-10 Solar induced chlorophyll fluorescence: Origins, relation to photosynthesis and retrieval. *Comprehensive Remote Sensing* **3**: 143-162.
- Mohammed, G. H., R. Colombo, E. M. Middleton, U. Rascher, C. van der Tol, L. Nedbal, Y. Goulas, O. Pérez-Priego, A. Damm, M. Meroni, J. Joiner, S. Cogliati, W. Verhoef, Z. Malenovsky, J.-P. Gastellu-Etchegorry, J. R. Miller, L. Guanter, J. Moreno, I. Moya, J. A. Berry, C. Frankenberg, Zarco-Tejada, P. J. 2019. Remote sensing of solar-induced chlorophyll fluorescence (SIF) in vegetation: 50 years of progress. *Remote sensing of Environment* **231**: 111177.
- ESA. 2018. FLEX Mission Requirement Document, European Space Agency. ESAEOP-SM/2221/MDru-md. Available in https://download.esa.int/docs/FLEX/FLEX_MRD_v3.0_20180605_issued.pdf
- Morissette, J. T., F. Baret, J. L. Privette, R. B. Myneni, J. E. Nickeson, S. Garrigues, N. V. Shabanov, M. Weiss, R. A. Fernandes, S. G. Leblanc, M. Kalacska, G. A. Sanchez-Azofeifa, M. Chubey, B. Rivard, P. Stenberg, M. Rautiainen, P. Voipio, T. Manninen, A. N. Pilant, T. E. Lewis, J. S. Iames, R. Colombo, M. Meroni, L. Busetto, W. B. Cohen, D. P. Turner, E. D. Warner, G. W. Petersen, G. Seufert, Cook, R. 2006. Validation of global moderate-resolution LAI products: a framework proposed within the CEOS land product validation subgroup. *IEEE Transactions on Geoscience and Remote Sensing*, **44**(7), pp. 1804–1817. Doi: 10.1109/TGRS.2006.872529.
- Mohammed, G.H., Colombo, R., Moreno, J. et al. 2016. FLEX Bridge Study, Final Report ESA/ESTEC Contract No. 4000112341/14/NL/FF/gp. P & M Technologies. Pp. 192. Available in [https://www.pmtech.ca/FLEX/Reports/FB-Study_FINAL_REPORT_Full_Report_\(Public\).pdf](https://www.pmtech.ca/FLEX/Reports/FB-Study_FINAL_REPORT_Full_Report_(Public).pdf)
- Cogliati, S., W. Verhoef, S. Kraft, N. Sabater, L. Alonso, J. Vicent, J. Moreno, M. Drusch, Colombo, R. 2015. Retrieval of sun-induced fluorescence using advanced spectral fitting methods. *Remote Sensing of Environment*, **169**, 344–357. Doi: 10.1016/j.rse.2015.08.022.
- Peón, J., Jiménez, M., Cendrero-Mateo, M.P., Moncholi-Estornell, A., Gorroño, J., Van Wittenberghe S., Moreno, J. 2024. Uncertainty Assessment in Sun-Induced Chlorophyll Fluorescence Retrieval for FLEX Calibration and Validation Campaigns. EARSel Valencia 2024.
- Moncholi-Estornell, A., S. Van Wittenberghe, M. Pilar Cendrero-Mateo, L. Alonso, M. Jiménez, P. Urrego, A. Mac Arthur, Moreno, J. 2023. FluoCat: A cable-suspended multi-sensor system for the vegetation SIF Cal/Val monitoring and estimation of effective sunlit surface fluorescence. *International Journal of Applied Earth Observation and Geoinformation*, **116**, 103147.

AUTHOR INDEX

B

Bai, Zhaoyang - 82
Battipaglia, Giovanna - 48

C

Cabrera, Josep Marí - 54
Camacho, F. - 92, 97
Campos-Taberner, M. - 23, 31, 92, 97
Cao, Haiyi - 87
Cendrero-Mateo, M^a P. - 102
Chen, Qi - 13
Chen, Ruo-han - 70
Crisafulli, Virginia - 7, 48, 58

D

Delegido, J. - 102
Díaz-Delgado, R. - 102

G

Gao, Caixia - 64
García-Haro, F.J. - 23, 31, 92, 97
Gilabert, M.A. - 23, 31, 92, 97
Gimeno, Sergio - 7, 58
Gómez-Giráldez, P.J. - 102
González-Dugo, Maria P. - 41
Grosso, N. - 41

H

Hou, Xiaoxia - 76
Huang, Jin - 87

I

Iranzo, C. - 17

J

Jiménez, A. - 31
Jiménez, M. - 102
Jiménez-Guisado, A. - 23, 92, 97

K

Kabala, Jerzy Piotr - 48
Khachoo, Yasir Hassan - 27

L

Li, Hua - 87
Li, Wan - 64
Liu, Yue - 70
Lu, Chen - 82

M

Mao, Yilan - 87
Marti-Rocafull, P. - 41
Martínez, Beatriz - 23, 31, 92, 97
Martínez-Mateo, Elena - 27
Martínez-Sánchez, E. - 92, 97
Meng, Yaru - 64
Mo, Fan - 87
Moncholí-Estornell, A. - 102
Moreno, J.F. - 102
Muñoz-Gomez, M. - 41

P

Peng, Yao - 36
Peón, J.J. - 102
Pérez-Cabello, F. - 17

R

Ruescas, Ana B. - 27, 54

S

Sánchez-Ruiz, Sergio - 23, 31, 92, 97

Sánchez-Zapero, J. - 92, 97

Shang, Guo-fei - 1, 70, 76, 82

Shen, Ye-lin - 1

Silvestro, P.C. - 41

Skokovic, Drazen - 7, 48

Sobrino, José Antonio - 7, 48, 58, 87

Sobrino-Gómez, Álvaro - 7, 58

T

Tian, Yi-ran - 70

Tian, Yu-jia - 1, 82

V

Van Wittenberghe, S. - 102

W

Wang, Keming - 13

Wang, Ting - 36

X

Xiao, Jieyun - 36

Xu, Yinhong - 82

Y

Yan, Zheng-hong - 1, 76

Yin, Yanhe - 87

Yu, Wenping - 13, 36, 64

Z

Zeng, Biao - 1

Zhang, Ce - 70, 76

Zhang, Haiyi - 87

Zhang, Xia - 1, 70, 76, 82

Zhang, Xinwei - 87

Zhao, Enyu - 64

Zhou, Wei - 13, 36